High-pressure states of bismuth

Author:
PHILIP BROWN
Trinity Hall

Supervisor:
DR. MALTE GROSCHE
Trinity College

Department of Physics
University of Cambridge

A thesis presented for the degree of
Doctor of Philosophy
April 2017

Declaration

This report is the result of work carried out in the Quantum Matter group of the Cavendish Laboratory, Cambridge, between October 2013 and April 2017, except where otherwise stated. It is the result of my own work, and includes nothing done in collaboration except where indicated in the text and acknowledgements. It is not substantially the same as any that I have submitted for a degree or diploma or other qualification at the University of Cambridge or any other university or similar institution. The total length of this dissertation does not exceed sixty thousand words.

Philip Brown
April 2017

Acknowledgements

This work would not have been possible without the helpful discussions and moral support provided by a large number of people.

In QM, Matt Coak, Jordan Baglo, Seb Haines, Hugh Glass, Sofia Taylor, Paromita Mukherjee, Kieron Murphy and myriad others too numerous to name undertook the thankless task of listening to my discussions, suggestions, digressions and rants. Jiasheng Chen has a special place in my heart for providing presumably the world's only (and certainly the world's best) next-day-delivery high-quality bismuth-related crystal growth service.

Dan Cross and Mariusz Naguszewski provided helium for the thirsty SQUID, and Chris Summerfield and Nigel Palfry made us parts at short notice whenever we broke something. Patrick Reuvenkamp from Cryogenic was always there to dispense SQUID advice and ^{3}He. At Trinity Hall, Adam and Ewa, Malcolm, Jess and Sarah, and many others supported me along the way.

Ruth Laing has never given up encouraging me or consoling me as required, and for this I am eternally indebted. Katie, Nancy and Freya forgave me for the many times I forgot their birthdays trying to remember the differences between amorphous and incommensurate polymorphs of bismuth.

Finally there are three others deserving of special mention. Konstantin Semeniuk has worked closely with me on many projects from the beginning, and shares credit for a significant fraction of this work. Patricia Alireza has never been less than inspirational with her combination of a demand for high standards, a willingness to help whenever asked, and a happiness to pass on whatever small fraction of her expertise I am capable of absorbing. Malte Grosche, whose understanding of physics is matched only by his joy in discovering it, has supervised me for many years and never complained once.

To my parents.

Outline

Bismuth is among the most studied of all elements, but its behaviour under pressure exhibits myriad unexpected puzzles even after many decades of research. Bismuth narrowly avoids being an insulator: a Peierls-type distortion almost completely gaps the electronic energy bands, producing a rhombohedral metal with a tiny overlap of conduction and valence bands. The resulting solitary free electron per 100,000 atoms can travel large distances in high-purity crystals, leading to a host of unusual properties.

We show that the rhombohedral structure can be tuned with pressure, driving the carrier concentration to nearly zero. We compare our measurements to recent experimental advances implying the formation of novel electronic order driven by the pairing of low-density electrons and holes, and show evidence for a previously unseen phase at very low temperatures in the semiconducting state. We also present a method for calculating the carrier density and resistivity as a function of pressure, based on phenomenological band parameters and a simple charge-balance argument, and demonstrate that this approach can quite well describe most - but not all - of the observed behaviour of the resistivity.

At higher pressures, bismuth undergoes a transition into a quasiperiodic host-guest structure. Here, two distinct crystal lattices coexist and interpenetrate, but the lattice parameters are incommensurate. This crystal thus lacks a single unit cell - an unexpected complexity for a simple element. The discovery of such unusual structures in elements is a new phenomenon and their physical properties are rather unexplored. We present experimental measurements of the resistivity and magnetic susceptibility in the incommensurate host-guest state. We argue that the experimental data (in particular, the shape of the normal-state electrical resistivity, and the high value of the low-temperature upper critical field) may be evidence for strong electron-phonon coupling. This strong coupling is consistent with theoretical predictions which suggest the presence of a low-energy phonon mode arising due to the vanishing energy cost of moving guest atoms through the host lattice.

Contents

1 Introduction

In this section, we provide a broad outline of several underlying themes in condensed matter physics: electrons in solids, their pairing to cause superconductivity, and their interaction with phonons. Then, we give a brief overview of this work's study of such themes.

1.1 Electrons in solids and the Fermi liquid

The interacting electrons in solids give rise to a vast and diverse range of phenomena, from electrical conductivity to magnetism to superconductivity. In most metals, electrons form a Fermi liquid - a sea of quasiparticles (electrons surrounded by the effects of their interactions) which behave like weakly-scattering electrons with altered masses. That this is the case is rather profound in its banality - the awkward fact that electron-electron interactions in metals are extremely strong can be largely ignored, as some of the interaction effects can be put into modifications of the quasiparticle mass. The resulting quasiparticles can be long-lived near the Fermi level (at least at $T = 0$), even if they remain strongly-interacting. These interaction effects can also give rise to the emergence of new many-body effects.

In some materials the effective mass can vary dramatically from that of the bare electron: in elemental bismuth the effective mass is as small as one thousandth of the electron's, and highly anisotropic, while in heavy fermion compounds quasiparticles look like electrons with a thousand times the usual mass. The same theory of the Fermi liquid proves fairly effective in describing quasiparticles with a mass spanning six orders of magnitude.

1.2 Superconductivity

Electrons in the Fermi sea are prone to an instability termed superconductivity. In a superconductor, the formation of a coherent state of paired electrons allows the flow of current without resistance and the expulsion of magnetic fields. Superconductivity is a cooperative phenomenon founded on the interaction of many electrons, and the pristine dissipationless nature of current flow has attracted the attention of many physicists. The fundamental physics of conventional superconductivity is now well-understood, being governed by the theory of Bardeen, Cooper and Schrieffer (BCS) [1]. This framework states that electrons condense through an attractive interaction mediated by phonons; the resulting many-body state cannot be perturbed without the payment of an energy cost which is unavailable at the low temperatures where BCS superconductivity is observed.

Superconducting wires (which can transmit very large currents without any energy loss from dissipative heating) are widely used in a range of technological applications, from magnets in MRI scanners to power cables in some parts of the US's national grid. However, conventional superconductors typically work only at low temperatures; indeed, the BCS theory constrains the transition temperature T_c to remain low: $T_c \sim \Theta_D e^{-1/VN(E_F)}$, where Θ_D is the Debye temperature (typically a few hundred kelvin in metals), $N(E_F)$ is the density of states at the Fermi level E_F, and V is the electron-phonon coupling energy. The superconducting transition temperature (in the BCS regime $VN(E_F) \ll 1$) is therefore exponentially small in comparison to the Debye energy, explaining the

observed transition temperatures of a few kelvin, at least for most elemental BCS superconductors[1].

It therefore came as something of a surprise when a whole new breed of superconductors were discovered near the end of the twentieth century. The host was rather unlikely: the ceramic cuprate $YBa_2Cu_3O_{7-x}$ and its sister compounds. At the ideal stoichiometry, these materials are ceramic insulators; it is thus quite striking that with the addition of excess hole charge carriers they transition into a zero-resistance state at remarkably high temperatures, in some cases above a hundred kelvin. After a quarter-century of intensive research in the field, a cohesive understanding of the nature of superconductivity in these materials is still lacking. Certainly the electrons form Cooper pairs; seemingly this is not caused by phonons. The pairing mechanism is speculated to be magnetic, but a fundamental understanding is still sought. A new piece has recently been added to the puzzle, with the discovery of unconventional superconductivity in the iron pnictides. These materials share many similarities with the cuprates - both form layered structures, both possess similar phase diagrams (in which the addition of holes drives the electronic structure out of an antiferromagnetic state), and both can superconduct at fairly high temperatures via a non-BCS mechanism. It is hoped that investigations in the iron pnictides will shed new light on mechanisms for superconductivity [2].

Many other families of materials are also superconducting (such as the strong-coupling A15 materials). There is a complex interplay between the crystal structure of such materials, their electronic properties, and their superconductivity.

1.3 The role of structure

The spatial arrangement of atoms largely dictates the electronic properties of a material. The atomic structure produces a periodic potential which acts upon the sea of conduction electrons; the details decide, for example, whether a material is metallic or insulating. In addition, electrons can interact with lattice distortions dynamically via the Coulomb interaction (lattice distortions cause an imbalance in local charge density which couples to the charged electrons), giving rise to electron-phonon coupling.

Much of condensed-matter physics has focused on the study of perfectly-ordered crystalline structures. The behaviour of a material can become more complex - and more interesting - when such order breaks down. A promising avenue for exploration is in materials which, while not being amorphous or disordered, lack the repeat unit that characterises a truly crystalline material (in a true ordered crystal, the system can be described by repeats of a single simple pattern termed the unit cell). One such example is quasicrystals; little-studied alternatives are the incommensurate host-guest structures that forms in many elements at high pressure.

1.4 The role of pressure

Pressure forces unwilling atoms closer together in a material, disrupting the balance between forces that gives a crystal its structure. This tunes a system's electronic properties, modifies its phonon

[1] There are a few recently-discovered exceptions, such as MgB_2, or H_3S at very high pressure, in which the superconductivity is of BCS type but the transition temperature is much higher; this is typically due to an enhancement of the Debye temperature due to unusually high-energy phonon modes.

spectrum, and can even force the atoms into an alternative structure with very different properties. Crucially, it does so in a very clean fashion: no additional impurities are introduced into a crystal as it is pressurised, and the exact same sample can be studied at many different pressures.

There are many examples in condensed-matter physics of high pressure producing unexpected results, such as the observation of coexisting ferromagnetism and superconductivity [3]. Magnetism has long been considered the mortal enemy of conventional superconductivity. The application of magnetic fields destroys superconductivity, and for the conventional BCS superconductors the required critical fields are fairly small (e.g. only a few tens of mT for lead or tin). Ferromagnetism, in which electron spins align, was thought fundamentally anathematic to the formation of Cooper pairs, which relies on the pairing of electrons with oppositely-directed spins. However, in the case of some heavy fermion materials (notably UGe_2) it has been observed that superconductivity appears to arise out of a ferromagnetic state [3]. In particular, applied pressure can drive the suppression of a ferromagnetic transition to zero kelvin, a so-called quantum critical point, leading to the emergence of unconventional superconductivity. The role magnetism has to play in this is still poorly understood, as are the similarities with cuprate superconductivity. Superconductivity in the cuprates may arise due to fluctuations associated with a quantum critical point, analogous to that observed in heavy fermion materials under pressure.

High pressure has often been used to drive other materials superconducting. Elements as unlikely as oxygen become superconducting under sufficiently high pressures [4]. Exceptionally high pressures can lead to exceptionally high transition temperatures: superconductivity has been observed in hydrogen sulphide at temperatures above 200 K - tantalisingly close to room temperature (for an Antarctic winter night), or temperatures attainable by conventional refrigeration techniques [5]. It is believed that hydrogen becomes metallic and superconducting at sufficiently high pressures, and theoretical predictions suggest its transition temperature may be above room temperature [6]. Pressure is thus a crucial and widely-used tool for driving materials superconducting.

Pressure can also lead to the emergence of very unexpected structures. For example, a number of elements undergo a structural transition at high pressures to an incommensurate host-guest phase, in which there are two interpenetrating unit cells with non-matching lattice parameters [7]. This leads to a structure which, while well-ordered, has a unit cell theoretically infinite in size. Little work has been done on what consequences this has for the physical properties.

1.5 This work

In this thesis, we investigate the behaviour of the element bismuth when compressed to pressures of up to 100,000 atmospheres. We use pressure as a tuning parameter to probe the Fermi liquid and investigate new superconducting structures. Bismuth, as a semimetal poised between metallic and insulating states, exhibits a plethora of unconventional physics even at ambient pressure. These in part arise because the Fermi liquid effective mass is very small ($< 0.001 m_e$ in some directions, where m_e is the bare electron mass), meaning electrons are exceptionally mobile [8]. Additionally, because the carrier density is so low, carriers do not effectively screen each other, and they may be much more correlated than might naively be expected from the low mass; this is hypothesised to lead to the emergence of various intriguing states at high field [9, 10, 11, 12].

In Chapter 2, we present a brief overview of the theoretical background of metals, semimetals and semiconductors, and discuss theories of charge transport and electrical resistivity. We briefly consider theories of BCS and strong coupling superconductivity, and the role of phonons in a material. Chapter 3 then describes the experimental methods employed to measure the physical properties of bismuth at high pressure, including a discussion of cryogenic techniques and high-pressure cells.

In the semimetallic phase of bismuth, pressure can disrupt the careful balance between metallic and insulating states, in principle turning this semimetal into an semiconductor. While this transition has been studied for many decades, a large number of open questions remain, and in Chapter 4 we present our attempts to resolve them with modern high-pressure techniques and recent experimental and theoretical advances. We show that, while pressure does indeed dramatically influence the electronic properties, the details are rather complicated. We demonstrate a method to calculate the resistivity of bismuth as a function of pressure, and show that this can fairly well describe most of the experimental behaviour, without a need to invoke complex many-body effects occuring at low temperatures, as has previously been suggested [11, 12]. We also present results down to low temperatures, suggesting the formation of a hitherto-unseen phase.

Bismuth has recently been shown to possess an incommensurate host-guest phase, occuring at rather low pressures in comparison to such phases in other elements [13]. The observable consequences of the loss of translational symmetry central to this structure remain almost unexplored; in this thesis, we begin to investigate them. We provide experimental evidence for the predicted appearance of an unusual feature in the phonon spectrum, as a direct result of the incommensurate structure. The lack of symmetry should give rise to a low-lying phonon mode (arising from the motion of one crystal lattice with respect to the other) which will cause dramatically enhanced electron-phonon coupling. Density functional theory calculations indicate that precisely this occurs. Experimentally, this phonon mode should result in the formation of a strong coupling superconductor, and we demonstrate that this is indeed what happens.

2 Theoretical overview

In this section, we summarise the fundamental condensed-matter theories underpinning our experimental results. We begin with a brief overview of electrons in a periodic lattice, the role of the periodic potential in producing multiple bands, and the division of materials into metals and insulators. Then we discuss models for the resistivity, including the semiclassical Drude theory with multiple bands, and consider the role of phonons. We examine the impact of the different contributions of the carrier density and scattering rate to a material's resistivity, and remark on how semimetals such as bismuth are unusual in this respect. Finally, we provide a brief overview of Ginzburg-Landau and BCS theories of superconductivity.

2.1 Electrons in metals

2.1.1 Electron dispersion and periodicity

It is a rather remarkable fact that any progress at all can be made in modelling the physics of electrons in materials. We can rather straightforwardly write down the Hamiltonian for the system, but solving it exactly even for the most trivial of systems is impossible. There are $\sim 10^{23}$ atoms and a similar number of electrons present in any macroscopic sample of a condensed-matter system, these electrons are strongly interacting (because of the large Coulomb repulsion between them), and Pauli exclusion means that the resulting wavefunction is a fermionic many-body state which feels the effects of the exchange interaction. Nevertheless, with a series of radical approximations a great deal of useful physics can be extracted from simple models.

If we treat the atomic locations as fixed (a plausible assumption, because $M \gg m_e$ where M is the ion mass and m_e the electron mass, so the ion kinetic energy is negligible), we find the main role of the lattice is to introduce a periodic potential acting on the electrons [14]. The eigenfunctions of the Hamiltonian (neglecting, for the moment, electron-electron interactions, which are briefly discussed in Section 2.1.4), are Bloch states with the same periodicity as the crystal lattice. If there was no interaction with the lattice, the electrons would possess a dispersion similar to that of free-space electrons:

$$E_k = \frac{\hbar^2 k^2}{2m_e} \tag{2.1}$$

where k is the wavenumber and $\hbar$ Planck's reduced constant. States outside the first Brillouin zone (the reciprocal space unit cell) are folded back into it; this gives rise to the formation of multiple bands of electron states.

The periodic potential induces splitting of these bands: states that are separated by a reciprocal-space lattice vector hybridise. This produces gaps in the electron dispersion (see Fig. 2.1). The band gap is of critical importance in determing the properties of a material. In particular, it sets whether the material is a metal or an insulator.

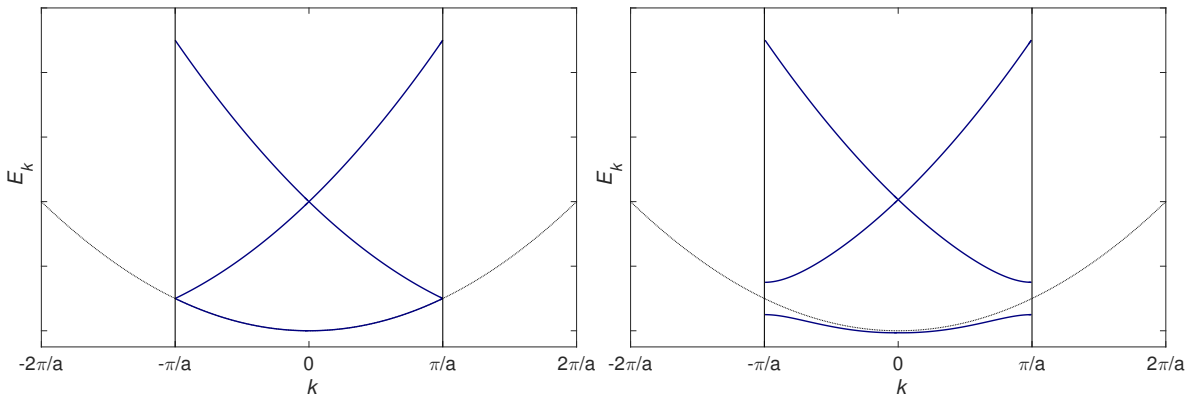

Figure 2.1: Schematic electron dispersion in the presence of a periodic potential, in one dimension. In the absence of periodicity, the dispersion is quadratic, $E_k \sim k^2$ (light dotted line). The periodicity maps states outside the first Brillouin zone $-\pi/a \leq k \leq \pi/a$ (solid vertical lines) back inside, giving rise to multiple bands. On the left, we assume no periodic potential, so the bands are degenerate at the edges of the Brillouin zone. On the right, we set the first Fourier coefficient of the periodic potential to a finite value. This causes bands at similar energies to repel, opening a band gap at the Brillouin zone edge. Including higher-order Fourier terms would induce hybridization between energy levels and a gap between bands (rather than a crossing) at the zone centre.

2.1.2 Metals and insulators

The theory above considered only a single electron, and depended only on the lattice periodic potential V_G. It did not consider the effects of having multiple electrons. However, if we assume that the electrons are only weakly correlated, then we can imagine that electrons merely fill up one-electron $k-$states until all the required electrons are accounted for. We term the energy that divides occupied from empty states at zero temperature as the Fermi level E_F.

There are two distinct cases for materials in the simple model above: E_F can sit within a band (in which case the material is a metal), or E_F can lie within the band gap (in which case the material is an insulator), as shown in Fig. 2.2. The position of E_F will be set by the number of valence electrons per atom and the number of atoms per unit cell, though some care must be taken to correctly account for spin degeneracy: every k-state can accommodate two electrons, one of each spin. The number of k-states in the first Brillouin zone is equal to twice the number of atoms in the unit cell, so a monovalent element with a simple cubic cell will only half-fill the first band with electrons. We would therefore expect such simple cubic monovalent elements to be metals, and indeed this is the case: lithium, sodium, potassium etc. are metallic.

The properties of a material are dominated by the behaviour at E_F. In the case of a metal, because E_F lies in a band there are unoccupied states arbitrarily close in energy to states at the chemical potential: this allows electric current to flow, for example, because all the states can be shifted from their equilibrium position k to $k+\delta k$, giving the electrons a finite net momentum. In contrast, for an insulator this at not possible at zero temperature, because there are no unoccupied states for electrons to be moved to by the application of an electric field - the whole band is full. At higher temperatures, some states in the filled band become empty, because electrons are thermally excited from lower to higher bands, and this allows current to flow in insulators at higher temperatures, as

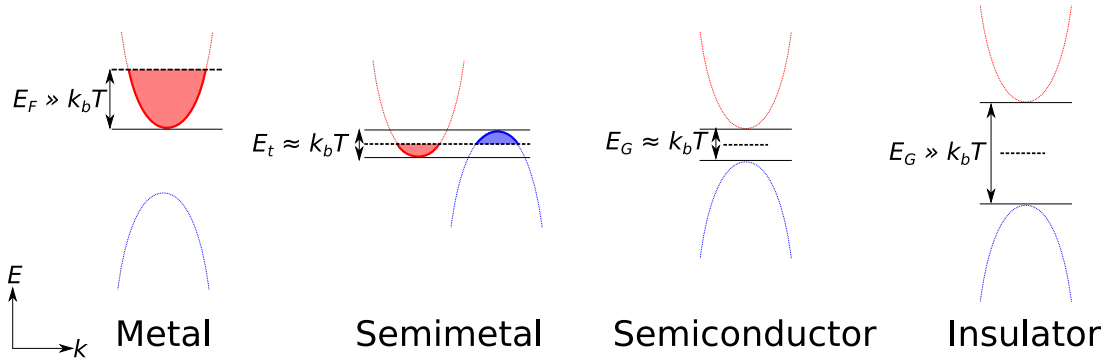

Figure 2.2: The Fermi level and its influence on occupied states. The valence and conduction bands are shown as red and blue light dashed parabolas; filled states are denoted by thicker lines and colours. The position of the Fermi level is shown by the thick dashed black line, as well as the location of the Fermi level E_G, overlap energy E_t, and band gap E_G in comparison to the room-temperature thermal energy k_bT .

seen experimentally.

Semiconductors, like insulators, possess a band gap with energy E_G, but the size of the gap is much smaller. A semimetal is distinguished from a metal by a band overlap between conduction and valence bands of a size $\sim k_bT$, the thermal energy, where k_b is Boltzmann's constant and T is the temperature. Semimetals are typically compensated, with equal numbers of electrons and holes.

In a metal, all the states up to the Fermi level E_F are filled at 0 K. In a simple isotropic free-electron model, this corresponds to filling all the $k-$states within a sphere whose radius is the Fermi wavevector k_F (where $E_F = \hbar^2 k_F^2/2m$):

$$k_F = \left(3\pi^2 n\right)^{1/3} \tag{2.2}$$

where n is the carrier density of electrons. At a given temperature T, the probability a state with energy E is occupied will be given by the Fermi-Dirac distribution:

$$f\left(E,\mu,T\right) = \frac{1}{e^{\frac{E-\mu}{k_bT}}+1}. \tag{2.3}$$

where μ is the chemical potential (the energy at which states have a 50 % chance of being occupied; at $T = 0$, $\mu = E_F$), and k_bT is the thermal energy. While the above model is fairly simple, the underlying ideas work well for many materials. Modern density functional theory (DFT) techniques allow the calculation of the actual dispersion relation E_k for a given material from first principles (with a few caveats, in particular that electron-electron interactions may not be accurately captured). The true band structure can be very complex for real materials, but the basic principle holds: materials where E_F lies in a band gap are insulating, while materials with bands crossing the Fermi level E_F are metallic. There are a few sub-classifications: semiconductors are insulators with a comparatively small band gap, and semimetals are metals where the Fermi level is extremely small.

2.1.3 Temperature dependence of the carrier density

One key difference between metals and insulators is the number of free charge carriers they possess as a function of temperature. The density of electrons $n_e(T)$ is given by:

$$n_e(T) = \int_{E_c}^{E_{c,u}} g_e(E) f(E, \mu, T) dE. \tag{2.4}$$

Here E_c is the energy of the bottom of the conduction band, $E_{c,u}$ that of the top, and $g_e(E)$ the electron density of states per energy. We set the conduction band edge at $E_c = 0$.

In the case of a metal, the Fermi level is ~ 1 eV above the band edge, meaning the Fermi temperature is at least 10,000 K. Then $f(E, \mu, T)$ is essentially a step function at $E = E_F$ for all practicable temperatures, and the carrier density $n(T)$ will remain approximately constant for all T.

By contrast, for a semiconductor the Fermi level lies below the conduction band edge, thus the Fermi level is negative. In this case, the carrier density will be strongly temperature-dependent. In the parabolic-band approximation, the density of electron states, $g_e(E)$, is given by the dimensionality d of the system:

$$g_e(E) = G_d \left(E - E_c\right)^{\frac{d-2}{2}} \Theta(E - E_c). \tag{2.5}$$

The Heaviside step function $\Theta(x) = 1$ for $x > 0$ and 0 else, ensuring $g(E)$ is not complex. G_d is a dimensionality-dependent constant, where d is the dimensionality of the system [14]:

$$G_3 = \frac{1}{2\pi^2} \left(\frac{2m}{\hbar^2}\right)^{3/2} \tag{2.6}$$

$$G_2 = \frac{m}{\pi h^2} \tag{2.7}$$

$$G_1 = \frac{1}{\pi} \left(\frac{m}{\hbar^2}\right)^{1/2}. \tag{2.8}$$

Putting everything together, and assuming that $E_{c,u}$ can be taken to infinity, as f will go to zero first, we obtain:

$$n_e(T) = G_d \int_0^\infty \frac{E^{\frac{d-2}{2}}}{1 + \exp\frac{E - E_F}{kT}} dE \tag{2.9}$$

In the case where $E - E_F \gg kT$, we can approximate the denominator and hence solve analytically (the non-degenerate case). Otherwise, we must do the calculation rigorously.

In the non-degenerate case, we have that the exponential is large. Then:

$$n_e(T) \approx G_d \int_0^\infty E^{\frac{d-2}{2}} e^{-\frac{E - E_F}{kT}} dE \tag{2.10}$$

$$n_e(T) = B_d T^{\frac{d}{2}} e^{-\frac{E_c - E_F}{kT}} \tag{2.11}$$

with B_d a dimension-dependent constant. Assuming that the Fermi level sits at the centre of the gap between a conduction and valence band, i.e. $E_c - E_F = E_g/2$ where E_g is the band gap, we

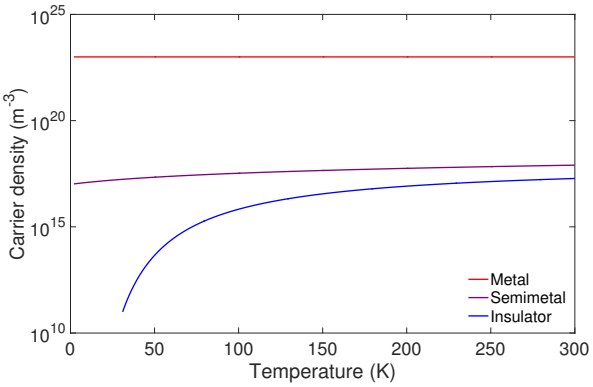

Figure 2.3: Schematic of carrier densities $n(T)$ for materials with different band structures as a function of temperature.

then obtain a carrier density that is Arrhenius-activated:

$$n_e(T) \sim T^{\frac{d}{2}} e^{\frac{E_g}{2k_bT}}. \tag{2.12}$$

From the above discussion, we can therefore make the following qualitative distinction between metals and insulators (assuming the insulator's band gap is $\gg k_bT$ at experimentally-accessible temperatures). In a metal, the carrier density is finite at all temperatures, and constant with temperature. In an insulator, the carrier density is strongly temperature-dependent: it falls sharply as T decreases, and vanishes as $T \to 0$; see Fig. 2.3 for a schematic.

Semimetals occupy an unusual position just on the side of metallic behaviour: their Fermi level may be only ~ 100 K. The result is that a semimetal possesses a finite carrier density even at zero temperature (although this carrier density will typically be very small compared to good metals such as copper), and this carrier density can be notably temperature-dependent. A detailed discussion of this phenomenon, as applied to the semimetal bismuth, is given in Chapter 4.

2.1.4 Fermi liquid theory

The assumption that electrons do not interact is, of course, not accurate: a metal contains many electrons, and these electrons should experience a strong Coulomb repulsion. Nevertheless, it proves to work reasonably well for many materials, if we instead replace the bare electrons in a material with composite objects termed quasiparticles. A quasiparticle can be thought of as the combination of an electron and its interactions with other electrons. This is termed a Landau Fermi liquid. Here we closely follow the arguments given by Ashcroft and Mermin [14].

The core idea of Landau Fermi liquid theory is that, while the approximation of metals as hosting weakly-interacting *electrons* may be flawed, we can arrive at a similar result by assuming they host some *other* sort of long-lived fermionic excitation. Then, the qualitative behaviour of the system will be essentially the same as that of the weakly-interacting picture outlined above, except the material properties of the particles involved (most notably, their mass) may change.

Consider an excited quasiparticles at an energy $E_1 > E_F$ and zero temperature, assuming only

that this quasiparticle is a fermion (so Fermi-Dirac statistics hold) and that quasiparticle scattering is weak (so the Fermi sea is a coherent concept). If we allow quasiparticle-quasiparticle interactions, then the one-particle states are no longer eigenstates of the Hamiltonian, and the quasiparticle will not have an infinite lifetime. This quasiparticle can interact with quasiparticles in the filled Fermi sea ($E_2 < E_F$), scattering both quasiparticles to new energy levels E_3 and E_4. The region of possible allowable energies $E_{2,3,4}$ must lie within an energy range $E_F \pm E_1$of the Fermi level; conservation of energy constrains the energies before and after the scattering to be equal, which means there are only two independent scattering energies, and the quasiparticle scattering rate τ_{qp}^{-1} must then be:

$$\tau_{qp}^{-1} \sim (E_1 - E_F)^2 . \tag{2.13}$$

At finite temperature, the range of partially-occupied energy levels includes a shell of width $k_b T$ around E_F, and by the same argument we get:

$$\tau_{qp}^{-1} \approx a_1 (E_1 - E_F)^2 + a_2 (k_b T)^2 \tag{2.14}$$

where a_1 and a_2 are constants. This implies that, at sufficiently low temperatures $T \ll E_F$, and sufficiently close to the Fermi surface, the scattering rate τ_{qp}^{-1} becomes extremely small - that is, the one-quasiparticle states, on the timescale of our system, *are* in fact eigenstates of the Hamiltonian, so the non-interacting picture is justified. Ashcroft and Mermin give a brief discussion of what "sufficiently close" involves [14]. The role of electron-electron interactions is to modify the exact dispersion relation E_k, without significantly affecting the qualitative behaviour of the many-body state.

At low enough temperatures, the rate of real quasiparticle scattering becomes low even if the quasiparticle interactions are strong (as they are, for example, in ^{3}He in its Fermi liquid state, where the Landau Fermi liquid parameters which describe the strength of interactions are not in fact small, but close to unity). Strong quasiparticle interactions, with large Fermi liquid parameters, may lead to high rates of forward scattering; this does not cause quasiparticle decay, but enhances some physical properties such as the Stoner factor in the magnetic susceptibility. This renormalization of physical parameters, beyond only the mass, can point to the appearance of new ground states for the electrons, often with novel physical properties.

2.2 Phonons

The above sections have completely neglected the role of atoms, except in using the periodicity of the potential they impose. In fact, experimentally the atomic lattice plays an important role in the physics of materials, in the form of phonons: discretised bosonic vibrations of the crystal lattice. At finite temperatures, they typically contribute significantly to many material properties: at 300 K, in most metals scattering of electrons from phonons outweighs electron-electron scattering by many orders of magnitude [14]. A simple heuristic explanation for why this is so considers the ratio of the characteristic energy scales of electrons and phonons: electrons are characterised by their Fermi level $E_F \approx 10,000$ K, while phonons have their energy scale set by the Deby energy $\Theta_D \approx$

100 K. Thus, for conventional metals, at all reasonable temperatures the electrons are very little influenced by temperature (for example, the Fermi-Dirac distribution barely changes), while the number of phonons is very strongly temperature-dependent. This is the whole rationale behind the low-temperature physics of materials: at room temperature, there are too many phonons present to observe electronic effects, thus we must cool to very low temperatures to reduce the effects of phonons in our systems.

Just as we use a simple theory of non-interacting electrons to derive the dispersion relation of electrons as a function of wavevector k, we can accomplish a similar feat for phonons beginning from a simple starting point. Assume that atoms in a material occupy their equilibrium positions at zero temperature (neglecting zero-point motion); at finite temperature, thermal energy will allow deviations from these positions. The system can then be described as set of masses coupled by springs, and we can use the periodicity of the system to obtain the normal modes. This defines a dispersion relation for phonons ω_q, linear in q at small q (see Ashcroft and Mermin for details [14]). By Taylor's theorem, for small displacements each atom has an excess energy quadratic in its displacement from equilibrium, regardless of the actual energy landscape. Interactions between several atoms, or more complex unit cells, complicate the phonon spectrum but do not significantly alter the basic physics, simply adding more oscillatory modes to the spectrum, with more complex dispersions.

At higher temperatures, anharmonic effects become relevant; these are missed in the simple quadratic energy approximation of the ball-on-spring model, which corresponds to only the first term in a full Taylor expansion of the lattice energy as a function of atomic displacement from equilibrium. At high temperatures, the higher thermal energy allows atoms to stray further from equilibrium, exploring higher-energy regions where higher-order terms in the expansion become relevant.

Because the ions are charged, their oscillation affects the behaviour of electrons, via electron-phonon coupling. This gives rise to two notable phenomena. The first is electron-phonon scattering, which at high temperatures is the dominant scattering process contributing to the resistivity (see Section 2.3.4). The second is superconductivity: the electron-phonon interaction can lead to an effective attractive interaction between electrons, giving rise to phonon-mediated (BCS and strong coupling) superconductivity. Of crucial relevance is the electron-phonon interaction strength, λ. This sets how strongly the electrons couple to the lattice vibrations, and is given by :

$$\lambda = 2 \int_0^{\omega_{max}} \alpha^2 F(\omega) \omega^{-1} d\omega. \tag{2.15}$$

The parameter $\alpha^2 F(\omega)$ is the electron-phonon spectral function (or Eliashberg function), and is related to the phonon density of states $F(\omega)$ and the electron-phonon matrix element at a given frequency, $\alpha(\omega)$. The electron-phonon spectral function can be obtained from first-principles calculations, or measured through superconducting tunnelling experiments (see [15, 16, 17, 18, 19]). The parameter λ is a critical component of the theory of phonon-mediated superconductivity, and also impacts the electrical resistivity (see below). An extremely useful overview of the electron-phonon coupling, particularly with relevance to superconductivity, is given by Allen [16, 17, 19].

2.3 Resistivity

Resistivity measures the strength of a material's objections to the flow of charge. It is a quantity which, while relatively straightforward to measure, is not so simple to interpret. We begin with the simple Drude model, which externally imposes a scattering time τ and a carrier density n, and considers the role of magnetic fields on the measured resistivity. Then we consider the different phenomenology between metals, insulators and semimetals, before looking at some scattering mechanisms.

2.3.1 Drude model of the resistivity

Consider the flow of charge carriers with a charge q, mass m (which may not be the bare electron mass), and number density n. They move at a velocity $\mathbf{v}$, with a characteristic time between scattering events τ.

The current density obeys:

$$\mathbf{J} = nq\mathbf{v}. \tag{2.16}$$

From the Lorentz force, the equation of motion is:

$$m\left(\frac{d}{dt} + \frac{1}{\tau}\right)\mathbf{v} = q\mathbf{E} + q\mathbf{v} \times \mathbf{B} \tag{2.17}$$

where $\mathbf{E}$ and $\mathbf{B}$ are the electric and magnetic fields. In equilibrium, we have $d/dt = 0$.

The conductivity and resistivity tensors $\underline{\underline{\sigma}}$ and $\underline{\underline{\rho}}$ are defined by:

$$\mathbf{J} = \underline{\underline{\sigma}}\mathbf{E} \tag{2.18}$$

$$\underline{\underline{\rho}} = \underline{\underline{\sigma}}^{-1}. \tag{2.19}$$

Assuming a single band, in the absence of $\mathbf{B}$ fields we straightforwardly solve the above equations to obtain the Drude conductivity:

$$\sigma_0 = \frac{nq^2\tau}{m}. \tag{2.20}$$

When $\mathbf{B}$ is non-zero, we must evaluate the cross-product. Picking $\mathbf{B} = B\hat{\mathbf{z}}$, defining $\gamma = qB\tau/m = \omega_c\tau$, where ω_c is the cyclotron frequency, we obtain [20]:

$$\underline{\underline{\sigma}} = \frac{\sigma_0}{1+\gamma^2}\underline{\underline{\gamma}} \tag{2.21}$$

$$\underline{\underline{\gamma}} = \begin{pmatrix} 1 & \gamma & 0 \\ -\gamma & 1 & 0 \\ 0 & 0 & 1+\gamma^2 \end{pmatrix}. \tag{2.22}$$

Real systems possess multiple bands, with different densities n_i, scattering rates τ_i, masses m_i and charges $q_i = \pm e$ for holes and electrons respectively. We can straightforwardly generalise the above equations by subscripting everything necessary with a band index i. When we have N bands,

we can simply add the conductivity together from each one [20, 21]:

$$\underline{\underline{\sigma}} = \sum_i^N \frac{\sigma_i}{1+\gamma_i^2} \underline{\underline{\gamma_i}}. \tag{2.23}$$

$$\underline{\underline{\sigma}} = \begin{pmatrix} \sum_i^N \frac{\sigma_i}{1+\gamma_i^2} & \sum_i^N \frac{\sigma_i \gamma_i}{1+\gamma_i^2} & 0 \\ \sum_i^N \frac{-\sigma_i \gamma_i}{1+\gamma_i^2} & \sum_i^N \frac{\sigma_i}{1+\gamma_i^2} & 0 \\ 0 & 0 & \sum_i^N \sigma_i \end{pmatrix}. \tag{2.24}$$

However, the conductivity is not measured: we measure the resistivity tensor $\underline{\underline{\rho}} = \underline{\underline{\sigma}}^{-1}$. Inverting the above matrix is not a trivial task.

When $N = 1$, we obtain:

$$\underline{\underline{\rho}} = \begin{pmatrix} \frac{1}{\sigma_0} & -\frac{B}{nq} & 0 \\ \frac{B}{nq} & \frac{1}{\sigma_0} & 0 \\ 0 & 0 & \frac{1}{\sigma_0} \end{pmatrix}. \tag{2.25}$$

For a single-band system, the off-diagonal resistivity $\rho_{xy} = RB$ is termed the Hall resistivity, with $R = 1/nq$; it gives a direct measurement of the carrier density. The diagonal terms are field-independent - in a one-band model there is no magnetoresistance.

In multi-band systems, inverting Eq. 2.24 becomes exhausting. It can be done, with some work, for one electron band and one hole band, with Hall coefficients $R_{e,h}$ and conductivities $\sigma_{e,h}$ (all defined to be positive) [20, 21]. We obtain:

$$\rho_{xy}(B) = \frac{\sigma_h^2 R_h - \sigma_e^2 R_e - \sigma_h^2 \sigma_e^2 R_h R_e (R_h - R_e) B^2}{(\sigma_e + \sigma_h)^2 + \sigma_e^2 \sigma_h^2 (R_h - R_e)^2 B^2} B \tag{2.26}$$

$$\rho_{xx}(B) = \frac{1}{\sigma_e + \sigma_h} \frac{\sigma_e \sigma_h \left(\sigma_h R_h + \sigma_e R_e\right)^2 B^2}{\left(\sigma_e + \sigma_h\right)^2 + \sigma_e^2 \sigma_h^2 \left(R_h - R_e\right)^2 B^2}. \tag{2.27}$$

where ρ_{xx} is the diagonal transverse magnetoresistance. We thus obtain the result that, for two bands, the Hall resistivity $\rho_{xy} \sim B$ in both the low- and high-field limits (but with different gradients, and perhaps with different signs), and that the transverse magnetoresistance $\rho_{xx} \sim B^2$ at low field. The high-field magnetoresistance will in general saturate, $\rho_{xx} \sim const.$, in the case of an uncompensated metal, where $n_e \neq n_h$ so $R_e \neq R_h$. For a compensated metal, $n_e = n_h$ and $R_e = R_h$, the factor $(R_h - R_e)^2$ vanishes from the bottom of the fraction and we obtain that $\rho_{xx} \sim B^2$ for all B, without saturation. This holds assuming closed Fermi surface orbits without magnetic breakdown; with open orbits or very high magnetic fields, the situation may be more complex [22].

2.3.2 Temperature dependence of the resistivity

So far, we have assumed that n and τ (or the scattering rate, τ^{-1}) are fixed quantities. In reality, both will be temperature-dependent. The result of measurements of the resistivity's temperature dependence, $\rho(T) \sim \tau^{-1}(T)/n(T)$, will depend on which dominates.

The scattering rate will typically increase with temperature, whether the source is electron-electron or electron-phonon scattering, and often follow some power law, such as $\tau^{-1} \sim T^2$ for

electron-electron scattering (see later sections). In an insulator, the carrier density is also temperature-dependent, $n \sim e^{-E_g/2k_bT}$ via an Arrhenius factor which changes over many orders of magnitude as T is reduced from 300 to 2 K. This exponential factor overwhelmingly dominates the resistivity: the rising carrier density means the resistivity of an insulator falls sharply with increasing T.

By contrast, a metal has an approximately constant carrier density. Its resistivity is therefore dominated by the temperature dependence of the scattering rate. This will fall as T is reduced: a metal thus has a resistivity which increases with increasing T.

In a semimetal, where n may not be constant but is not Arrhenius-activated, both factors compete. The result will be quite a complex temperature dependence of $\rho(T)$ which will depend on the relative magnitudes of the two effects (which may be different for different bands), as well as the details of both $n(T)$ and $\tau^{-1}(T)$. This is considered in Chapter 4.

2.3.3 Electron-electron scattering

As noted in Section 2.1.4, the scattering rate between electron (or, really, quasiparticle) states is quadratic in temperature:

$$\tau_{ee}^{-1} \sim T^2. \tag{2.28}$$

This is typically the behaviour seen in metals at low temperatures, once phonon scattering becomes irrelevant [14].

Deviations from the standard Fermi liquid theory are often manifested in changes in the scattering exponent, as measured by resistivity at low temperatures. This is seen, for example, in the "marginal Fermi liquid" $ZrZn_2$, where in zero field the resistivity obeys $\rho \sim T^{5/3}$; the application of a field results in a transition back to the Fermi liquid behaviour $\rho \sim T^2$, as shown in Fig. 2.4 [23, 24].

2.3.4 Bloch-Gruneisen resistivity

At high temperatures, the resistivity of conventional metals is typically dominated by electron-phonon scattering. This is described by the generalised Bloch-Gruneisen equation [19, 25, 26]:

$$\rho_{ph}(T) = \frac{4\pi m}{ne^2} \int_0^{\omega_{max}} \alpha^2 F(\omega) \frac{xe^x}{(e^x-1)^2} d\omega \tag{2.29}$$

$$x = \frac{\hbar\omega}{k_bT}. \tag{2.30}$$

Here ω_{max} is the maximum phonon frequency, $\alpha^2F(\omega)$ is the electron-phonon spectral function (or Eliashberg funtion), and ρ_{ph} is the phonon resistivity. The factor $xe^x/(e^x-1)^2$ arises from bosonic statistical factors for the phonons. For reference to the Drude model, we have:

$$\tau^{-1}(T) = \frac{1}{4\pi} \int_0^{\omega_{max}} \alpha^2 F(\omega) \frac{xe^x}{(e^x-1)^2} d\omega \tag{2.31}$$

where τ^{-1} is the Drude scattering rate.

In general, $\alpha^2F(\omega)$ may be rather complicated, but at high temperatures $\rho_{ph}(T)$ becomes fairly

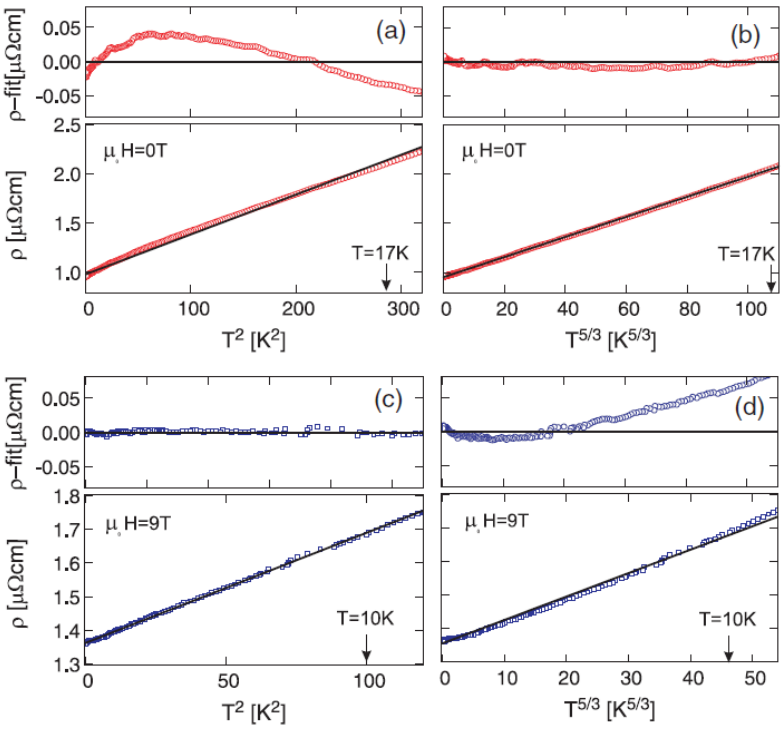

Figure 2.4: Resistivity of $ZrZn_2$ in a field of 0 T (top) and 9 T (bottom). In zero field, the resistivity obeys $\rho \sim T^{5/3}$, while in 9 T there is a better fit to $\rho \sim T^2$, indicating a crossover from marginal Fermi liquid to conventional Fermi liquid behaviour in field [24].

simple. For $\hbar\omega_{max} \ll k_bT$, we have $e^x \approx 1 + x$, and expanding to first order in x:

$$\rho_{ph}(T) \approx \frac{4\pi m k_b T}{\hbar n e^2} \int_0^{\omega_{max}} \alpha^2 F(\omega)\omega^{-1} d\omega \tag{2.32}$$

This integral is seen elsewhere: it is (half of) the definition of the electron-phonon coupling strength introduced in Section 2.2:

$$\lambda = 2\int_0^{\omega_{max}} \alpha^2 F(\omega)\omega^{-1} d\omega. \tag{2.33}$$

We thus have that the high-T phonon resistivity is *always* T-linear, independent of the form of the Eliashberg function's actual $\omega-$dependence [16, 17, 27]:

$$\rho_{ph}(k_bT \gg \hbar\omega_{max}) = \frac{2\pi m k_b T}{\hbar n e^2}\lambda. \tag{2.34}$$

This proves rather convenient because, as noted by Allen, the prefactor can be expressed in terms of the unscreened optical plasma frequency Ω_p, which can be quite easily obtained from band structure calculations [16, 17]:

$$\Omega_p = \left(\frac{ne^2}{\epsilon_0 m}\right)^{1/2} \tag{2.35}$$

where ϵ_0 is the permittivity of free space. Then:

$$\rho_{ph}(T) = \frac{2\pi k_b T}{\epsilon_0 \hbar \Omega_p^2}\lambda. \tag{2.36}$$

We therefore find that the high-temperature gradient of the resistivity gives a measurement of the electron-phonon coupling strength relevant for superconductivity, as long as Ω_p is also known[2] [16, 17, 19]. As explained by Allen, simple high-temperature resistivity measurements, coupled with band structure calculations - which typically give quite accurate values for Ω_p, an average over the whole Fermi surface, even if the details of the calculated band structure are not perfect - then provide estimates of λ which agree to within $\sim 10\,\%$ with those obtained from (much more complicated and difficult) superconducting tunnelling measurements [16, 17, 19, 27].

The reader may enquire why we have $\rho_{ph} \sim \lambda T$, rather than, say, $\rho_{ph} \sim \lambda\,(\lambda + 1)\,T$ - why does the electron-phonon coupling not renormalise the mass that features in the resistivity? In particular, the mass that enters the (unscreened) optical plasma frequency Ω_p is the band mass, which does *not* include electron-phonon coupling, but it is not immediately obvious why this should be the same mass that enters the resistivity; the discrepancy might be expected to give an additional factor of $(1 + \lambda)$ in the resistivity. This issue is discussed in an excellent review by Grimvall [27], who explains that "*the renormalization of the electron mass m exactly cancels against the renormalization of the scattering matrix element as it enters τ. This result turns out to be valid for all temperatures, not only in the limit of low temperatures (i.e. low excitation energies) where the quasiparticle concept is*

[2] We should note that the parameter measured by the resistivity is the transport electron-phonon coupling, λ_{tr}, rather than the "true" electron-phonon coupling strength λ. However, these tend to be identical to within experimental error, as noted by Allen [16, 17, 19].

strictly valid".

The low-temperature details of the phonon resistivity, when $x \gtrsim 1$, will depend on the details of the Eliashberg function. Typically, this is approximated with one of two simple models. The Einstein phonon spectrum assumes atoms can oscillate only at a single frequency ω_E. The Eliashberg function is then:

$$\alpha^2 F_E(\omega) = \frac{1}{2}\lambda\omega_E\delta\left(\omega - \omega_E\right). \tag{2.37}$$

Alternatively, in the Debye model for phonons, we assume the phonon modes are evenly-distributed in reciprocal space. The Debye frequency ω_D is put in to ensure that the total number of modes is correct (i.e. it ensures that there are $3N$ modes for a three-dimensional material containing N atoms). This model is commonly used for calculations, and typically works rather well, even though the true Eliashberg function may look very different, because it correctly conserves the total number of modes - the area under $F(\omega)$ is correct, even if the shape is wrong.

The Debye spectral function is then:

$$\alpha^2 F_D\left(\omega\right) = 2\lambda\left(\frac{\omega}{\omega_D}\right)^4 \tag{2.38}$$

The corresponding resistivity is [16, 17]:

$$\rho_{ph,D}(T) = \frac{2\pi m\lambda}{\hbar n e^2} k_b T \int_0^{\omega_D} \omega^{-1}\left(\frac{\omega}{\omega_D}\right)^4 \left(\frac{x}{\sinh\frac{x}{2}}\right)^2 d\omega. \tag{2.39}$$

This can be calculated with straightforward numerical methods; typically n (or equivalently Ω_p) are obtained from band structure calculations, the Debye temperature $\Theta_D = \hbar\omega_D/k_b$ from the experimental heat capacity, and λ from fitting the experimental resistivity data.

In the low-T limit $x \gg 1$, we then obtain:

$$\rho_{ph} \sim T^5. \tag{2.40}$$

Thus for the Debye model, we expect a crossover in $\rho(T) \sim T^\alpha$ from $\alpha = 5$ at low temperatures, $T \lesssim \Theta_D/4$, to linear T-dependence, $\alpha = 1$, at higher temperatures. This is indeed seen in many materials [16, 19].

Fig. 2.5 shows numerical solutions to the generalised Bloch-Gruneisen function for a Debye phonon spectrum with different choices of Θ_D, for Einstein and Debye phonons, assuming a carrier density $n = 3.35 \times 10^{28}\text{m}^{-3}$, and a quasiparticle mass $m = m_e$.

The Bloch-Gruneisen model is appropriate in the case where electron-phonon scattering is the dominant process. This holds, at least at elevated temperatures, for most "good" metals (i.e. those with a large carrier density and high ratio $E_F/k_b\Theta_D$). We should note that, for a low-carrier-density semimetal such as ambient-pressure bismuth, it may not be appropriate: the experimental evidence suggests electron-electron scattering is dominant even up to quite high temperatures. This is discussed in Chapter 4.

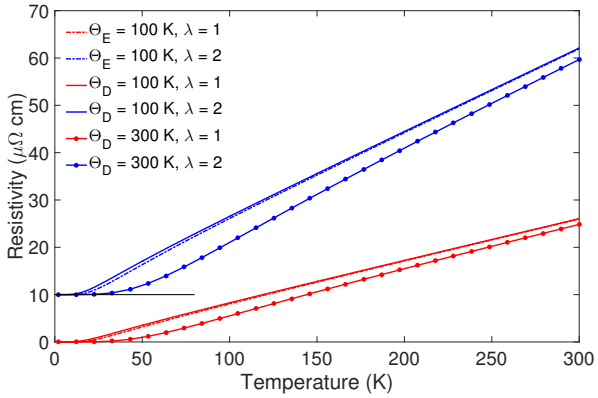

Figure 2.5: Calculated Bloch-Gruneisen resistivity $\rho_{ph}(T)$ as a function of the phonon temperature $\Theta_{D,E}$, where E, D denotes Einstein and Debye phonon models, and electron-phonon coupling strength λ. The gradient of the high-temperature linear region is set by λ; all models with $\lambda = 2$ (blue) are offset by 10 $\mu\Omega$ cm for clarity. The phonon temperature Θ sets the temperature at which the transition from $\rho \sim T^5$ to $T-$linear behaviour occurs. For a fixed value of λ and Θ, the Einstein and Debye models are essentially identical at high temperatures (compare e.g. blue dashed and solid line)

2.3.5 Resistivity saturation

Previously, we have seen that the resistivity exponent is $\alpha = 2$ for electron-electron scattering in a Fermi liquid, $\alpha = 5/3$ in some more exotic cases, $\alpha = 5$ for low-temperature Debye phonon scattering and $\alpha = 1$ for general high-temperature phonon scattering. All these mechanisms suggest that $\rho(T)$ should be at least linear in all metals. However, in some materials the resistivity is observed to be sub-linear. This is quite a general phenomenon, observed most notably in the A15 strong-coupling superconductors such as Nb_3Sn, but also seen in e.g. elemental niobium and quasi-skutteridites such as $Ca_3Ir_4Sn_{13}$ [28, 26].

A mechanism for this has been proposed for the A15 materials. It is suggested that the resistivity cannot rise above a certain value, where the mean free path l is of the same size as the interatomic spacing d. At this point, electrons are scattering at every lattice site, thus they can't scatter any more, and the resistivity should saturate [28, 29].

A phenomenological model introduces a saturation resistivity ρ_s in parallel with the ideal resistivity $\rho_{id}(T) = \rho_0 + \rho_{ph}(T)$, where ρ_0 is the temperature-independent resistivity from impurity scattering. The measured resistivity will then be:

$$\rho(T) = \left(\frac{1}{\rho_{id}(T)} + \frac{1}{\rho_s} \right)^{-1}. \tag{2.41}$$

When $\rho_{id}(T) > \rho_s$, the saturation resistivity short-circuits the ideal resistivity; $\rho(T)$ continues to rise with temperature, but more slowly than T-linear.

This simple model predicts curvature for the resistivity when $\rho_{id}(T)$ rises to match ρ_s, and works well for many A15 materials [28, 29]. Conceptually, it may leave a little to be desired - it is unclear why there should be negative curvature in $\rho(T)$ rather than just a linear rise followed by sharp sat-

uration, it is not obvious why the resistivity should keep rising slowly above this point, and it is debatable if any of the conventional formulation of resistivity theory will work when $l \approx d$, at which point the treatment of scattering as an isolated event characterised by a single scattering time τ is invalid.

The model was put on a firmer theoretical basis by the work of Calandra and Gunnarsson [30, 31, 32]. They introduced a fully quantum-mechanical model, calculating $\rho(T)$ for Nb_3Sn and Nb by evaulating hopping matrices and the current-current correlation operator. The effect of phonons was put in by adjusting the positions of the atoms away from their ideal locations on the crystal structure; at higher temperatures, the atoms become more disordered by phonons, changing the hopping matrices. Gunnarsson found that this does rather accurately predict the resistivity saturation observed in Nb_3Sn and Nb, giving quite good estimates of $\rho(T)$ with no adjustable parameters. It also provides a *post hoc* justification for the parallel resistor model of Weismann [28]: the conductivity can be considered as a temperature-dependent coherent phonon part in series with an incoherent saturation conductivity; the corresponding resistivities will then add in parallel [30, 31, 32].

An alternative, perhaps more physically reasonable, explanation for the saturation of resistivity could arise from phonon anharmonicity [33]. In the Bloch-Gruneisen formalism, we assume that in the linear-ρ high-T region, the system can be well-described by a constant Debye temperature. This requires that the characteristic frequency of phonon oscillations does not change with temperature. At high temperatures, this does not hold: the thermal energy available means atoms will undergo quite large oscillations, and no longer be confined to a purely parabolic lattice potential. Depending on the sign of higher-order terms in the Taylor expansion of the lattice potential, this can lead to an increase in the effective phonon frequency - that is, the Debye temperature becomes T-dependent. In heuristic terms, at high temperatures there will then be "fewer phonons than expected" for a given amount of thermal energy; $\rho(T)$ can therefore grow in a sub-linear fashion dependending on the exact $T-$dependence of Θ_D.

2.4 Superconductivity

2.4.1 Ginzburg-Landau theory

A simple yet effective description of superconducting phenomenology was obtained by Ginzburg and Landau, and uses a free energy expansion in a complex order parameter Ψ, where $|\Psi|^2 = n_s$, the superfluid density [14, 34]. For small n_s (i.e. close to the transition temperature T_c), the free energy is:

$$F = a|\Psi|^2 + b|\Psi|^4 + \frac{1}{2m_s}|\left(-i\hbar\nabla - q_s\mathbf{A}\right)\Psi|^2 + \frac{|\mathbf{B}|^2}{2\mu_0}. \tag{2.42}$$

where a and b are constants, m_s is the superfluid mass, q_s the superfluid charge, $\mathbf{A}$ the magnetic vector potential and $\mathbf{B} = \nabla \times \mathbf{A}$ the magnetic field, with μ_0 the permeability of free space. Minimisation with respect to Ψ and $\mathbf{A}$ gives the Ginzburg-Landau equations:

$$a\Psi + b|\Psi|^2\Psi + \frac{1}{2m_s}\left(-i\hbar\nabla - q_s\mathbf{A}\right)^2\Psi = 0 \tag{2.43}$$

$$\nabla \times \mathbf{B} = \mu_0 \mathbf{j} \tag{2.44}$$

$$\mathbf{j} = \frac{q_s}{m_s} \Re \left\{ \Psi^* \left(-i\hbar\nabla - q_s \mathbf{A} \right) \Psi \right\} \tag{2.45}$$

where **j** is the current density, and $\Re$ denotes the real part.

This simple approach captures a significant fraction of the physics. In particular, it implies that, for $T < T_c$ when $\Psi \neq 0$, there is a vanishing electrical resistivity, and it predicts two types of behaviour in field. These are classified by the Ginzburg-Landau parameter $\kappa_{sc} = \lambda_{sc}/\xi_{sc}$ where λ_{sc} is the London penetration depth (a measure of how far magnetic fields can reach into a superconductor), and ξ_{sc} is the superconducting coherence length (a measure of the lengthscale over which Ψ changes). For $\kappa_{sc} < 1/\sqrt{2}$, a material is a type I superconductor characterised by a single critical field B_c, above which superconductivity is destroyed. Most elements are type I superconductors, and B_c is usually $\sim 5 - 50$ mT.

When $\kappa > 1/\sqrt{2}$, type II superconductivity occurs. In this case, when the applied field $B > B_{c1}$, the lower critical field, the Meissner state (which fully excludes flux) is replaced with a more complex Abrikosov lattice of magnetic flux lines: some flux penetrates a sample through the cores of superconducting vortices. A field B_{c2}, the upper critical field, is required to destroy the Abrikosov lattice; typically $B_{c2} \gg B_{c1}$. Few elements are type II superconductors, though many alloys are. Typically $B_{c1} \approx 1$ mT, and B_{c2} can be well above 1 T.

The Ginzburg-Landau theory works well on the assumptions $q_s = 2e$ and $m_s = 2m_e$ - that is, that charge in the superconducting state is carried by pairs of electrons.

2.4.2 BCS theory

Modern descriptions of superconductivity begin with the formalism of Bardeen, Cooper and Schriefer [14]. They showed that superconductivity arose as an instability of the Fermi sea to formation of a many-body coherent state of opposite-spin quasiparticles (termed Cooper pairs), caused by an attractive electron-electron interaction, which can be arbitrarily weak. At low temperatures, if the electron-electron interaction were to be attractive, the ground state becomes a superposition of these Cooper pairs, which are spin-zero bosons with no Pauli restriction on occupation, and this state is separated from the normal-state Fermi sea by a small energy gap Δ. Any scattering out of the BCS state (which would give rise to electrical resistivity) has to pay this energy cost, and at temperatures below T_c the thermal energy is not available.

This BCS theory of superconductivity works well for superconductivity in most of the elements, with typical values of T_c around 5 K. The attractive interaction arises from phonons (although in fact the BCS theory doesn't attempt to explain where the interactions come from). It might seem surprising that electron-electron interactions could be attractive (when for bare electrons in free space they are strongly repulsive at close range). Qualitatively, the attractive phonon interaction can be understood as follows: an electron moving through the lattice produces a distortion in both the electron density and the position of the positive ions. From the simple theory of the harmonic oscillator, the relaxation frequency $\tau^{-1} \sim \sqrt{K/M}$ where K is the effective spring constant for an equivalent quadratic potential and M is the mass, meaning the relaxation time for ions is very much larger than for electrons (because the ion has a mass at least a thousand times larger). Thus, long

after the itinerant electron has disappeared, and the background electron cloud has relaxed, there is still a clump of positive charge density, which attracts other itinerant electrons.

The second-quantised Hamiltonian for a general electron-electron interaction is:

$$\hat{H} = \sum_{k\sigma} \epsilon_k \hat{c}^+_{k,\sigma} \hat{c}_{k,\sigma} + \sum_{kk'q\sigma} V_{kk'q} \hat{c}^+_{k+q,\sigma} \hat{c}^+_{k'-q,\sigma} \hat{c}_{k,\sigma} \hat{c}_{k',\sigma} \tag{2.46}$$

where $\hat{c}^+_{k,\sigma}$ creates an electron with wavenumber k and spin σ. The first term counts electrons in state k with spin σ, with a dispersion ϵ_k, and the second term considers interactions between two electrons, where the interaction matrix element for scattering a state k into a state k' with momentum transfer q is $V_{kk'q}$.

BCS theory assumes an attractive isotropic interaction with $q = 0$ within an energy $\hbar\omega_D$ on the Fermi level. Using a trial wavefunction based on a superposition of Cooper pairs, and either a variational approach or a Bogoliubov transformation, gives the self-consistent equation for the BCS gap Δ:

$$\Delta(T=0) = V \sum_k \frac{\Delta}{2E_k}. \tag{2.47}$$

This can be solved numerically to obtain:

$$\Delta(T=0) = 1.764 k_b T_c \tag{2.48}$$

where T_c is the transition temperature. The gap is a critical property of BCS superconductivity. At low temperatures $T < T_c$, the electron gas is unstable to the formation of a coherent state of Cooper pairs, stabilised by an energy gap of order a few kelvin. Tunnelling measurements can accurately measure Δ, and provide an experimental confirmation of the accuracy of BCS theory.

BCS theory also produces a value for the transition temperature, at which $\Delta \to 0$:

$$k_b T_c = 1.13 \hbar\omega_D e^{-1/VN(E_F)} \tag{2.49}$$

BCS theory has proved fairly successful at describing weak-coupling superconductivity in the elements and some compounds. It explains why superconductivity occurs, and gives an estimate of the transition temperatures:$T_c \sim \Theta_D e^{-1/N(E_F)V}$ where $V = V_{kk'q}$ is the strength of the attractive electronic interaction and Θ_D is the Debye temperature.

In the BCS limit of a weak electron-electron interaction, we have that $VN(E_F) \ll 1$. This implies that T_c should in general be fairly low (some small fraction of the Debye temperature, which is typically of the order of a few hundred kelvin) - and this is observed experimentally for many BCS superconductors.

2.4.3 Strong coupling superconductivity

The above theory is valid for weak coupling, where $N(E_F)V \ll 1$. It does not hold for systems where the electron-phonon interaction $\lambda \sim N(E_F)V$ is strong [16, 17, 35]. In the search for higher

transition temperatures, this is arguably the more interesting region - even the simple BCS theory captures the essential physics that an increase in λ gives an increase in T_c.

A more sophisticated expression for the dependence of T_c on λ was obtained by McMillan [15]. He showed that λ is a critical parameter for determining transition temperatures. McMillan used the phonon spectrum of niobium to numerically solve the strong-coupling phonon superconductivity equations worked out by Eliashberg, Migdal and others, thereby obtaining an expression for T_c set by only three parameters: the Debye temperature Θ_D, the electron-phonon coupling strength λ and the renormalised Coulomb pseudopotential μ^*:

$$T_c = \frac{\Theta_D}{1.45} e^{-\frac{1.04(1+\lambda)}{\lambda-\mu^*(1+0.62\lambda)}}. \tag{2.50}$$

Rather conveniently, the renormalised Coulomb pseudopotential always has approximately the same value ~ 0.10, because it is reduced from the bare Coulomb energy $\mu = N(E_F)V_{Coulomb}$ by:

$$\mu^* = \frac{\mu}{1 + \mu \ln \frac{\Omega_p}{\omega_D}} \tag{2.51}$$

and $\Omega_p \gg \omega_D$ for typical metals.

McMillan's expression is widely used and found to fit the data for quite a large number of materials. These include the elemental superconductors niobium ($\lambda \approx 1.1$) and lead ($\lambda \approx 1.5$), as well as many superconducting compounds such as the A15 materials V_3Si and Nb_3Sn. The Debye temperature can be obtained fairly accurately from heat capacity measurements; λ is trickier to measure but can be found from superconducting tunnelling measurements, or the high-temperature resistivity [16, 17].

3 Experimental methods

In this section, we provide an overview of the experimental techniques used to investigate our samples. We first consider the three cryostats used for resistivity and DC magnetisation measurements, and then provide a description of the high-pressure apparatus used.

3.1 Resistivity measurements

Resistivity is one of very few material properties than can be measured as well at high pressure as at ambient pressure. Resistivity measurements provide a comparatively straightforward diagnosis of significant transitions in the sample, although a detailed analysis can be complex (see Section 2.3).

We measure resistivity with a four-point technique: two wires attached to the sample apply current, and two measure voltage. See Fig. 3.1 for an example. Because the input impedance of the voltmeter is enormous (> 10 MΩ), the voltage wires drain very little current, and the voltage measurement therefore does not pick up a significant contribution from the contact resistance between the wires and the sample (which can be several orders of magnitude higher than the resistance of the sample). The resistivity is then given by:

$$\rho = \frac{wt}{l}\frac{V}{I} \tag{3.1}$$

where w, t are the sample's width and thickness, l is the separation between voltage contacts, V is the measured voltage, and I the applied current. Typically currents $I \approx 1$ mA are applied, a level at which the resistive heating of the sample is insignificant. For our resistive measurements we use 25 μm 99.999% pure Au wires. These are attached to the samples by two techniques. Spot-welding traps the wire between a sharp tungsten tip and the sample itself, which is positioned on a grounded plate. A sharp current discharge through the tip and sample then heats the wire, bonding it to the sample. Alternatively, contacts are made with conducting epoxy. We use either DuPont 4929 epoxy diluted with 2-n-butoxyethyl acetate (which dries in ~ 10 minutes at room temperature), or DuPont 6838 epoxy (which requires heat treatment; we typically use 2 hours at 160 °C).

We have found that spot-welding to bismuth works straightforwardly, and makes contacts with a resistance of $\sim 1\,\Omega$ at room temperature. However, there is some concern that the significant pressure that must be applied by the tungsten tip could damage the crystal structure or cause twinning; the resulting contacts are also quite weak. Contacts made with 6838 epoxy are generally preferred; these are much quicker to prepare (it takes only ~ 10 minutes to attach four wires to a sample, rather than ~ 1 hour), but have a higher resistance ($\sim 5 - 12\,\Omega$). However, this does not appear to be a problem: in bismuth, features as delicate as quantum oscillations are so large that they can easily be seen even with quite high-resistance contacts. Contacts made with 4929 have a still higher resistance ($\sim 20\,\Omega$), but also yield perfectly sensible results. The 4929 epoxy makes rather weak bonds, which are prone to breaking when the wires are bent to connect to measurement electronics, so is avoided if possible.

Superconductivity corresponds to the total vanishing of $\rho(T)$ below $T = T_c$. Applied magnetic fields will suppress the superconducting transition temperature. In the normal state, the tempera-

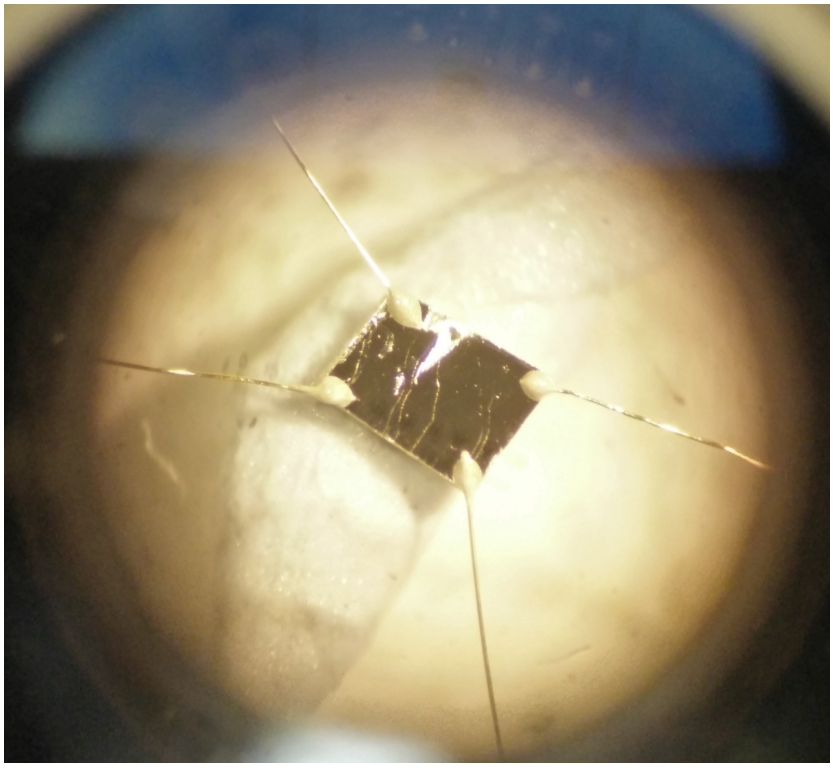

Figure 3.1: A sample of bismuth contacted for resistivity measurements using DuPont 6838 conducting epoxy.

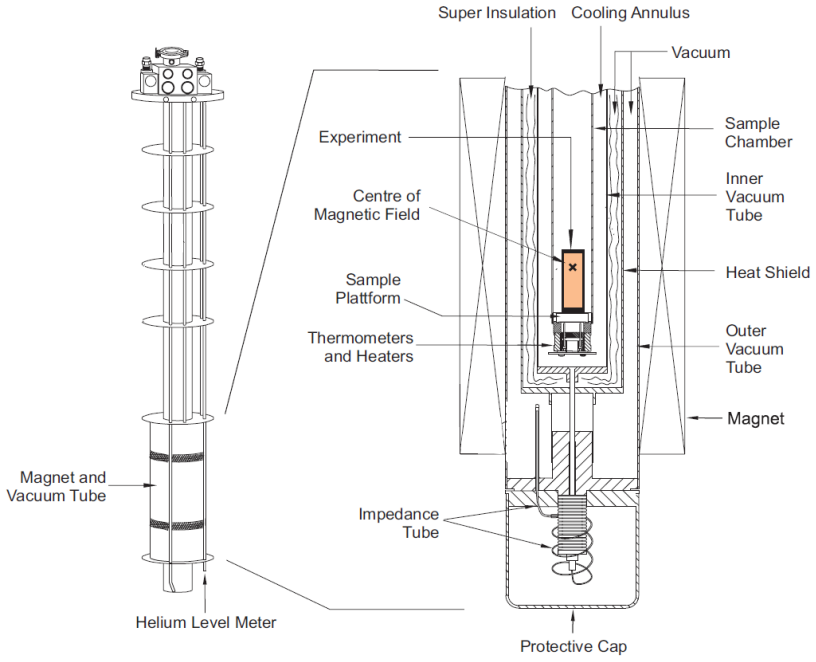

Figure 3.2: Schematic of the PPMS crysostat probe, taken from [36].

ture dependence $\rho(T)$ will provide insight into the scattering processes. We therefore require accurate control over both applied field and sample temperature, and the ability to reach temperatures of ~ 1 K.

3.2 Physical Properties Measurement System (PPMS)

3.2.1 Cooling and field

The PPMS cryostat provides a robust and versatile platform for resistivity and heat capacity measurements down to 2 K with ^{4}He, in magnetic fields up to 9 T. It possess a 24 mm bore (setting the maximum radius of our pressure cells), with a circle of 12 metallic pins at the bottom, which connect to the experiment mounted on a puck. The experiment (whether a pressure cell or samples at ambient presure) must be carefully lowered from the top of the bore with a handheld loading rod to avoid damage to the pins (see Fig. 3.2).

The pins at the bottom of the cryostat are attached to wires that lead back up to to a 12-pin LEMO feedthough at the top. A cable connects this to the measurement electronics and control computer in the instrument rack. The pins are attached to a large block of copper, termed the cooling annulus. ^{4}He gas taken from the reservoir is passed through a heat exchanger; electric heaters heat the gas to the required temperature, as registered by a field-calibrated thermometer on the annulus. This gas flows past the outside of the cooling annulus, setting its temperature. The sample space contains a low pressure (~ 4 mbar) of ^{4}He exchange gas, which improves heat transfer between the annulus and the sample.

This thermal control setup allows rapid and accurate control of the temperature. Warming rates

from $0.01 - 15$ K/minute can be obtained. The sample thermalises via a combination of metallic contact through the pins and cooling annulus, and conductive heat transfer through the exchange gas. When measurements are being undertaken on piston cylinder cells some care is required: the cell has (particularly at higher temperatures) an extremely large thermal mass. This means that the temperature of the cell and the samples will lag behind the temperature recorded by the cryostat, an error that manifests itself as a clear offset in the data between up and down temperature sweeps. A temperature sweep rate of 2 K/min is far too high and will lead to noticeable thermal lag: for careful temperature sweeps, rates of $\lesssim 0.3$ K/min should be used. Of course, a balance must be struck between minimising thermal lag and completing measurements within a reasonable timescale: a full 2 to 300 K temperature scan at the minimum rate of 0.01 K/min will take around 3 weeks and antagonise other users of the instrument. Typically, for detailed low-temperature measurements we would use a temperature sweep rate of 0.05 K/min, having first performed an up and down temperature sweep at this rate to check for the absence of thermal lag.

Outside the bore of the cryostat sits a superconducting magnet cooled by liquid helium from the reservoir, capable of applying a 9 T field. This magnet can be run in both persistent and driven mode. When driven, the current through the magnet is continuously ramped by a high-current power supply, increasing the field at a constant rate. Alternatively, the magnet can be set to a constant field and connected from the driving power supply by means of a superconducting persistent switch, which if allowed to cool will short the current supply leads and permit the continuous circulation of any current already present in the magnet. This means a field can be set, the persistent switch closed, and the current supply ramped down again; the magnetic field will stay constant for the duration of the experiment.

One small downside of the magnet is its rather coarse precision and rapid ramp rate. Field sweep rates below 1 mT/s cannot be achieved, and this can prove problematic if very detailed measurements are required, e.g. for a quantum oscillation study. For such a measurement, it can be necessary to step the field in discrete steps of e.g. 0.5 mT using the persistent switch, which is extremely time-consuming but at least gives a high point resolution.

The major advantage of the PPMS is its reliability: the software and hardware can usually be trusted to provide the desired field and temperature without much effort on the part of the user, and allow the programming of detailed extended measurements encompassing many precisely-controlled temperature and field sweeps. The downside of the system is that, as it allows many types of measurements, it is not entirely optimised for any. The default alternating current (AC) transport option gives both a data acquisition rate and a signal-to-noise ratio around ten times lower than we obtain using our own custom-built setups.

3.2.2 Sample mounting

For ambient-pressure resistivity measurements, samples are mounted on resistivity pucks manufactured by Quantum Design. The samples are placed on a thin gold-covered copper plate, insulated from the plate by a thin layer of paper stuck in place with GE varnish. Traditionalists use cigarette paper, though a small square of half-thickness tissue paper works equally well; the key criteria are that the material reliably insulates the sample from electrical shorts to the metallic plate

beneath it, and that it allows some heat conduction from the plate to aid in thermalisation of the sample.

The sample is stuck to the insulating paper with a small dab of Dow Corning vacuum grease, which serves to hold it in place and greatly simplifies subsequent soldering of wires from the sample. Once the sample is in place, its four 25 μm Au measurement wires are soldered to pads on the edge of the puck.

This can be a tiresome process, because making four contacts to the sample can take several hours, and when the (very fragile) Au wires are bent to reach the soldering pads, they are prone to breaking at the contact point. This necessitates the removal of the sample and a repeat of the contacting process - made a little more challenging because the sample is now covered in vacuum grease - so great care should be taken to avoid breaking the contacts. We have two approaches. Firstly, for robust metallic samples (like bismuth) where the use of 6838 epoxy allows fairly strong contacts to be made, the wires can be freely bent by tweezers as long as they are supported. Typically the wire will be held in one pair of tweezers close to the contact, and bent around this point using another pair of tweezers or the pressure of a pin.

An alternative approach, more time-consuming but more robust, is necessary for fragile samples, which are prone to breaking in half when any pressure is applied on the contacts. These samples are contacted as normal, and have their dimensions measured, then a small paper stage is made for them. We find the instruction sheet that comes with Double Bubble epoxy (DBE) to be structurally ideal for this purpose. A thin mound of DBE is painted along one side of the stage, and the sample is turned upside down and dropped onto the stage so that the wires - but not the sample itself - are stuck in place by the epoxy. If necessary the wires can be pushed into the epoxy with a pin; care should be taken to ensure the sample itself does not become trapped in the epoxy, or anistotropic stress may be applied as the epoxy contracts upon cooling. After waiting 20 minutes for the first layer of epoxy to set hard, a second layer of DBE is painted over the wires to ensure they are firmly trapped. Once this epoxy has dried, the wires can be bent around it without any stress being applied to the contacts; the sample can also be tranported by moving the stage around, so there is no need to touch the sample again. This simple technique has proved fairly reliable in contacting extremely fragile and delicate samples which would break upon being squeezed with tweezers.

For measurements in pressure cells, there are two alternatives to connect the cell to the puck. Firstly, the cell can be attached to a T-shaped adapter which fits onto a standard AC transport (ACT) or resistivity puck. Wires from the cell are soldered to the puck pads in the usual PPMS configuration. We have found this method rather unreliable: the (very large and heavy) cell exerts a significant force on the adapter, which can easily loosen or even break the small M1.6 screws holding the T-piece in place. In addition, the large heavy cell applies a significant moment to the puck pins, making it more likely that either the pins will bend, or the cell will simply fall over to one side. This was often observed to happen in our PPMS runs: looking down the PPMS the upper end of the cell was clearly off-centred and at a small angle. Typically this does not affect the measurements - in fact it may have slightly improved thermalisation, as now the top part of the cell is in contact with the cold cryostat wall as well as the bottom part - but it makes extraction of the cell a rather challenging task, so should ideally be avoided.

A superior alternative was the attachment of the pressure cell to a blank PPMS puck with an M3 hole through its centre. A short piece of brass M8 studding is screwed into the safety cap of the cell; this studding has an M3 hole tapped along its axis, and a small slot cut in the top to enable easier unscrewing (neglecting the slot can cause some issues when attempts are made to remove the studding from the cell). The cell is placed with the safety cap against the blank face of the puck, and an M3 screw is used to firmly screw the puck flat against the safety cap. The wires of the cell are then led down channels in the sides of the puck, soldered directly to the pads on the bottom of the cell, and taped in place. This approach has many advantages. Soldering the wires in place is much easier (when the T-shaped adapter is used, the screws that hold it in place impede soldering to the puck pads). The cell is held much more firmly against the puck, and this improves thermal conductivity and mechanical stability. Finally the length of the whole setup is shorter, so there is a smaller moment on the pins and less chance of the cell falling to one side.

3.2.3 Data acquisition

We use three data acquisition (DAQ) setups for resistivity measurements on the PPMS, each with their own advantages and disadvantages; these are summarised in Fig. 3.3.

The simplest option uses the inbuilt PPMS ACT option. This closed-system module is essentially a single lock-in amplifier and current source, capable of driving between 0.1 mA and 2 A of low-frequency (< 10 kHz) AC current. A little caution should be taken when setting the current; the ACT option will happily drive 2 A of current through the small and delicate samples in a piston cylinder cell, but this procedure tends to be exceedingly terminal for the samples involved. The ACT option possesses a relay that allows switching between two separate channels (samples) on the same puck. We would typically drive a 1 mA current at 23 Hz, with an averaging time of three seconds.

The ACT option allows measurements on only two samples, so we often use a home-built multiplexer circuit controlled by the PPMS software to switch between up to five channels. As the PPMS puck has only 12 pins, this setup requires that the sample current wires are connected in series. This is an easy-to-use approach which allows much faster measuring of the several samples inside a piston cylinder cell.

A final alternative is the use of an external lock-in amplifier, a custom 1 mA/V current source, and a $\times 100$ room temperature transformer (RTT), controlled using the PPMS MultiVu software scripting language. This allows much more rapid measurement of the voltage, and in practice a signal-to-noise ratio around a factor of $10\times$ higher than the ACT option. The downside is a much worse autoranging algorithm, and the ability to measure only a single sample at once.

3.3 Dryogenic Measurement System (DMS)

3.3.1 Cooling and field

More detailed measurements require lower temperatures than the 1.9 K obtainable in the PPMS. This can be achieved with a number of methods; the most common is a closed-cycle ^{3}He refrigerator, which can attain temperatures of ~ 300 mK. Such a probe exists for the PPMS; however, ^{3}He systems tend to possess a small sample space and a low cooling power,which makes them poorly

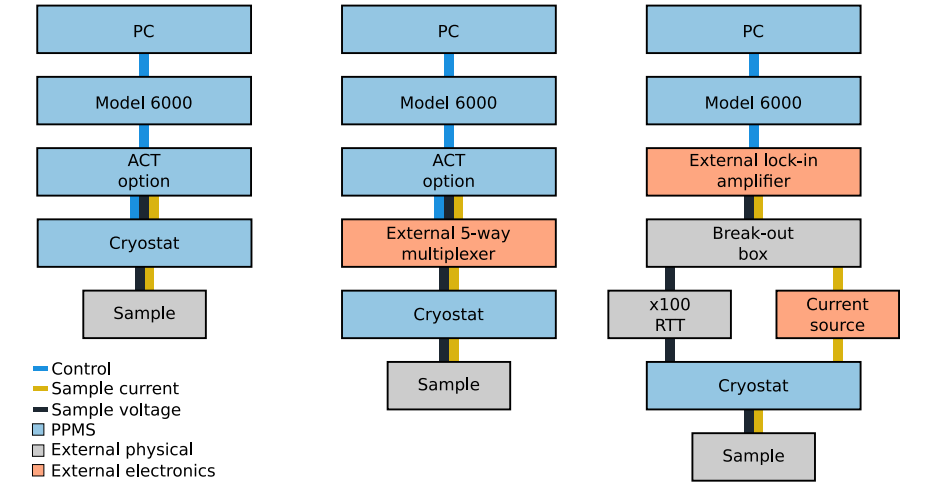

Figure 3.3: Comparison between different DAQ setups for the PPMS, and indication of the positives (+) and negatives (-) for each.

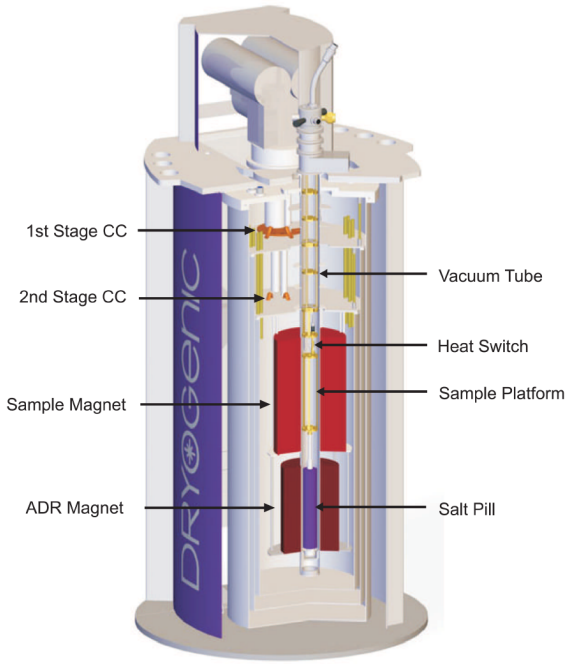

Figure 3.4: Schematic of the DMS cryostat, from [34].

adapted for working with piston cylinder cells. The PPMS ^{3}He probe possesses an sample space several orders of magnitude smaller than our pressure cells.

We therefore turn to the use of an adiabatic demagnetisation refrigerator (ADR), in our case a commercially-built but extensively modified Dryogenic Measurement System (DMS). This ADR possesses a large sample space with easily enough room to mount a piston cylinder cell, and allows cooling to temperatures around 200 mK; see Fig. 3.4 for a schematic. The downside is significantly increased complexity and reduced reliability compared to the PPMS: the DMS requires rather more careful attention, and the many more failure modes coupled with significantly increased cooldown times mean the DMS is used only for more detailed and extensive measurements at very low temperatures once the measurement has been tested on the PPMS.

The general principle of an ADR can be explained as follows. The sample is typically mounted on a long probe, and pre-cooled to near 4 K. The probe consists of a low-temperature stage comprising a sample space and diagnostic thermometry, connected to the upper part of the probe via a weak thermal link and a heat switch. The upper part of the probe is cooled to low temperatures with a conventional refrigeration technique - for some ADRs this involves the use of a pumped ^{4}He dewar, but in the case of the DMS cooling comes from a closed-cycle ^{4}He cryocooler. Below the sample stage is mounted a large salt pill of a paramagnetic salt (we use chromium potassium alum); it is this that provides cooling to well below 1 K. With the heat switch closed, the whole of the probe, including the low-temperature stage, is cooled to temperatures of a few kelvin.

Then a magnetic field is applied to the salt pill, which aligns the spins of the paramagnetic salt ions. Thermodynamically, this reduction in entropy must result in an increase in temperature, and

this is exactly what happens: the temperature of the salt pill and low-temperature stage increase, but this excess heat is removed from the probe by the conventional cooling mechanism. The heat switch is then opened, so the low-temperature stage is thermally isolated from the rest of the probe, and the magnetic field on the salt pill is reduced, allowing the spins to align randomly again. Now the reverse happens: the temperature of the salt pill falls rapidly; in a naive interpretation entropy is taken from the heat of the pill and converted to entropy of the spins. The result is a fall in the temperature of the low-temperature stage. With this technique, temperatures ~ 100 mK can be obtained, if a suitably low starting temperature can be achieved.

DMS samples are mounted near the bottom of a long probe suspended from a winch, on a low-temperature stage below which the paramagnetic salt pill is attached. The samples are connected via a 24-pin plug to wiring (either superconducting NbTi or resistive BeCu) which runs from the sample space of the probe to a vacuum-tight socket at the top. The low-temperature stage of the probe is attached to the upper part with three very thin Kapton straws, which have a negligable thermal conductivity at low temperatures. While the samples are being mounted, three metallic bracer bars are used to secure the low-temperature stage - it is important to remove these before starting a measurement run.

The upper part of the probe has several sets of three radially-directed spring-loaded metallic pins. Once all the pre-measurement diagnostics have been completed, the probe is lowered into a vacuum can which possesses sloped grooves to direct the pins. At several points during the lowering process, the can must be twisted to allow the pins to pass; once the probe is fully inserted, a final twist causes the pins to lock against ramps inside the can, giving strong metallic contact between the upper part of the probe and the can. Although the Kapton tubes that hold the low-temperature stage are weak in compression and easy to bend, they are fairly strong in tension; as long as the probe is vertical, the low-temperature stage and attached salt pill should hanging freely, clear of the can walls. A mechanical heat switch allows a metallic thermal link between the low-temperature stage and the upper part of the probe to be opened or closed; this consists of a nut on a threaded rod, which can press against a thin-fingered copper piece inside a metallic can mounted on the low-temperature stage. To close the heat switch, the nut is screwed up to press the fingers open, where they touch against the can, thereby linking the high-temperature part of the probe to the low-temperature stage. To open the heat switch, the nut is screwed down, and the fingers spring closer together, no longer touching the can. The status of the heat switch can be measured through the resistance between the outside of the metallic cryostat tube and an insulated wire which runs up from the low-temperature stage: this resistance is > 1 MΩ when the heat switch is open and there is no metallic contact, falling to $\sim 22\,\Omega$ when the heat switch is closed.

The vacuum can is then then pumped out to $\ll 1$ mbar of pressure with a turbo pump, taking around 15 minutes. It is not necessary to aim for a very low pressure as when cold any gases will freeze onto the surfaces of the can and probe. The can is then winched up, moved across to the cryostat, and lowered through a sliding seal into the cryostat bore.

For the DMS, pre-cooling to low temperatures is provided by means of a ^{4}He pulse-tube cryocooler. The compressor unit for this is next to the cryostat: this mechanically expands and contracts ultrapure helium gas, and pumps it via gas lines to the cold head in the cryostat. Analogous

to a domestic refrigerator, rapid gas expansion at the cold head lowers the gas temperature, taking heat out of the cryostat; this same gas then returns to the compressor, where it can be compressed, causing heating; this heat is carried away by cooling water in the compressor.

The cold head of the cryocooler is in contact with both the cryostat bore, and two 7 T unidirectional superconducting magnets; the sample magnet applies a field to the measurement region of the probe, while the demagnetisation magnet applies field to the salt pill. This cools the magnets and cryostat tube to ~ 3.8 K. The bore is filled with a slight overpressure (1.1 bar) of gaseous helium; this exchange gas ensures that there is a good thermal link between the cryostat tube and the probe can, as well as reducing the amount of air that enters the cryostat tube when the probe is inserted.

Lowering the probe must be done fairly slowly and carefully, ideally over ~ 4 hours. The insertion procedure lowers a rather large amount of 300 K metal (the probe and can) into helium at ~ 4 K. If done too quickly, the helium gas will heat and rapidly expand. Ideally, this over-pressure will be released through a pair of relief valves just below the sliding seal; however, if the expansion is too rapid, it can push the can and probe out of the cryostat tube again. This happens rather rapidly, and can be fairly destructive for the low-temperature stage: once free of the straitjacket of the cryostat tube, the can and probe swing around alarmingly on the winch, and the Kapton tubes that hold the low-temperature stage - including a heavy pressure cell and heavy salt pill - will easily tear.

Once lowered in place, the can cools through thermal contact with the cryostat tube via helium exchange gas, cooling the probe through metallic contact via the spring-loaded pins. It is important to check that the heat switch is fully closed, to ensure the low-temperature stage and salt pill also cool. The cooling process takes around 12 hours; typically we lower the can in during the day, and leave the probe to cool overnight.

Typically the sample stage will cool to ~ 4.8 K, at which point the first demagnetisation run can be conducted. The demagnetisation magnet field is ramped up to 6.3 T over around 20 minutes, which causes the salt pill to heat up, and the low-temperature stage to warm to around 8 K. Because the heat switch is still closed, this excess heat will slowly be lost, over a period of $1-2$ hours. Then, the heat switch is opened, and the demagnetisation magnet ramped down to 0 T over a period of 20-30 minutes. The temperature of the salt pill, and correspondingly of the low-temperature stage, fall as the magnetic field on the salt pill is reduced. Typically a base temperature of ~ 200 mK can be reached; this varies depending on how firmly the salt pill is screwed on, how much resistive heating of the samples is occuring, and whether there are any tiny touches between the salt pill and the cryostat tube.

The low-temperature stage will usually remain below 500 mK for up to 10 hours, after which it begins to warm more rapidly, heated by the current to the samples and the small heat leak down the Kapton tubes. At this point, either the heat switch can be closed and the cycle repeated, or (if obtaining the lowest available temperatures is not necessary for this measurement) the salt pill can be magnetised again, the sample field changed if needed, and another demagnetisation conducted.

The DMS possesses two major advantages. The first is that it does not use liquid helium, so is comparatively simple to run - the compressor is left running continuously, so the cold head itself is always cold, and there is no need to fill a liquid helium bath every few days. The second is that the ADR approach allows cooling to very low temperatures with a large sample space: a recondensing

^{3}He system, the standard approach for temperatures below 1 K, typically has a much smaller sample space, unsuitable for large piston cylinder cells.

However, there are a number of tradeoffs to be made. The first and most significant is that an ADR system is poorly equipped to stabilise temperature while sweeping the sample field[3].

Additionally, while one of the theoretical advantages of the system is that the cryostat can be kept cold at essentially no cost for prolonged periods of time, in reality this is not possible. Each insertion of the probe lets a small amount of air into the cryostat tube, where it will freeze on the walls; eventually, this ice blocks the passage of the probe, meaning the whole cryostat must be warmed up and de-iced, a process that takes ~ 1 week and must be done every ~ 4 months.

The final flaws arise from the mechanical nature of several elements of the thermal conduction path. The spring-loaded pins that link the probe to the can do not always lock perfectly in place, meaning there is only a poor thermal link between the tube and the probe. This typically means that the probe will cool to ~ 180 K and then stop cooling. It can be possible to twist the probe and improve the connection while the can is inserted in the cryostat, without breaking the vacuum seal between probe and can, but this is a rather risky process: if the seal is broken, air rushes into the can and immediately freezes, and the can must be winched out of the cryostat tube and the entire cooling procedure aborted, which can waste several days' work. In addition, the mechanical heat switch is not totally reliable at low temperatures, and typically requires manual operation to ensure it closes or opens fully.

3.3.2 Data acquisition

Measurements on samples mounted on the DMS probe are taken using a custom-built data acquisition circuit housed in the instrument rack adjacent to the cryostat. The measurement is connected to a 24-pin female LEMO adapter, which plugs in to an equivalent male adapter connected to the measurement loom at the low-temperature stage. This loom is well heat-sunk at the low-temperature stage, the 4K plate, and up the length of the probe. It consists of a number of NbTi twisted pairs and a number of BeCu twisted pairs. At low temperatures the NbTi is superconducting, and therefore conducts negligable heat down to the samples; these wires are used for the application of current to the samples as their zero resistance means they do not generate Ohmic heating at the low-temperature stage. The BeCu wires are used for voltage measurements, as their large resistance means that they again do not conduct much heat, and they are being used for voltage measurements so do not draw significant current.

These heating considerations are very important for the successful operation of an ADR. There are three main paths for heat flow into the low-temperature stage, which will limit the achievable base temperature and reduce the hold time: conduction down mechanical supports, conduction down wires, and resistive heating due to flowing currents. The first of these is minimised by using thin-walled Kapton tubes to suspend the low-temperature stage, and ensuring the heat switch is fully open for the demagnetisation. The second is reduced by the use of superconducting current wires and highly resistive voltage wires, both of which allow negligable heat flow into the low-

[3] In principle such stabilisation could be achieved by finely controlling the demagnetisation magnet field to exactly compensate any heating of the system. In practice this approach is unreliable.

temperature stage. The final mechanism for heating is the most insidious. Obviously current flow is essential for a successful four-point measurement, and in general larger currents will give less noisy signals. However, we have observed that current flow through the samples heats the low-temperature stage, in particular increasing the temperature of the stage before it is demagnetised. For example, after ramping the demagnetisation magnet field to maximum and waiting for two hours, the LTS temperature may fall to 4.8 K and stabilise there. If the measurement current source is then unplugged from the cryostat, the LTS temperature will rapidly fall to 4.6 K and again stabilise, giving a slightly better base temperature and hold time. After the demagnetisation has been conducted, plugging the current source in again causes a slight increase in the warming rate.

At the top of the probe, a vacuum-tight feedthrough connects the measurement loom to an external cable and breakout box. This box allows access to all twelve twisted pairs of the measurement loom individually. Voltage measurements are conducted using a standard lock-in amplifier (typically a Stanford Research SR7260). The lock-in amplifier outputs a sinusoidal AC voltage (typically 1 V at 23 Hz), which is passed to a custom-built balanced current source connected to the breakout box to supply current to the samples. The resulting voltage is passed through a $\times 100$ room-temperature transformer, and then to the voltage input of the lock-in amplifier.

3.4 Magnetisation measurements

3.4.1 Bulk probes of superconductivity

Resistivity is one of few physical properties that can be measured as accurately under pressure as in ambient conditions. However, particularly when applied to superconductivity, measurements of resistivity provide only one aspect of the full picture of the properties of a material.

Firstly, observing a vanishing $\rho(T)$ does not mean the entirety of a sample is superconducting, merely that a small fraction is. If flowing current can find a superconducting percolative path through a sample then the resistivity will vanish even if the bulk of the sample is not superconducting; thus, superconductivity arising from impurities or surface effects would be erroneously attributed to the bulk. Resistive measurements are therefore seldom sufficient to convince the scientific community of the intrinsic superconductivity of a new material.

Secondly, the behaviour in field of the resistivity is rather complex. For type II superconductors with $B_{c2} \gg B_{c1}$, an applied field broadens the superconducting transition: over an extended temperature region, the sample transitions continuously between superconducting and normal states. The resistivity $\rho(T)$ across the transition is governed by complex flux trapping physics.

To investigate the details of bulk superconductivity, there are two widely-established thermodynamic probes. A jump in the specific heat capacity$C(T)$ at the transition provides clear evidence for the bulk nature of the transition, while the low-temperature form of the specific heat can be used to probe the details of the gap function $\Delta(T)$. Such a measurement is exceptionally challenging under pressure - typically measurement techniques require the sample to be thermally isolated from its surroundings, and this cannot easily be achieved when the sample is confined in a pressure medium.

An alternative probe is the observation of flux expulsion through the Meissner effect, via mea-

surement of the sample's magnetisation. Superconducting samples screen applied magnetic fields (provided $B < B_{c1}$), a consequence of their infinite conductivity. If the sample's magnetisation M or susceptibility $\chi = M/H$ can be measured as a function of temperature, it should show a sharp fall at T_c, with a value $\chi = -1$ corresponding to complete flux expulsion and therefore bulk superconductivity in the entirety of the sample [14, 34].

3.4.2 SQUID magnetometry

We probe the Meissner effect in our superconducting measurements with DC SQUID magnetometry, the most precise probe of magnetisation in existence. This allows the measurement of sample magnetic moments as small as $Z = 10^{-12}$ A m^2.

Obtaining a measured moment Z from such a magnetometer is a two-step process which relies on physically moving the sample through a superconducting coil set connected to a SQUID sensor; for this reason this technique is often termed *extraction magnetometry*. At each physical position z of the sample in the coil, the voltage across the SQUID sensor is measured to obtain a voltage curve $V(z)$. This curve is then fit to that expected for an ideal magnetic dipole, to obtain a quantitative value for Z.

The analysis procedure to obtain Z from $V(z)$ is described in some detail later, so here we focus on the first step. The critical component of the sensor is a superconducting coil through which the sample is passed, coupled via a flux transformer to a SQUID. The SQUID itself consists of two parallel Josephson junctions (physically, a superconducting ring whose two halves are separated by very narrow strips of non-superconducting material). When there is no external magnetic field, current flows equally across each junction; when an external field is applied (in this case, by the flux transformer, which essentially applies the field generated by the sample's magnetisation to the SQUID sensor), the SQUID is constrained by the Aharonov-Bohm effect to allow only an integer multiple of the flux quantum $\Phi_0 = h/2e$ through the ring. It does this by modifying the flow of supercurrent around the ring, which produces its own magnetic field, thereby changing the flux through the ring so it remains an integer multiple of Φ_0. If this supercurrent is larger than the Josephson junctions' critical current, a voltage appears across the SQUID [34, 37].

The result is a voltage across the junction that depends on the applied magnetic flux: the SQUID acts as an (extremely sensitive) flux-to-voltage converter. An observation of the voltage as a function of sample position can then be compared to that expected for an ideal dipole, to give an absolute value of the sample's dipole moment.

3.4.3 Cooling and field

We use a Cryogenic S700 commercially-available cryostat implementing the DC SQUID extraction magnetometry technique, as shown in Fig. 3.5. The sample is mounted on the end of a long rod, and lowered into the bore of the cryostat, where it sits in an atmosphere of ~ 10 mbar of flowing ^{4}He gas.

Temperature control is provided by first passing the ^{4}He through a heat exchanger. The bore of the cryostat is continuously pumped with a rotary pump, drawing liquid helium from the helium

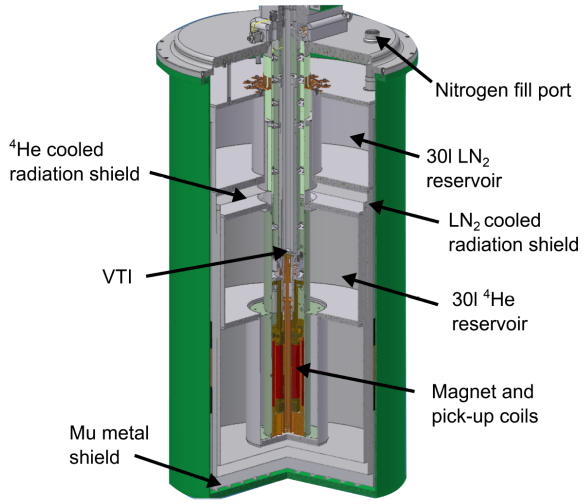

Figure 3.5: Diagram of the Cryogenic S700 DC SQUID magnetometer, from [34].

bath through a needle value and heat exchanger. A thermometer and heater on the heat exchanger, operating a PID loop controlled by a Lakeshore 340 resistance bridge, ensures that the low-pressure helium gas that flows into the cryostat sample space is at the desired temperature. The actual temperature of the sample space is measured by a secondary thermometer.

This design ensures the sample is well-thermalised with its surroundings, as it sits in a low pressure of exchange gas. It also provides highly-responsive temperature control (at least at low temperatures where the heat capacity of the sample space is small); the temperature can be changed from 2 to 30 K in less than 10 seconds. The sample can also be inserted while the sample space is at low temperatures; fully inserting an ambient-pressure sample and allowing it to cool to 10 K takes only ~ 10 minutes. The rod on which the sample is mounted should be lowered in smoothly in several steps - if it is inserted all the way in at once, the heat of the sample will rapidly warm the helium in the sample space, and we have found this results in a much longer total insertion time than if the sample is inserted in a controlled fashion.

There are two downsides to the design of the temperature control system. Firstly, temperatures below 2.15 K cannot be reliably stabilised: typically, the sample space begins to fill with liquid ^{4}He rather than gas at the desired temperature, which results in a drop in the cavity pressure, followed by a rapid fall in the sample space temperature to below 1.7 K (as now significant quantities of liquid ^{4}He are being pumped on). To remove this liquid, the sample space must be warmed to 5 K for several minutes. In principle, obtaining lower temperatures would be possible by careful manipulation of the needle valve to ensure a sufficient flow of helium gas, coupled with use of a heater in the sample space itself to prevent the collection of any liquid, but in practice this is very seldom worth the time or effort. Secondly, temperature control is done using a thermometer on the heat exchanger, which is often around 0.2 K lower than the actual temperature of the sample space. This is a minor problem for temperature sweeps, but it means taking points at exactly the required temperature can be challenging.

Magnetic field is provided using a 7 T bidirectional superconducting magnet mounted outside

the sample space. The magnet is cooled with the liquid ^{4}He bath, and (as with the PPMS) possesses a superconducting persistent switch. This is particularly important for the SQUID, as to ensure only the sample's magnetisation is being measured (rather than the applied magnetic field), the field must be extremely stable when the extraction magnetometry procedure is conducted. This means field sweeps with the SQUID are rather slow, as the field must be stabilised and the persistent switch closed at every point (unlike in a PPMS resistivity field sweep, where the field can be ramped continuously).

3.4.4 Measurement coils

The sample is pulled through a set of counterwound coils; as the sample is moved, the flux through the coils (and therefore the SQUID junction) changes. The magnetometer thus very accurately measures the sample magnetisation through the voltage across the SQUID junction. The result is a measurement of $V(z)$, the sample voltage as a function of position in the coils, which (for an ideal sample) would give rise to the shape expected for a point dipole moving through the coils. The signal can be fit to the expected shape, which gives a measurement of the size of the dipole that would generate a system.

Of course, our samples are not ideal - they are around one millionth of the volume of the pressure cell they live inside. To remove the background signal of the cell, a couple of tricks are required. Firstly, the counterwound coils (two wound clockqwise, two anticlockwise) serve to cancel any *uniform* background from the measured $V(z)$. The cells are designed to be highly uniform, so this dramatically reduces the cell background. Secondly, instead of directly fitting the dipole shape to the measured $V(z)$ (for example via the Levenberg-Marquadt algorithm for non-linear fitting), a more elaborate but much more powerful approach is used: the matrix decomposition technique of singular value decomposition (SVD).

3.4.5 Fitting procedure using SVD

SVD allows the extraction of the sample signal from the large, irregular background of the cell. In our view it is an essential part of high-pressure SQUID magnetometry; attempts to perform similar measurements by carefully subtracting the measured background of the cell, and then fitting to the dipole shape, work much less well. The SVD technique allows the observation of superconducting transition in the raw data without any need to remove a background at all (in fact doing so has little impact - see Fig 5.18 in Chapter 5 for an example).

The basic idea is as follows [34, 37]. The raw signal $V(z)$ can be considered as a superposition of a series of terms in a multipole expansion. Only the dipole term arises from the sample itself; higher-order multipole terms arise from the background of the cell. We therefore project the measured $V(z)$ onto the set of multipole basis functions, to pick out the coefficient of the dipole term which corresponds to the sample signal.

Mathermatically, the procedure is as follows. Assume the signal is composed of a sum of basis functions $f_j(z)$:

$$V_{sig}(z) = \sum_{j=1}^{N} a_j f_j(z) \tag{3.2}$$

In discrete form:

$$\mathbf{V_{sig}} = \underline{\underline{F}}\mathbf{a} \tag{3.3}$$

where $\mathbf{V_{sig}}$ is a column vector of size M where M is the number of datapoints in the scan, $\mathbf{a}$ is a column vector of size N where N is the number of basis functions to be used, and $\underline{\underline{F}}$ is an $M \times N$ matrix, where each column is the basis function signal if the multipole coefficient was 1. To find the best fit, we want to minimise:

$$\mathbf{r} = |\underline{\underline{F}}\mathbf{a} - \mathbf{V_{sig}}|. \tag{3.4}$$

This can be done exactly using linear least-squares. There is no need to guess starting values or iterate; instead $\mathbf{r}$ is minimised exactly with matrix algebra. The vector $\mathbf{a}$ measures the weights of the different basis functions, and we are trying to find the values of $\mathbf{a}$ required to best describe our signal from the available basis functions.

$\mathbf{F}$ can be described using its singular values matrix $\mathbf{S}$, according to:

$$\underline{\underline{F}} = \underline{\underline{USV^T}}. \tag{3.5}$$

The matrices $\underline{\underline{U}}$, $\underline{\underline{V}}$ and $\underline{\underline{S}}$ can be straightfowardly found with standard matrix algebra packages. The best fit of $\mathbf{a}$ is then given by [37]:

$$\mathbf{a_{fit}} = \underline{\underline{VS^{-1}U^T}}\mathbf{V_{sig}}. \tag{3.6}$$

In the case of the SQUID signal, the basis functions are the terms in a multipole expansion: $f_1(z) = f(z)$, $f_2(z) = df/dz$, etc. The function f is given by the expected signal for a dipole moving through the coils. Because we have counterwound coils, this is:

$$f(z) = D(h,z) + D(-h,z) - 2D(0,z) \tag{3.7}$$

$$D\left(h,z\right) = \left(\frac{1}{a^2 + \left(z-h\right)^2}\right)^{3/2}. \tag{3.8}$$

The function D is that obtained from a point dipole; a is the coil radius, and h is the separation between coils of different directions. These parameters are fixed by the geometry of the actual coils.

When we find $\mathbf{a_{fit}}$, we basically measure how much of the signal can be described with a dipole, how much with a quadrupole, etc. Assuming the sample is centred at $z = 0$, the multipole decomposition will work even in the presence of a very large and poorly-shaped background from the cell, because all the background contributes only to higher-order multipole terms. This technique works rather well for observing the sharp jumps associated with superconducting transitions, which can be seen without any need for background subtraction of the cell signal.

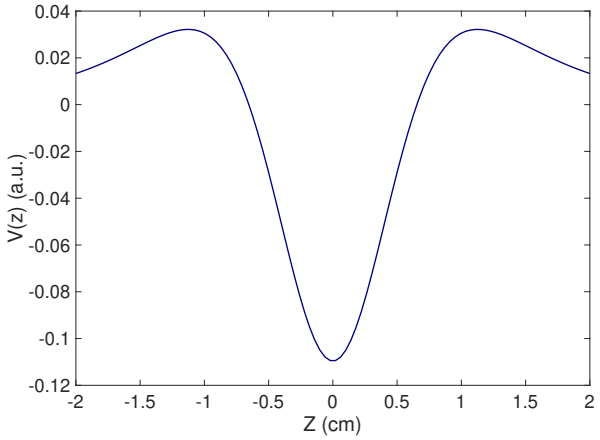

Figure 3.6: Ideal dipole $V(z)$, as calculated from Eq. 3.9, with $c_1 = 0$, $c_2 = 1$, $a = 1.25$ cm and $d = 0.35$ cm.

3.4.6 Example of the background-subtraction process

The ideal position-dependent voltage $V(z)$ arising from a point dipole is (evaluating Eq. 3.7-3.8):

$$V(z) = c_1 + c_2 \left(\frac{1}{\left(a^2 + (z-d)^2\right)^{3/2}} + \frac{1}{\left(a^2 + (z+d)^2\right)^{3/2}} - \frac{2}{\left(a^2 + z^2\right)^{3/2}} \right) \tag{3.9}$$

where $c_1$and c_2 are respectively a constant offset and the dipole magnitude, and here we set $a = 1.25$ cm and $d = 0.35$ cm, the coil parameters of our Cryogenic S700X SQUID magnetometer. Fig. 3.6 shows an example of the ideal calculated signal.

Because of the cell's extended background, our $V(z)$ certainly does not look like such a neat dipole. Fig. 3.7 shows an example signal for both an empty cell background $V_{bg}(z)$, and a cell containing a superconducting sample $V_{meas}(z)$, at the same temperatures and fields. This means it is not practicable to use a conventional non-linear fitting routine (e.g. the Levenberg-Marquadt algorithm) to directly fit Eq. 3.9 to the raw $V(z)$.

There are a number of options available to extract the sample signal. We could try subtracting $V_b(z)$ from $V_{meas}(z)$ (carefully matching background and measurement sweeps to be at the same sample and field) to obtain the actual sample signal $V_s(z)$ - this should show us a dipole signal, to which we could then fit Eq. 3.9 using a non-linear fitting routine. This works moderately well - after subtracting the background, a clear dipole is visible (at least near $z = 0$), which qualitatively has a sharp change in behaviour across T_c (Fig. 3.8). However, there are a number of flaws in this process, because the background and the sample signal do not match very well. This gives rise to artifacts away from the centre of the signal, and it means the fit must be performed over a narrow range of z. The cause of this mismatch is an unavoidable small change in the location of the cell with respect to the magnetometer between the background and sample runs (likely a shift in position of ~ 1 mm). There may also be a small change in the cell's magnetic background - for example, using a needle to load the sample may leave tiny ferromagnetic iron impurities near the sample space,

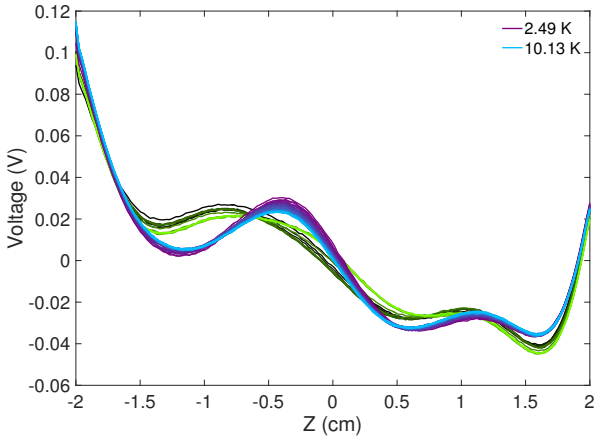

Figure 3.7: Raw $V(z)$ from the SQUID magnetometer for an empty cell and a superconducting sample inside a cell, taken with T increasing beween 2.5 and 10 K at $B = 3$ mT . Blue/purple traces show the signal from the empty cell at 0 kbar before the sample was inserted; purple indicates lower T, blue indicates higher T. Black/green traces show the signal from a cell containing superconducting Bi-III with $T_c = 7$ K (the sample is SMAC16-7 at 29 kbar, discussed in Chapter 5); black indicates lower T, green indicates higher T. Note that the signal does not match the background well (even above T_c), due to tiny changes in the position of the cell with respect to the magnetometer coils between runs. There is a qualitative change to the sample signal (black to green) near $z = 0$ due to the superconducting transition - this is the feature we wish to extract.

which will change the magnetometer signal. In practice, we find this background-subtraction and fitting process requires a large amount of careful fine-tuning for each temperature sweep to give sensible fit results, because the non-linear fitting process is not very robust.

Using the SVD method described in Section 3.4.5 gives superior results, without even the need for a measurement of $V_{bg}(z)$, or any background subtraction and post-processing of the $V(z)$ data. Figure 3.9 shows an example of this process: SVD fits (with $N = 4$) to the Bi-III data with and without subtracting the background. As before, subtracting the background shows a clear dipole (which the SVD process accurately fits for $|z| = \pm 1$ cm); the SVD process can also fit the raw data, even though there is no clear dipole. Plotting the a_1 coefficient as a function of temperature (i.e. the coefficient of the dipole term in the projection of the data onto an $N = 4$ multipole basis) shows that the background subtraction actually has quite a minimal impact (Fig. 3.10) - it leads only to a constant shift in a_1 along the y-axis, but does not change the clarity of the transition. Typically, we remove this shift by subtracting the high-temperature value of the magnetisation from the data before calculating the susceptibility, on the assumption the high-temperature dipole moment (in the absence of superconductivity) is negligible. Here, we present the fitted c_2 and a_1 coefficients in arbitary units; in the SQUID magnetometer, these values are converted to absolute magnetisations using a conversion factor obtained from measuring a sample with known magnetisation.

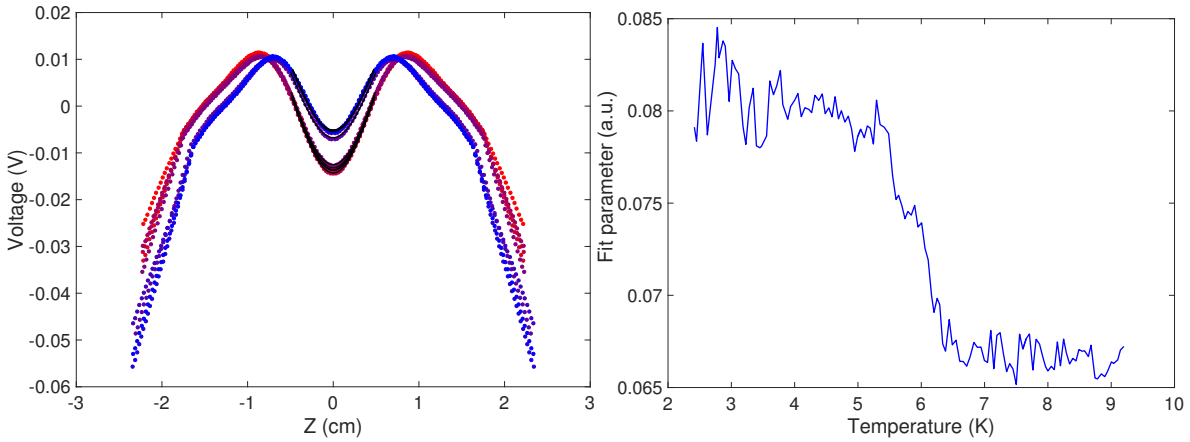

Figure 3.8: Left: Dipole signal $V_s(z)$ of a superconducting Bi-III sample, after subtracting the empty cell background, at 3 mT and from 2.5 to 10 K (blue indicates low T, red indicates higher T). This gives rise to a clear negative dipole signal, and the size of the dipole changes visibly across $T_c = 7$ K. Solid black lines indicate fits to the ideal dipole shape for $|z| = \pm 0.5$ cm. Right: size of the c_2 fit parameter as a function of temperature (in arbitrary units). A broadened transition near $T = 6$ K indicates the superconducting transition.

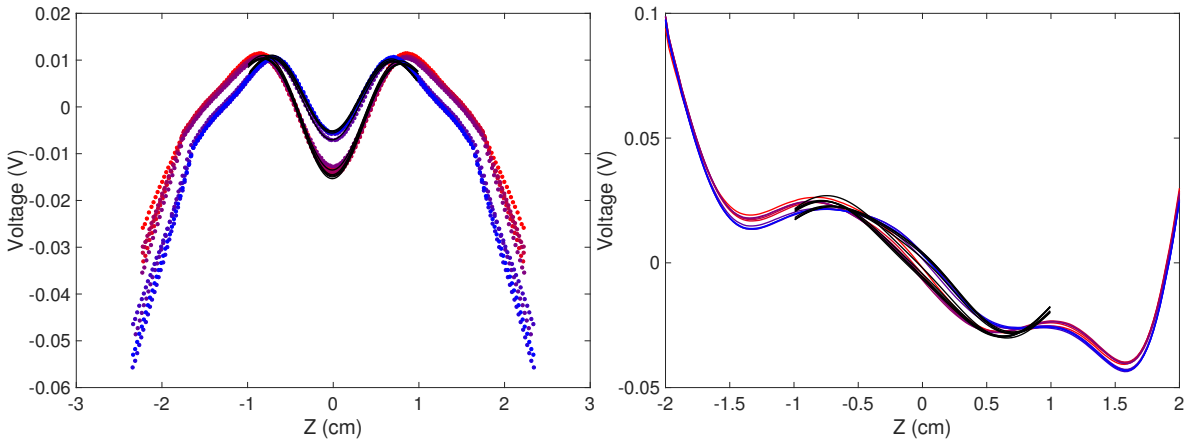

Figure 3.9: Left: Dipole signal $V_s(z)$ of a superconducting Bi-III sample, after subtracting the empty cell background, at 3 mT and from 2.5 to 10 K (blue indicates low T, red indicates higher T). This gives rise to a clear negative dipole signal, and the size of the dipole changes visibly across $T_c = 7$ K. Solid black lines indicate SVD fits ($N = 4$) for $|z| = \pm 1$ cm. Right: The raw data $V_{meas}(z)$ without background subtraction, and the SVD fit.

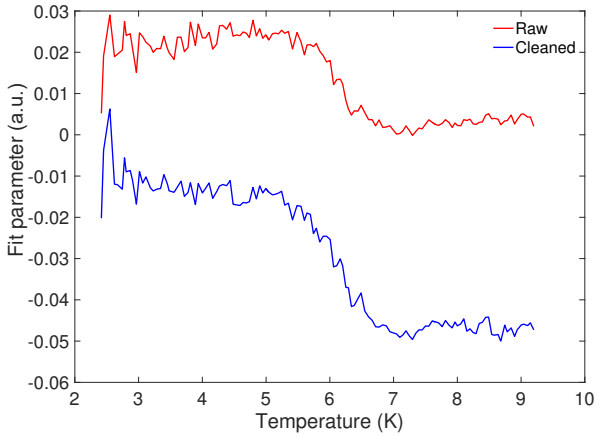

Figure 3.10: Temperature dependence of the a_1 (dipole) coefficient of the SVD multipole fit up to $N = 4$ (in arbitrary units). The blue line shows the value extracted from fits to the background-subtracted data (Fig. 3.9, left); the red line shows the value obtained by fitting to the raw data (Fig. 3.9, right). Both clearly show the superconducting transition around $T = 6$ K. As can be seen, there is qualitatively no change in the shape of the transition between the two methods (only a linear translation of the data in the y-direction).

3.5 Pressure cells

3.5.1 Piston cylinder cells

Pressures up to ~ 30 kbar can be obtained with a piston cylinder cell (PCC). This cell can accommodate several samples with a typical dimension of ~ 1 mm simultaneously, and allows determination of the pressure at low temperature, typically the temperature regime of interest for the measurements.

The basic principle of a PCC is as follows: the samples are mounted on a small card stage, which is placed inside a hollow Teflon tube filled with liquid pressure medium; the open end of the tube is sealed with a high-pressure feedthough, which carries wires into the high-pressure region (see Fig. 3.11 for a schematic). The tube is inserted into the bore of a metal cylinder, and compressed from one end with a piston. The volume reduction of the tube transmits hydrostatic pressure to the samples.

The cells used here consist of an insert made of an MP35N alloy comprised of Ni, Cr, Co and Mo. MP35N after heat treatment is exceptionally strong and tough, and rather surprisingly non-magnetic; as such it is an ideal material for withstanding the enormous pressures in the heart of a pressure cell [38]. The inserts are machined with a taper, and pushed into a matching taper in a BeCu jacket. This allows inserts to be replaced when necessary without having to make a whole new cell. The taper also exerts a compressive stress on the insert, helping to counteract the tensile stress from the high-pressure region. The bore diameter is 4.00 mm; Teflon tubes are machined to precisely match the diameter of the bore.

The high-pressure feedthroughs are made of MP35N, with a small hole bored to allow wires to pass through. Around 16 twisted pairs of 90 μm enamel-insulated copper are pushed through the feedthrough hole and sealed in place with Stycast 2850FT epoxy. The feedthrough is a common

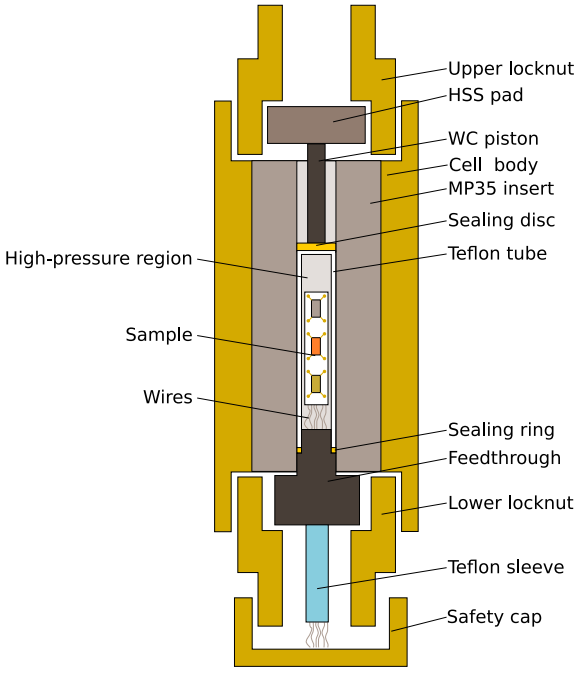

Figure 3.11: Schematic of a piston cylinder cell. Pressure is applied from the top, with a WC piston that fits through the upper locknut and presses against the HSS pressure pad. The sample stage can accomodate at least three four-point resistivity samples, as well as a Sn manometer mounted on the rear.

failure point for the cell, particularly at higher pressures, where a small bubble in the epoxy can collapse, allowing the rapid escape of all the pressure medium and typically the total annihilation of all the samples. As such, it is important to prepare the feedthroughs carefully, using as many wires as will fit (to support the epoxy) and thoroughly outgassing the epoxy to ensure no bubbles are trapped. Each feedthrough should be tested up to the maximum pressure of the cell; typically around 50 % of the feedthroughs will fail at this testing stage, but that is preferable to them failing at the final pressure point of a six-month measurement.

A small sample stage, typically made out of the cardboard cover of a pressure cell logbook, is attached to the high-pressure wiring. Wires are run along the back of the stage then poked through to provide a set of four metallic posts for each sample; the gold wires from the sample are soldered to these posts. The card stage is 8×1.8 mm long, with room for four samples (16 wires) on the front. *Before* mounting the samples, the copper sealing ring should be slid over the feedthrough. The wiring between the stage and the low-pressure end of the feedthrough should be tested, to ensure that all wires work and to acertain which is which. The low-pressure wires should be labelled e.g. with coloured paint or the coloured plastic insulation stripped from a multistrand wire.

For samples with strong contacts, it is straightforward to rest the sample on the stage, wrap its gold wires around the sample stage posts, and solder the gold wires into place (the lowest soldering temperature possible should be used, ~ 230 °C, or the gold sample wires will be destroyed). More fragile samples will require more elaborate setups. One approach which can be used to mount thin

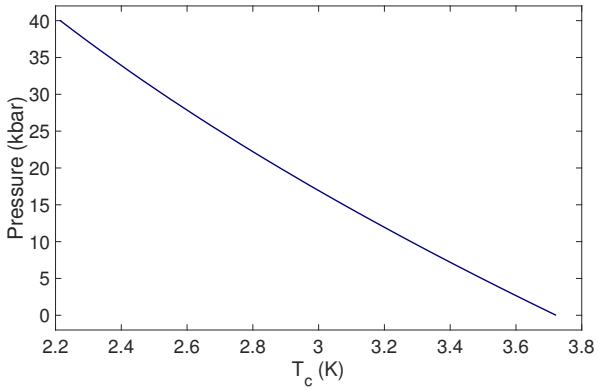

Figure 3.12: Calibration curve for the superconducting transition temperature of a Sn manometer, based on data from [39].

platelet samples normal to the plane of the sample stage is to rest them on a small block of Hysol plastic cut into shape with a scalpel. The sample should be rested on the block and the wires glued onto the corners of the block with Double Bubble epoxy. Once the epoxy has set, the wires can be bent around the block and glued more firmly with Double Bubble epoxy. The block can then be glued to the sample stage, and the wires soldered to the posts, without exerting any stress on the sample. This approach proved to be a reliable way to mount thin and brittle samples.

One of the samples should be a tin or lead manometer. The superconducting transition temperature of the manometer is a well-known function of pressure, allowing determination of the pressure in the cell to within $\lesssim 0.5$ kbar at low temperatures (see Figs. 3.12 and 3.13) [39]. The tin or lead should be pressed flat between two glass slides to a thickness of $< 20\ \mu$m, and cut into a long thin strip, before being contacted with four 25 μm Au wires for resistivity measurements. A long, thin manometer is essential to give a significant resistance jump at T_c. To save space and allow the mounting of more samples, it is possible to place this manometer on the back of the sample stage; however this can cause difficulties when the cell is closed, as the dangling manometer is quite likely to break.

Once all the samples are mounted and tested, the cell can be closed. Typically cells are pressurised to ~4 kbar; below this is is impossible to guarantee the Teflon tube has fully sealed.

3.5.2 SQUID moissanite anvil cells

To attain pressures above ~ 30 kbar, one must move to more advanced devices than the PCC. At higher pressures, the forces on the metallic parts of the PCC approach the metal's yield stress; plastic deformation leads to the loss of pressure, and eventually the failure of the cell.

Higher pressures (up to the Mbar range) are attainable in anvil cells. These work in essence as follows: a tiny liquid-filled hole drilled in a metallic disk (the gasket) is forced to shrink by pressure applied with two blocks of an extremely hard material (the anvils). The reduction in hole volume produces hydrostatic pressure in the liquid, and this pressure is transmitted to the sample, which lives inside the hole.

A detailed decription of the theory and practice of anvil cells is given by [40, 41]. Modern anvil

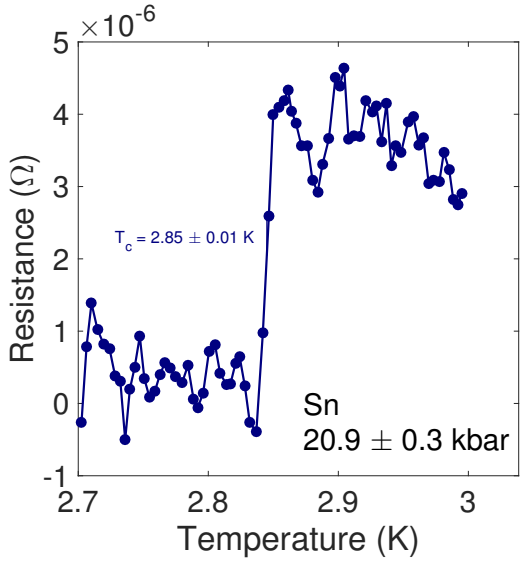

Figure 3.13: Superconducting transition of a Sn manometer, used to calibrate pressure at low temperatures.

cells are specialised to allow a particular measurement technique, including resistivity, AC susceptibility, x-ray structure determination, and neutron scattering. Typically, the anvils are diamond or moissanite. Moissanite is crystalline silicon carbide, with a hardness beaten only by diamond. The anvils are seated in a piston, and one moving piston has pressure applied with a hydraulic ram. This pressure is transmitted to the anvil, and causes deformation of the gasket hole. The smaller the gasket hole, the higher the pressures that can be attained, but a small hole of course severely compromises the straightforwardness of setting up a measurement in the hole.

Here, we describe a cell designed for DC magnetisation in a SQUID magnetometer, as shown in Fig. 3.14, termed a SQUID moissanite anvil cell (SMAC). This technique has many advantages over other measurement methods. The SQUID magnetometer is extremely sensitive, and thus well-adapted to picking up signals from tiny samples. Crucially, no wires are required, so setting up such a cell is comparatively simple: a sample of the material to be measured can be placed into the gasket hole, along with a small ruby chip for pressure determination, and the cell sealed without having to worry about the concerns with getting measurement wires out of the high pressure region that plague resistivity techniques. The cell is then placed in the magnetometer, and pulled throught the coils in a small applied field [42].

Of course, the significant downside of such a cell is that the entire cell has its magnetisation measured, rather than just the sample. It is in fact startling that this technique works at all - the typical sample dimensions are $\sim 250 \times 100 \times 50\,\mu$m, so the cell has at least one million times the volume of the sample. Nevertheless, with careful precautions, significant changes in the sample's magnetisation (such as a superconducting or ferromagnetic transition) can be observed by the magnetometer.

The cell body and pistons are a copper-titanium alloy (97 % Cu, 3 % Ti), chosen due to its tiny magnetic background [42]. This material is mechanically weaker than BeCu, but with a much lower

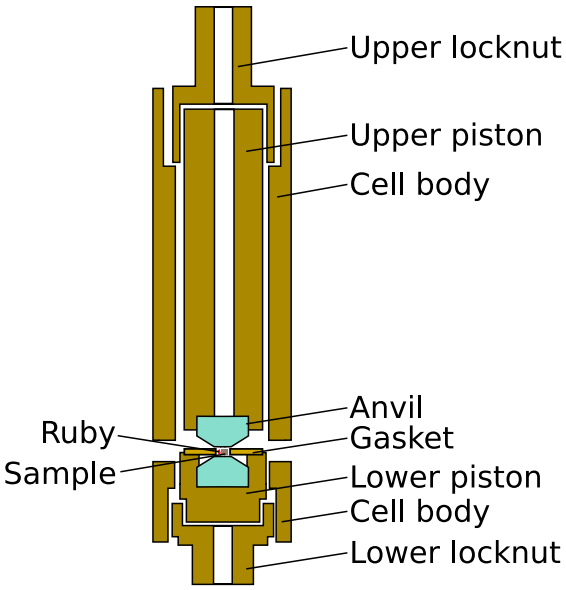

Figure 3.14: Cutaway schematic of a moisannite anvil cell. The cell body and pistons are constructed of CuTi, which has a very low magnetic susceptibility. The sample space contains both a sample (grey block) and ruby chip (red block). The cell's long thing shape allows it to fit inside the narrow bore of a SQUID magnetometer, while providing sufficient length for the upper piston to be centred without the need for additional screws (which would produce a large contribution to the magnetic background).

susceptibility. The anvils are polished moissanites with a 0.8 mm culet. The gasket is BeCu, pressed from a sheet of 560 μm stock using a custom-made punch. The gaskets are ellipses (rather than the circles found in conventional anvil cells) as this avoids the necessity of centring them with pins (which provide a significant contribution to the magnetic background) - instead, the lower piston is machined such that the gasket sits snugly on top of it.

Before use, a gasket is pre-indented, to reduce the thickness of the high-pressure region, making the flow of the metal more reliable when pressure is applied. The pre-indentation also serves to guide the anvils to ensure they align accurately. In the SMAC, the severe geometry constraints mean there is no room for alignment screws for the pistons, and the CuTi is prone to deforming slightly in the ram. This means the anvil alignment in the SMACs is inferior to in a conventional anvil cell.

The pre-indentation is done by repeatedly applying pressure to the cell with the gasket between the anvils; the central region of the gasket will be pressed thin by the anvils, and material will build up around the edges of the culet. Typically, pressure is applied in five steps, with three repeats of each pressure. Critically, between each step, the gasket is removed from between the anvils and flipped about its long axis, so that the "top" of the gasket is changed. This serves to ensure that any slight misalignment of the anvil culets is essentially cancelled out, and is a simple but effective way of ensuring the hole drilled in the middle of the pre-indented region is centred on both sides. The thickness is measured at each pre-indentation, and the final pre-indented region should have a thickness of $95 - 110\,\mu$m.

The centre of the pre-indented region is marked with a pin, and a 0.3 mm hole drilled with a high-speed drill and a fresh drill bit. The hole and the region around it are cleaned with a scalpel to remove any BeCu swarf. The gasket is then heat treated at 330 C for 15 minutes to harden it and reduce its deformation under pressure, and cleaned in ethanol in an ultrasonic bath for 15 minutes.

The gasket is placed back between the anvils, and a small load applied on the ram. The cell locknut is sealed, and the gasket glued in place on the lower piston with Double Bubble epoxy. When the epoxy has set, the lower piston can be removed from the cell, and the gasket should be flush against the anvil, with a centred hole.

The sample is then placed in the hole using a needle, and a single ruby chip of $\sim 30\,\mu$m length placed in the hole as a manometer. Impurities of chromium (IV) in the ruby give rise to sharp peaks in its fluorescence spectra at ~ 694 nm at ambient pressure. The application of pressure shifts these peaks; illumination of the ruby with a laser, and measurement of the fluorescence spectra with a spectrometer, thus allows a rapid and convenient measure of pressure at room temperature. To obtain a large signal, the ruby should be a cuboid block, rather than a thin sliver. Fig. 3.15 shows a typical ruby fluoresence signal obtained from our setup (measuring for 5 s, averaging 3 measurements). A large clear double peak can be discerned, which shifts upwards with pressure. A Gaussian fit to the R1 line (upper peak) gives a wavelength which can be used to obtain the pressure [43].

Use of the spectrometer allows determination of the pressure to within 1 kbar - while the error in the location of the ruby fluoresence peak is significantly smaller than this, the ruby's ambient-pressure peak position can fluctuate by a significant fraction of a kbar, and cell pressure falls by around 1 kbar upon cooling to 2 K. The cell's pressure can be set to within around 3 kbar of the

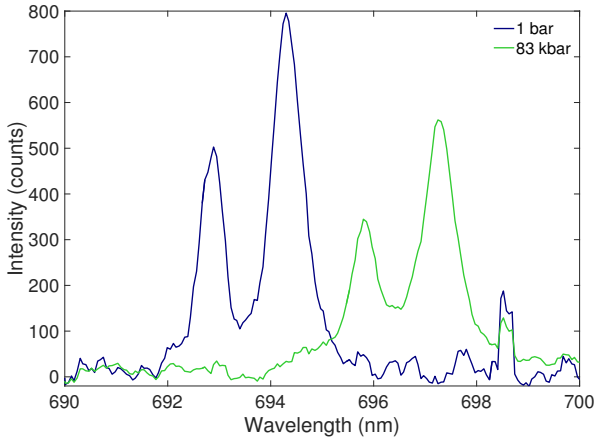

Figure 3.15: Ruby fluoresence signals (after subtracting a constant background) for the ruby chip inside a SMAC at ambient pressure, and at 83 kbar.The large peak corresponds to the R1 line, which shifts upwards with pressure in a well-characteristed manner.

desired pressure. While in principle a slight reduction in pressure is possible (a large reduction will result in the seal between gasket and anvil being lost, along with the pressure medium), in practice trying to take a cell down in pressure tends to be rather unreliable, so most samples are on a one-way trip to high pressures.

Before measurement, the cell is centred, using a small chip of Co or Ni attached to the edge of the gasket with GE varnish. This can be used to locate the dipole in the centre of the SQUID coils. This chip is then removed and measurements of the sample can take place.

The sample's volume is $\sim 1.25 \times 10^{-12}$ m^3, so a fully superconducting sample ($\chi = -1$) will yield a signal of 10^{-10} A m^2 in a field of 0.1 mT, above the magnetometre's resolution of 10^{-12} A m^2. The effectiveness of this measurement technique relies on the SVD fitting routine of the S700X. While the cell contributes a total magnetisation signal many orders of magnitude larger than the sample's, the irregular $V(z)$ this produces does not correspond to a dipole, so does not contribute significantly to the fitted dipole moment (as the cell is an extended object, so does give a significant contribution to the term corresponding to a point dipole source). Instead, the cell background will contribute weight to higher-order terms in the multipole expansion, which are ignored. Any small dipole contribution arising from the cell is assumed to be approximately constant, at least at low temperatures; this gives rise to a constant shift of the signal χ, which is removed by subtracting the high-temperature value above any transitions (where it's assumed χ is vanishingly small).

While this process is imperfect, it proves to be fairly effective for low-field measurements ($B \sim 1$ mT) of samples with clearly-defined jumps in temperature-dependent magnetisation $M(T)$. Such jumps are typically visible in the raw data, often with no need for subtraction of the background of an empty cell. In higher fields, the low-temperature tail of the BeCu gasket's magnetisation starts to contribute a significant background.

4 Semimetal-to-semiconductor transition in Bi-I

The semimetal bismuth possesses a tiny carrier density and small effective mass, giving rise to a host of interesting physics, such as the possible existence of correlated states at high field, and an apparent anisotropy in the Fermi surface inconsistent with the crystal structure. The electronic structure is exceptionally tunable, and some evidence suggests that the application of pressure can continuously tune the carrier density to zero.

This section presents results focused around measurements of the resistivity near the hypothesised semimetal-semiconductor transition. We aimed to extend the results of previous measurements of the resistivity and provide a much more detailed set of data for theoretical models of the semimetal-semiconductor transition to draw on, to investigate evidence for interesting new behaviour in the low-carier-concentration regime, and to assess recent predictions of the formation of novel phases which intervene before the semimetal-semiconductor transition is realised.

First, we describe a simple numerical model to calculate the carrier density and resistivity as a function of pressure based on the experimentally-measured parameters for the band structure and scattering rate. Then we present experimental results of detailed measurements of the resistivity up to 27 kbar, in five different samples at a total of over 60 pressure points, greatly expanding the available data on the subject. These results indicate that it is not necessary to invoke the onset of complex new phases near the semimetal-semiconductor transition to explain the data. Instead, it can be understood in terms of an interplay between the very low carrier density and scattering rate calculated by our numerical model, which can explain most - but not quite all - of the qualitative behaviour. Finally, we report measurements at high pressures down to temperatures as low as 17 mK. We show intriguing evidence for a new phase emerging below a temperature of ~ 1 *K when bismuth is close to the semimetal-semiconductor transition, whose existence has never previously been reported. We consider possible explanations, such as the formation of superconducting minority phases due to close proximity to a structural transition, or even a direct transport measurement of surface states.*

4.1 Literature review

4.1.1 An introduction to bismuth

Element 83 in the Periodic Table, with valence electron structure $6s^2\ 6p^3$, bismuth is a shiny, soft metallic material. Among the solid-state community bismuth could lay plausible claim to being the best-studied metal in the periodic table. Its strikingly complex and tunable electronic structure exhibits many fascinating properties which often defy the expectations of conventional theories of metals. Most notably, measurements on bismuth provided the first evidence of quantum oscillations and the existence of the Fermi surface, thereby experimentally confirming the underlying paradigm of all modern solid state physics [44, 45]. Landau had long predicted that quantum oscillations would be too small to observe experimentally; measurements on bismuth demonstrated that this was not the case, giving us the Shubnikov-de-Haas and de-Haas-van-Alphen effect as powerful tools for probing the Fermi surface fingerprint of a metal. A fairly accurate model for the relatively simple Fermi surface and the dispersion relation of the bands has been known since the

1960s[4].

Bismuth has been used since the time of the Incas (and perhaps long before) to produce bismuth bronze, a malleable, corrosion-resistance alloy. It was one of the first metals to be have been "discovered" - in 1546 it was known to be a distinct metal, and the name may stem from long before. One hypothesis for the etymology is rather intriguing: the name may come from the Arabic *bi ismid*, meaning *like antimony*. From the point of view of a condensed matter physicist bismuth is indeed exceptionally like antimony - the two are isovalent group V semimetals with tiny Fermi surfaces, details presumably unknown to ancient Arabia.

As a relatively non-toxic heavy metal bismuth is used in cosmetics, and it forms the basis of some pharmaceutical compounds, though the amounts used are small. In recent times it has begun to replace lead as an alloying material due to the reduced health concerns, in particular in low-melting-point solders used for electronics or food processing equipment. It currently - and in our view surprisingly, given its host of exceptional physical properties - has little use in advanced technological applications. This may in part be because of the difficulty of growing high-quality thin films that retain the bulk properties; bismuth has considerable potential as a magnetic field sensor [46].

To a solid-state physicist bismuth is a material of near-inexhaustible fascination. It is a compensated semimetal with an exceptionally tiny carrier concentration (around one free charge carrier per hundred thousand atoms [47]), giving it a tiny Fermi surface and a tiny, highly-anisotropic effective mass around one-thousandth that of the electron in some directions [8]. These properties mean it has the highest Hall coefficient of all metals and the largest diamagnetism, as well as exceptionally small thermal conductivity [48]. The tiny effective mass and availability of high-purity crystals mean the low-temperature mean free path can be hundreds of micrometers and the magnetoresistance at low temperatures in fields of several tesla can be around six orders of magnitude. In field, the ultraquantum limit (when all carriers occupy the lowest Landau level) can be reached in fields of only around 10 T, leading to a host of novel physics. Bismuth is one of few elements to contract upon melting (like water), and the electrical conductivity of the liquid is higher than of the crystalline solid [48]. The tiny carrier density corresponds to a Fermi temperature of around 300 K, meaning the carrier density of bismuth is notably temperature-dependent (unlike for conventional "good" metals). The enormous magnetoresistance, large mean free path and tiny carrier mass mean quantum oscillations and direct measurements of the Fermi surface are straightforwardly accessible, even in fairly low fields or temperatures well above 20 K.

4.1.2 The structure and band structure of bismuth

The unique properties of bismuth arise from its structure, which is unusually complex for an element. Bismuth adopts a rhombohedral structure with the $R\bar{3}m$ space group, which is most easily understood as arising from a slight distortion from a cubic structure as a result of a form of Peierls distortion.

[4] Recently this well-established model has come under unexpected attack from more modern measurements, which suggest that the structure-enforced threefold symmetry of the electron Fermi surface pockets may be lifted by some currently unknown mechanism. Additionally, modern attempts to directly probe the band structure with ARPES have been unsuccessful due to the hitherto-unknown presence of surface states. See section 4.1.3 and 4.1.6 for details.

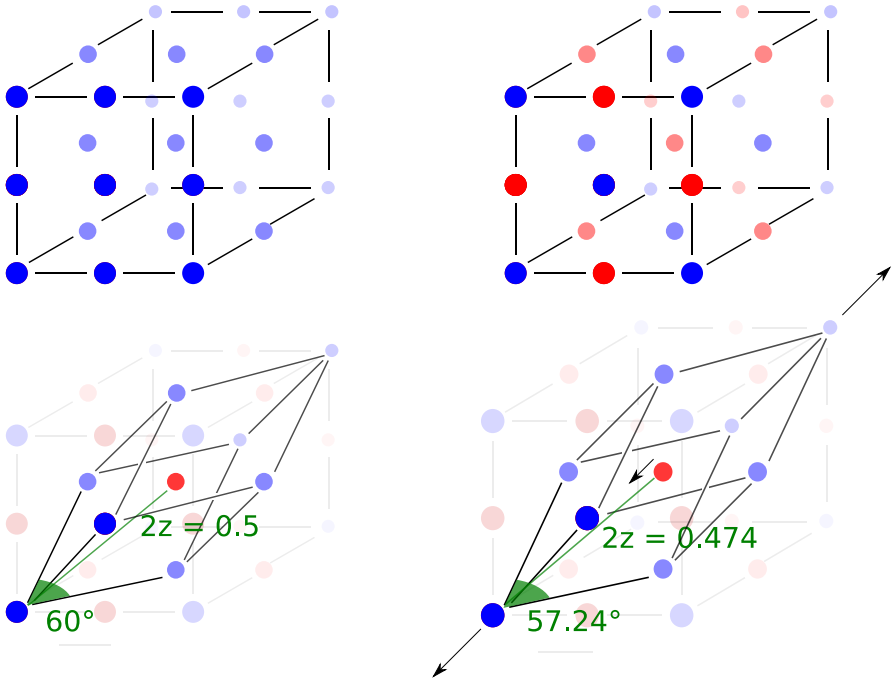

Figure 4.1: The structure of bismuth. Atom size and shade indicates depth. Top left: simple cubic structure. Top right: the simple cubic structure as two interpenetrating face-centred cubic (fcc) lattices (red and blue). Bottom left: the alternative rhombohedral unit cell of the interpenetrating fcc structure, with an angle of 60°, and the atom from the second lattice at the centre of the cell. Bottom right: distortion along the (111) direction, resulting in the two-atom rhombohedral cell of the real material.

The structure and electronic properties of bismuth can be arrived at as follows. First, consider a simple cubic structure for bismuth with one atom per unit cell; as bismuth is pentavalent, the resulting crystal should be metallic (as there would be an odd number of free electrons per unit cell). The structure will therefore be vulnerable to an instability analogous to the one-dimensional Peierls distortion: if a structural distortion can double the size of the unit cell, and thereby halve the size of the first Brillioun zone, there will be an even number of electrons in the unit cell, which will fill states up to the edge of the Brillouin zone. The effects of the periodic potential lower the energy of states at the edge of the Brillouin zone; one-dimensional metals are therefore always *vulnerable* to a Peierls distortion and the formation of dimers, although whether such a distortion *actually occurs* depends on whether the reduction in electronic energy outweighs the increase in elastic energy caused by dimerisation.

In bismuth, such a structural distortion does indeed occur. Let us return to the simple cubic structure, but label alternating atoms bismuth-A and bismuth-B. The bismuth-A sublattice now forms a face-centred cubic unit cell which interpenetrates a similar bismuth-B face-centred cubic lattice. An alternative unit cell can be constructed by joining a bismuth-A atom to its three nearest

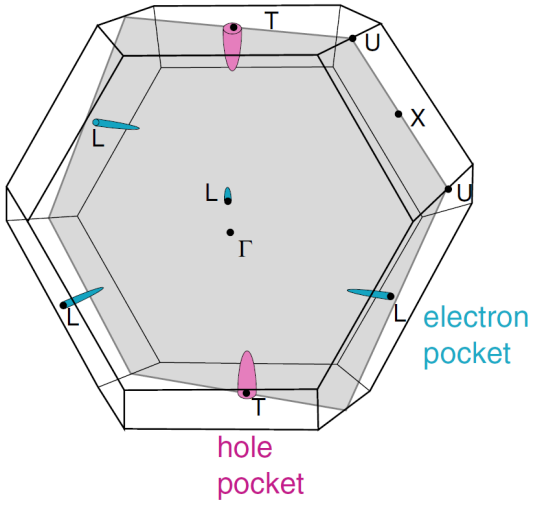

Figure 4.2: First Brillouin zone of bismuth, indicating the electron and hole pockets at the $L-$ and $T-$points. Taken from [51].

neighbours on the faces, and those atoms to the bismuth-A atom on the opposite corner of the original face-centred cubic cell. This new cell is rhombohedral, with a rhombohedral angle of 60°, and contains one atom of bismuth-A and one of bismuth-B. The Peierls-type distortion manifests as a slight stretching of this cell along the 111 face-centred cubic direction (reducing the rhombohedral angle to 57.24°), and a slight shift of one fcc sublattice with respect to the other (meaning the shifted lattice sits at (0.474 0.474 0.474), rather than the (0.5 0.5 0.5) of the undistorted case) [49]. DFT calculations have demonstrated that the transition from simple cubic to rhombohedral unit cell indeed converts a metal to a semiconductor; the small shift of one fcc lattice with respect to the other results in a transition from a semiconductor to semimetal [50].

There are now two atoms per unit cell; however, because the distortion is only small, the Fermi surface does not become completely gapped. Instead, tiny Fermi surface pockets remain. At the T-point of the Brillouin zone there exists a hole ellipsoid, and at the $L-$points three electron ellipsoids, but these are exceptionally small in size. Fig. 4.2 shows the first Brillouin zone of bismuth, including the location of the $T-$ and $L-$points. Fig. 4.3 gives a schematic of the Fermi surface in reciprocal space, as well as the dispersion at the $T-$ and $L-$ points . Bismuth is therefore a compensated semimetal, with equal numbers of electrons and holes: this number is as small as one electron (or hole) per one hundred thousand atoms. These exceptionally tiny Fermi surface pockets give bismuth its host of intriguing properties.

The primitive axes of the rhombohedral structure are not orthogonal; conventionally, a new set of orthogonal axes are defined. The (111) body diagonal of the original fcc cubic cell is termed the trigonal axis, and the structure also possesses a binary axis (which joins two bismuth-A atoms in the fcc representation), and a bisectrix axes (which is perpendicular to both the other two axes). In the alternative hexagonal representation, the trigonal axis points along (0001) - see Hofmann's review for an extremely useful overview of the details of the structure [51]. The hole ellipsoid is directed along the trigonal axis, while the three electron ellipsoids lie almost (but not quite) in the trigonal

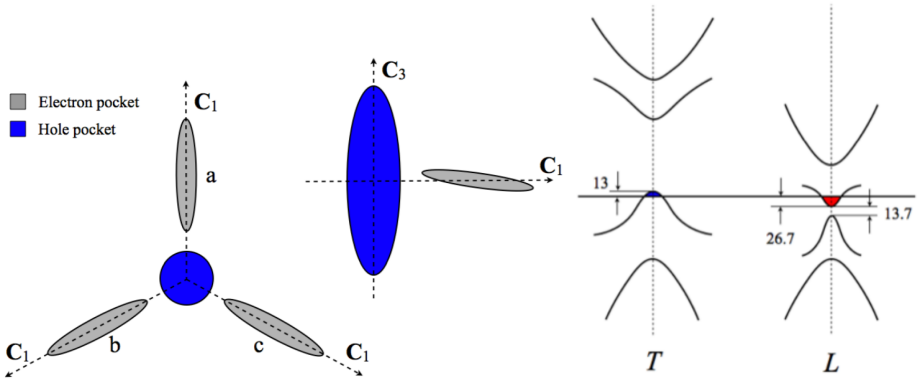

Figure 4.3: The band structure of bismuth. Left: schematic of the Fermi surface; note that both hole and electron ellipsoids are (enormously) magnified in size to be visible. The axes $C_{1,2,3}$ are respectively binary, bisectrix, and trigonal. Right: Dispersion relation $E(k)$ at the $T-$ and $L-$ points of the Brillouin zone, showing the tiny band overlap. Text values are energy scales in meV taken from a tight-binding model [52]. Adapted from [11].

plane: one such ellipsoid points along the binary axis, and the other two are rotated by 120° around the trigonal axis; their tilt angle with respect to the trigonal plane is 6°. The structure (and Fermi surface) therefore possess threefold symmetry around the trigonal axis.

4.1.3 Physical properties of bismuth

Bismuth's exceptionally tiny carrier density gives it the highest Hall coefficient of any metallic element (as $R \sim 1/n$) [48]. As the Fermi surface ellipsoids are exceptionally small, they have a very high curvature; they are also highly anisotropic. Carriers in bismuth have an extremely small effective mass which is strongly direction-dependent: in some directions $m \leq 0.001 m_e$ [48, 49, 8]. A useful modern reference for the relevant electronic properties is provided by Fuseya *et al.* [49].

Bismuth single crystals can be made rather free from impurities. This means the mean free path of electrons in bismuth can be on the order of hundreds of micrometers [8, 49]. The room-temperature value for the resistivity is ~ 120 μΩ cm (although this is slightly direction-dependent; experimentally, the ratio of ρ along the trigonal axis to that along a perpendicular axis is 1.15 [11, 48]). High-purity samples have a RRR of about 100 (though this measurement of sample purity is complicated by a temperature dependence of the carrier density, as outlined below).

The long mean free path and tiny value of m give rise to one of bismuth's most striking properties, which is its enormous magnetoresistance. Recall from Section 2.3 that the approximate value of two-band magnetoresistance is set by $\omega_c \tau$; for bismuth both $\omega_c = eB/m$ and $\tau = l/v_F$ are enormous. The resistivity of bismuth at 2 K therefore increases by over six orders of magnitude in fields of 9 T (for conventional metals, the increase is typically a few tens of per cent).

The condition $\omega_c \tau \gg 1$ is precisely that required for the observation of quantum oscillations, which are straightforwardly seen in bismuth at fields below 1 T and temperatures above 20 K. Bismuth was the material in which quantum oscillations were first observed (in both the magnetisation, the de Haas-van Alphen effect, and the resistance, the Shubnikov-de Haas effect) [44, 45].

Carriers	m_1	m_2	m_3	ϕ_e	ϕ_h	ϵ_F (meV)	ϵ_g (meV)	n (m^{-3})
Electrons	0.00119	0.266	0.00228	6 ± 2	-	27.2	13.6	2.7×10^{23}
Holes	0.064	0.064	0.69	-	0	10.8	-	2.7×10^{23}

Table 1: Parabolic band model parameters for bismuth at $T = 0$ K, as summarised by Issi *et al.* [8]. Entries are the three components of the effective mass tensor (in units of m_e, defined positive for both electrons and holes), the angle of the electron and hole ellipsoids in degrees, the Fermi energies, the band gaps, and the total carrier densities.

The relatively simple Fermi surface of bismuth has been studied with the powerful probe of quantum oscillations for around seven decades, and is well-understood experimentally. An exhaustive review of the experimental determination is given by Edelman [53]. It can be parametrised with a number of pleasingly tractable models [8]. The simplest of these assumes all the bands are parabolic; the Fermi surfaces will therefore manifest as a number of ellipsoids (exactly as observed experimentally). The dispersion relation near a pocket is:

$$\epsilon(k) = \frac{\hbar^2}{2m_e}\mathbf{k}M^{-1}\mathbf{k} \tag{4.1}$$

where the inverse mass matrix is:

$$M^{-1} = \begin{pmatrix} m_1 & 0 & 0 \\ 0 & m_2 & 0 \\ 0 & 0 & m_3 \end{pmatrix}^{-1}. \tag{4.2}$$

Here, the m_i are the components of the effective mass tensor; their values in terms of the free eletron mass m_e are given in Table 1, where it can be seen that, in particular for the electrons, the masses are both very small and very anisotropic.

This elegant model for the band structure works well for the hole pocket of bismuth, but fails for the conduction electron bands, as these are not truly parabolic (the effective mass is energy-dependent). Such non-parabolicity arises from the very small band gap $\epsilon_{g,e}$ separating electron from hole states. The result of this is to slightly complicate the expression for the electron dispersion:

$$\epsilon(k) \to \epsilon\left(1 + \frac{\epsilon}{\epsilon_{g,e}}\right) \tag{4.3}$$

A further - and potentially rather significant - complication arises in bismuth, because the band parameters are noticeably temperature-dependent [8]. The Fermi level at 0 K lies at only ~ 100 K for holes in bismuth, and at temperatures well below this the Fermi-Dirac distribution will begin to noticeably broaden (recall that in conventional metals the Fermi level is around 10,000 K, so the approximation that the Fermi-Dirac distribution is a sharp step at ϵ_F is generally valid). In bismuth, for example, the band gap $\epsilon_{g,e}$ increases by a factor of around $3\times$ from 2 to 300 K, and the band overlap between electrons and holes also changes, as shown in Fig. 4.4 [54, 55, 8, 56].

As a result, the carrier density is strongly temperature-dependent, and increases by a factor of

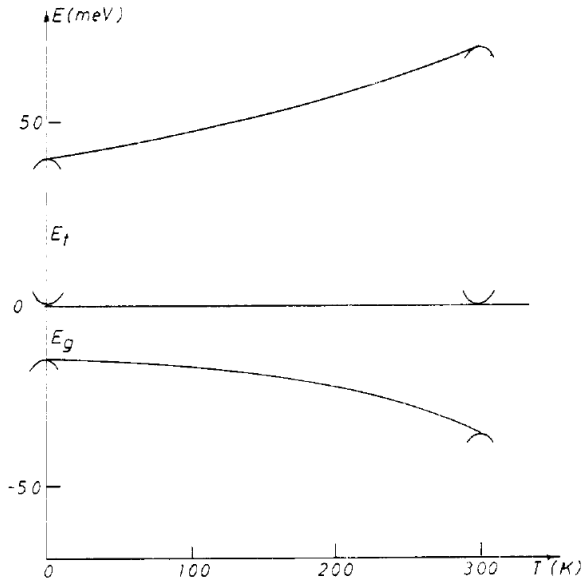

Figure 4.4: Temperature dependence of the band parameters of bismuth, taken from [56]. The band gap E_g increases with rising temperature, as does the overlap energy between holes and electrons E_t.

around $4-9\times$ from 0 K to 300 K (see Fig. 4.5) [54, 8]. While the carrier density is a crucial ingredient of many physical properties, it has not been subjected to a detailed investigation. Issi states that the carrier density increases by $8\times$ from 2 to 300 K, but measures only down to liquid nitrogen temperatures [54, 8]. Balla and Brandt, in their seminal study of the semimetal-to-semiconductor (SMSC) transition, collate the data from a number of Russian authors and obtain an increase of $9\times$ [57]. Recent measurements by Armitage *et al.* of the plasma frequency imply an increase of $4\times$; they present calculations in support of such an increase, but the parameters used for the band overlap are not in agreement with published values [12]. Collaudin *et al.*, who have conducted a very detailed magnetoresistance study, state that $n(T)$ is T-dependent and use it as an adjustable parameter, but do not show the result [58]. Our own calculations, detailed below, suggest the increase is a factor of $5.3\times$; we use temperature-dependent band parameters derived from Norin [56].

The temperature-dependent carrier density explains the rather low RRR of most bismuth samples, which is typically only ~ 100, even though the mean free path may be in excess of 100 micrometers [8, 49]. Such an RRR corresponds to a reduction in the scattering rate of $\sim 500\times$ at 2 K compared to room temperature; in the resistivity, some of this reduction is offset by the fall in $n(T)$.

One might expect the conductivity of bismuth to be rather small, as n is four orders of magnitude smaller than conventional metals. In fact, at room temperature $\rho \approx 120$ μΩ cm (there is some slight dependence on the crystallographic direction), a value not that much larger than might be expected for a good metal. This arises for three reasons. Firstly, due in part to the low melting point and in part to the ease of forming large crystallites, obtaining high-purity samples of bismuth (with a small impurity concentration, and therefore a long mean free path) is fairly straightforward. Secondly, as noted in Table 1, the effective mass is extremely low. Finally, phonon scattering in bismuth is quite

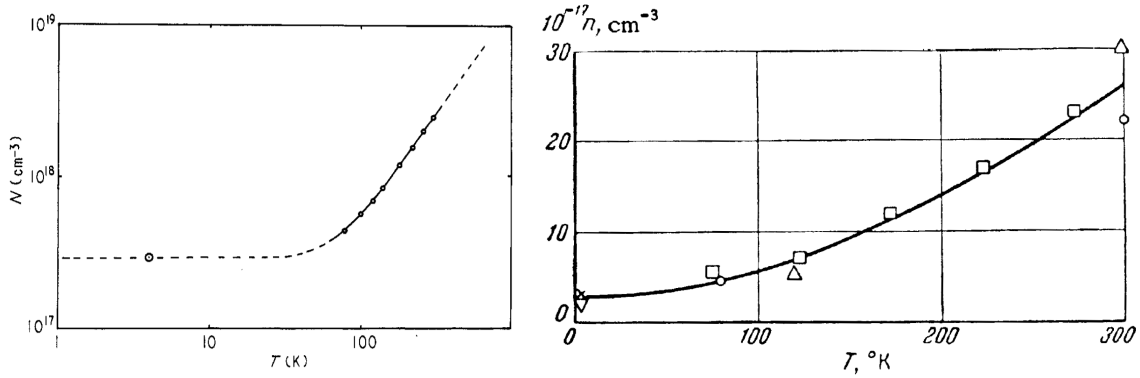

Figure 4.5: Temperature dependence of the carrier density of bismuth, taken from (left) [54] and (right) [57]. Increasing temperature causes an increase in carrier density arising from the broadening of the Fermi-Dirac function, activation of carriers across the L-point gap, and an increase of the band overlap with temperature.

different to in conventional metals because of the tiny Fermi surface. At elevated temperatures there are relatively few phonons with a *low* enough wavevector to effectively scatter electrons, thus much less phonon scattering occurs than might be expected at high temperature [8].

An alternative - perhaps more rigorous, but less tractable - approach to the behaviour of conduction electrons in bismuth is to consider the conduction band dispersion relation as an example of the Dirac Hamiltonian (strictly, electrons in bismuth are described by the Wolff Hamiltonian, which allows the effective velocity to be anisotropic; the Dirac Hamiltonian is the isotropic-velocity case) [49]. Much of the interesting physics observed for Dirac quasiparticles in graphene may also appear in bismuth, and the Wolff Hamiltonian has been effectively used to explain many properties such as the Hall effect or the exceptionally large diamagnetism of bismuth. However, it should be noted that for an experimentalist the Wolff Hamiltonian is a complication which may have little impact on observable results, and the conventional ellipsoid Fermi surface picture may be more useful.

Recent investigations of bismuth continue to yield new and intriguing results. One particular area of interest is the high-field region above the quantum limit. The quantum limit corresponds to the field at which the magnetic lengthscale $l_B = \sqrt{\hbar/eB}$ becomes shorter than the Fermi wavelength $\lambda_F = 2\pi/k_F$; above this field, all electrons are in the lowest Landau level. For most conventional metals, the field required is many hundreds of tesla, but for bismuth, thanks to its tiny Fermi surface, the field is less than 10 T. Recent measurements have probed the Nernst effect in fields up to 30 T [59, 9], and found surprising results with a variety of possible explanations. With the field along the trigonal axis, the quantum limit should be reached at 6.4 T for holes and 8.6 T for electrons, yet the Nernst effect showed very sharp peaks even at higher fields, at which point all carriers are expected to be in the lowest Landau level (see Fig. 4.6). The peaks do not display the expected $1/B$ periodicity observed for Landau level crossings at lower fields.

Further investigations beyond the quantum limit used torque magnetometry to probe quantum oscillations in the magnetisation [61]. These measurements provided further support for the use of the Dirac Hamiltonian, which reproduced the observed quantum oscillation spectrum while the conventional approach did not. It was argued that additional peaks at high field are evidence

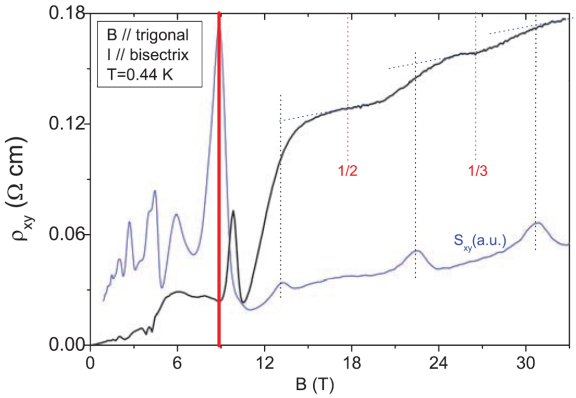

Figure 4.6: Oscillations in the Nernst effect and resistivity in bismuth in high field, taken from [9]. The red line indicates the quantum limit, but oscillations are still observable at higher fields, ascribed to electron fractionalisation. Later experiments indicated this may instead be due to measurements on a twinned crystal [60].

of a complex new phase, perhaps forming due to strong Coulomb repulsion between the tightly-confined electrons. In addition, the high-field state appears to be unexpectedly anisotropic - that is, the three electron ellipsoids are no longer equivalent.

The observation of the high-field Nernst peaks, well above the quantum limit, was later attributed to measurements on a twinned crystal [60]. Bismuth is prone to twinning (a secondary crystallite forms sharing a binary axis, but with a trigonal axis rotated by 108^o from that of the main crystal) - for a full explanation, see Section 4.1.4. A two-crystal model was shown to accurately describe all measured Nernst peaks. However, even this rather prosaic explanation led to new complexities: the two-crystal model could only decribe the data if it was assumed that each crystallite had a different chemical potential (and therefore carrier density) in field, and it remains unclear how this could arise. In addition, the size of the Nernst peaks resulting from the twin was very much larger than expected, and a full explanation is still lacking.

The apparent high-field anisotropy is a feature which has been observed by a number of authors [62, 63, 58]. Zhu *et al.* demonstrated that in an applied field, the conductivity of the three electron pockets is very different, and that the magnetoresistance of each pocket behaves differently with temperature, similar to the torque magnetometry results reported by Li *et al.* [61]. A study on the angular dependence of the magnetostriction came to a similar conclusion: contrary to the result expected from the symmetry of the Fermi surface, in high field the three electron valleys are not equivalent. This may arise due to many-body effects; these are typically neglected in bismuth, but in high fields, the electrons are tightly constrained in the lowest Landau level, and Coulomb repulsion and therefore many-particle effects may become significant [63]. The magnetostriction measurement decisively ruled out effects such as strain or twinning; the effect is observed in the density of states at the Fermi level of each valley, rather than the total occupation. A very detailed study of the magnetoresistance at all possible angles further confirmed the loss of the valley degeneracy [58] at low temperatures and high fields (see Fig. 4.7). For the moment, the details of this 'valley-nematic' state remain unexplored.

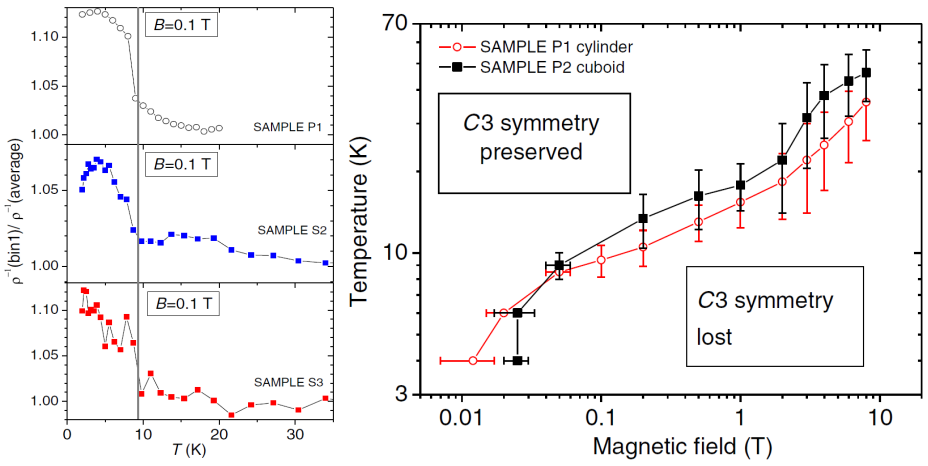

Figure 4.7: Left: Angular anisotropy of the resistivity along the binary axis for three samples of Bi. Along the three binary axes $\rho_{bin,i}, i = 1,2,3$ the resistivity should be the same as the Fermi surface has threefold symmetry, but this is not the case at low temperatures or high fields. Right: phase diagram for Bi, showing the loss of threefold symmetry at low temperatures and high fields. Adapted from [58].

Very recently, superconductivity was reported for the first time in a high-purity single crystal of ambient-pressure bismuth. The superconducting properties - and the experiment that discovered them - are rather remarkable: $T_c = 530$ μK, and the upper critical field is 5.2 μT [64]. Previous measurements of bulk bismuth have looked for superconductivity at temperatures down to 10 mK but observed nothing (while superconductivity has been observed in amorphous bismuth, bismuth under pressure, thin films of bismuth, and bismuth nanoparticles [64, 65]). A fairly recent ab initio study of superconductivity in bismuth suggested that the transition temperature for the bulk material would be below 1 mK, as proved to be the case [66]. Prakash *et al.*, perhaps inspired by this challenge, used a DC SQUID sensor on a nuclear demagnetisation refrigerator attached to a dilution refrigerator, to obtain a base temperature of 100 μK. Because the critical field is well below the Earth's magnetic field, the whole setup had to be shielded using a lead superconducting can. The superconductivity is clean type I, and is of particular interest because the BCS theory appears not to apply. In bismuth, the carrier density (and hence DOS at E_F) is exceptionally small, so the usual BCS relation $T_c \approx \Theta_D e^{-1/VN(E_F)}$ would predict an (even) smaller transition temperature. Similar results were observed in oxygen-deficient $SrTiO_3$, another very low carrier density superconductor ($T_c \approx 50$ mK) [64]. Bismuth at exceptionally low temperatures therefore provides a well-charateristed prototypical material for investigations into non-BCS superconductivity, perhaps mediated by enhanced electron-electron attraction due to the complex phonon and Coulomb effects of the tiny carrier density [64].

4.1.4 Twinning in bismuth

Of some relevance to our own experimental results is the nature of twinning in bismuth. Bulk bismuth single crystals are very soft, and very prone to mechanical twinning if mishandled. Zhu *et*

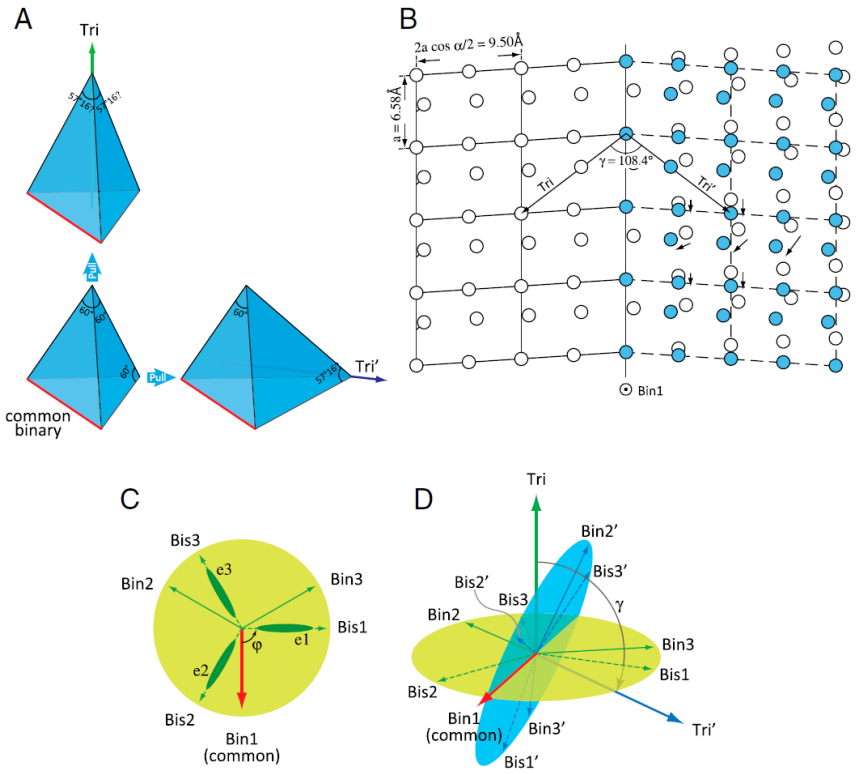

Figure 4.8: Twin boundary formation in bismuth, taken from [60]. Top left: the two possible deformations of binary-axis-sharing bismuth tetrahedra. Top right: the resulting displacement of the atoms; solid blue circles show the displaced atoms of the twin. Bottom left: view down the trigonal axis before twin formation, showing the three-fold symmetry of the electron Fermi surface pockets and the three possible binary (Bin) and bisectrix (Bis) axes. Bottom right: relation of the twinned axes to the original crystallographic axes: the twin shares a binary axis, but has its trigonal axis rotated 108°with respect to the original crystal.

al. give an excellent description of the twinning process [60], but the basic idea is as follows. As described above, the bismuth structure can be considered as a distortion of two interpenetrating fcc lattices along their (111) direction, and there are four such equivalent directions. Around each, the lattice has threefold rotational symmetry (hence the three electron Fermi surfaces). Before the distortion, the four nearest-neighbour bismuth-A atoms form the vertices of a tetrahedron with a 60° angle between each edge. Define one such edge as the binary axis; the distortion can pull on either of the other *two* atoms while retaining the same binary axis. At the twin boundary, the two crystallites therefore share a binary axis; their trigonal axes are rotated by 108°, as shown in Fig. 4.8.

The formation of twins in bismuth is a well-known phenomenon. In an exhaustive description of the growth of single-crystal bismuth, Kapitza in 1928 remarks that *"during bending, the less flexible rods [of bismuth], if held close to the ear, emitted cracking sounds, whereas others, being more flexible, did not... These sounds are probably caused by the development of the cracks and imperfections already existing in the lattice of the bismuth crystals."* [67]. This sound is likely related to the formation of twins. By 1934, Berg was remarking that "*Single crystals of bismuth are stated by many*

authors to exhibit mechanical twinning... Rather large twins ... were observed when a tensile test at high temperature was applied to a bismuth crystal." [68]. A description of the process is given by Hall [69]. In 1970, Brown states that twins likely give rise to spurious additional quantum oscillation frequencies reported by several previous studies: "*Carefully annealed samples with resistivity ratios above 400 did not show these [spurious] periods. However, the periods could be induced by straining...*" [70].

4.1.5 The semimetal-to-semiconductor transition

The already exceptionally-small carrier density in bismuth can be tuned with hydrostatic pressure. In principle, this could allow a Lifshitz transition (a continuous topological change in the Fermi surface), in which the Fermi surface pockets are shrunk continuously until they vanish. Such a SMSC transition would be of considerable interest, particularly in the context of a material with already tiny Fermi surfaces such as bismuth: it would allow the continuous tuning of the carrier density to zero, perhaps resulting in the formation of exotic strongly-interacting states such as excitonic condensates: eventually the carrier density is so low that screening of the Coulomb interaction breaks down, and electron-hole pairs form composite particles [12].

The exact mechanism for the SMSC have been investigated for over fifty years, but the details remain unclear. Applied pressure shifts the electron band down and the hole band up, and perhaps also moves the chemical potential with respect to the band edges. The result is a resistivity which becomes highly non-metallic: at 0 kbar, $\rho(T)$ rises by a factor of > 100 from 2 to 300 K, while at 20 kbar it falls by a factor of > 1000.

The situation is complicated dramatically by the existence of a structural transition occuring at 25 kbar at room temperature, where the rhombohedral structure (termed Bi-I) converts to monoclinic Bi-II [71]; the high-pressure structure is unambiguously metallic (and superconducting, with $T_c \approx 4$ K). However, 25 kbar is also approximately the pressure where the SMSC transition is expected to occur; it therefore remains unclear whether, in a formal sense, bismuth truly does become semiconducting (i.e. the band overlap energy ϵ_t falls to zero) before the structural transition intervenes.

A number of studies have investigated the room-temperature resistivity of bismuth as a function of pressure, precisely because of the structural transition: sharp structural changes at 25 kbar and again at 27 kbar allow bismuth to be used as a high-pressure calibration material [39, 72]. However, details of the SMSC transition require information about the temperature dependence $\rho(T)$, first undertaken by Balla and Brandt in 1965 [57]. They found that while applied pressure slightly increases the room-temperature resistivity (as also seen in [39, 72]), it has a dramatic impact on the qualitative behaviour of $\rho(T)$. At pressures of around 12.6 kbar, $\rho(T)$ was seen to develop a small, broad peak at $T \approx 50$ K; at lower pressures $\rho(T)$ rose monotonically with temperature as expected for a semimetal. Increasing pressure led to a rise in the peak height and a shift of the peak position to lower temperatures, ascribed to a reduction in the carrier density and a continuous decrease in the low-temperature carrier density $n_0 = n(T = 0)$. Fig. 4.9 shows Balla and Brandt's measurements of $\rho(T)$ at increasing pressures. Assuming that the dispersion is quadratic, that the Fermi level shifts linearly with applied pressure, and that the carrier mobility (i.e. τ) is not strongly influ-

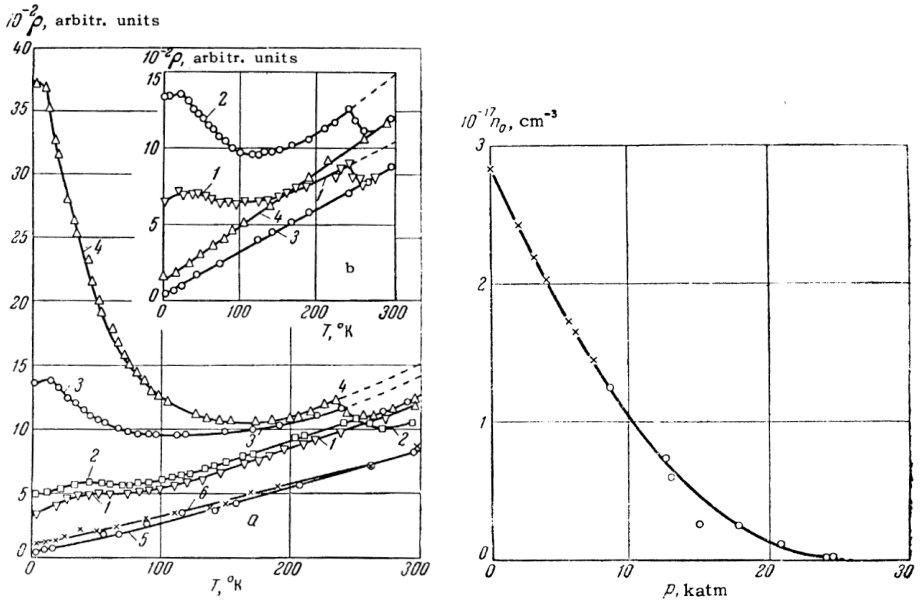

Figure 4.9: Left: resistivity $\rho(T)$ with current along the trigonal axis at a number of pressures, as measured by Balla and Brandt [57]. Curves 1-4: $p = 8.6, 12.6, 17.8, 20.6$ kbar; curves 5-6: after removing pressures, for several different samples. Inset: $\rho(T)$ wth current perpendicular to the trigonal axis. Curves 1-2: $p = 13, 15$ kbar; curves 3-4: after removing pressures, for several different samples. Right: zero-temperature carrier density as a function of pressure obtained by the same authors from their resistivity measurements.

enced by pressure, Balla and Brandt suggested a pressure-dependence $n_0(p) \sim (1 - p/p_c)^{3/2}$, where p_c is the critical pressure at which the Fermi surface vanishes; see Fig. 4.9. This fit their resistivity data rather well, and suggested $p_c = 25$ kbar. However, this interpretation of the data is not wholly satisfying. In particular, it remains unclear why at intermediate pressures a *peak* should be expected in $\rho(T)$ (rather than, for example, a monotonic increase with falling temperature), and why at higher pressures the resistivity does not diverge at low temperature, as would be expected for a true semiconductor.

Early Hall effect measurements aimed to directly probe the pressure-dependence of the carrier density [73]. Because of the simple Fermi surface of bismuth, a straightforward link between the band overlap and the Hall coefficients could be obtained, which implied that the carrier density would vanish at $p_c = 19$ kbar. More detailed estimates of the carrier density's pressure-dependence were obtained with the powerful technique of quantum oscillations, which give a direct value of the Fermi surface volume (and hence carrier density) without the many complexities arising from analysis of the Hall resistivity in the presence of both multiple bands and bismuth's enormous magnetoresistance [74, 75, 76, 77]. These studies indicate a rapid fall in the Fermi surface volume with applied pressure: Itskevitch and Fisher found that by 15 kbar the ellipsoid volume has reduced by a factor of ~ 5 [76, 77]. Extrapolations indicate the Fermi surface volume should vanish at around 25 kbar, in good agreement with the results of Balla and Brandt [77, 76].

Another early measurement of the resistivity at high pressures looked at whether it could be

made to obey an activated Arrhenius law, implying a reduction in activated carriers at low temperatures, and therefore the existence of a band gap [78]. The results indicate such a band gap does exist, being ~ 5 meV at 14 kbar, and extrapolating to -0.4 meV at zero pressure- a significant underestimate of the real $p = 0$ band overlap. However, it should be noted that Brandt and Ginzburg, in their much more detailed study, explicitly reject the notion that $\rho(T)$ obeys an Arrhenius law.

Ventsell and Rakmanina looked at the magnetoresistance at 78 K in fields up to 10 T and pressures up to 50 kbar using a Bridgman anvil cell [79]. They noted that up to 20 kbar, $\Delta R/R = \rho(B)/\rho(B = 0)$ scales as $\sim B^{1.5}$ and climbs to around $100\times$ the zero-field value, but at higher pressures $\Delta R/R$ saturates, and the saturation value falls with increasing pressure.

As discussed in Section 2.3, saturation in the magnetoresistance arises, in a simple two-band model, from an imbalance between the numbers of electrons and holes, and Ventsell and Rakmanina argue that this imbalance arises from carriers localising on impurities or defects in high fields; as the band parameters of the electrons and holes differ slightly, their behaviour in field will also be slightly different (i.e. in high fields bismuth is no longer a compensated semimetal or semiconductor). They argue that the pressure dependence of the magnetoresistance implies such a phenomenon, that the SMSC transition indeed occurs at 25 kbar, and that the band overlap changes with pressure at a rate $d\epsilon_o/dp \approx 0.7$ meV/kbar - a value which implies an extremely large value of the critical pressure p_c at which the band overlap vanishes [76, 80].

The temperature dependence of the resistivity was investigated again by Kraak *et al.* in 1982 [81]. They looked only at lower pressures (up to 15 kbar), and performed careful and detailed measurements from 2 to 77 K to look at the power law dependence $\rho \sim T^\alpha$ as the Fermi level E_F is tuned by pressure. At low temperatures $\rho(T)$ is quadratic, and at higher temperatures linear. The high-temperature T-linear resistivity arises from phonon scattering; it should be noted that in bismuth, the condition for linearity is not strictly $T \geq \Theta_D$ because the Fermi surface is so small; the relevant energy scale is the reduced Debye temperature $\Theta_D^{eff} = \frac{2\hbar c k_F}{k_B}$, where c is the speed of sound [8, 81]. At low temperatures, the resistivity varies as $\rho \sim T^2$, crossing over to $\rho \sim T$ at a temperature T^* which falls with increasing pressure. There are numerous possible explanations considered by Kraak *et al.* for the low-temperature quadratic behaviour (not necessarily just Fermi liquid behaviour), the most likely being carrier-carrier interaction. It should be noted that up to 15 kbar, all of the resistivity traces are clearly metallic, with no sign of the SMSC behaviour.

Even at ambient pressure, the metallic resistivity is - of course - unexpectedly complex. Down to ~ 1.5 K, the resistivity was seen to obey a $\sim T^2$ law, ascribed to carrier-carrier scattering [11]. However, at lower temperatures, the emergence of a $\rho \sim T^5$ law is observed [82, 11]. This was initially ascribed to an exceptionally low effective Debye temperature (in a similar argument to that given by Kraak above), although to fit the data requires $\Theta_D^{eff} \approx 1$ K. Recent calculations by Chudzinski and Giamarchi suggested that the behaviour can be well-explained with an acoustic plasmon mode that interacts with the charge carriers [11]. They note that as pressure is increased and the carrier density falls, the plasmon-plasmon interactions will strengthen. This could favour the formation of a strongly-correlated semimetal rather than a semiconductor.

A recent investigation by Armitage *et al.* in 2010 studied the optical conductivity of bismuth at elevated pressures, in an attempt to reopen the debate on the SMSC transition [12]. With such mea-

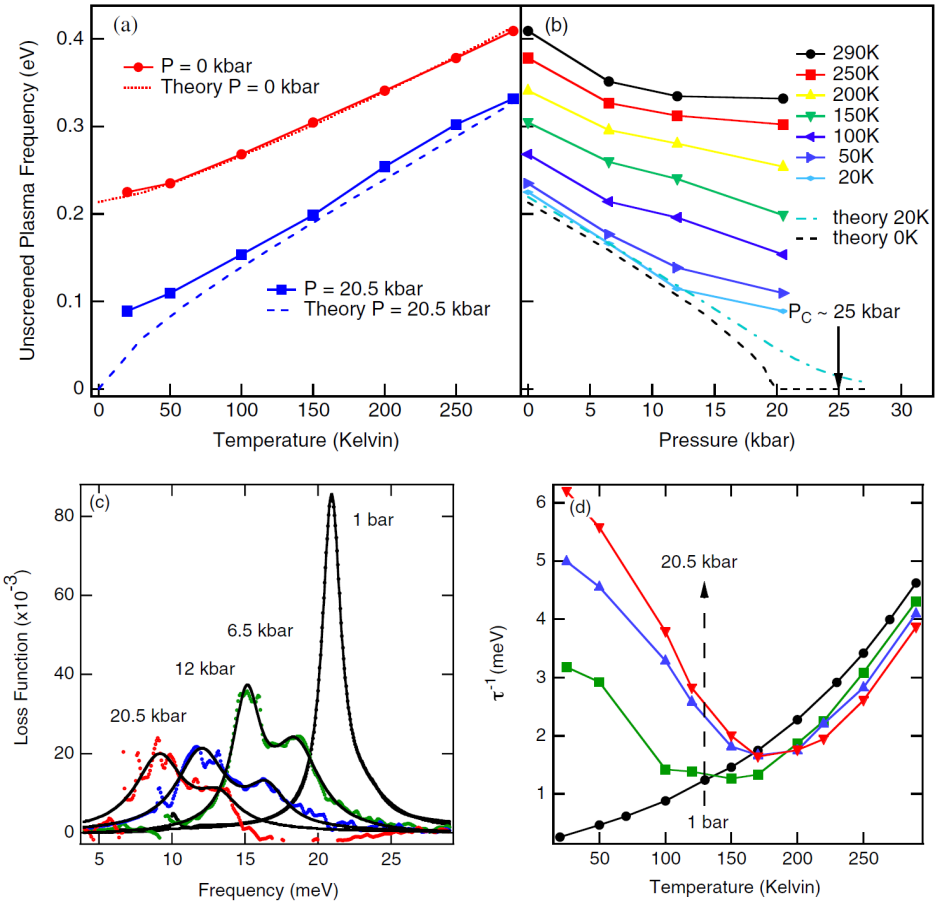

Figure 4.10: Results of optical scattering measurements on bismuth under pressure, taken from [12]. Top: unscreened plasma frequency Ω_p as a function of temperature (left) and pressure (right). In particular, note the low-temperature line in the top right figure. Theory predicts that at low temperatures, if the SMSC transition occurs the plasma frequency $\Omega_p \sim n$ should vanish; however, this is not observed experimentally. Bottom left: loss function as a function of frequency at various pressures. Solid lines are fits to a numerical model: at 1 bar, a single plasmon peak describes the data well, but at elevated pressures, weight is shifted to a "plasmaron" peak, implying increasing interactions. Bottom right: scattering rate $\tau^{-1}(T)$ as a function of temperature. This valuable measurement allows a separation between the density and scattering dependence of the resistivity of bismuth.

surements it is possible to separately obtain the plasma frequency Ω_p, proportional to the square root of the carrier density n, as well as the Drude scattering rate τ^{-1}; conventional DC resistivity measurements observe a combination of the two. The scattering rate measured by Armitage *et al.* is shown in Fig. 4.10. They indicate that the physics of the Lifshitz transition may be more complicated than previously expected. As for bismuth the necessary parameters are all well-known, it is possible to calculate the temperature- and pressure-dependence of the plasma frequency. At low pressures, the calculation agrees very well with the data (and extrapolates to a vanishing Ω_p, and therefore a vanishing n, at around the critical pressure $p_c \approx 25$ kbar), but at high pressure the fit fails, and the experimental plasma frequency at 20 kbar does *not* fall to near zero (Fig. 4.10).

Armitage *et al.* therefore suggest that the Lifshitz transition is screened by some novel ordering driven by the low carrier density. One possible and intriguing possibility is the formation of an excitonic insulator: at the very low carrier densities near p_c, there may be too few carriers to effectively screen the Coulomb interaction, and the electrons and holes may form bound pairs. Other alternatives include the formation of a hole crystal, while the electrons remain mobile, or the formation of charge-rich and charge-poor regions.

As noted by Kraak *et al.*, there are other routes to realising the SMSC transition in group V semimetals [81]. While pressure remains the cleanest tuning parameter, doping with Pb, Sn or Te, or alloying with antimony perform the same function. $Bi_{1-x}Sb_x$ alloys have also been investigated under high pressure [83, 80, 84, 85]. Sb, appearing below Bi in the periodic table, is also a semimetal, but the addition of approximately 8 % antimony to bismuth results in the alloy becoming semiconducting. The impact of alloying on the bands has been investigated theoretically in some detail [86, 87]; essentially, increasing x linearly shifts the T-point valence band down in energy while narrowing the L-point gap, and at $x \approx 8$ % the band overlap falls to zero, after which a band inversion occurs [86, 87, 80]. The application of pressure to such alloys accomplishes the same thing as additional antimony; for example, at x =1.65 %, the critical pressure after which the material becomes semiconducting is ~ 15 kbar, after which the band gap rises linearly with pressure. The temperature-dependent resistivity of such alloys under pressure is very similar to that of pure bismuth [57, 83].

$Bi_{1-x}Sb_x$ alloys have recently attracted renewed attention as topological insulators [88, 89]. At $x = 0.1$, they exhibit topologically-protected surface states and massive Dirac particles [89]; calculations indicate that the Furmi surface encloses an odd number of Dirac points, as required for a strong topological insulator [88].

Yet another route to the SMSC transition is by quantum confinement - a reduction in the dimensions of the material to length around the Fermi wavelength. Bismuth's tiny Fermi surface make it an ideal material for such thin-film experiments, although growing such films has proved challenging [46]. Films of a few hundred atomic layers possess an additional energy scale, the quantum confinement energy $E_c \sim d^{-2}$ where d is the film thickness; in bismuth, because the band structure is so finely balanced at the very edge of the metallic state, a confinement energy of a few tens of meV will be enough to push the electron band above the hole band, reducing the band overlap to zero and resulting in the formation of a semiconductor. This has been realised experimentally: a film with a thickness $d = 20$ nm is a semiconductor with a band gap $E_g \approx 40$ meV [90]. Later

experiments have applied high pressure to thin films [91]. The results are at times inconclusive, in particular because the presence of surface states greatly complicates attempts to probe the carrier density of the bulk (see Section 4.1.6 for details).

Some authors have suggested that a metal-insulator transition can also be accomplished in bismuth with the application of moderate magnetic fields [92], on the basis that while at low fields, $\rho(T)$ rises metallically with temperature, in fields of a few tesla $\rho(T)$ falls sharply with increasing temperature. Interestingly there are strong superficial similarities between the shape of $\rho(T)$ when field is applied and when pressure is applied [57, 92]. However, the in-field behaviour would appear to be rather an abuse of the term insulator, as there are no suggestions the carrier density vanishes with falling temperature (indeed, all quantum oscillation measurements, down to very low temperatures, demonstrate that precisely such vanishing carrier density does *not* happen). It therefore seems unlikely bismuth provides a means of realising the high-field metal-to-excitonic-insulator transition theorised by Abrikosov [93].

4.1.6 Surface states in bismuth

Much like the bulk, the surface of bismuth possesses a number of intriguing properties, and measurements have been conducted on both thin films and cleaved bulk crystals. A useful recent review is given by Hofmann [51]. Of particular interest are the facts that firstly, the surfaces tend to be better metals than the bulk, and secondly that bismuth's strong spin-orbit coupling plays a particular role in the surface electronic structure [51]. Bismuth surfaces act as essentially two-dimensional metals with intriguing spin properties, and may therefore be of particular interest for applications in spintronics [51, 94, 95]. The delicate balance between the nearly simple cubic structure (five electrons per unit cell - a good metal) and the actual rhombohedral unit cell (ten electrons per unit cell - naively, an insulator) means that even small surface structural reconstructions will significantly impact the electronic structure.

As mentioned previously, Hoffman *et al.* have observed surface states in magnetoresistance measurements on thin films, with their presence confirmed in later studies [90, 91]; the estimated hole carrier density is $p_s \approx 8 \times 10^{12}$ cm^{-2}, meaning they dominate charge conduction for film thicknesses of < 30 nm (frustratingly, that is exactly the thickness required for the hypothesised quantum confinement SMSC transition [96]). This motivated detailed angular-resolved photoemission spectroscopy (ARPES) on the bulk and surface bands of single bismuth crystals [96, 97, 98, 99].

The results of Ast *et al.* on the Bi(111) surface unambiguously identify surface hole states lying in six Fermi surface pockets, with a carrier density of $p_s = 1.1 \times 10^{13}$ cm^{-2}, and an electron density of $n_s = 5.5 \times 10^{12}$ cm^{-2}, close to the value found experimentally in thin films [96]. Later, more detailed ARPES measurements resolved more electron pockets, and a revised value $n_s = 1.5 \times 10^{13}$ cm^{-2}, implying a charge-balanced surface; it is suggested that the states reside in the upper bilayer of the bulk bismuth crystal [98]. Measurements of the Bi(110) surface again indicate it is highly metallic [99]. Scanning tunnelling microscopy measurements obtain broadly comparable values for the surface carrier density: $n_s = 3.13 \times 10^{12}$ cm^{-2}, $p_s = 5.8 \times 10^{12}$ cm^{-2}, and effective masses of $\sim 0.16 m_e$ [95]. An example of the Bi(111) surface states as observed by ARPES is shown in Fig 4.11. It is intriguing to note that the carrier density for the surface states of bulk bismuth is comparable

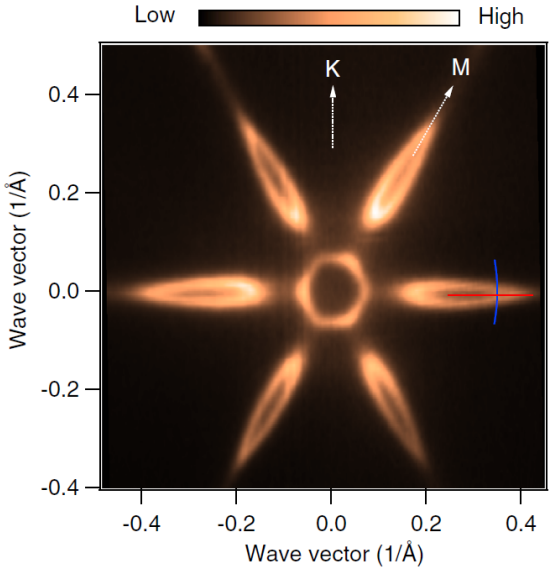

Figure 4.11: ARPES intensity of the surface states of Bi(111), taken from [100].

to that seen in thin films. Previously the thin film surface states had been assumed to exist due to film-substrate interactions; it would seem likely they are in fact a fundamental property of bismuth.

Multiple different surfaces were investigated by Koroteev *et al.* using ARPES, who found that spin-orbit coupling (SOC) is a critical component of any model describing the surface electronic structure [101]. Koroteev *et al.* also speculate on the impact of SOC on scattering of surface carriers: spin-split electrons and holes will have very different lifetimes with respect to the non-split surface state, as well as a modified (likely enhanced) electron-phonon coupling strength.

Hirahara *et al.* conducted further spin-dependent ARPES measurements on Bi(001) ultrathin films a few bilayers thick. They emphasise, again, that the surfaces are highly metallic, and SOC significantly splits the surface bands [102, 103]. Their DFT calculations suggest that the quantum confinement SMSC transition may in fact not occur due to hybridisation between surface and bulk states: even for very thin layers with $d < 20$ nm, the band structure remains metallic. Later, Ohtsubo *et al.* found similar surface states, with an enormous anisotropy of the SOC for states above and below E_F [100].

Further evidence for the metallic surface states is provided in studies of bismuth nanostructures; with dimensions of a few nanometers, these will be dominated by surface properties. Examples include ultra-thin nanowires or very thin films, and these have recently been studied by a number of authors [104, 105, 106, 107, 108]. In ultra-thin ribbons, clear quantum oscillations from a two-dimensional Fermi surface are visible, converting to a three-dimensional Fermi surface as thickness is increased, providing "*unambiguous transport evidence of the topological 2D metallic surface states in thinner nanoribbons with an insulating bulk*" [104, 105]. More recent measurements on single-crystal thin films claim to unambiguously observe the SMSC transition as a function of film thickness, and see a resistivity which is the sum of bulk and surface parts (in some cases the surface may dominate) [106, 107, 108].

A useful overview of the relevance of surface states is given by Seradjeh *et al.* [109]. They invoked surface states to explain the high-field Nernst anomalous quantum oscillations. They note that, because the surface states are far more metallic than the bulk, even though they are only a few nanometres thick, they correspond to "*a number of carriers equivalent to a 1* μm *thick sample of the bulk*" [109]. Interestingly, if we take results from a completely different field, that of bismuth thin films, the surface carrier density is stated as $2 - 8 \times 10^{16}$ carriers m^{-2}, which gives an effective thickness of ~ 0.5 μm - a value within $2\times$ that of the ARPES value for the bulk [91]. This implies the surface states are indeed a generic property of the material, rather than an artifact of film-substrate interactions.

Recent results suggest that the question of whether bismuth itself in fact possesses topological order may be far from closed. While $Bi_{1-x}Sb_x$ has long been accepted as a prototypical strong topological insulator, it was previously believed that, before the band inversion at $x \approx 8$ % antimony, the band structure of bismuth was topologically trivial. This interpretation may be flawed, with some recent DFT calculations and ARPES studies suggesting that bismuth may not be topologically trivial as was previously thought [110, 111, 112, 113]. As outlined by Ohtsubo *et al.*, who also provide a useful summary of previous calculations suggesting a topologically-trivial band structure, probing the surface states of a topologically-ordered semimetal (as opposed to a topological insulator) may be challenging: the bulk possesses a far larger total number of states and will therefore dominate transport properties, even if the topologically-protected surface is more metallic [110]. However, the metallic surface states should persist in the presence of continuous deformation - for example, by pressure. With the recent evidence for superconductivity and topological order, it currently remains an open question whether there is any condensed-matter physics[5] not observable in bismuth.

4.1.7 Calculations of the electronic structure of bismuth

Calculations of the band structure of bismuth pose an interesting challenge to theory. Crystallographically the system is rather simple (only two atoms per unit cell, in a well-understood structure), there is very extensive experimental data on the Fermi surface, and the Fermi surface is also fairly simple. However, in practice ab initio calculations have proved a complex task. The very small band overlap often lies below the resolution of ab initio techniques, which must resolve features with a precision below 10 meV to yield sensible physics, and the inclusion of strong spin-orbit coupling is essential.

Early calculations by Golin using a pseudopotential approach in 1968, obtaining a good qualitative agreement with experiment (at the time, the Fermi surface was not fully established) [114]. However, even by varying many parameters it was not possible to accurately obtain the experimental effective masses. Norin later extended the pseudopotential framework to consider the impact of pressure, and emphasises both the role of SOC and the choice of potential [56]. In a useful paper, he summarises the pressure and temperature dependence of the various parameters, as measured by experiment, and compares these to calculated values (Figs. 4.4 and 4.12).

The first full DFT calculations on bismuth were conducted in the late 1980s by Gonze *et al.*,

[5] Except perhaps skyrmions.

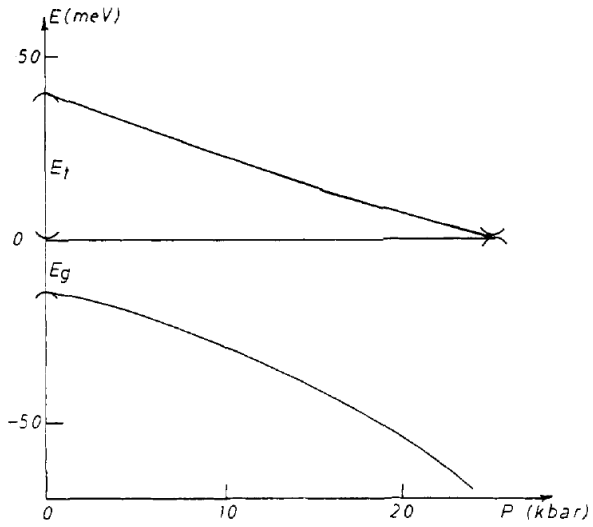

Figure 4.12: Pressure dependence of the band properties of bismuth, taken from data summarised in [56]. The band gap E_g at the L-point increases, while the band overlap between electrons and holes falls, eventually reaching zero at the SMSC transition.

who again comments on how the inclusion of SOC is essential to obtain reasonable results [115, 116]. They reproduced the experimental Fermi surface, and obtained very good agreement with experiment for the holes, but rather poorer agreement for the electrons. Gonze *et al.* comment on their surprise that the calculations reproduce experiment so well: they obtain values for the electron and hole Fermi energies within a few meV of the experimental values, when often DFT calculations are incorrect about the size of a band gap by $0.5 - 1$ eV [116].

An alternative approach used to determine the electronic structure is the use of a tight-binding model based on experimentally-determined parameters, and with bismuth this has proved rather successful. Xu *et al.* obtained good estimates for the overlap energies, but did not focus on the details of the band structure near E_F [117]. A much more detailed calculation was conducted by Liu and Allen, with a view to its possible usefulness in semimetal-semiconductor devices [52]. Liu and Allen fitted a tight-binding model to experimental data, accurately reproducing the band overlaps and calculating reasonable estimates of the effective masses. This tight binding model has subsequently been used by many later authors, and should be considered the best calculation of the band structure currently available.

Shick *et al.* looked at the mechanism by which bismuth becomes metallic (rather than semiconducting), and how the SMSC transition may occur [50]. DFT calculations were used to investigate the total energy, density of states, and band structure as a function of the two key structural parameters: the displacement of one fcc sublattice with respect to another (by a dimensionless distance $\delta = 0.25 - u$, where $2u$ is the distance of the second atom in the rhombohedral cell along the (111) trigonal direction) and the trigonal angle α. The values $\delta = 0$, $\alpha = 60^{\circ}$ correspond to the simple cubic structure, which (for the simple electron counting reasons outlined in Section 4.1.2) should be metallic, and this is what DFT calculations found. A displacement to the experimental value $u = 0.234$ yields a narrow band-gap semiconductor, and a reduction of the rhombohedral angle to

the experimental value $\alpha = 57.3^{o}$results in a semimetal, thereby neatly demonstrating the efficacy of the Peierls distortion explained in Section 4.1.2 as a mechanism for understanding the properties of bismuth. As the distance δ is decreased, or the angle α increased, the SMSC transition arises, and this may describe what occurs under pressure. Indeed, when the volume of the unit cell was artificially reduced, the dependence of the total energy on δ moved from a double-well behaviour (i.e. the equilibrium structure possesses a finite δ, and is therefore metallic) to a single-well form with a minimum at $\delta = 0$ (at reduced volumes, the system is closer to simple cubic, and therefore semiconducting) [50].

4.1.8 The state of the art

In summary, there are three areas of particular recent interest. Firstly, the signatures of novel behaviour in the ultraquantum limit may lead to hitherto-unsuspected forms of ordering in systems with highly-confined, strongly-interacting electrons [60, 61]. There remain unresolved questions about a mechanism for the apparent lifting of the valley degeneracy in field. Secondly - and rather surprisingly, given the decades of experimental and theoretical work - the jury is still currently out on whether bismuth itself is topologically non-trivial, and what role surface states play [112].

Finally, there remains remarkable uncertainty about the nature and indeed existence of a pressure-induced SMSC transition [12]. Since the early measurements of Balla and Brandt, evidence from the resistivity has been that at least qualitatively such a transition appears to occur, but other results from the Hall effect or quantum oscillations have proved inconclusive [57]. The most recent optical experiments indicate that the SMSC transition may be preceded by the emergence of new and interesting physics such as the formation of an excitonic insulator, and this could allow transport measurements to be interpreted in a new light, in particular given the determination of $\tau^{-1}(T)$ provided by optical scattering data [12]. In addition, the details of the surface states were unknown to Balla and Brandt in 1965.

We therefore resolved to undertake detailed measurements of the SMSC transition in bismuth using high-pressure resistivity measurements. We believe our results possess three salient advantages over previous measurements. With modern high-pressure techniques, we can obtain highly hydrostatic conditions up to 30 kbar (while many of the previous measurements have been taken with solid pressure media). We can simultaneously measure under high pressure in fields up to 7 T and temperatures down to ~ 200 mK using an adiabatic demagnetisation refrigerator (to our knowledge, all previous transport measurements investigating the SMSC transition have extended to at best 1.8 K, and seldom in high field). Finally, we have a modern knowledge of the Fermi surface and band parameters, and modern calculational tools to investigate the interplay between carrier density and scattering.

4.2 Calculations

4.2.1 Overview

From the above section, and the work by Balla and Brandt, it will be seen that the resistivity of bismuth under pressure provides an insight into the SMSC transition. However, resistivity is, while

relatively straightforward to measure, with no loss of accuracy inside a pressure cell, quite complex to interpret or model.

The temperature-dependent Drude resistivity is:

$$\rho(T) = \frac{m\tau^{-1}(T)}{e^2 n(T)} \tag{4.4}$$

where m is the effective mass, e the electron charge, τ^{-1} the scattering rate and n the carrier density for a given electronic state. In general, multiple states will contribute, and their conductivities $\sigma = 1/\rho$ will add. There may be multiple bands (in which case the theory of Section 2.3 is relevant), an energy-dependent effective mass, or even a scattering rate τ_k^{-1} which depends on a state's location in the Brillouin zone, indexed by its wavenumber k. Such calculations rapidly become extremely complicated and rather opaque to meaningful interpretation.

The situation is even more complex for bismuth, poised as it is between metallic and semiconducting states. The reader will recall from section 2.3 that in general, the resistivity of a semiconductor is dominated by $n(T)$ and a metal by $\tau^{-1}(T)$. In bismuth, both are relevant, and their competing influence sets the behaviour of $\rho(T)$ as a function of pressure.

We present here a method for simple calculations of the resistivity of bismuth as a function of both pressure and temperature, using measured values of the relevant band parameters. This model quite neatly captures the essential physics without becoming mired in the complexities of Boltzmann transport calculations. We treat $\tau^{-1}(T)$ and $n(T)$ as separate quantities, assume a simple phenomenological form for $\tau^{-1}(T)$, and calculate $n(T)$ using an integral over the known Fermi surface, while requiring that the numbers of electrons and holes remains equal at all temperatures: the Fermi level is allowed to drift to ensure charge remains compensated.

This calculation is similar to the one briefly outlined by Armitage *et al.*, who used an identical approach to obtain $n(T)$ at each pressure and thereby find Ω_p [12]. They found that, up to ~ 15 kbar, it agreed quite well with the measured Ω_p, as seen in the top two panels of Fig. 4.10. This would suggest that the assumptions we make below about the pressure dependence of the band parameters are justified. At higher pressures, Armitage *et al.* observed a significant deviation from the observed value of Ω_p; they ascribed this to the emergence of many-body effects.

We found that an extension of this model to the resistivity, performed by assuming a simple form for the scattering rate, can quite well reproduce the qualitative behaviour of $\rho(T, p)$ as measured by Balla and Brandt from 0 to 25 kbar, as well as our own data presented later. The resistivities of Balla and Brandt are shown digitised in Fig. 4.13 [57].

4.2.2 Theoretical approach to calculation of the carrier density

In semimetallic bismuth, there are three mechanisms which yield a temperature dependence of the carrier density:

1. At higher temperatures, the Fermi-Dirac occupation probability of higher-energy states increases (as the Fermi-Dirac distribution widens), and these higher-energy states also have a higher density of states. In a single-band conventional one-band metal, this process would violate conservation of charge if the Fermi level ϵ_F remained constant, therefore ϵ_F shifts down

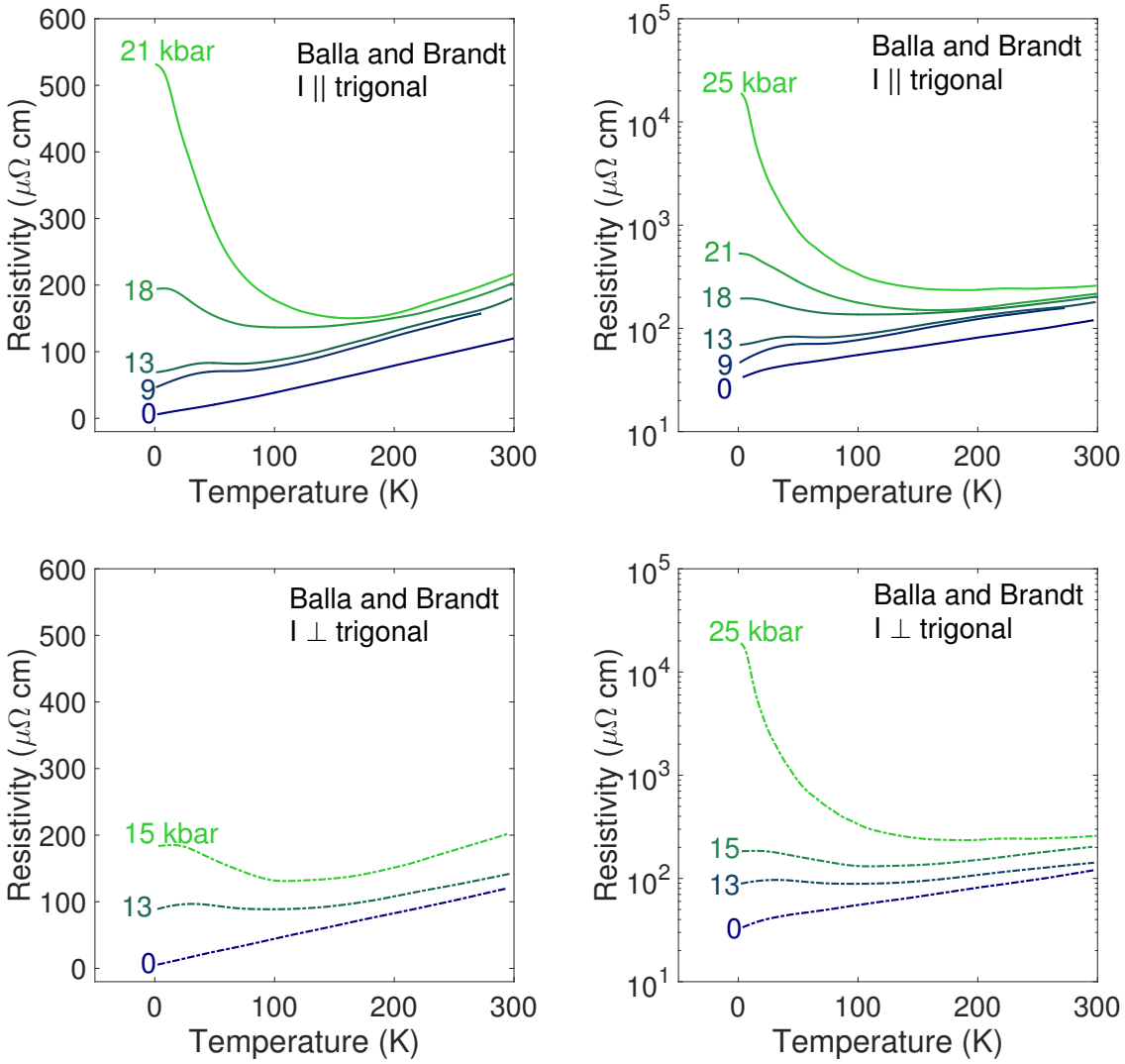

Figure 4.13: Temperature dependence of the resistivity as measured by Balla and Brandt, on normal (left) and semilog (right) axes, for current passed parallel (top - solid lines) and perpendicular to (bottom - dashed lines) the trigonal axis. Data taken from [57].

with temperature (although for a conventional metal $\epsilon_F \approx 10,000$ K so this effect is usually negligable). In bismuth, the charge conservation constraint is that electron and hole densities remain equal, not constant, thus the Fermi level may move in such a way as to create electrons, as long as this creates an equal number of holes.

2. The band parameters themselves are temperature-dependent . In particular, the band overlap ϵ_t increases significantly with temperature, presumably due to slight changes in the structure, which will increase the carrier density [56]. Qualitatively, the band overlap increase with increasing temperature and fall with increasing pressure are likely manifestations of the same effect: an increase in the atomic spacing would appear to increase ϵ_t.

3. Thermal activation of electrons across the $L-$point gap to produce valence band holes will occur even at moderate temperatures: the band gap is only ~ 100 K.

In bismuth, all three mechanisms are relevant. We implement a numerical model to calculate the carrier density $n(T,p)$, initially using the well-known $p=0$ band parameters, and then extend the results to high pressure by making plausible assumptions about the unknown pressure dependence of the band parameters.

Issi gives a straightforward expression for the carrier density arising from an single ellipsoidal Fermi surface:

$$n_i\left(T,\epsilon_{F,i}\right) = \frac{8\pi(2m_e)^{3/2}}{3h^3}\left(\det \mathbf{m}_i\right)^{1/2}\int_0^\infty \left(-f_0'\left(\epsilon,\epsilon_{F,i}T\right)\right)\gamma_i^{3/2}(\epsilon)d\epsilon \tag{4.5}$$

where $i=e,h$, labels the electron and hole bands at the $L-$ and $T-$points, and $\mathbf{m}_i$ is the effective mass tensor for the relevant band [8]. The function f_0' is the energy derivative of the Fermi-Dirac distribution:

$$f_0'\left(\epsilon,\epsilon_{F,i}T\right) = \frac{\partial f_0}{\partial \epsilon} \tag{4.6}$$

$$f_0\left(\epsilon,\epsilon_{F,i}T\right) = \left(1+\exp\left(\frac{\epsilon-\epsilon_{F,i}}{k_bT}\right)\right)^{-1} \tag{4.7}$$

with $\epsilon_{F,i}$ the Fermi level of the ith band (here, as we are dealing with a semimetal, $\epsilon_{F,i}>0$). At low temperatures, f_0' approximately a delta-function around $\epsilon=\epsilon_{F,i}$, but at 300 K it can become rather broad.

The function γ_i arises from the three-dimensional density of states, but for the electron band it requires a non-parabolic correction, yielding:

$$\gamma_h(\epsilon) = \epsilon \tag{4.8}$$

$$\gamma_e(\epsilon) = \epsilon\left(1+\frac{\epsilon}{\epsilon_{g,e}}\right). \tag{4.9}$$

with $\epsilon_{g,e}$ the electron band gap (in principle, a similar correction exists for the hole band, but as $\epsilon_{g,h} \gg \epsilon_{F,h}$ it has negligable impact so we neglect it here).

As summarised by Norin, the various band parameters are both small and temperature-dependent, but those temperature-dependences are known [56]. The electron and hole Fermi energies are re-

lated by the band overlap:

$$\epsilon_{F,e} + \epsilon_{F,h} = \epsilon_t. \tag{4.10}$$

At ambient pressure, experimental measurements show this is approximately a linear function of temperature (Fig. 1) [56]:

$$\epsilon_t(T) = \epsilon_t(0) + a_1 T. \tag{4.11}$$

The band gap, by contrast, is quadratic in the temperature:

$$\epsilon_{g,e}(T) = \epsilon_{g,e}(0) + b_1 T + b_2 T^2. \tag{4.12}$$

Finally, we appeal to the fact that bismuth is a *compensated* semimetal. This means that, at every temperature, charge conservation requires the difference in carrier densities between species to vanish. There are carriers present from three sources: the hole pocket at T, with density n_h, the three electron pockets at L, each with density n_e, and holes produced by thermal activation across each L-point gap, with density $n_{h,a}$. We thus have:

$$\delta n(T, \epsilon_{F,e}, \epsilon_{F,h}) = 3n_e(T, \epsilon_{F,e}) - n_h(T, \epsilon_{F,h}) - 3n_{h,a}(T, \epsilon_{F,a}) = 0. \tag{4.13}$$

This is fulfilled (at all T) by allowing the Fermi levels to shift, while requiring that their sum is always $\epsilon_t(T)$ - if there are more holes than electrons, we can reduce $\epsilon_{F,h}$, thereby increasing $\epsilon_{F,e}$, to correct this imbalance. By moving $\epsilon_{F,h}$ and ensuring charge conservation, we find that the carrier density is temperature-dependent, but there are always the same number of electrons as holes. The carrier densities (and $T-$dependent Fermi energies) are therefore obtained via a relatively straightforward zero-finding operation on the function $\delta n(\epsilon_{F,h})$, which has only a single free parameter. The effective Fermi level for activated holes is $\epsilon_{F,a} = -(\epsilon_{F,e} + \epsilon_{g,e})$.

In this section, we will frequently refer to the carrier density n; this is the total carrier density of electrons, i.e. $n = 3n_e$ (as n_e is the density of electrons from only one band). Because of the charge balance condition, we also have $n = n_h + 3n_{h,a}$.

The band parameters are less well-known at elevated pressures, though a similar approach should hold. We assume that (as evidenced experimentally) both ϵ_t and $\epsilon_{g,e}$ are pressure-dependent. Problematically, only the low-temperature values are known; there is no experimental data on the pressure dependence of the temperature dependence (i.e. the coefficients a_1, b_1, b_2).

The pressure dependence of $\epsilon_t(0)$ is linear, according to Norin, falling to zero at $p = p_c = 25$ kbar [56]. We assume, in line with Armitage, that the gradient of $\epsilon_t(T)$ is not pressure-dependent [12]. This gives:

$$\epsilon_t(T, p) = \left(1 - \frac{p}{p_c}\right) \epsilon_t(0) + a_1 T. \tag{4.14}$$

The pressure dependence of $\epsilon_{g,e}(0)$ is approximately quadratic, and rises from 13.6 meV at $p = 0$ to ~ 60 meV at p_c [56]. The pressure dependence of the temperature coefficients is completely unknown. However, this is relatively unimportant: recall that $\epsilon_{g,e}(T)$ is a non-parabolic correction that appears in the energy integral in the form $(1 + \epsilon/\epsilon_{g,e})$, so an increasing $\epsilon_{g,e}$ will have a small effect on the numerical values but not impact the qualitative results (in the model of Armitage *et al.*, the

pressure-dependence of $\epsilon_{g,e}$ was neglected). We assume for simplicity that the other temperature coefficients are pressure-dependent in the same way as the zero-temperature band gap, giving:

$$\epsilon_{g,e}(T,p) = \left(1 + c_1 \left(\frac{p}{p_c}\right)^2\right) \left(\epsilon_{g,e}(0) + b_1 T + b_2 T^2\right). \tag{4.15}$$

Using these pressure corrections, we can in principle calculate $n(T,p)$ at any pressure up to (and even beyond) p_c, and any temperature.

4.2.3 Numerical calculation of the carrier density

From data by Norin and Issi, we obtain all the band parameters required for a numerical calculation of n_e and n_h [56, 8]; these are summarised in Table 2. We then adopt the following numerical approach:

1. At a given T, calculate $\epsilon_t(T)$ and $\epsilon_{g,e}(T)$.
2. At this T, finding the zero of the function $\delta n(\epsilon_{F,h})$ as a function of the hole Fermi level $\epsilon_{F,h}$, noting the electron Fermi level is simply $\epsilon_t - \epsilon_{F,h}$, and performing a numerical integral with the trapezium rule to obtain the carrier density of each band.
3. Calculate, at this temperature, the corresponding carrier densities n_e, n_h and $n_{h,a}$ corresponding to these Fermi energies.
4. At the next temperature, use the previously-obtained values of the Fermi energies as start points for the numerical root finding in step 2.

At high pressures the values used for $\epsilon_{g,e}(T)$ and $\epsilon_t(T)$ must be modified. The parameters used are shown in Table 3, and are taken to approximately reproduce the graphs in Norin [56].

Some care must be taken when evaluating f_0'. There will always be some numerical error in the integration, as the upper limit cannot truly be $\epsilon = \infty$; instead, we use that fact that at $\epsilon \gg \epsilon_F$, $f_0' \to 0$ rapidly. At low temperatures this works well, because f_0' is approximately a Dirac $\delta-$function centred on $\epsilon = \epsilon_F$, but this requires an extremely fine lattice of $\epsilon-$points around $\epsilon = \epsilon_F$ for the numerical integration to yield the correct results. At high T, by contrast (when $k_b T \geq \epsilon_{F,h}$), f_0' is a rather broad function of ϵ, so the integration must be taken to a very high value of ϵ to give the correct result. When $k_b T/\epsilon_F < 0.1$, we therefore use an adaptive lattice which focuses 90 % of the points within $20 k_b T$ of ϵ_F, ensuring $f_0(\epsilon)$ is at most 1×10^{-9} before it is set to zero.

By far the slowest step is the numerical minimsation of $\delta n(\epsilon_{F,h})$, which requires repeated evaluation of a numerical integral. However, after the first point, provided the T-lattice is finely spaced, every subsequent point will have a reasonable startpoint for $\epsilon_{F,h}$. The whole process is extremely rapid: a calculation with 200 $T-$points and a 5,000-point $\epsilon-$grid takes ~ 3 seconds on a 3.2 GHz processor. Increasing the number of $\epsilon-$points to 20,000 gives slightly more accurate results (as the trapezoidal integration is less discretised) but these values differ by < 1 % from the 5,000-point grid.

Symbol	Description	Value
$\mathbf{m}_h$	Hole effective mass tensor (in units of m_e)	diag(0.064, 0.064, 0.69)
$\mathbf{m}_e$	Electron effective mass tensor (in units of m_e)	diag(0.00119, 0.266, 0.00228)
$\epsilon_t(0)$	Band overlap at zero temperature	38 meV
a_1	Linear coefficient of band overlap's temperature dependence	0.1 meV/K
$\epsilon_{g,e}(0)$	Electron band gap at zero temperature	13.6 meV
b_1	Linear coefficient of electron band gap's temperature coefficient	2.1×10^{-3} meV/K
b_2	Quadratic coefficient of electron band gap's temperature coefficient	2.5×10^{-4} meV/K
$\epsilon_{F,h}(T=0)$	Hole Fermi energy at zero kelvin	10.8 meV

Table 2: Band parameters of bismuth at $p = 0$ used in the numerical calculations, taken from Issi and Norin [8, 56].

Symbol	Description	Value
p_c	Critical pressure where $\epsilon_t(0)$ vanished	25 kbar
c_1	Pressure coefficient of quadratic pressure dependence of $\epsilon_{g,e}(T)$	3.41

Table 3: Band parameters of bismuth at $p = 0$ used in the numerical calculations, taken from [56].

4.2.4 Numerical calculation of the resistivity

Having calculated $n(T, p)$, we can extend our approach to obtain the resistivity:

$$\rho(T, p) = \frac{m\tau^{-1}(T, p)}{e^2 n(T, p)}. \tag{4.16}$$

This requires a number of rather severe approximations. Firstly, the scattering rate and effective mass are strongly direction-dependent, secondly they differ (significantly) between bands, and finally their temperature and pressure dependence is not well-known. In addition, bismuth suffers strongly from size effects: the scattering length at low temperatures can be of the same order as the sample dimension, meaning the existence of a generally-applicable τ^{-1} becomes debatable [8].

A full description would calculate the resistivity tensor ρ_{ij} considering three electron and two hole bands, using the electron and hole mobility tensors which have four and two components respectively, all with their own temperature dependence. The data of Collaudin *et al.* would form a reasonable starting point, and would allow calculation of the resistivity at any temperature along any crystallographic direction [58]. An extension to the high-pressure region requires a further set of assumptions about how the detailed measurements of the mobility will be affected by the pressure dependence of the carrier density. Further corrections would have to be made to correct for finite-sized samples. This arduous task is beyond the scope of this work. Instead, we here attempt to make headway by assuming a simple form for $\tau^{-1}(T)$ based on experimental data.

The key simplification regarding the different carrier densities and bands can be clarified as follows. Ideally, we should calculate the resistivity ρ_i for all three carrier species in all three directions, using the effective mass tensor $\boldsymbol{m}_i$, scattering time tensor $\boldsymbol{\tau}_i$ and carrier density n_i, where the three values of i refer to the electron band at L, the hole band at T and activated holes at L. This cannot be accomplished easily: the components of $\boldsymbol{\tau}_i$ are not known at all temperatures even at ambient pressure, their pressure dependence is unknown, and the resulting resistivity tensor will be direction-dependent. The quantitative temperature dependence of the resistivity may then be different in different directions, and quite complex if the different bands have different temperature dependences for $\boldsymbol{\tau}_i$. These drastic complications do not add any insight into calculations of the qualitative behaviour of $\rho(T)$ as a function of pressure. However, it should be noted that the approximations introduced here are significant: in practice, both electron and hole bands in bismuth contribute separately to the resistivity, but we are considering only the experimentally-measured total. We effectively average over the directions (by assuming a scalar m) and the bands (by assuming a single τ^{-1}) to obtain a scalar phenomenological resistivity which corresponds to the resistivity which might be observed in experiments on polycrystalline bismuth.

For the scattering rate, we use a power law dependence $\tau^{-1}(T) = \tau_0^{-1} + d_1 T^n$, with τ_0^{-1} and d

Symbol	Description	Value
τ_0^{-1}	Zero-temperature scattering rate	8.61×10^{10} s^{-1}
d_1	Temperature prefactor of scattering rate	5.06×10^{7} s^{-1} K^{-2}

Table 4: Parameters for the scattering-time model.

adjustable parameters and $n = 2$, based on multiple comments about the temperature-dependent scattering from a number of authors [8, 58, 118, 119]. The factor e^2/m scales all the other parameters: we choose $m = 0.011m_e$, which matches Armitage's value for the scattering rate to the resistivity at 300 K and 1 bar.

We fix τ_0^{-1} and d_1 by requiring that:

1. At $T = 300$ K and $p = 0$ kbar, $\rho = 120$ μΩ cm.
2. The RRR at $p = 0$ kbar is 10.
3. The carrier density is 2.71×10^{23} m^{-3} at $T = 0$ K and $p = 0$ kbar, and rises by a factor of 5.32 up to 300 K.

The resulting values are given in Table 4.

It is interesting to compare our values for τ^{-1} to Armitage's measured ambient-pressure value, as shown in Fig. 4.34 . Armitage's $\tau^{-1}(T,p)$ rises by a factor of only $\sim 40\times$ from 2 to 300 K at ambient pressure, implying his sample had a RRR of only $\sim 5-10$ [12]. At room temperature our model agrees quite well with Armitage's result: we obtain $\tau^{-1} = 4.6 \times 10^{12}$ s^{-1}, while Armitage measured $\tau^{-1} = 6.9 \times 10^{12}$ s^{-1}.

No detailed galvanomagnetic data is available to provide experimental values of $\tau^{-1}(T,p)$ at high pressures. The simplest approximation is that $\tau^{-1}(T,p)$ is simply pressure-independent, an assumption used by Balla and Brandt [57]. The more likely alternative is that it is the scattering length $l(T,p)$ which is constant with pressure for a given temperature, corresponding to the physical distance between scattering events remaining unchanged. To incorporate this, we define $l(T,p) = v_F(T,p)\tau(T,p)$ where v_F is the Fermi velocity. We determine this as $\hbar k_F = mv_F$, and use that $k_F \sim n^{1/3}$; this assumes a spherical Fermi surface, but in reality the Fermi velocity's dependence on the carrier density will be direction-dependent. The constant-l assumption then gives a resistivity:

$$\rho(T,p) = \frac{m\tau^{-1}(T)}{e^2 n(T,p)} \left(\frac{n\,(T,p)}{n(T,0)} \right)^{1/3}. \tag{4.17}$$

We perform our calculations for both constant τ and constant l. Qualitatively the results are unchanged; quantitatively the main effect is that with constant l the low-temperature resistivity increases less rapidly with increasing pressure than for constant τ, because we have $\rho \sim n^{-2/3}$ rather than $\rho \sim n^{-1}$.

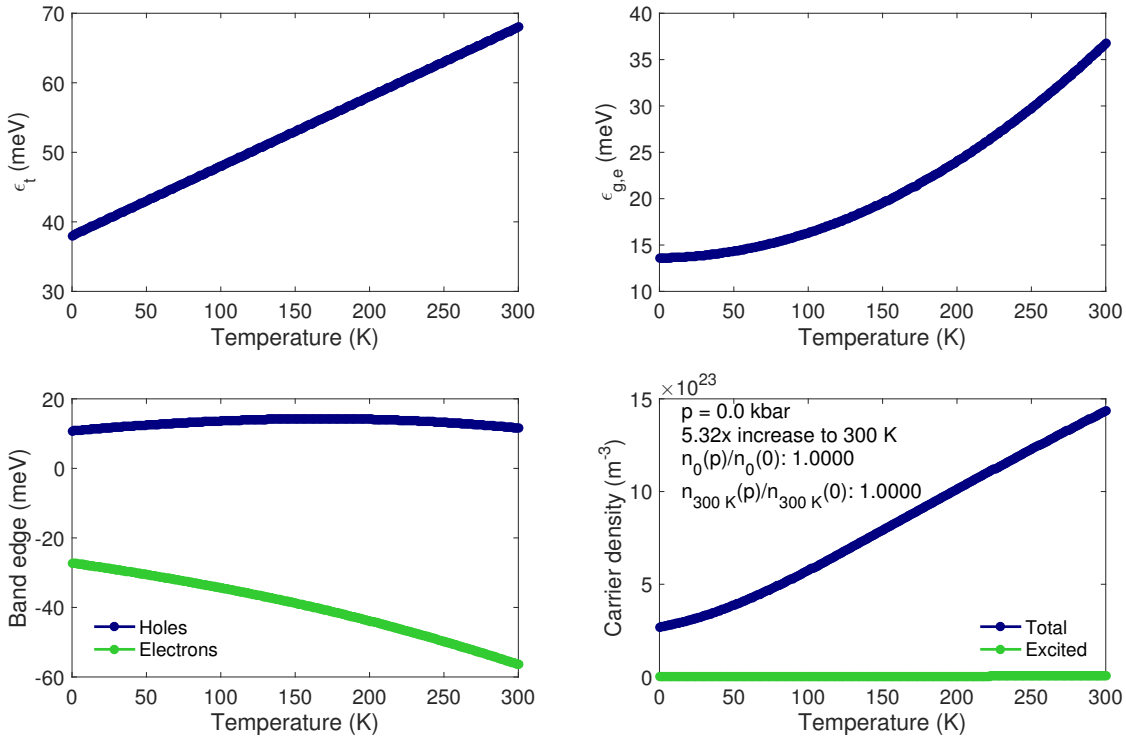

Figure 4.14: Temperature dependence of various band parameters at $p = 0$. The total carrier density, n, refers to the combined carrier density of all three electron bands; this is equivalent to $n_h + 3n_{h,a}$ by the charge balance condition. The excited carrier density shown is the total carrier density of excited holes, $3n_{h,a}$; as can be seen this is negligably small compared to the density of non-excited carriers.

4.2.5 Numerical results

Fig. 4.14 shows the temperature dependence of various properties at $p = 0$ (where the numerical values are best-known). All calculations are done for $0.2 \leq T \leq 300$ K, typically at 300 temperatures, with a 20,000-point $\epsilon-$lattice for the carrier density integration; this takes ~ 10 s per pressure point. Increasing the density of lattice points has negligable impact (< 1 %) on the accuracy.

As expected, $n(T)$ increases (by a factor of $5.32\times$) from low temperatures to 300 K. Fig. 4.15 shows equivalent results for $p = 20$ kbar; as expected, the low-temperature carrier density n_0 is much lower, and it increases much more steeply with temperature. Fig. 4.16 summarises the pressure dependence of various band parameters. For clarity, we plot the position of the band edge, which we define as the distance of the bottom (top) of the electron (hole) band from its relevant Fermi level - that is, for holes the band edge is equal to $\epsilon_{F,h}$, and for electrons to $-\epsilon_{F,e}$. At each temperature, the distance between the two band edges is always $\epsilon_t(T)$. In this representation, the zero of energy is kept fixed, and, as ϵ_t increases with temperature, the top of the hole band slides up while the bottom of the electron band slides down.

In Fig. 4.17, we plot the calculated $\rho(T)$ at a number of pressures, assuming both constant τ and constant l. Qualitatively, the calculated resistivity matches fairly well with the results of Balla and Brandt (see Fig. 4.32), and with our own results. The behaviour of $\rho(T, p)$ can be understood

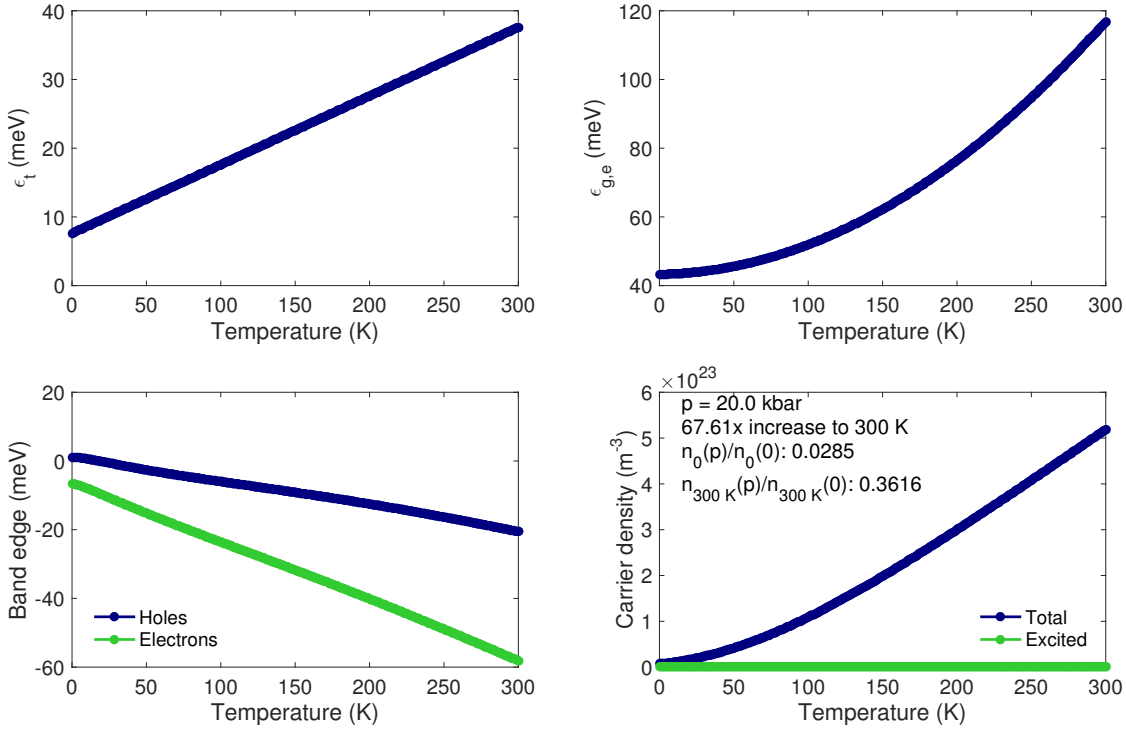

Figure 4.15: Temperature dependence of band properties at $p = 20$ kbar.

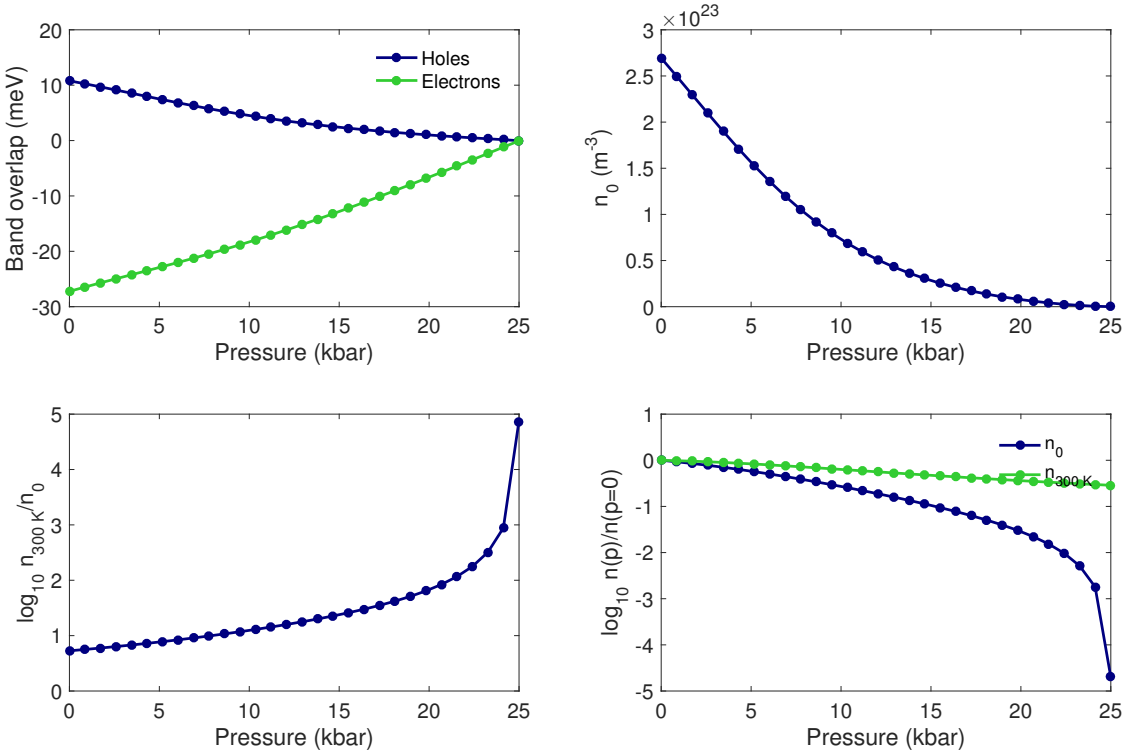

Figure 4.16: Pressure dependence of various band parameters.

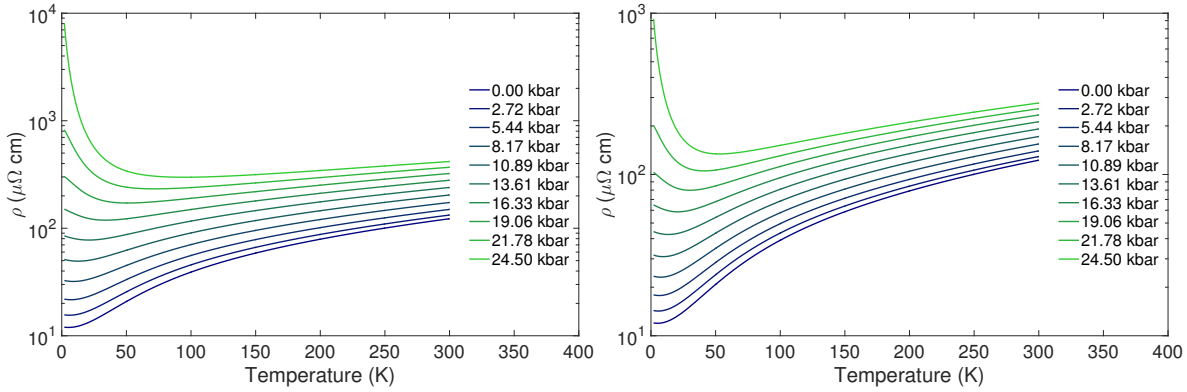

Figure 4.17: Calculated resistivity assuming constant τ (left) and l (right) from 2 to 300 K, for a resistivity giving an ambient-pressure RRR of 10.

as follows. At low pressures, the scattering rate increase with T ($\sim 50\times$) by far outweights the carrier density increase ($\sim 5\times$), so $\rho(T)$ increases steeply. As pressure is increased, τ^{-1} remains fairly unchanged. However, the low-temperature carrier density becomes much lower (meaning ρ_0 rises dramatically), and n increases much more steeply with T. Eventually, this results in the carrier density increase winning over the scattering rate increase at low temperatures: $\rho(T)$ first falls with increasing temperature.

These calculations can also be extended to $p > p_c$. In Fig. 4.18, we show a log-scale plot of the resistivity from 2 to 300 K. Here, the band parameters are less well-known; in particular, assumptions about the high-temperature dependence of ϵ_t and $\epsilon_{g,e}$ become uncertain. At finite temperatures there is no qualitative difference between $\epsilon_t > 0$ and $\epsilon_t < 0$, and the evolution of the resistivity across p_c is smooth. The difference occurs only at the lowest temperatures (typically below ~ 1 K): here, the resistivity diverges to infinity when $p > p_c$, while it remains finite for $p < p_c$. This arises because in the truly semiconducting state above p_c, the carrier density vanishes at zero temperature; in the semimetallic state below p_c, there is always a finite carrier density at zero temperature (although this may become very small). Additionally, in the same plot we show Arrhenius plots of $\log \rho$ against $1/T$. In the semiconducting state, at the very lowest temperatures this plot is approximately linear (and the gradient can be interpreted as $-\epsilon_t$), while at lower pressures there is no clear region of linearity.

4.2.6 Comparison to experiment

Fig. 4.19 compares the ambient-pressure carrier density $n(T)$ and the zero-temperature carrier density $n_0(p)$ to the data of Balla and Brandt [57]. The results for $n_0(p)$ agree to within ~ 15 % with those of Balla and Brandt. This is remarkably good given that our model makes a rather dramatic set of simplifications about the pressure-dependent band parameters, and that Balla and Brandt also simplify the link between carrier density and resistivity by assuming constant τ.

Agreement with the $n(T)$ data is less good, and this is an issue that seems to have received little attention in the literature. We obtain an increase in the carrier density of $5.32\times$, while Issi reports $8\times$ and Balla and Brandt suggest $9\times$ [8, 57]. Armitage's calculations yield $\sim 4\times$, though this is because

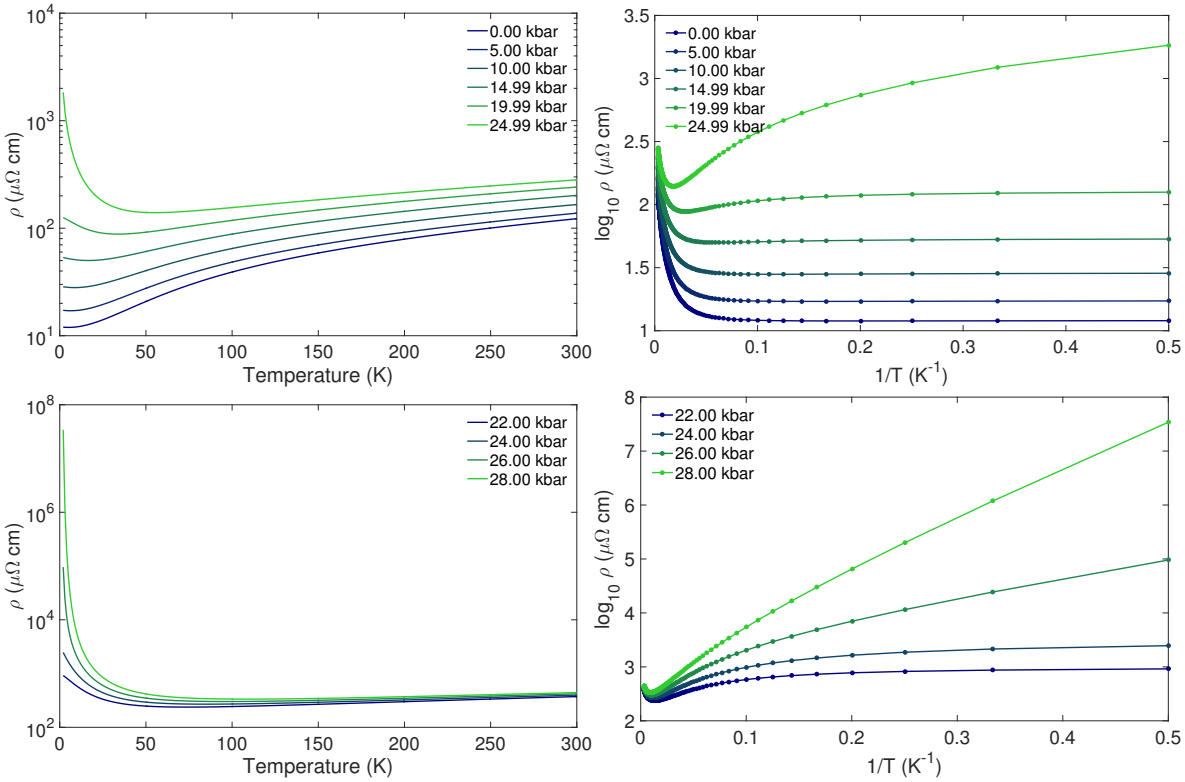

Figure 4.18: Calculated resistivity below $p_c = 25$ kbar (top), and for several pressure points crossing p_c (bottom), on semilog axes (left) and as Arrhenius plot (right). For $p > p_c$, at low temperatures the carrier density vanishes, so ρ diverges, while this is not the case for $p < p_c$. As a result, Arrhenius plots have a region of linearity at low temperatures for the high-pressure data not seen in low-pressure results.

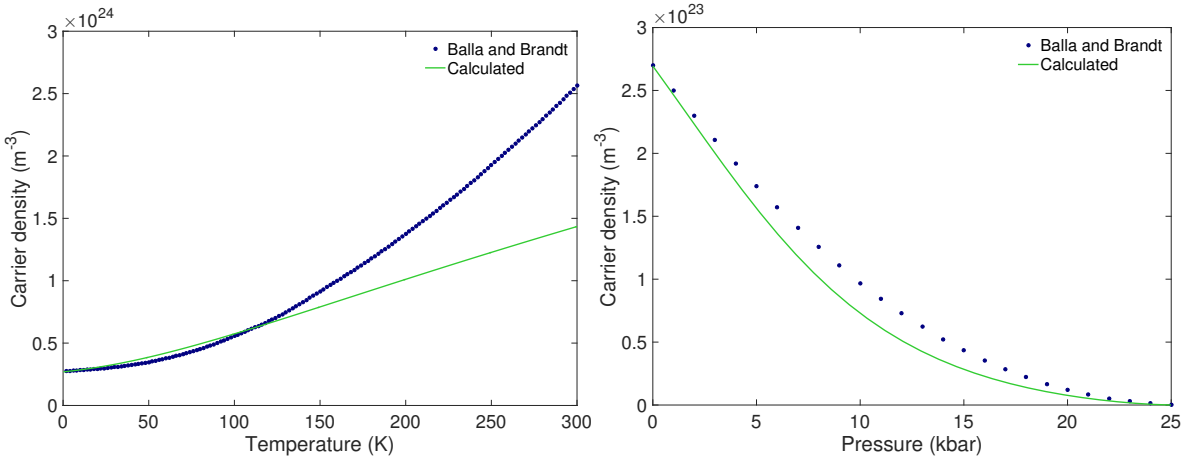

Figure 4.19: Comparison of calculated results with those of Balla and Brandt [57]: temperature dependence of the carrier density $n(T)$ at $p = 0$ (left), and pressure dependence of the low-temperature carrier density (right). Data from Balla and Brandt was taken from digitisation of the smooth curves they put through the experimental points.

he uses a lower value of a_1 [12]. Our calculated $n(T)$ is linear at high T because we approximate $\epsilon_t(T)$ as linear; in practice, it has a slight positive curvature (Fig. 4.4), which the calculated $n(T)$ should follow. In addition, there appears to be some uncertainty about where these carriers come from in the literature. Issi ascribes them to thermal activation across the $L-$point gap [8]. This appears to be incorrect; we find the number of carriers arising from activation from the hole to electron band, $n_{h,a}$, to be negligably small, making up < 1 % of all carriers at every pressure, because these carriers have a large, negative Fermi level. The carrier density increase arises primarily because ϵ_t increases with T, with some significant increase (~ 25 % of all carriers at $p = 0$) because of thermal broadening of f_0.

An alternative explanation for the larger increase in carrier density seen experimentally could be that the experimentally-obtained temperature dependence of the band overlap is incorrect. If we double the a_1 coefficient we obtain a carrier density increase of $7.79\times$, much closer to the experimental values. Further fine-tuning may slightly change the numerical results, but qualitatively the details will not change.

Our values for the pressure-dependent room temperature resistivity agree to within a factor of about 2 with the results of Balla and Brandt [57], who found that ρ_{300} increased by $1.5 - 2.2\times$ as p rises from 0 to 25 kbar; we observe $\sim 4\times$. This is likely related to the unknown behaviour of $\epsilon_t(T)$ at high pressures: if ϵ_t rises with temperature faster than at ambient pressure, the carrier density will be higher at 300 K than our calculations show, and the resistivity will therefore fall.

It is worth noting a crucial feature of the SMSC transition: a merely decreasing $\rho(T)$ does *not* imply a semiconducting material, i.e. one with $\epsilon_t < 0$. Even with positive values of ϵ_t, the resistivity can fall sharply (by $\sim 10^3\times$) from 2 to 300 K. This has some relevance for the behaviour of bismuth in high magnetic fields, where a very similar shape of $\rho(T)$ is observed to the 25 kbar calculation shown here. However, this does not mean that bismuth undergoes a field-induced metal-insulator transition, as suggested previously - instead, the behaviour in field is likely because the magnetoresistance is large and strongly $T-$dependent [92].

When fixing τ_0^{-1} to obtain the same RRR as that measured by Balla and Brandt, we find that using a simple $\tau^{-1} \sim T^2$ model for the scattering rate gives a reasonable qualitative description of the data (Fig. 4.20, top right panel). In particular, the crossover from increasing to decreasing $\rho(T)$ with pressure is reproduced; the calculated values of ρ typically lie within ~ 50 % of the experimental result.

Three factors contribute to discrepancies between the model $\rho(T)$ and that measured by Balla and Brandt:

1. The shape of $\rho(T)$ depends sensitively on the low-temperature scattering rate τ_0^{-1}, which sets the RRR. This property is essentially sample-dependent, and may also be pressure-dependent. In the data of Balla and Brandt, we note that the measured RRR at 0 kbar taken *after* depressurising is very low (only 3.64). Pressurising would appear to introduce significant numbers of defects and a commensurate increase in the low-temperature resistivity. It is possible that higher pressures introduce more defects; we would expect that at low temperatures our model then overestimates low-pressure resistivity and underestimates high-pressure resistivity. We see precisely this.

2. The temperature dependence of ϵ_t is known only at $p = 0$; even there it may not be very accurate, based only on a simple linear model taken from Norin [56]. We extrapolate this to higher pressures in a simplistic fashion, and might not expect the high-temperature, high-pressure resistivities to be very accurate (we find the calculated values are $\sim 2\times$ too large).

3. Our model for the scattering rate is very simple. In practice, whatever the mechanism causing scattering, we might expect it to change with pressure (for example, the phonon spectrum and Debye temperature will vary as p increases; if the dominant scattering mechanism is Baber scattering, this will impact $\tau^{-1}(T)$).

The assumption $\tau^{-1} \sim T^2$ may seem naive but is in fact fairly well-supported by experiment: for example, recent very detailed measurements of the angular dependence of the scattering rate indicate precisely such a temperature dependence from 4 to 100 K, confirming the results of Hartman [58, 120]. It remains an interesting open question why exactly this temperature dependence is seen even at high temperatures [8]. We can straightforwardly adapt the model to include more complex scattering rates. Three reasonable options would appear to be the measured pressure-dependent Drude scattering rate observed by Armitage, a more accurate Bloch-Gruneisen phonon scattering model, or a model including low-temperature plasmon scattering as suggested by Chudzinski, or [11, 12]. As we shall demonstrate, none of these give better agreement with the data of Balla and Brandt than the simple $\tau^{-1} \sim T^2$ model.

The scattering rate data of Armitage was obtained by digitisation of the data in Fig. 4.10, and passing of a smooth curve through the sparse datapoints, as shown in Fig. 4.34 [12]. Linear interpolation can then be used to obtain $\tau^{-1}(T,p)$ at any temperature and pressure. We should note that this linear interpolation might not be expected to work well at low pressures, because there $\tau^{-1}(T,p)$ is qualitatively changing in a rapid and (presumably) non-linear fashion. The resulting resistivity agrees very poorly with the measurements of Balla and Brandt (Fig. 4.20, bottom left panel). Armitage suggested that $\tau^{-1}(T,p)$ increased sharply with pressure at low temperature; even a pressure of 6 kbar was enough to yield a significantly increased τ^{-1} at low T, which would correspond to a resistivity that similarly rises at low temperatures. This is not observed in Balla and Brandt's experimental measurements. A similar enhancement in $\rho(T,p)$ at 6 kbar is not seen in any of our data, as will be discussed later.

Alternatively, a recent theoretical paper considered the existence of a low-energy acoustic-plasmon mode in bismuth [11], and proposed a more detailed temperature dependence of the resistivity as a result: $\rho \sim T^5$ below about $2-5$ K due to plasmon scattering, $\rho \sim T^2$ due to Baber scattering[6] of electrons and holes from about 5 to 120 K, and $\rho \sim T^1$ above the Debye temperature $\Theta_D \approx 120$ K (the standard high-temperature Bloch-Gruneisen temperature dependence).

As a simpler demonstration, instead of attempting to fully implement the acoustic-plasmon model, we have calculated $\rho(T)$ assuming a Bloch-Gruneisen scattering rate with a Debye phonon

[6] Baber scattering can be considered as a form of Fermi liquid $\rho \sim T^2$ scattering peculiar to carriers with very different masses. Because the different carrier species have charge-to-mass ratios that vary dramatically, scattering processes that conserve momentum do not necessarily conserve current, giving rise to resistivity.

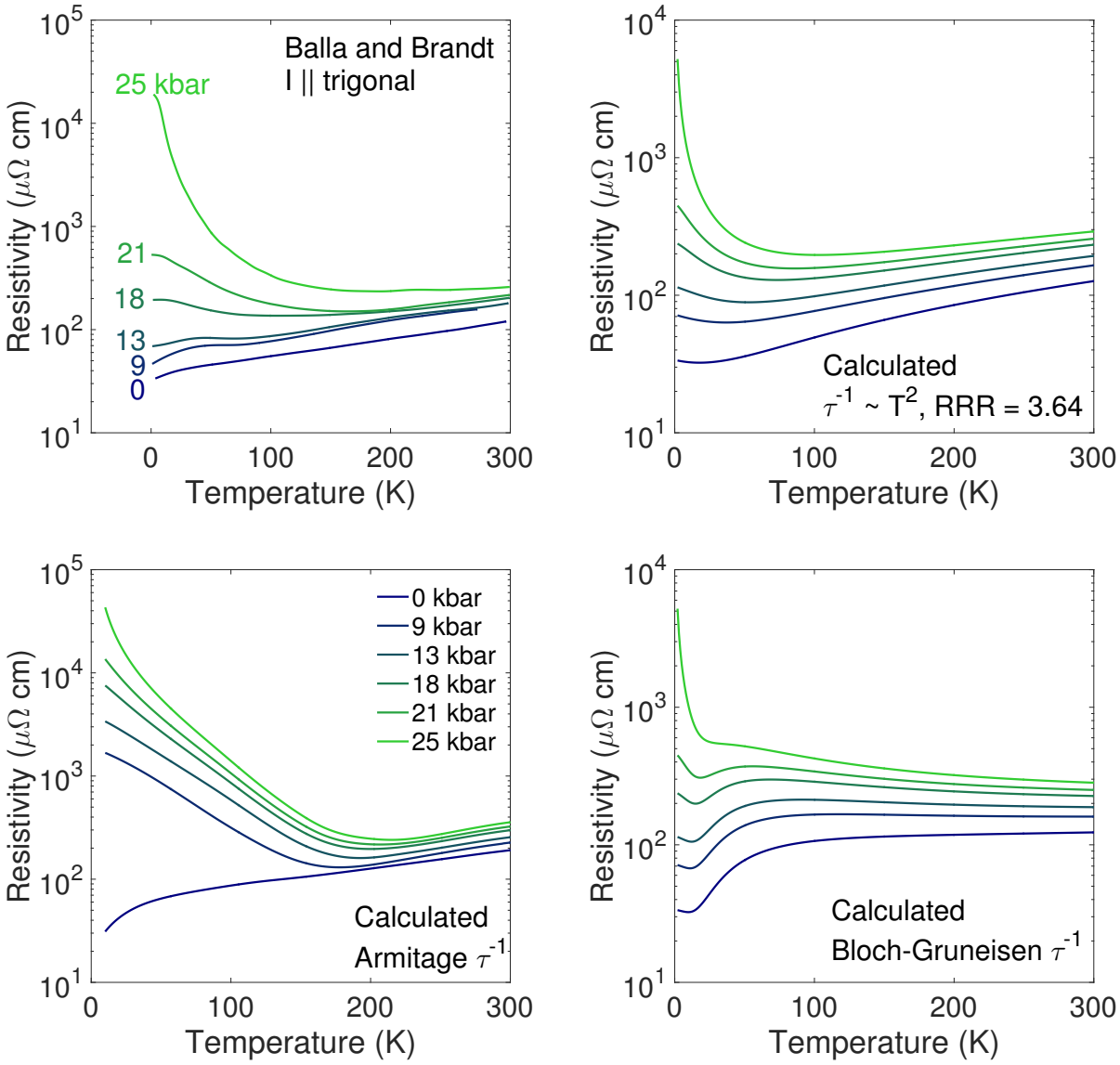

Figure 4.20: Comparison of the calculated models to the data of Balla and Brandt (top left), taken from [57]. The power law and Bloch-Gruneisen models for $\tau^{-1}(T)$ fix the low-temperature scattering rate τ_0^{-1} to match the RRR measured by Balla and Brandt after depressurising (which is very low, at only 3.64). The models are a simple power law dependence $\tau^{-1} \sim T^2$ (top right), the optical scattering rate measured by Armitage τ_A^{-1} (bottom left), and a Bloch-Gruneisen model (bottom right).

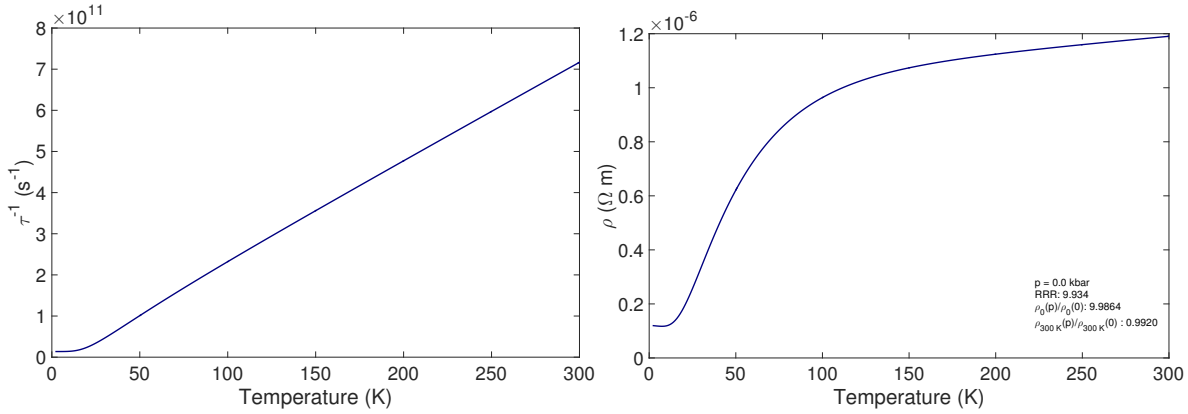

Figure 4.21: Results for calculations using a Bloch-Gruneisen model for phonon scattering in bismuth. The scattering rate (left) shows the expected crossove from T^5 behaviour at low T to linear behaviour above $T \approx \Theta_D/4$. The resistivity (right) exhibits more complex behaviour, as the carrier density is not constant.

spectrum (see Section 2.3.4):

$$\tau_{BG}^{-1}(T) = \tau_0^{-1} + A_{BG}T \int_{\omega=0}^{\omega=\omega_D} \frac{\omega^3}{\omega_D^4} \left(\frac{\hbar\omega/k_bT}{\sinh\left(\hbar\omega/2k_bT\right)} \right)^2 d\omega \tag{4.18}$$

where $\omega_D = k_b\Theta_D/\hbar$, and A_{BG} is a prefactor chosen to give the correct RRR. This model gives $\tau^{-1} \sim T^5$ at low temperatures $T \ll \Theta_D$ (albeit for different reasons to the model of Chudsinski [11]), and $\tau^{-1} \sim T^1$ at high temperatures. We should remark that we do not expect this model to be valid for semimetallic bismuth; the Bloch-Gruneisen model holds for good metals where phonon scattering is dominant, which is certainly not the case here. Table 5 gives the parameters chosen for bismuth to give an RRR of 10. Fig. 4.21 shows the corresponding scattering rate and zero-pressure resistivity, and Fig. 4.22 plots the pressure dependence of $\rho(T)$ assuming constant l. Plainly the results do not agree well with experiment: the conventional Bloch-Gruneisen picture is not appropriate here even at high temperatures. Of course, there is a significant simplification here, because Θ_D will in reality change with pressure, but the qualitative shape of $\rho(T)$ even at $p = 0$ is not correct. When τ_0^{-1} and A_{BG} are modified to give the RRR observed by Balla and Brandt, the agreement with their experimental data is also poor (Fig. 4.20, bottom right panel).

Finally, it is intriguing to remark that one key aspect of $\rho(T)$ is never observed in our calculations: a *peak* at low temperatures. All our calculations indicate that the resistivity instead either rises monotonically (when τ^{-1} wins over n at all T), or first falls and then rises (when n initially wins over τ^{-1}). In the data of Balla and Brandt, and our own data reported below, our measurements frequently show such a peak in $\rho(T)$.

If we assume that the temperature dependence of the carrier density is approximately correct, then such a peak can arise from three possibilities. The first and more interesting option is a second

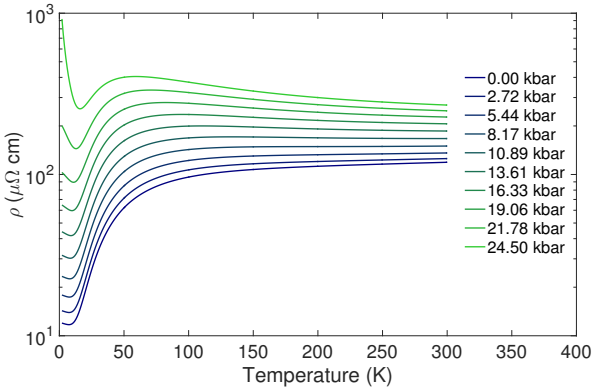

Figure 4.22: Calculated pressure dependence of Bloch-Gruneisen phonon scattering in bismuth, assuming constant scattering length. This model gives very poor agreement with experiment.

Symbol	Description	Value
Θ_D	Debye temperature for bismuth	120 K
A_{BG}	Bloch-Gruneisen prefactor, chosen to fix the calculated RRR to 10	2.36×10^9 s^{-1} K^{-1}

Table 5: Parameters used in calculating the Bloch-Gruneisen phonon resistivity.

scattering channel - that is, the total resistivity is given by :

$$\rho_{total}(T) = \left(\frac{1}{\rho_{bulk}(T)} + \frac{1}{\rho_{add}(T)} \right)^{-1} \tag{4.19}$$

where $\rho_{bulk}(T)$ is the resistivity calculated by the method above, and $\rho_{add}(T)$ is the resistivity of an alternative transport channel - for example, of surface states. Without many more details of the transport parameters of such states, we cannot attempt to include them here.

A second and more prosaic option is a dramatic change in the scattering rate's temperature dependence. As observed in, for example, the Bloch-Gruneisen model, a smooth crossover in the temperature dependence of τ^{-1} does not reproduce such a peak. It is unclear where such a sharp change in $\tau^{-1}(T)$ would arise from.

The third alternative could be the qualitative difference in behaviour when $k_bT \ll \epsilon_F$ (i.e. a good metal) and $k_bT \gg \epsilon_F$ (in which case the Fermi-Dirac distribution, and hence $n(T)$, is changing rapidly). The former case gives $n \sim const.$ and therefore $\rho \sim T^2$ if $\tau^{-1} \sim T^2$. The latter case, as discussed by Balla and Brandt, gives $n \sim T^{3/2}$ [57]. In reality, we should note that we generally observe $n \sim T$, because ϵ_t is itself T-linear, and this is the dominant contribution to the change in carrier density, rather than the broadening of the Fermi-Dirac distribution considered by Balla and Brandt [57]. To observe a peak in $\rho(T)$, we must then have a scattering rate that rises with T more slowly than $T^{3/2}$. If the scattering rate is, for simplicity, purely $T-$linear, we would observe a crossover from increasing to decreasing ρ when k_bT crosses ϵ_F, and therefore a peak. In practice this works poorly. Using $\tau^{-1} \sim T^1$ and fixing τ_0^{-1} to give an RRR of 10, at ambient pressure $\rho(T)$ now exhibits significant negative curvature (because the carrier density is increasing rapidly compared

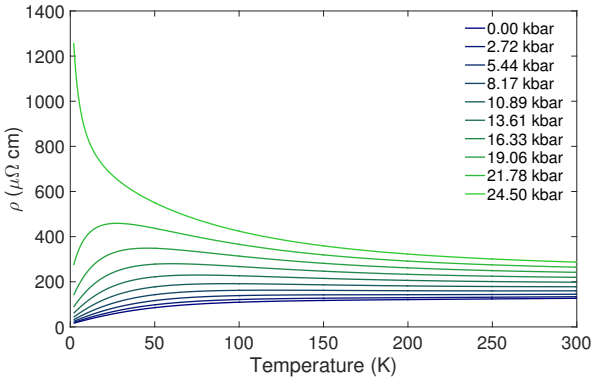

Figure 4.23: Calculated pressure dependence of the resistivity of bismuth with$\tau^{-1} \sim T^1$, assuming constant scattering length and RRR = 10. This model also gives very poor agreement with experiment.

to the scattering rate). At moderate pressures, $\rho(T)$ exhibits a broad maximum, then falls monotonically, in contrast to the fairly sharp peak, broad minimum and increasing $\rho(T)$ near 300 K observed by Balla and Brandt (Fig. 4.23).

4.3 Experiment

4.3.1 Samples and pressure cells

We have conducted resistivity measurements on a total of five samples of bismuth in four piston cylinder cells, at pressures spanning the Bi-I stability range. In this section we present data on two (nominally identical) samples of bismuth, #6.1 and #7.1, measured side-by-side in the same pressure cell run, denoted PCC10; the pressure medium was 4:1 methanol:ethanol. Results for the other samples, which are qualitatively identical but less detailed, can be found in Appendix A. The measurements were performed in collaboration with Konstantin Semeniuk.

Additionally, we present data on three different samples in cells measured to low temperatures. These results provide the first hint that at high pressure, new features exist in the resistivity of Bi-I just below 2 K that have never been previously observed.

4.3.2 Issues with twinning

All our high-pressure measurements are taken on samples cut from a 99.999 % pure sample purchased from MaTecK. This piece is in principle a large single crystal oriented in the trigonal direction; however, our experiments demonstrated that this was not the case. In this section we present a cautionary tale on the dangers of not personally checking every detail of an experiment.

The large crystal proved to be twinned, as demonstrated by x-ray diffraction measurements and quantum oscillation measurements. Issues with twinning are rather common in bismuth, as described in Section 4.1.4, and a number of claims about novel high-field physics were later attributed to measurements on a twinned crystal [59, 9, 60].

Measurements of quantum oscillations (which, due to the small effective mass, can be easily done in bismuth at 2 K and fields below 1 T), should yield a single quantum oscillation frequency of $F = 6.37$ T when B is applied along the trigonal axis [70]. However, no measurements on our MaTecK samples yielded such a frequency (although all samples measured showed clear Shubnikov-de-Haas oscillations). We tried a number of approaches to resolve this issue, including:

1. Cleaving the samples at low temperature. As documented by many authors, the (111) plane of bismuth (perpendicular to the trigonal axis) forms a perfect cleavage plane [67]. At room temperature, bismuth is cut by a scalpel like a knife cuts butter: easily, but with disastrous consequences for crystallographic order in the butter. We found that by submersing our samples in liquid nitrogen for two minutes, then cutting along the (111) face with a fresh No. 11 (sharp-tipped) scalpel blade, the crystal would cleave easily, forming a smooth and mirror-shiny face.

2. Cutting samples with a spark eroder. We were initially concerned that the force applied by a wire saw lubricated with glycerol and tungsten carbide powder was too large, and causing the mechanical formation of twins. Bismuth cut easily with our spark eroder; a black surface layer forms, but this can be easily etched away.

3. Etching samples in 30 % HNO_3 for ~ 2 minutes. We thought it possible that significant damage was being caused to a surface layer when samples were cut or cleaved, and that this layer was preventing us from measuring quantum oscillations. A sample with a typical dimension of ~ 1 mm immersed in 30 % HNO_3 will have its surface etched, leaving bright and shiny faces. This etch also neatly shows up crystallites.

None of these techniques resulted in measurements of the correct quantum oscillation frequencies. Etching revealed that some samples cut from the MaTecK crystal contained visible twins; however, even those samples that did not appear to contain twins still gave incorrect frequencies. From this, we concluded that microscopic twins exist in almost all our bismuth samples, and the quantum oscillation frequencies observed could not be relied on.

Measurements were also undertaken on some samples of bismuth grown several decades ago in our lab (we denote these $\#69 - x$). Bismuth does not oxidise or degrade significantly in air, and we found that these samples were oriented in the trigonal direction, and gave precisely the correct quantum oscillation frequencies, as well as having a similar RRR to our 99.999% pure sample. From the very good match with literature values obtained from these samples compared to the poor quantum oscillations observed in the MaTecK samples, it seems likely that microscopic twins appear to play a significant role in charge transport. No attempt was made to obtain a quantitatively accurate twin fraction for the MatecK crystals, but from the magnitude of XRD peaks we would estimate it to be below 10 %. Zhu *et al.* remarked that "*it is therefore quite a surprise that the contribution of one of these [twin] domains is such that the magnitude of the Nernst peaks caused by their Landau levels is comparable to those of the primary crystal...*", and we would make a similar remark [60]. It seems quite unexpected that a rather small twin fraction leads to such a complete disruption of the quantum oscillation spectrum, in both Nernst and Shubnikov-de-Haas oscillations.

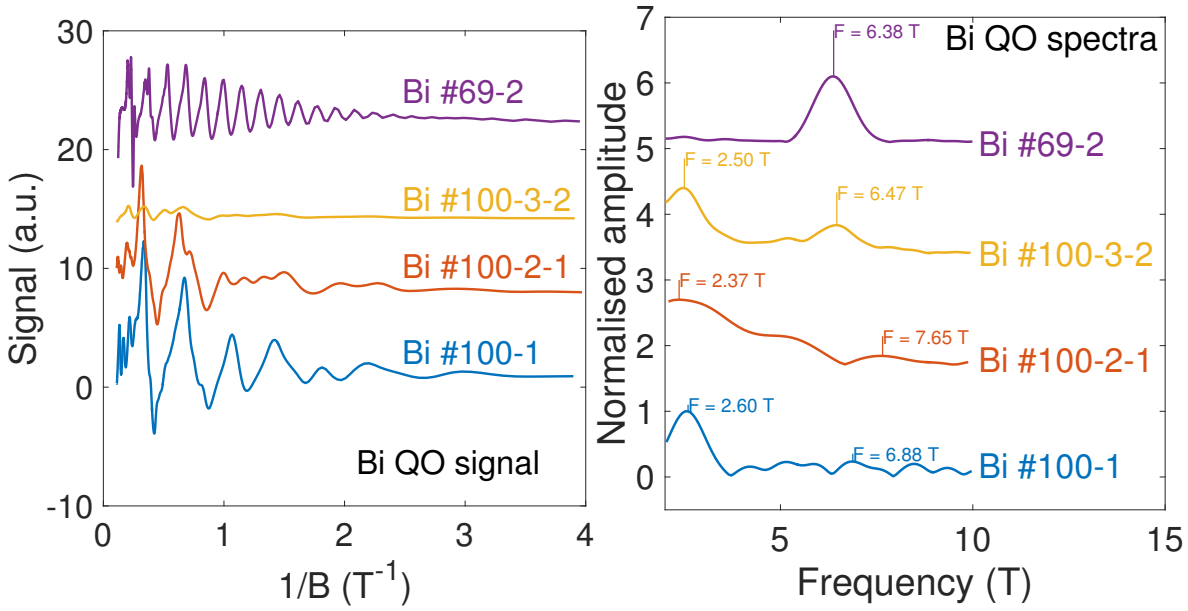

Figure 4.24: Left: quantum oscillation results for various bismuth samples, with B nominally along the trigonal axis. Signal is obtained by differentiating the measured $V(B)$. Sample Bi #69-2 (cut from a 1969 sample) is the only one showing the expected behaviour, with regularly-spaced oscillations in $1/B$. While the Bi #100 samples (cut from the MaTecK crystal and etched in a variety of ways) show oscillations, they are not regularly-spaced. Successive sweeps offset for clarity. Right: quantum oscillation spectra, obtained by fast Fourier transform of the signal and normalisation to the maximum peak height. The expected frequency for B along the trigonal axis is $F = 6.37$ T. This is clearly observed for Bi #69-2; all three MaTecK samples show additional spurious peaks and an incorrect value for F.

Fig. 4.24 shows results obtained from measurements of Shubnikov-de-Haas oscillations in the resistivity for three samples from the MaTecK crystal and one from the #69 batch; only in this sample is the single sharp peak at $F = 6.37$ T visible.

With the #69 samples, we found that cutting samples from the parent block with a spark eroder, then cleaving at liquid nitrogen temperatures along the trigonal face, provided mirror-bright flat trigonal faces. Making contacts to this cleaved face using DuPont 6838 epoxy cured for 2 hours at 160 °C (rather than spot-welding contacts) provided reliable observation of the 6.37 T trigonal frequency; the samples had an RRR of $\sim 50 - 75$, and an enormous fractional magnetoresistance of $\sim 100,000\times$ in 9 T at 2 K. The two-point contact resistance is typically $\sim 6\ \Omega$; this value might seem large, but we have found that quantum oscillations can easily be observed in bismuth even with contact resistances of $\sim 100\,\Omega$.

The results presented here should therefore be considered to be taken on polycrystalline samples; the twinning may explain the qualitative differences between each measurement. Future work on the #69 batch should investigate the behaviour of quantum oscillations under pressure; care should be taken to ensure that the sample preparation process, and pressurisation up to 25 kbar, does not introduce twinning defects.

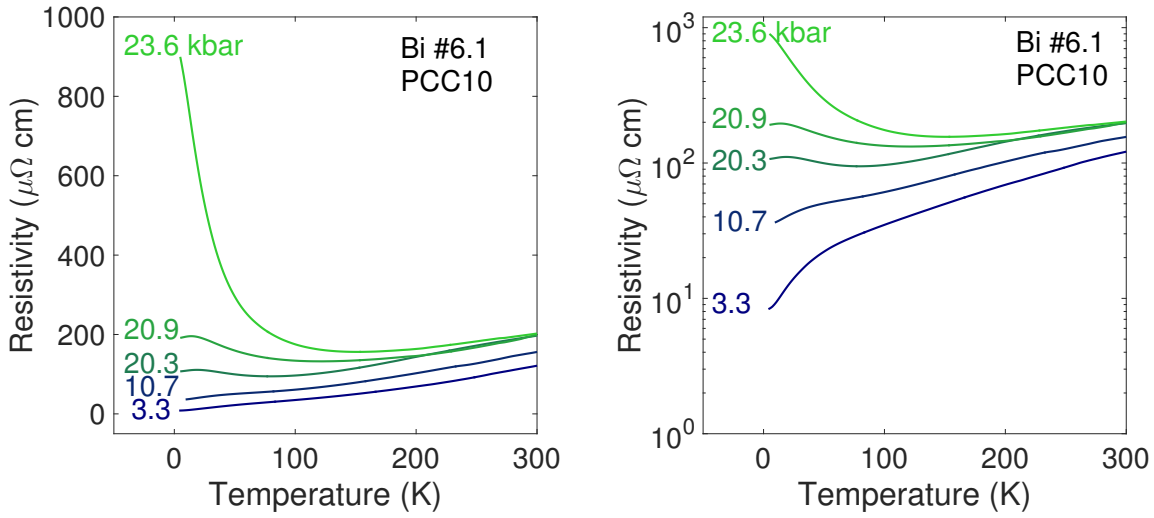

Figure 4.25: Temperature dependence of the resistivity for sample Bi #6.1 in PCC10, on linear (left) and semilog (right) axes.

4.4 Results

4.4.1 Resistivity as a function of pressure

In Figs. 4.25-4.26, we summarise the temperature-dependent resistivity traces of the five samples measured; a subset of all available data is shown for clarity, as these pressure cell runs involved 20 pressure points. Obtaining a numerically accurate value for our resistivities is challenging given the small dimensions of our samples; therefore we scaled $\rho(T)$ at the lowest pressure so that it matched the literature value for ambient-pressure bismuth of 120 μΩ cm at 300 K, corrected using the curve of Eiling and Schilling [39]. This involves only a single numerical scaling factor for each sample obtained at low pressure. It neglects any differences in the resistivity's magnitude parallel to and perpendicular to the trigonal axis; as our crystals are twinned, we make no attempt to correct for this uncertainty. In effect, we assume our samples are perfectly polycrystalline, when in reality they likely have a significant preferential orientation, which could vary from sample to sample. However, the variation in the resistivity along the two directions is only $\sim$ 15 %, and a small error in the absolute value does not affect our conclusions [11]).

Qualitatively, both samples show identical behaviour. At lower pressures (typically $<$ 5 kbar), $\rho(T)$ is unambiguously metallic, with ρ falling with T. We note that the RRR of the samples appears to fall very sharply even at quite low pressures (at ambient pressures, our Bi samples typically have a RRR of $>$ 50). At the highest pressures, $\rho(T)$ shows an increase at low temperatures. For comparison to the data of Balla and Brandt, see Fig. 4.13 [57].

The intermediate pressure region, and the details of the change of ρ with pressure, are more complex. At lower pressures, increasing p leads to an increase in ρ throughout the whole temperature region, but the greatest increase occurs in the low-temperature part. At modest pressures, a clear kink in $\rho(T)$ emerges, which develops into a peak as pressure increases. This can be seen quite

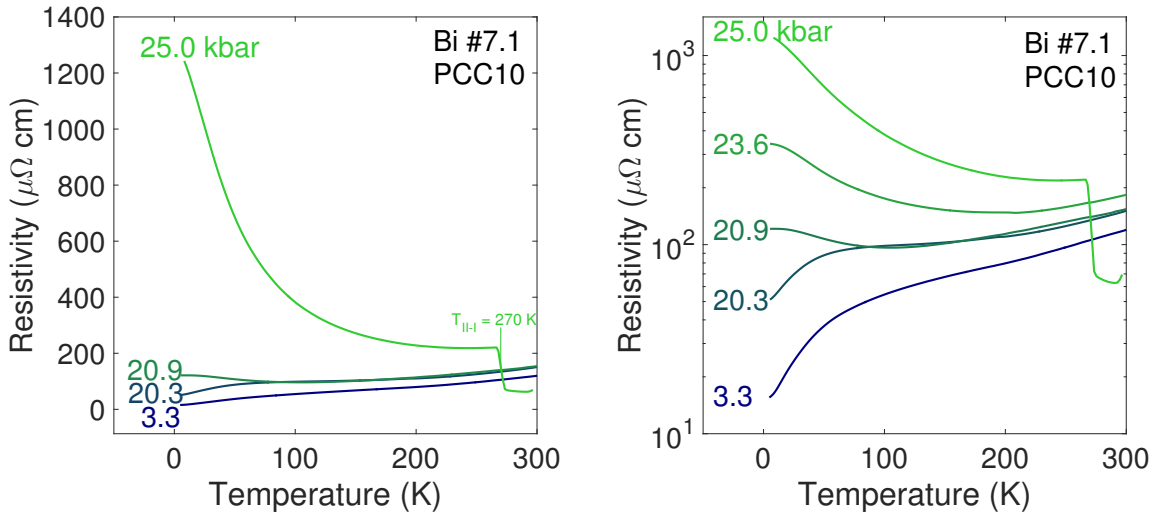

Figure 4.26: Temperature dependence of the resistivity for sample Bi #7.1 in PCC10, on normal (left) and semilog (right) axes. The arrow at the jump in $\rho(T)$ at 270 K in the left plot marks the II-I structural phase transition.

clearly in Fig. 4.29.

4.4.2 Pressure dependence of the resistivity

In Fig. 4.27 we plot the low-temperature conductivity $\sigma_{4.2} = 1/\rho(T = 4.2\,K)$ as a function of pressure. The low-temperature conductivity falls by a factor of $\sim 100\times$. Fig. 4.28 shows the experimentally-obtained residual resistance ratio (RRR), defined as the ratio of the 300 K resistivity to the lowest-temperature resistivity. This gives a qualitative indication of the metallicity of the sample: an RRR above 1 indicates the resistance rises with T, and is therefore "metallic", while an RRR below 1 indicates the sample is "semiconducting"[7]. This guideline is only approximate, as some samples at intermediate pressures have $\rho(T)$ describing a convex curve, so may have an RRR above 1 while still showing a negative gradient $d\rho/dT$ at the lowest temperatures.

The RRR is, above a few kbar, rather small. An extrapolation of the RRR to zero pressure would usually yield a value of $\sim 7-15$. This suggests there may be a rather abrupt introduction of defects associated with pressurisation. Similar behaviour is observed in the data of Balla and Brandt (Fig. 4.13) - their samples after depressurising from 25 kbar have an RRR of only 3.64.

There are two results evident from these plots. The first is that, while qualitatively all show the same behaviour, quantitatively there are differences in the values of σ_0. Between 10 and 20 kbar, σ_0 for Bi #6.1 continues to fall smoothly, while σ_0 for Bi #7.1 remains essentially constant. Fig. 4.29 demonstrates this clearly.

The second feature of interest is that σ_0 does not appear to evolve in a continuous fashion. There is a fairly sharp step visible in Fig. 4.27, with an onset occuring at $p_k \approx 17-20$ kbar. Recall that Fig.

[7] As noted previously, an RRR < 1 does not in fact imply $\epsilon_t < 0$.

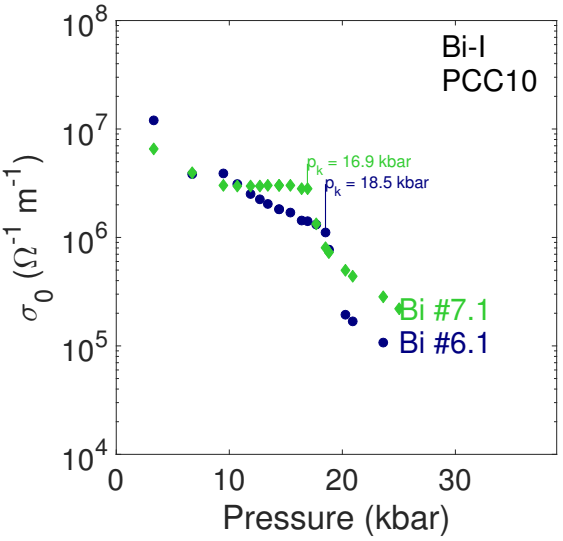

Figure 4.27: Pressure dependence of the conductivity $\sigma_{4.2\,\mathrm{K}} = 1/\rho_{4.2\,\mathrm{K}}$ at 4.2 K under pressure with logarithmic y-axis, for samples in PCC10 (blue circles: Bi #6.1; red triangles: Bi #7.1). The arrows at p_k mark apparently discontinuous changes in σ_0, at a pressure which varies a little between samples.

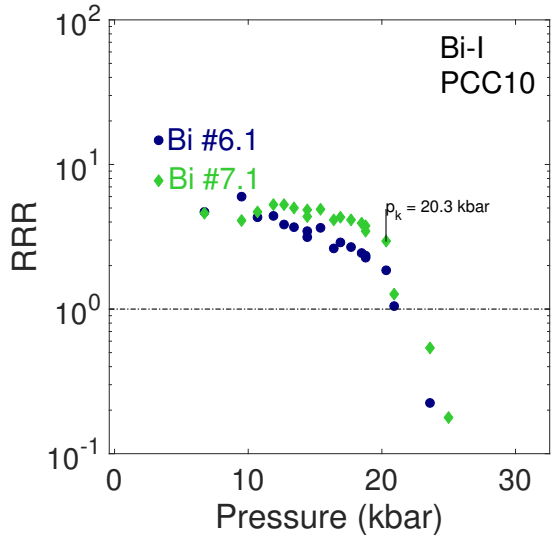

Figure 4.28: Pressure dependence of the residual resistance ratio RRR $= \rho_{300}/\rho_0$ for samples in PCC1,2 and 111 (left) and PCC10 (right), on linear (top) and logarithmic (bottom) scales. The dashed line at RRR$= 1$ on the log-scale plots indicates approximately the transition between "metallic" behaviour ($\rho(T)$ increasing with T) to "semiconducting" behaviour ($\rho(T)$ falling with T). At the pressure p_k there is an apparently discontinuous change in the RRR, an effect which is apparently consistent between samples.

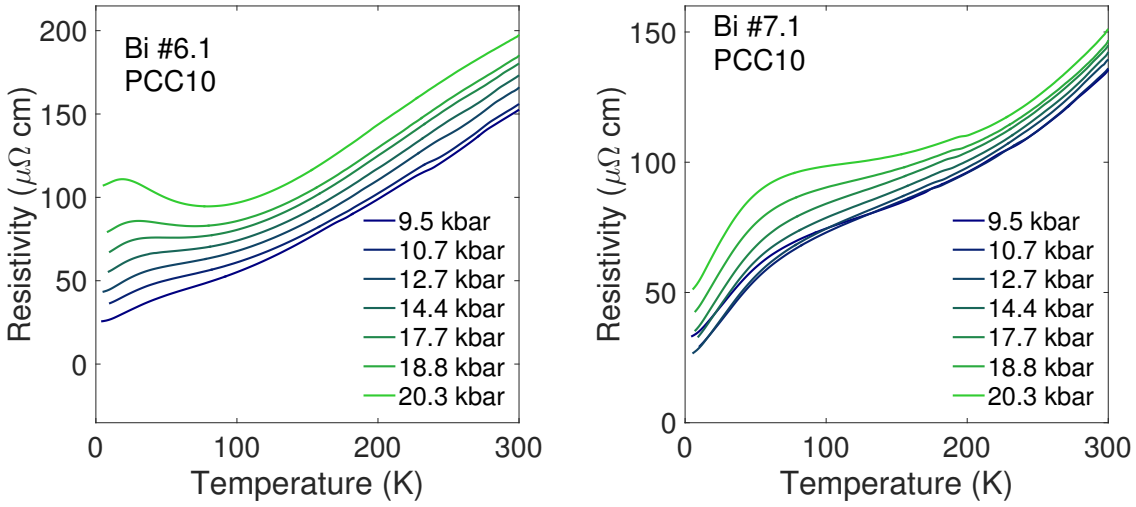

Figure 4.29: Resistivity $\rho(T)$ from $\sim 10-20$ kbar for Bi #6.1 (left) and Bi #7.1 (right), both in PCC10; a subset of all available pressure points is shown. Plainly the qualitative behaviour is different: for Bi #6.1, a clear peak emerges in the low-temperature resistivity, while for Bi #7.1 there is instead a broad hump.

4.27 shows σ_0 on a logarithmic scale, so this step corresponds to an increase in the low-temperature resistivity by over an order of magnitude. The precise value of p_k varies a little between the two samples. When we instead consider the RRR, the value of p_k above which the RRR falls rapidly is ~ 20.3 kbar, with both samples showing very similar behaviour (Fig. 4.28).

4.4.3 Pressure dependence of features in the resistivity

There are four distinct behaviours in $\rho(T)$, common to all samples measured. At the lowest pressures, $\rho(T)$ increases monotonically and featurelessly from low temperature, with a nearly-constant gradient. At intermediate pressures, a distinct kink emerges in $\rho(T)$, at a temperature $T_k \approx 50$ K. At higher pressures, this kink appears to evolve into a clearly-defined peak; there is additionally a trough in $\rho(T)$ above the peak. At the highest pressures, the peak is suppressed to at most 2 K (i.e. its low-temperature side cannot be observed in our data); typically, in this state the resistivity decreases continuously with rising T, and there is no minimum. This kink is seen reliably above ~ 10 kbar in all our measurements (see e.g. Fig. 4.29). The kink is not described in the literature, although it is visible in the data of Balla and Brandt [57], as we show in Fig. 4.31.

We define the peak temperature T_{max} as the temperature at which the resistivity falls on both sides; the kink temperature T_k is found by fitting straight lines to the approximately linear region below and above the kink, and taking T_k as the temperature where these fits meet. Fig. 4.30 shows examples of how T_{max} and T_k were determined.

In Fig. 4.33, we plot the pressure dependence of T_k and T_{max}, to demonstrate the behaviour described above. From approximately 10 to 20 kbar, the kink is the main feature in the resistivity, remaining at around $30-50$ K. At higher pressures, the kink is replaced with a peak, and T_{max} rapidly

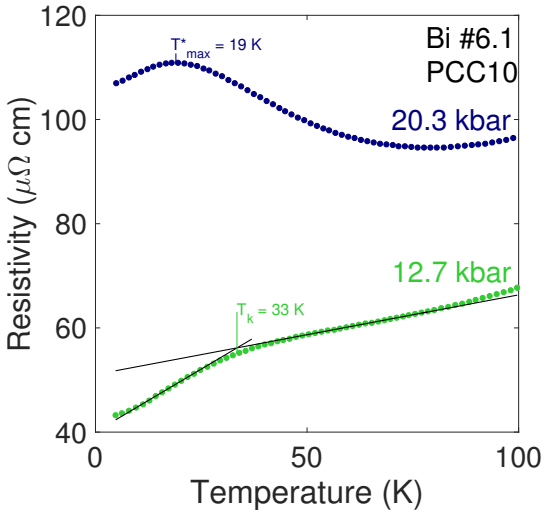

Figure 4.30: Resistivity $\rho(T)$ for Bi #6.1, showing the determination of the kink temperature T_k as the meeting-point of two linear fits, and the peak temperature T_{max}.

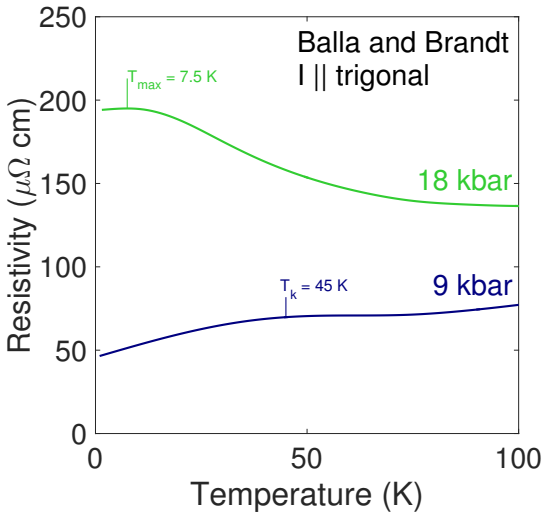

Figure 4.31: Resistivity $\rho(T)$ from the data of Balla and Brandt, indicating a similar kink and peak to that seen in our data [57].

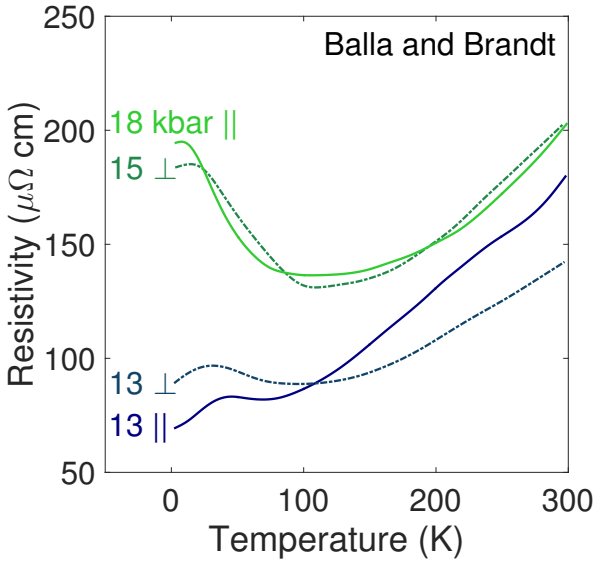

Figure 4.32: Comparison of the data of Balla and Brandt between samples with current applied parallel to the trigonal direction (solid lines) and perpendicular to the trigonal direction (dashed lines). For currents applied in the two directions, measurements at the same pressure do not give the same results.

falls to zero temperature (or at least, below the 2 K limit of our measurements).

From this figure it can be straightforwardly seen that, while the qualitative behaviour is similar between measurements, there is a significant sample dependence. As described above, this is particularly noticeable for the two samples together in PCC10: at 18 kbar, Bi #6.1 clearly shows a peak in $\rho(T)$ with a T_{max} rapidly suppressed by pressure; for Bi #7.1 (in the same cell), the kink temperature is about 20 K higher, and falls only a little up to 21 kbar. A similar discrepancy is clearly visible in the results of Balla and Brandt [57]. As shown in Fig. 4.32, when they applied current parallel to and perpendicular to the trigonal axis, they observed some differences in the pressure dependence. However, they presented far fewer pressure points, and made no remark on the differences between their results.

4.5 Analysis

4.5.1 Armitage scattering data

Recently, the Drude scattering rate $\tau^{-1}(p,T)$ has been measured by Armitage *et al.* [12]. This allows us to attempt an estimate of the low-temperature carrier density, and compare our data to the observation by Armitage *et al.* that the scattering rate is strongly enhanced at low temperatures. This requires a few significant approximations, which we lay out here. First, recall that in the Drude model, the resistivity is:

$$\rho(p,T) = \frac{m\tau^{-1}(p,T)}{e^2 n(p,T)}. \tag{4.20}$$

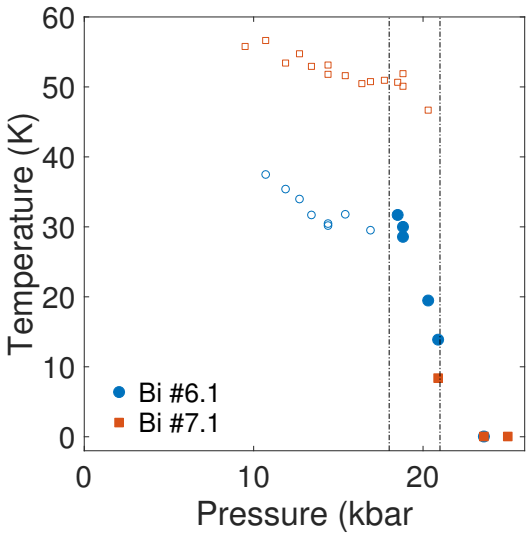

Figure 4.33: Pressure dependence of the kink temperature T_k (small open markers) and peak temperature T_{max} (large solid markers), for samples in PCC10. Values $T_{max} = 0$ imply no fall in the resistivity was observed down to 2 K. Vertical dashed lines at 18 and 21 kbar indicate the approximate region of the transition from a kink to a peak.

Typically, for the resistivity of metals we assume that the temperature-dependence of the effective mass is negligable - that is, the band structure does not change curvature with temperature. In the case of bismuth this is debatable (see Norin and references therein [56]); in particular, as applied pressure shifts the Fermi level to lower and lower values, the non-parabolic electron conduction band may well have an effective mass that changes with pressure.

Secondly, we are totally neglecting any anisotropy in the resistivity. The data of Armitage *et al.* do not give different scattering times for the different crystallographic directions. Recent careful measurements of the conductivity tensor for bismuth as a function of angle suggest that the mobility is highly anisotropic, but *less anisotropic* than would be expected based on the anisotropy of m alone [58]. This implies that τ^{-1} itself is *also* highly anisotropic, but in such a way that the product $m\tau^{-1}$is more isotropic than m. This anisotropy is irrelevant for our measurements, as we do not have a good understanding of the relation of our current direction to the crystallographic directions, due to twinning in our crystals.

Finally, we are assuming that the Drude scattering rate measured optically by Armitage *et al.* is the same rate probed by DC resistivity measurements. Armitage *et al.* argue this is the case, in that the shape of τ^{-1} they observe corresponds quite well to the resistivity results of Balla and Brandt; additionally, the size of the zero-pressure, high-temperature scattering rate would appear to agree quite well with experimental values of the DC resistivity. Our calculations (e.g. Fig. 4.20) suggest this assumption likely does not hold.

Here, we neglect complexities arising from anisotropy of both m and τ^{-1}, and calculate $n(p,T)$ from our resistivity data and the Drude scattering rate of Armitage *et al.* The resistivity $\rho(p,T)$ is taken from our data; the scattering rate $\tau^{-1}(p,T)$ from Armitage *et al.* [12]. Armitage gives a scat-

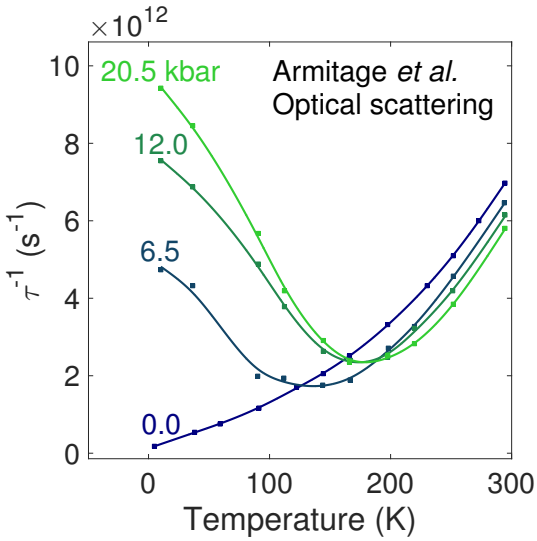

Figure 4.34: Temperature and pressure dependence of the scattering rate, as obtained from the optical conductivity data of Armitage *et al.* [12]. Solid points are taken from their data; smooth lines are interpolating cubic smoothing splines.

tering rate in meV; we convert to a frequency with:

$$\tau^{-1} = 10^{-3}\frac{e}{\hbar}\tau_A^{-1} \tag{4.21}$$

where τ_A^{-1} is Armitage's numerical value in meV (the other factors ensure our scattering rate has dimenions of inverse seconds).

Our values for the scattering rate as measured by Armitage *et al.* are given in Fig. 4.34. The datapoints are rather sparse (with only ~ 10 temperatures measured at each pressure point), so we fit a 1000-point cubic smoothing spline through the Armitage data. This allows values of τ^{-1} to be obtained for $10 < T < 300$ K using linear interpolation without unphysical sharp corners appearing in the analysed data.

From this method, we can rearrange Eq. 4.20 to obtain the carrier density $n(T)$ at a given pressure. We use the measured pressures for our resistivity traces, taking pressure points as close as possible to Armitage's values, and linearly interpolate on the two-dimensional $T - p$ surface taken from the smooth curves fitted to Armitage data to obtain an estimate for $\tau^{-1}(T)$ at the pressure where our resistivity data was taken. To obtain a quantitative ρ we must choose a value for m; we estimate this from Armitage's τ^{-1} by assuming that, at $p = 1$ bar, the carrier density increases by a factor of $8\times$ from 2 to 300 K, based on the data of Issi [8], and that at 1 bar and 300 K the resistivity is 120 μΩ cm. This gives $m = 0.011m_e$. As we have discussed previously, different authors give $n(T)$ increasing by a factor of $4 - 9\times$, so the correct value of m is quite uncertain. However, this contributes only a single global scaling of n and does not affect the qualitative results.

Fig 4.35 plots the measured resistivity, the measured and interpolated data from Armitage, and the resulting carrier density. Plainly, the carrier density extracted from this process is not physically

reasonable: it typically shows a dramatic *fall* as T increases. This can be easily understood by a comparison between the resistivity and Armitage's data at e.g. $p = 6.7$ kbar. Armitage observes a fall in $\tau^{-1}(T)$ as T increases; however, our resistivity is monotonically increasing. If Armitage's results are correct, then (because $\rho \sim \tau^{-1}/n$) we must have an n that is steeply falling. There does not appear to be a mechanism for this to occur. The high-temperature behaviour of $n(T)$ extracted from this process, by contrast, is quite reasonable. It typically falls with pressure, by a factor of $\sim 2\times$ from 0 to 20 kbar.

Armitage suggested that their dramatic enhancement in τ^{-1} arose from the formation of some exotic phases when the carrier density becomes particularly low, and they argue that the shape of their curves for τ^{-1} approximately match the resistivities of Balla and Brandt. Our resistivity data does not support this hypothesis. Armitage *et al.* observe an enhancement in τ^{-1} at low T even at only 6.5 kbar, while our own data, and that of Balla and Brandt, only indicates metallic resistivity at this pressure. For the magnitudes of the resistivity and scattering to be consistent, we would need minimal change in the carrier density $n(T)$, but our calculations indicate this does not hold - at high pressures, the carrier density is strongly temperature-dependent. One possibility could be that the Drude scattering rate estimated by Armitage is very distinct from that probed by the resistivity; why this should be the case is unclear.

4.5.2 Evidence for a semiconducting state

How might we distinguish between the semimetallic and semiconducting states? As the numerical calculations demonstrate, at finite temperatures, there is in fact no qualitative change in $\rho(T, p)$ as we cross p_c; at high temperatures the resistivity remains very similar. The only difference is at the lowest temperatures. For $p < p_c$, the carrier density remains finite at $T = 0$, and the resistivity therefore appears to saturate at low T, while for $p > p_c$ the low-temperature resistivity diverges.

If we had truly obtained a semiconducting state, we might expect that - at least at low T, where the carrier density's thermal activation is much more relevant than the scattering rate's change with T - we would observe Arrhenius behaviour, $\ln \rho \sim 1/T$, with the gradient proportional to the band gap, $-\epsilon_t$, over some extended temperature range. Previously, it has been suggested that this Arrhenius behaviour is observed in bismuth even at quite moderate pressures above around 10 kbar [78]; this is disputed by Balla and Brandt [57]. When $\epsilon_t > 0$, the Arrhenius plot will flatten at the lowest temperature (highest $1/T$), because the carrier density does not diverge. Such behaviour is observed in the numerical calculations (Fig. 4.18), and provides a reasonable way to distinguish between semimetallic and semiconducting states.

The existence of a region of Arrhenius resistivity in our data is debatable (Fig. 4.36). At the highest pressures there is a region of positive gradient in the Arrhenius plot, between $0.02 < 1/T < 0.05$ K^{-1}, which could be identified with an Arrhenius region; the gradient appears to increase with pressure. The gradient of an Arrhenius plot corresponds to the activation energy $E_0 = k_b T_0$ when $\rho(T) = \rho_0 e^{\frac{T_0}{T}}$. In our data, the gradient is quite strongly temperature-dependent, i.e. there is not a single clearly-identifiable gap energy that extends over a significant temperature range. Typical values of the gradient correspond to a T_0 of $\sim 20 - 40$ K. At the lowest temperatures, the Arrhenius plots saturate.

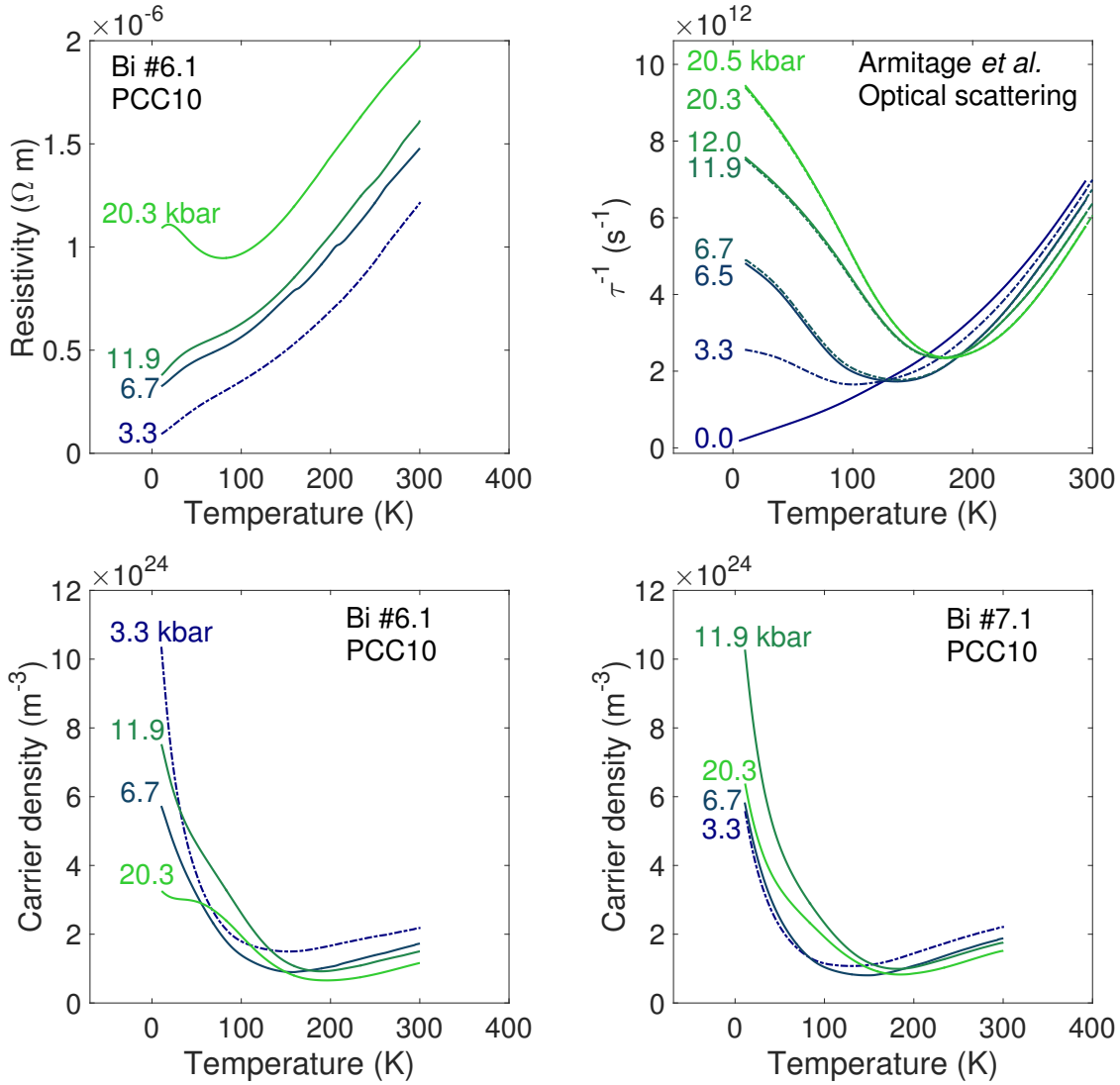

Figure 4.35: Method of extracting carrier density from resistivity using the data of Armitage. First, we obtain the measured resistivity at pressures as close as possible to those of Armitage (top left). Dashed lines show a pressure point a significant distance from one of Armitage's. Then, we use interpolation to estimate τ^{-1} at our pressures from Armitage's data (top right). Solid lines are Armitage's measurements; dashed lines are the interpolations. Finally, we divide τ^{-1} by ρ (and multiply by the relevant prefactor) to obtain the carrier density for samples Bi #6.1 (bottom left) and #7.1 (bottom right).

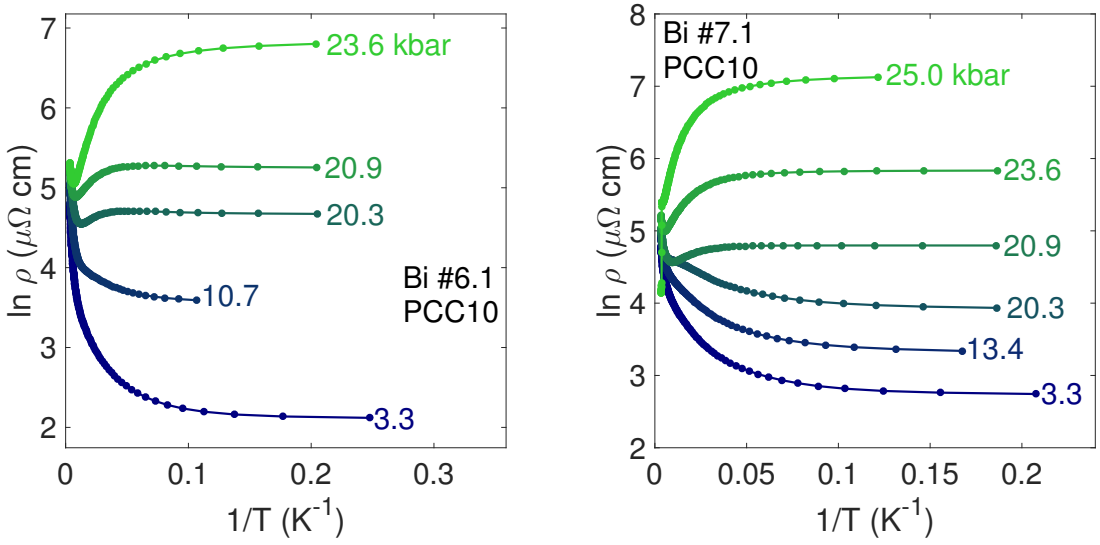

Figure 4.36: Arrhenius plots for $\rho(T)$ for bismuth samples in PCC10: Bi #6.1 (left) and #7.1 (right).

One might conceive a situation in which the divergence in the resistivity occurs only at the lowest temperatures - perhaps below the 2 K attained here - but the numerical results, and our own later low-temperature measurements, indicate this is false (Fig. 4.18). Of course, the calculations assume the temperature dependence of the band parameters and scattering mechanisms remains the same at 26 kbar as it is at 1 bar of pressure, which may be flawed. However, near p_c the low-temperature resistivity is not sensitive to the exact details of the value of ϵ_t, only its sign - if there is a finite bandgap, the carrier density must diverge.

There are then a number of possible interpretations to the absence of a low-temperature Arrhenius regime in our data. The first is simply that, even at 26 kbar, the SMSC transition has not yet occured, and higher pressures are required. As originally remarked by Balla and Brandt, this is a considerable experimental difficulty, because at higher pressures and ambient temperature higher-pressure structures of bismuth intervene [57]. We have found that these structures are likely retained as minority phases upon cooling through the II-I or III-I structural transition. Experiments would then need to apply pressure to the Bi-I phase at low temperatures, which is technically challenging.

Alternatively, it may be that the semiconducting regime (and corresponding Arrhenius form of ρ) exists but is not accessible, for which there are a number of possible explanations. Firstly, even if $\epsilon_t < 0$, its magnitude will be small and the behaviour may be susceptible to the same complexities that arise when ϵ_t is small and positive. In particular, the temperature dependence of the band parameters may cause ϵ_t to vary in magnitude, or even change sign, as a function of temperature. This would lead to non-Arrhenius resistivity at finite T even if the electronic structure was gapped at $T = 0$. Secondly, there may be a significant role for dopant impurities: these could contribute a significant fraction of the bulk carrier density at high pressure even if they exist only at the part-per-million level.

An intriguing alternative would be that a metallic conduction channel is short-circuiting the semiconducting resistivity. There is in fact already some evidence for this, in the presence of the peak in $\rho(T)$ that we observe across quite a wide pressure interval from $\sim 15 - 21$ kbar (see, for example, the solid markers in Fig. 4.33). This feature is also clearly visible in the data of Balla and Brandt (Fig. 4.13).

Currently, there appears to be no discussion in the literature of this peak, and no clear explanation for it. Our numerical calculations demonstrate that it is not expected to appear based on the simplistic assumption that the overlap energy ϵ_t changes in a linear fashion with both temperature and pressure, and neither can a slow crossover in the scattering rate. We propose four possible explanations.

Such a peak could appear if ϵ_t has a rather complicated temperature-dependence at high pressure (e.g. if it first drops at low T, before starting to increase above T_{max}). This has not been investigated experimentally, but it would appear unlikely. The value of ϵ_t is set by the crystal structure, and it is hard to envisage a scenario in which this would change in such a non-monotonic fashion with temperature.

Alternatively, it could arise if there was a sudden dramatic enhancement in scattering at T_{max}. However, as we note in the calculation using a Bloch-Gruneisen scattering rate, a smooth crossover (e.g. from $\tau^{-1} \sim T^5$ to $\tau^{-1} \sim T^1$, whether from conventional phonon scattering or from the more involved plasmon-enhanced scattering proposed by Chudzinski [11]) neither agrees with the experimental data nor produces such a peak. Neither does the data of Armitage, which suggests an enhanced τ^{-1} which falls monotonically at low T [12]. To produce a peak requires a peak in the scattering rate occuring over a temperature regime only~ 10 K wide. This hypothesis is lent adddditional weight by the fact that the maximum clearly emerges from an obvious kink in the resistivity (Figs. 4.30 and 4.33), implying the scattering mechanism still exists at lower pressures.

In semiconductors, one typically sees a change in the Arrhenius-activated carrier density arising from impurity states or dopants, which typically have a much smaller activation energy than the intrinsic band gap (i.e. the impurity states are situated very close to a bulk band edge). This leads to the measured resistivity at low temperatures being much lower than expected from the purely intrinsic carrier density. Such a scenario could apply here. We would require an impurity that lived just below the Fermi level (or else we would still see diverging resistivity at low T). Our Bi samples are 99.999 % pure, but the unusual band structure corresponds to an intrinsic carrier density of only around 1 electron per 100,000 atoms even at ambient pressure, and this number is much lower at high pressures. Impurities at the parts per million level could therefore noticeably influence the carrier density.

The final, intriguing, alternative, would be to draw on the explanation used for similar results in topological insulators. In SmB_6, a similar clear saturation is observed in the low-temperature resistivity, despite the bulk being an insulator. This was later ascribed to conducting surface states; these have a much lower carrier density than all reasonable samples measured in transport experiments, except for at the lowest temperatures, where there are no longer thermally-activated bulk carriers, and so the surface states become relevant to transport [121]. The surface carrier density in SmB_6 is $\sim 2 \times 10^{14}$ cm^{-2}, the same order of magnitude as in bismuth. Bismuth is not a topological

insulator (although there have been recent suggestion that it may in fact have a topologically non-trival band structure [112]). However, it does possess metallic surface states (see Section 4.1.6 for details). At ambient pressure these have a carrier density equivalent to a slab of bismuth ~ 1 um thick, and would therefore be irrelevant to charge transport (our samples typically have a thickness around $100\times$ larger). At high pressures, where the bulk carrier density is reduced, this may no longer be true: if the surface carrier density remains constant, at moderate pressures it could equal that of the bulk. If this were the case, we would expect to see a saturating resistivity, or even one that exhibits a peak (if, for example, the surface states possess a resistivity that increases rapidly with temperature).

This hypothesis draws a rather ironic parallel to that complicating the SMSC transition as a function of film thickness in ultra-thin films. As noted in Section 4.1.6, the full transition to a semiconducting state could not be observed in thin films because metallic surface states intervene, providing an alternative charge conduction channel which obscured that of the (perhaps semiconducting) bulk. Perhaps a similar issue is occuring here. Further work would be needed to ascertain whether this can also explain the smooth evolution of the kink in $\rho(T)$.

This approach does not explain all the data, for two reasons. The first is that the maximum in the resistivity appears to evolve quite smoothly out of a kink in the resistivity, clearly observable at lower pressures. Such behaviour would not be expected from a parallel-conducting model (where, at such low values of the bulk resistivity, the surface states would be irrelevant to transport). The second is that the absolute value of the peak in the resistivity appears to be quite variable. As an example, consider the sharp peak in $\rho(T)$ shown in Fig. 4.25 at 20.3 kbar, corresponding to $\rho \sim 100$ $\mu\Omega$ cm. At higher pressure, the low-temperature resistivity attains much higher values (two times larger at 20.9 kbar, around ten times larger at 23 kbar). If there were a pressure-independent metallic resistivity in parallel with that of the bulk, it should define a limiting value which cannot be exceeded.

4.6 Low-temperature measurements at high pressure

Bismuth under high pressure has never previously been measured down to temperatures below 2 K. Given the various predictions of novel phase formation, which might be expected only in the ~ 1 K region, we resolved to rectify this [12, 11]. We observed that, for pressures of > 20 kbar, there was an unexpected steep downturn in the resistivity below a temperature $T^* \approx 1.4$ K. Later measurements down to 15 mK suggest that in fact ρ vanishes at the lowest T.

4.6.1 Experimental results

Measurements on two cells were undertaken in Cambridge, using the DMS, to temperatures of ~ 0.3 K. Typically, these were collected rather incidentally, with the focus of the measurement run on other samples in the pressure cell. As a result, a full systematic dataset is not available. Both these cells used samples taken from the MaTecK twinned bismuth crystal, contacted with spot-welding and 6838 epoxy (samples Bi #10.11 in PCC111, and Bi #7.1 in PCC11[8]). For sample Bi #7.1 we do not have an accurate value for the sample dimensions, so present the measured voltage.

[8] Further evidence for the author's hypothesis that only pressure cell runs labelled by solely the number '1' (and perhaps also '0') yield the most high-quality results.

Having obtained some suggestions of a new phase existing at very low temperatures, a further cell was set up. Measurements were taken at the National High Field Magnet Laboratory in Tallahassee by Jordan Baglo and Konstantin Semeniuk. A dilution fridge and high-field magnet allowed measurements down to 17 mK, and fields up to 16 T. The sample in this cell was spark-cut from the #69 single crystal (it is labelled #69-2-1-1); inside the pressure cell, it is aligned with the field approximately in the same direction as the current flow. Magnetoresistance measurements will therefore measure the longitudinal magnetoresistance ρ_{zz}, not the transverse magnetoresistance ρ_{xx}. Contacts were made on the spark-cut trigonal face with 6838 epoxy.

In all measurements presented here, note that the low-temperature pressures in the cell are above the nominal stability range of Bi-I. All the data shown here arise from samples that exhibit a structural phase transition from either Bi-II or Bi-III at room temperature, and we believe that a small amount of the high-pressure phase is frozen in. This gives rise to superconducting jumps at $T_c = 4$ K (for trapped Bi-II) or $T_c = 7$ K (for trapped Bi-III). The jump does not always occur in the same direction - for example, it sometimes corresponds to an *increase* in the resistivity. This implies the presence of isolated, small pockets of the high-pressure phase (the jump corresponds to a change in the resistivity of $\sim 5 - 10$ %). Likely, the structural transition results in the formation of a polycrystal of Bi-I. We would not expect to observe quantum oscillations or the enormous MR characteristic of single-crystal Bi.

Fig. 4.37 shows $\rho(T)$ down to < 1 K for the two cells measured on the DMS. Down to 2 K, the resistivity agrees well with the results presented so far: the steep upturn in $\rho(T)$ at these pressures yields to a saturating, approximately constant resistivity. At $T_c \approx 3.9$ K, there is a jump associated with the small fraction of Bi-II becoming superconducting.

At a temperature $T^* = 1 - 1.8$ K, there is then a sharp downturn in the resistivity. This appears to happen rather smoothly, and at the temperatures accessible here, corresponds to a drop of ~ 50 % of ρ. This feature has never been noted in the literature before.

In Fig. 4.38, we show the response of this feature to field, which is remarkably robust. A field of 0.1 T totally destroys the Bi-II superconducting transition; the low-temperature downturn is seemingly unchanged.

In Fig. 4.39 we show the data taken at Tallahassee, from 2.5 K to 17 mK. The behaviour is similar to that seen in the DMS previously, but the data down to the lowest temperatures suggests the resistivity drops to zero - a superconducting transition. The temperature scales are broadly comparable: the onset of the downturn is at about 0.7 K, which is a little lower than that seen in the PPMS, and by 0.4 K, the lowest temperature measured by the DMS, the resistivity has fallen by ~ 50 %.

Field sweeps up to 16 T were performed at temperatures from 20 mK to 0.85 K. The results, across the full field range, and at lower fields, are shown in Fig. 4.40. An applied field appears to suppress the low-resistance state: at 20 mK, a field of ~ 1.6 T is required for the resistance to climb to its normal-state value. The normal-state magnetoresistance is negative and small - recall that in ambient-pressure bismuth, it is positive and large.

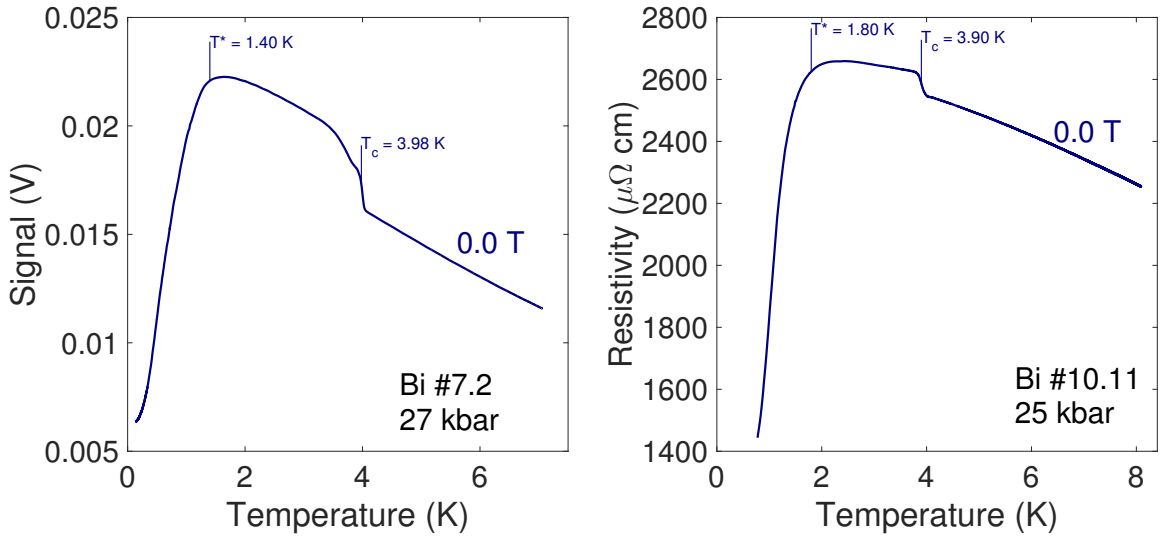

Figure 4.37: Resistivity of Bi-I down to below 1 K, for (left) a sample in PCC11, and (right) in PCC111. Both samples show a clear jump associated with a small fraction of trapped Bi-II at ~ 3.9 K; there is then an additional, unexpected downturn below around 2 K.

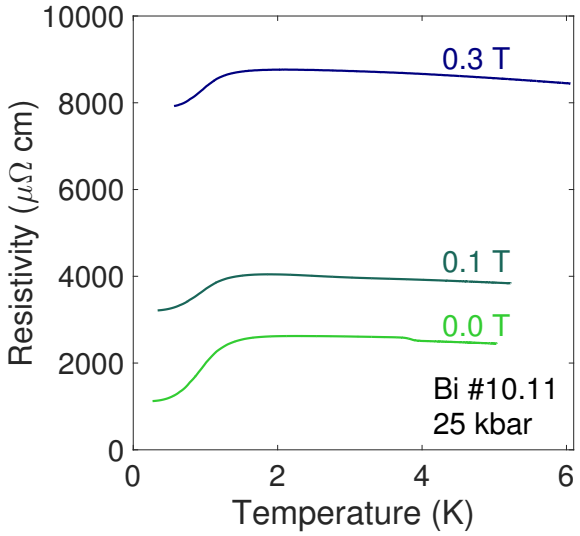

Figure 4.38: Low-temperature resistivity for a bismuth sample in PCC111, in a number of applied fields. At 0 T, the Bi-II transition is visible, but this is destroyed in fields of 0.1 T. The low-temperature feature appears unchanged.

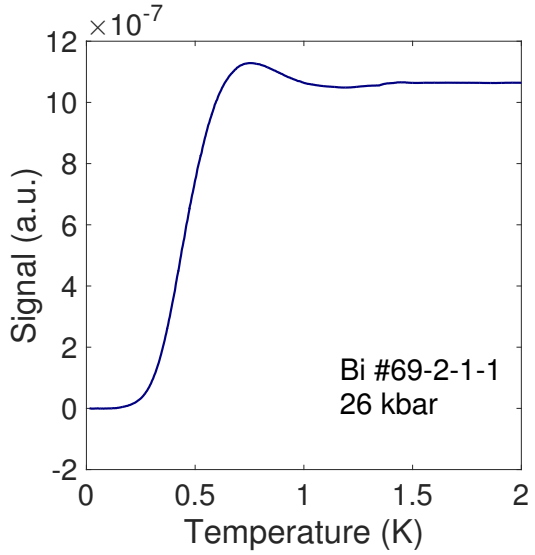

Figure 4.39: Resistivity of Bi at 26 kbar, down to 17 mK. As seen previously, there is a steep drop below ~ 1 K.

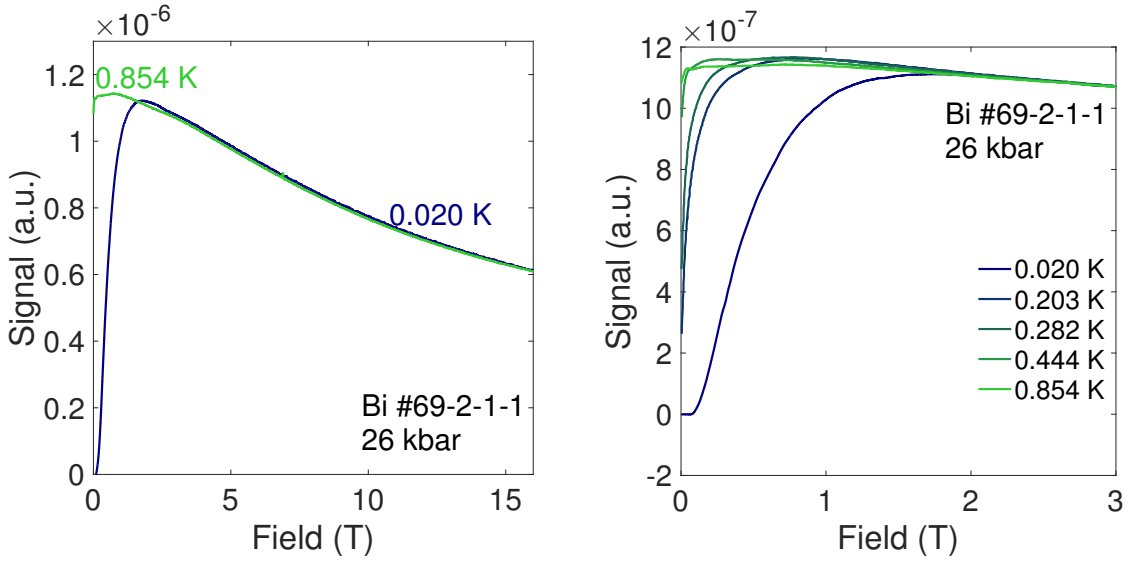

Figure 4.40: Resistivity of Bi at 26 kbar down to 20 mK, in fields up to 16 T (left), and details at lower fields (right).

4.6.2 Discussion

We have shown that, rather repeatably, there is a sharp downturn in the resistivity of bismuth at high pressures, reminiscent of a superconducting transition. This has not previously been reported in the literature. We see that at the lowest temperatures, an applied field of > 1 T is required to suppress the low-resistance state, and that the magnetoresistance then appears to be negative, and rather small. In this section, we consider a few plausible explanations for these observations, and suggest experiments to distinguish between the different possibilities.

Firstly, let us consider the most prosaic explanation for the negative magnetoresistance (MR): current jetting due to the enormous magnetoresistance anisotropy and a slight misalignment of the sample with the applied field. We believe this is almost certainly the explanation for the measurement here.

As noted by Collaudin, from semiclassical transport theory the transverse magnetoconductivity is $\sigma_{xx} \sim ne\mu/\left(1+(\mu B)^2\right)$, while the longitudinal magnetoconductivity is $\sigma_{zz} \sim ne\mu$, where $\mu = e\tau/m$ is the mobility; to a first approximation, the longitudinal MR should be constant in field [58]. The detailed dependence may be more complex, but the idea essentially holds: the transverse MR is field-dependent, and very large, because μ is large for bismuth, while the longitudinal MR is fairly small and not strongly field-dependent. The longitudinal MR has been measured by a number of authors [97, 122, 123], and they observe precisely this.

In such a case, the results of the measurement of a sample with a current axis slightly misaligned with the field axis will be complex. As the transverse MR is large, current will try to take the shortest path between the two current contacts of the four-wire measurement; the current density flowing past the voltage contacts may be smaller than expected, and will be strongly field-dependent. As the transverse MR rapidly increases with field, the current will become more and more tightly focused between the two current contacts, so the voltage measured across the voltage contacts could fall - even if the longitudinal MR is in fact positive. This phenomenon is termed current jetting. Precisely such behaviour in bismuth was investigated in some detail by Yoshida [122, 123]. It is also a significant complication in the recent study of the topological Weyl semimetals, where negative longitudinal MR is a key prediction of a Weyl material [124, 125]; great care is required in contact placement to avoid spurious observations of negative MR arising only from current jetting [126, 127]. It may be that current jetting also explains the negative MR observed in bismuth nanostructures [104, 128].

Current jetting requires a small misalignment between the current axis and the applied field, a large anisotropy between ρ_{xx} and ρ_{zz}, and voltage contacts off the axis between the current contacts; all these conditions apply for the sample Bi #69-2-1-1. We have tested for such behaviour on a bismuth sample cut from the #69 block at ambient pressure, and observe precisely this. A sample aligned with $I||B$ to within < 5 degrees exhibited a small negative longitudinal MR (which in fact unphysically passed through $\rho = 0$) when the voltage was measured across contacts on the opposite corner of the sample to the current contacts;. When the voltage was instead measured using contacts placed in a line with the current contacts, the longitudinal fractional MR was positive and moderately large ($\sim 1000\times$ at 2 K and 9T), but much smaller than the transverse MR ($\sim 100,000\times$ in the same conditions). Great care must therefore be taken to align bismuth samples for longitudinal MR measurements in a pressure cell, and voltage contacts should be placed directly between

current contacts to ensure the current jetting effect is minimised.

We now turn to separate possibilities for the "superconductivity". Clearly, samples that are cooled through the III-I or II-I structural transitions trap some of the high-pressure phase: this is evidenced in the fairly sharp transitions at $T_c \approx 4$ K (Bi-II) or $T_c \approx 7$ K (Bi-III). If these pockets are highly disordered, and form a percolative path through the sample, there could be an additional distribution of T_c focused at much lower temperature. The highly disordered nature, or small size, of such paths might be the cause of the suppression of T_c well below the bulk value, as well as the relatively large "critical field" required to destroy superconductivity at the lowest temperature, of about ~ 1.6 T.

As always with bismuth, similar physics has been observed previously in a different context: the insulator-superconductor transition that occurs as a function of film thickness in ultra-thin amorphous bismuth films deposited at low temperatures, or apparent superconductivity in ultra-thin bismuth nanowires [129]. In the context of thin films, very careful measurements as a function of film thickness have found that, over a thickness range of a few angstroms centred around 9 Å, such bismuth thin films are superconducting: thicker films have a $T_c \approx 6.1$ K, similar to that of bulk amorphous bismuth, but the T_c can be suppressed as low as 0.2 K as the thickness is reduced (there is then an abrupt change from superconducting to insulating behaviour at still lower thicknesses) [130, 131, 132]. The critical field of such films is also quite variable, but is $\sim 1-2$ T. However, the sheet resistivity of such films is extremely large ($\sim 10,000\ \Omega$), and the negative MR is ~ 50 %, so we would not expect to observe such an effect here: the majority Bi-I phase should have a resistance of well below 1 Ω.

Bismuth nanowires, with diameters of $20-72$ nm, have also been seen to exhibit superconductivity: the critical temperature $T_c \approx 1.3$ K and the upper critical field $H_{c2} \approx 4$ T [129]. Both these values are in reasonable agreement with the resistivity observed here. The resistivities of such nanowires are $\sim 600-800$ μΩ cm- rather comparable to the resistivity of the Bi #69-2-1-1 at 2 K measured here.

Given that alternative high-pressure structures clearly remain when bismuth is cooled through a structural transition, it could be plausible that some sort of amorphous filament forms a percolative path through the sample. It appears to be the case that bismuth is prone to forming superconducting states - in fact, it appears to be only the Bi-I structure that is *not* superconducting above 1 K, with all three high-pressure phases, amorphous bismuth, bismuth thin films, and bismuth nanowires all exhibiting superconductivity. The normal-state resistivity of such a filament would presumably be orders of magnitude higher than the majority Bi-I, so we would not observe any effects of this filament except at the very lowest temperatures, where its vanishing resistivity would eventually short-circuit the bulk, and cause the whole sample's resistivity to drop to zero. This explanation reasonably explains the apparent vanishing of the resistivity at zero temperature, as well as the field scale required to return to the normal-state resistivity. It is not wholly satisfying, as it would seem a little reliant on fine-tuning. In the case of a film, being merely a few angstroms too thick would give superconductivity at 6 K (which is never observed); in the case of a nanowire, it requires a percolative path through the entire sample, and it appears a little unclear how a nanowire could form that was isolated from the bulk - here, the "substrate" on which such a wire lives is also made of

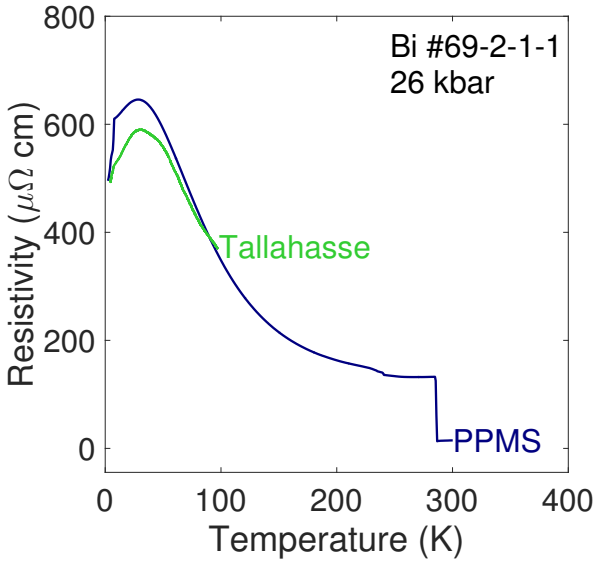

Figure 4.41: Resistivity of Bi #69-2-1-1 as measured on our PPMS, and in Tallahassee. The sharp drop at ~ 7 K corresponds to superconductivity in a trapped Bi-III minority phase; at lower temperatures the resistivity flattens again.

bismuth. Additionally, a careful examination of the critical field curve of such nanowires does not give very good agreement on the field scales we observe: for our data, at 0.2 K the transition is completely destroyed by 0.7 T of field, while the bismuth nanowires require a field of ~ 6 T at the same temperatures. It could also be interesting to consider the critical current density of such filaments - we typically apply $0.1 - 1$ mA of measurement current while observing such a transition, which for a filament with a diameter of a few nanometers would imply a gigantic current density.

One intriguing alternative hypothesis invokes the recent interest in surface states in bulk bismuth, which correspond to the carrier density of a bulk bismuth slab ~ 1 μm thick, as discussed in Section 4.1.6. At ambient pressures, such surface states would be almost irrelevant to transport; even our thinnest bulk samples have a thickness $\sim 80\times$ larger than the effective thickness of the surface states. However, recall that with pressure the bulk carrier density can be tuned continuously to zero (of course, this may also affect the surface carrier density; the details are not known). In the simplest interpretation, we would assume the surface states will start to contribute to transport when they have an equivalent carrier density to the bulk. If we assume the scattering length (rather than time) remains constant under pressure, implying that the low-temperature resistivity is inversely proportional to the carrier density, this corresponds to the requirement that, before we observe the surface states, we must increase the low-temperature resistivity by a factor equal to a sample's thickness in micrometres.

Sample Bi #69-2-1-1 has an ambient-pressure resistivity of 6 μΩ cm at 2 K and a thickness of 100 μm (we believe the RRR is rather low because contacts were made directly to a spark-cut rather than cleaved face). By the above criterion we would expect to notice a surface contribution when the low-temperature resistivity is ~ 600 μΩ cm (at this point the carrier density has, simplistically, fallen by a factor of $100\times$, so is now equal to the surface carrier density). Fig. 4.41 shows the resis-

tivity as measured on the PPMS, and in the rapid Tallahassee cooldown; it can be seen that this is precisely the value of the low-temperature resistivity at which saturation occurs. At lower temperatures, we would then have a semiconducting bulk in parallel with a metallic surface; the resistance would be expected to fall as T decreases. This is precisely what we observe in many of our resistivity measurements down to 2 K; perhaps we are seeing a continuation of this phenomenon when we measure down to the lowest temperatures. The transition would then not be a superconducting transition, but merely the conventional metallic resistivity of the surface states, dropping not to exactly zero but some small finite value corresponding to the residual resistance of the surface.

This idea is intriguing, but does not explain all the observations. The low-temperature collapse in $\rho(T)$ occurs quite abruptly, implying a superconducting transition, and emerges out of a nearly-constant resistivity which typically then exhibits another peak at temperatures of a few tens of kelvin. The temperature dependence of the surface resistivity would have to be rather complex to explain both phenomena.

4.7 Conclusions

In this section, we have presented results on a systematic study of the pressure dependence of $\rho(T)$ in bismuth. Much of the literature on the SMSC transition in bismuth has used the results of Balla and Brandt to frame the discussion [57]. We have greatly expanded on their results. Our work extends the existing data in three main ways. First, we have conducted a much more detailed pressure study, meaning the changing behaviour of $\rho(T)$ with pressure can be observed more clearly. Second, we have carefully investigated the reproduceability of these results, measuring samples in identical pressure conditions. Finally, we have for the first time attempted to marry our results to theory, using a simple model of the band overlap as a function of temperature and pressure, and a phenomenological form for the scattering rate, to calculate what *should* happen to $\rho(T)$ in bismuth as pressure is applied. We would draw the following main conclusions:

1. Pressure has a dramatic impact on the band structure of bismuth, which is clearly observed in the resistivity. At low pressures, the temperature dependence of the scattering rate dominates over the temperature dependence of the carrier density, and $\rho(T)$ climbs by $\sim 100\times$ from 2 to 300 K. At high pressures, this is not the case: the temperature dependence of the scattering rate becomes much less important than that of the carrier density, and $\rho(T)$ can instead *fall* by a factor of $\sim 1000\times$ from 2 to 300 K. At pressures of 20-25 kbar, the carrier density can be made exceptionally small by careful pressure tuning, and this could prove an interesting region for more detailed examination.

2. A fall in $\rho(T)$ is, in the context of semimetals, not evidence for a band gap: our calculations show that even with a finite positive ϵ_t, a resistivity reminiscent of that seen in semiconductors can be observed. Some previous authors have suggested that the resisitivity obeys an Arrhenius law $\ln \rho(T) \sim 1/T$ implying a positive band gap (i.e a negative ϵ_t) at pressures of only ~ 15 kbar [78]. We would suggest that from 0 to 25 kbar the temperature dependence of the resistivity can instead be described by our numerical model assuming a positive ϵ_t.

3. The pressure dependence of $\rho(T)$ is not perfectly reproduceable and varies from sample to sample. Later work that draws on the data of Balla and Brandt overlooks this fact. We have found that, even for samples cut from the same piece of bismuth, in the same pressure cell, the exact pressure dependence of $\rho(T)$ is a little variable. All samples show the same qualitative features, but the pressures at which these features occur vary. This is likely related to the crystallographic orientation of the samples with respect to the current. Given bismuth's propensity to form twins, this is an aspect which should be considered with great care in future experiments.

4. We do not find compelling evidence for the onset of novel phases just below $p = p_c$ arising from the ultra-low carrier density, such as Armitage's suggestion of an excitonic insulator [12]. Armitage's data shows an upturn in the scattering rate $\tau^{-1}(T)$ at low temperatures even at quite low pressures. This is not observed in any of our measurements. Similarly, the behaviour of $n(T)$ implied by the combination of our results and those of Armitage's is not physically reasonable: it corresponds to a much more complex temperature dependence of n than seems likely. We believe that, in contrast to the hypothesis of Armitage, the unusual shape of $\rho(T)$ in bismuth near 25 kbar can be explained almost entirely in terms of the temperature dependence of $n(T)$ for ultra-low-band-overlap semimetals.

5. The cause of a peak in $\rho(T)$ remains uncertain. This is a quite reproduceable feature that appears at pressures of $\sim 15 - 20$ kbar in all our samples. Simple explanations could be either a sudden enhancement in the scattering rate or a drop in the carrier density. The latter seems unlikely, although it could arise if the lattice parameters obey a more complex and non-monotonic relationship than was previously thought under pressure; this could be investigated with high-pressure x-ray diffraction. The former seems a more likely explanation, though a mechanism is currently lacking. It seems unlikely it is related to conventional scattering mechanisms. The conventional Debye-Gruneisen form for $\rho(T)$ would have the phonon scattering rate cross from $\rho \sim T^5$ to $\rho \sim T$ at a reduced Debye temperature which is in bismuth ~ 50 K, around the temperature of the peak. However, the Debye-Gruneisen scattering remains monotonically increasing with temperature, so it seems unlikely to lead to a peak then fall in $\rho(T)$. One possibility is interesting: second-order interactions between the carrier density and resistivity could lead to such behaviour. For example, at low temperature the lower carrier density will less effectively screen electrons, and this could enhance electron-electron or electron-phonon scattering. As the temperature increases, the carrier density rises, and this could also push the scattering rate down (until a carrier density is reached at which the electrons are effectively screened). The interplay between such effects could lead to such a peak. An alternative explanation could invoke the existence of metallic surface states, whose existence is now well-established in ambient-pressure bismuth.

6. The low-temperature behaviour at high pressure has not been previously investigated. We find that there is a sharp downturn in $\rho(T)$ at temperatures below 2 K and pressures above 20 kbar. This is in sharp contrast to what would be observed if bismuth at these pressures truly was semiconducting.

4.8 Outlook

From the above results, it will hopefully be apparent that the hypothesised SMSC transition in high-pressure bismuth is both more complex and more interesting that might have previously been thought. We have shown that many aspects of the resistivity up to 25 kbar can be explained in terms of a simple phenomenogical model considering the interplay between $n(T)$ and $\tau^{-1}(T)$. It may not be necessary to invoke exciting alternative suggestions such as the intervention of excitonic insulator formation to explain our results. However, several aspects remain unexplained: in particular, the low-temperature behaviour of $\rho(T)$ at the highest pressures.

A more accurate knowledge of the carrier density under pressure is required, to disentangle n from τ^{-1}. There are two routes to this. Firstly, quantum oscillation measurements under pressure would provide an accurate guide to n. This should in principle be straightforward for bismuth, but there are two difficulties. Firstly, the samples must of course not be twinned. Work is ongoing to conduct such measurements on high-quality non-twinned single-crystal samples. Secondly, and more problematically, the frequency of oscillations $F \sim n^{2/3}$, assuming the Fermi surface shrinks isotropically with pressure. Thus, even at moderate pressures, when n becomes exceedingly small, the frequency becomes tiny, and the period is therefore enormous - that is, only a very small number of oscillations will be seen in fields up to 9 T. It may therefore prove impossible to accurately estimate F from resisistivity $\rho(B)$ in experimentally-measurable fields. Measurements at very low fields (≤ 0.5 T) typically suffer from a negligably small quantum oscillation amplitude; a carefully-designed low-field measurement setup could overcome this issue. In addition, it would be desirable (although not essential) to accurately align the field along the sample's trigonal axis, and this is not straightforward inside a pressure cell. An alternative approach to obtain n would be Hall effect measurements under pressure. Measuring the Hall effect in bismuth is non-trivial, because the enormous magnetoresistance $\rho_{xx}(B)$ typically overwhelms the Hall resistivity $\rho_{xy}(B)$ if contacts are even slightly misaligned. However, this should be possible, perhaps using a five-wire nulling technique to cancel the longitudinal contribution, followed by careful antisymmetrisation of the resulting data. With modern piston cylinder cell techniques, such a measurement could be done in parallel with quantum oscillation measurements as well as observation of $\rho(T)$.

One aspect to be wary of when trying to accurately determine ρ in zero field, and therefore estimate the carrier density, is the very large magnetoresistance of bismuth. A field of only ~ 1 mT can change the resistivity by 10 % or more (depending on the quality of the sample and its alignment with the field), and many superconducting magnets can trap flux to produce remanent fields of this size even when the nominal applied field claims to be zero. The true zero-field state is then obtained only by applying a small compensating field B_0 to offset any remanent field in the magnet. To evade this issue, the low-temperature resistivity should be determined by very slowly sweeping B at low field and fitting a parabola; we would recommend the use of this method at every pressure point. We would note that any very careful fits to $\rho(T)$ at $B = 0$ will also suffer from this issue: in particular, the error in the experimentally-measured resistivity arising from the remanent field will change with temperature, as the size of the magnetoresistance changes, and these errors are not necessarily small. Circumvention of this problem would require the careful shielding of the sample from remanent fields, and this may not be experimentally trivial for a pressure cell. An alternative

approach would be to take careful low-field B sweeps at a number of closely-spaced temperatures to obtain a set of correction factors for the true zero-field resistivity, before conducting temperature sweeps.

Instead of trying to find n, it could also prove insightful if more accurate measurements of τ^{-1} can be obtained. The IR conductivity results of Armitage are obtained by extrapolation to low frequency to obtain the Drude (zero-frequency) scattering rate [12]. Measurements of the microwave conductivity might allow a more accurate determination of the Drude rate. This could also, in principle, be obtained from the magnetoresistance: the expression for the two-band magnetoresistance could be fit to the data to extract τ at each temperature. In reality this may prove difficult, as for both bands the scattering rate is in fact a tensor (and so is the effective mass), so very accurately-aligned samples would be required for accurate results. The work of Collaudin *et al.* at zero pressure has laid the groundwork [58]. They present an approach for doing such fits to angular-resolved magnetoresistance measurements, and if this aproach could be extended to high pressures, it could prove an effective method. This would rely on a pressure cell that can be rotated in a cryostat; a miniature anvil cell is likely more suited for such a task, though that greatly complicates the preparation of samples. This would also allow an investigation into the apparent anisotropy between the electron pockets in bismuth at low temperatures. As observed by Collaudin, this anisotropy develops at low temperature or high field. If it is an effect related in some sense to the quantum limit, where all electrons are in the lowest Landau level, then in high-pressure bismuth one would expect the field scales involved to be significantly suppressed.

An explanation is currently lacking for the flattening of the resistivity at temperatures of ~ 2 K above around 20 kbar. One intriguing possibility is that this is the direct observation of surface states. Similar behaviour is observed in the topological insulator SmB_6, ascribed to the conductivity of the metallic surface, even though the bulk is insulating [121]. There is extensive recent literature on highly-metallic surface states in bismuth, and some recent evidence suggest these are topological in character. At ambient pressure, these states would not be observed by conventional bulk probes, because the bulk carrier density of a typical sample is many orders of magnitude higher than that of the surface. At high pressures this may longer be true.

Finally, there is the previously unobserved high-pressure low-temperature state. It is unclear if this is superconductivity, or an intrinsic property of Bi-I in the ultra-low-carrier-density region. There is one relatively straightforward approach to discriminate between hypotheses involving superconductivity of minority phase and other alternatives. Resistivity measurements should be made at low temperature at ~ 20 kbar, on a sample that has never been above 25 kbar, and therefore has not trapped minority phases. It is difficult to see how such a sample could contain filamentary amorphous inclusions (if it did, we would expect to observe this when measuring the sample at ambient pressure). Therefore, if the superconductivity arises from minority phases such a sample should *not* show any downturn below 1 K. Any downturn observed in the resistivity of such a sample could therefore be convincingly ascribed to the intrinsic behaviour of bismuth, rather than some complication arising from minority structural inclusions. If no such downturn was observed, a logical extension would then be to measure at 25 kbar, thereby transitioning out of the ambient-pressure structure at room temperature. This would presumably yield the appearance a downturn

at low temperatures, which must then be attributed to the formation of a superconducting impurity phase.

An alternative, although perhaps more challenging, approach to shed useful light on the impurity phases would be high-pressure SQUID magnetometry down to low temperatures. For samples cooled from pressures above 25 kbar, this could provide a useful insight into the volume fraction of the minority phases - presumably, a Meissner superconducting jump would occur at either 7 or 4 K, with a volume fraction much less than 100 %. If practical, measurements at low temperatures could then investigate the superconducting transition below 1 K. However, if this arises from filamentary superconductivity, we might expect that no visible superconducting signal would appear, as the signal would be far too small.

5 Bi-III

Above a pressure of 27 kbar, bismuth converts into a phase, Bi-III, exhibiting superconductivity at 7 K. Very few of the properties of this high-pressure phase are known.

Recently, the structure was determined to be an incommensurate host-guest lattice, comprised of two distinct unit cells which interpenetrate but are not mutually periodic. Such structures are (surprisingly, given their complexity) quite common among elements at high pressure. The incommensurate structure is theoretically predicted to give rise to a very unusual phonon spectrum, possessing an additional acoustic mode at very low frequencies arising from the sliding of one structure through the other, a process which has almost no energy cost. This phonon mode should remain at low energies over an extended region of the Brillouin zone, and might therefore be expected to dramatically enhance electron-phonon coupling, perhaps providing an explanation for the rather high superconducting T_c.

Bi-III is the only incommensurate host-guest phase accessible by highly hydrostatic piston cylinder cell measurements currently known. We have conducted a detailed investigation of the resistivity up to 31.4 kbar. We have additionally measured the DC magnetisation using moissanite anvil cell SQUID magnetometry up to 100 kbar. We find that Bi-III is a type II superconductor with an exceptionally high critical field of $H_{c2} \approx 2.3$ *T - to our knowledge the highest reported among the elements. The critical fields, and the anomalous behaviour of the resistivity, suggest strong electron-phonon coupling, a low Debye temperature and strong phonon anharmonicity, all features arising naturally from the unusual phonon spectrum. Ab initio calculations of the phonon spectrum confirm the existence of the low-energy mode. These results are presumably applicable to many other incommensurate host-guest elements.*

5.1 Literature review

5.1.1 Resolution of the structure of Bi-III

At a pressure above $p \approx 27$ kbar, bismuth converts into a phase termed Bi-III [133, 134]. The details of the structure have long eluded refinement; it has variously been indexed as tetragonal and orthohombic [13]. In addition, the physical properties are largely unknown. Bi-III has long been known to be a superconductor [135, 57, 136, 137], with $T_c \approx 7$ K, but little else about it has been measured.

The crystal structure was finally resolved only in 2000 [13]. Bi-III was indexed as an incommensurate host-guest lattice. It consists of two interpenetrating structures, with "guest" atoms forming chains within cylindrical cavities in the "host" lattice. While in the *ab* plane, the unit cells of guest and host match, in the *c*-direction they do not, and the ratio of the *c*-axis lattice parameters is incommensurate: $c_H/c_G = 1.309$. This gives Bi-III the rather surprising property that the crystallographic unit cell is infinitely large. This structure is rather unexpected in an element - it seems unclear how there can be two very different atomic environments, each occupied by atoms of the same type. In fact, a number of elements form incommensurate host-guest lattices, from the alkali earth metals such as barium to the other Group V semimetals such as Sb and As [7].

Bismuth is of particular interest because the pressure at which the host-guest structure forms is exceptionally low in comparison to other elements; 27 kbar is a pressure regime accessible by

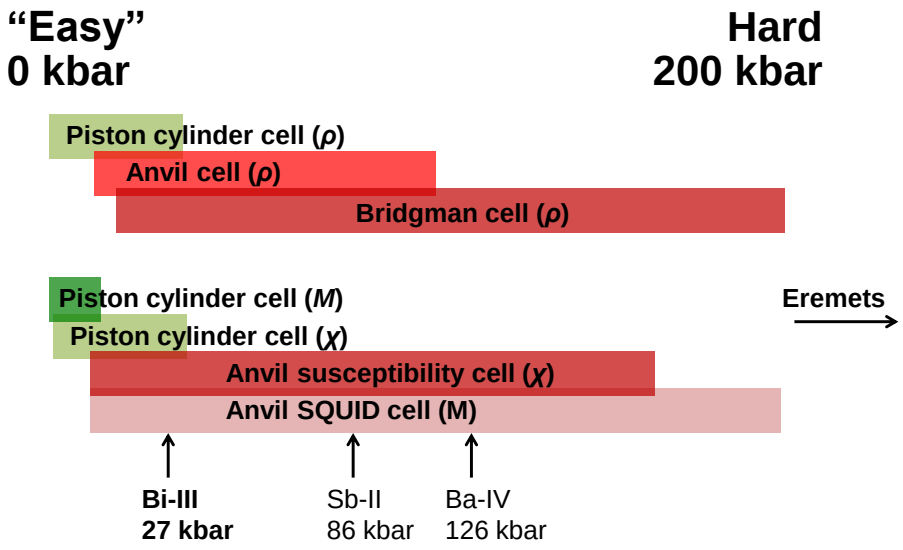

Figure 5.1: Accessible pressure regimes of various high-pressure techniques, and the unusually low pressures required to obtain Bi-III compared to other incommensurate host-guest materials.

piston cylinder cells, allowing relatively straightforward access to highly hydrostatic measurement conditions. For most other host-guest structures the pressures required are at least three times higher, which often precludes a detailed investigation of the physical properties - see the schematic in Fig. 5.1. We present here a detailed investigation of the resistivity and magnetisation of superconducting Bi-III, which we believe is the first comprehensive set of measurements performed for an incommensurate host-guest element.

5.1.2 Bi-III as an incommensurate host-guest lattice

The structure consists of a body-centred tetragonal host cell (space group *I4/mcm*), with a body-centred tetragonal guest cell filling the cavities (space group *I4/mmm*) - see Fig. 5.2. Lattice parameters are given in Table 6. At 68 kbar, the host unit cell volume is 311 Å^3 and contains 10.620 atoms (a value which changes little across the phase); the cell volume has fallen to $\sim$ 81 % of its ambient-pressure value. The most recent structural measurements indicate the phase is stable at room temperature from 27 to 77 kbar, although the existence of further high-pressure phases is a matter of some debate, as described below.

Fully resolving the details of the structure is a complex task. Fig. 5.3 shows a diffraction image of a single crystal sample at 45 kbar. On first crossing the phase boundary, the diffraction pattern is highly textured, indicating the formation of a polycrystal. A Bi-III single crystal can be obtained by taking the sample to pressures above 100 kbar, then reducing pressure slowly. The structure remains

Name	Symbol	Value
Host & guest a-parameter	$a_{H,G}$	8.5182 Å
Host c-parameter	c_H	4.1642 Å
Guest c-parameter	c_G	3.1800 Å
Host unit cell volume	V_H	302.15 Å^3
Lattice parameter ratio	c_H/c_G	1.310
Atoms in host unit cell	$n_{Bi/u.c.}$	10.620

Table 6: Lattice parameters of Bi-III at 68 kbar[13].

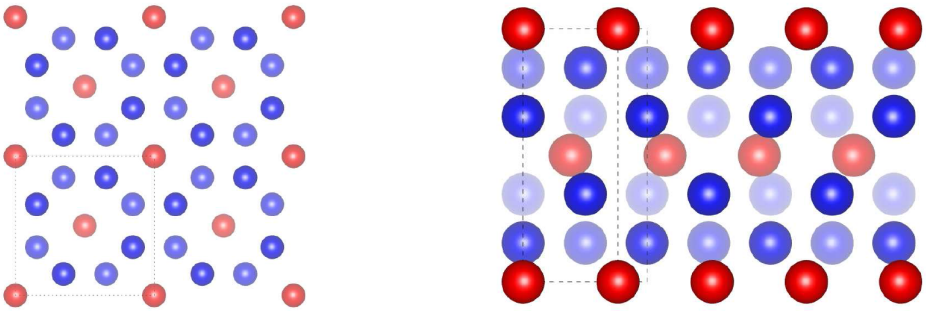

Figure 5.2: Structure of Bi-III. Left: looking down the c-axis at the a-b plane. Right: looking down the b-axis at the a-c plane. Dashed lines show the unit cells for the host lattice (blue atoms) and guest lattice (red atoms). In the a-b plane, these are commensurate (there is a single unit cell), but in the c-direction, the two unit cells do not match up.

relatively unchanged throughout the Bi-III stability region. In particular, the ratio c_H/c_G is almost constant across the whole region, and never approaches a commensurate value.

As with many other high-pressure incommensurate host-guest elements (on which more later), the Bi-III structure exhibits additional complexities. There are significant modulations of both host and guest atoms away from their ideal positions [138]. The atoms in the guest chains are modulated along the *c*-direction, showing a tendency to pair. The size of the modulations is quite significant - up to 4 % of the host unit cell lattice parameter. The main result is that the intrapair Bi-Bi spacing is reduced - to as low as 3.08 Å at 55 kbar, comparable to the value for Bi-I [138] - but the interpair spacing rises as high as 3.31 Å. In the unmodulated structure the spacing is 3.195 Å.

The displacement of the host atoms is very much smaller but far more complicated, being up to 0.4 % of the lattice parameter, but occuring in all three dimensions. Host atoms are most significantly displaced in the *ab* plane, leading to distortions in the size of the "squares" of host atoms that surround the guest chains, and in the square's orientation. In the unmodulated structure, the closest approach for host-guest atoms is 3.24 Å, but this falls to 3.20 Å when modulations are included. The minimum host-host distance also falls from 3.14 Å to 3.12 Å.

If we treated the two lattices as separate, non-interacting structures, it is hard to see how the guest lattice would be stable (the interchain spacing is as high as 5 Å), yet Bi-III is stable up to 450 K [138]. DFT calculations suggest the same tendency to pairing [71]. One plausible scenario is that the distortions in the host are a result of indirect chain-chain interactions, which help to stabilise

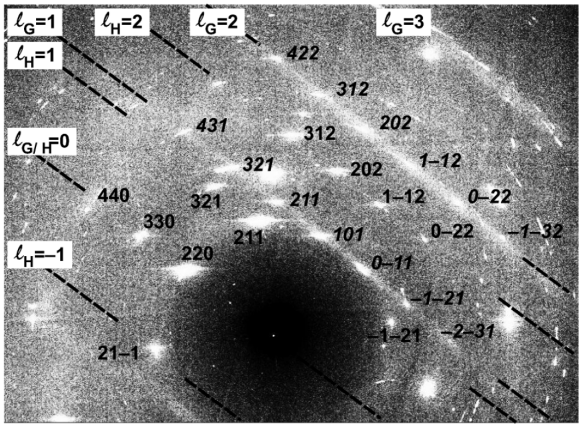

Figure 5.3: X-ray diffraction image for a single crystal of Bi-III, from [138]. The pattern is complex and textured, with the lines of diffuse scattering arising from the guest layers.

the guest structure [138].

5.1.3 Uncertainty about additional high-pressure phases

The full details of the high-pressure phase diagram of bismuth remain unresolved even now. It is unclear whether Bi-II and Bi-III are thermodynamically stable at low temperatures, and it is uncertain whether the Bi-III phase extends all the way to 77 kbar, or if further transitions occur. Further confusion ensues as different authors adopt different numerals for their proposed phases. We therefore instead term the phase that exists above 77 kbar at room temperature bcc Bi.

The I-II, II-III and III-bcc transitions are well-established at room-temperature, occuring at 25, 27 and 77 kbar respectively. However, there are conflicting results about the behaviour at lower temperatures and the presence of additional phases.

Some evidence suggests that, while Bi-III forms at 27 kbar at room temperature, the II-III (or perhaps I-III...) phase boundary reaches 0 K at pressures of at least 30 kbar. Phase diagrams in support of this have been given by a number of authors [139, 140, 141, 142, 143, 144]. The Bi-II phase likely extends down to only 200 K, at which point there may be a I-II-III triple point [142, 144], or there may not [143]. However, the superconducting Bi-III phase has been observed at low temperature at pressures of 27 kbar (by us and by many others). Several authors have also reported superconductivity in Bi-II at pressures of ~ 25 kbar, with $T_c \approx 4$ K [136, 145, 137]. It therefore seems likely that Bi-II and Bi-III are metastable to low temperatures. In Fig. 5.4 we show the most recent phase diagram, obtained by Homan.

There is also some evidence that additional phases may exist within the stability field of Bi-III. These "transitions" occur at around 44, 53 and 65 kbar [133, 146, 144, 145, 137, 13]. For example, some authors have reported a jump in the volume or resistivity around 45 kbar [133, 139, 146, 145, 144], In constrast, a number of authors have measured $\rho(p)$ throughout the Bi-III phase, and they find it is continuous [140].

Lotter and Witting tracked $T_c(p)$ up to 100 kbar [137]. They observe that T_c remains flat from

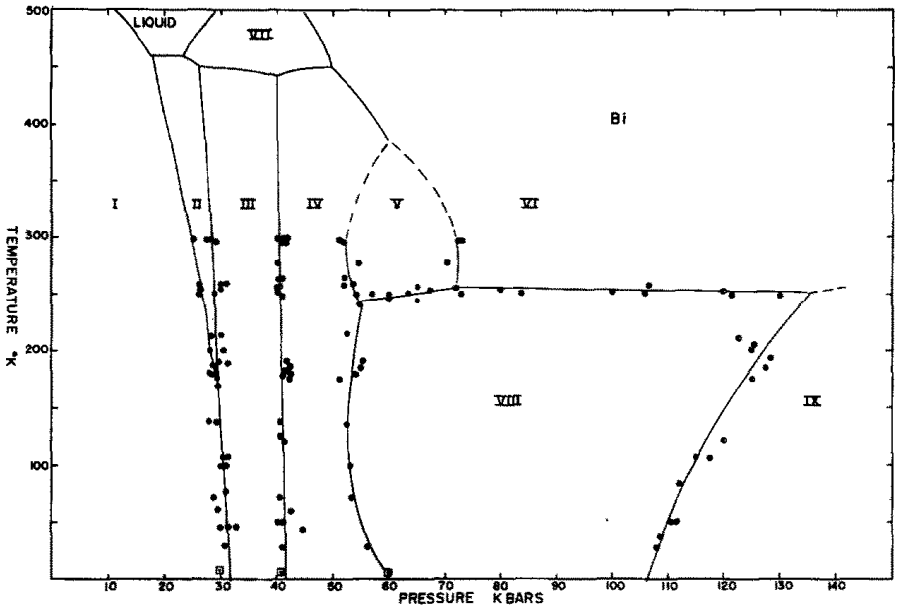

Figure 5.4: High-pressure phase diagram of bismuth, taken from [144]. As outlined in the text, there remain disputes about the details of the I-II and II-III transitions (particularly at low temperature), and the existence of the phases marked IV, V and VIII.

30 to 52 kbar, then exhibits a clear kink, but not a discontinuous change (while such discontinuous jumps are clearly observed in $T_c(p)$ across the II-III and III-V phase boundaries). Firstly, it is rather surprising that T_c should be pressure-independent, particularly as it is strongly pressure-dependent in the other observed phases. Secondly, it is unclear what mechanism would lead to a change in dT_c/dp while T_c remained continuous. They suggest that this may arise from a Lifshitz transition which modifies $N(E_F)$.

Recent DFT calculations qualitatively support the I-II-III-bcc structural phase transitions, though the exact values of the zero-temperature transition pressures differ from experiment by up to a factor of 2. Hausserman *et al.* suggest that, from their calculations (which quite accurately reproduce pressure-induced phase transitions in As), the Bi-III structure should form at 35 kbar at low temperature, and further that the transition to bcc Bi occurs at 155 kbar, significantly higher than the 77 kbar experimental value [71]. A suggested explanation is that the III-bcc phase transition line may therefore be strongly temperature-dependent. Very recently, an investigation of the properties of Bi up to high pressures conducted in anvil cells observed similar superconducting behaviour to that described above [147]. These results appeared to suffer from phase coexistence at pressures near the II-III boundary, where no full Bi-III superconducting transition is observed at 7 K, and inspection of the behaviour of ρ in field suggests there may also be Bi-I present. This likely arises from pressure inhomogeneity inside the anvil cell. Our later detailed measurements of the resistivity show a full, sharp superconducting transition at $T_c = 7.05 \pm 0.05$ K.

Material	Pressure required (kbar)	Superconducting T_c (K)	References
Bi-III	27	7.05	This work
Ba-IV	140	5	[151]
Sb-II	88	3.6	[152]
$Hg_{3-\delta}AsF_6$	Ambient	4†	[153]

Table 7: Superconductivity in host-guest phases. †There is some uncertainty in the literature about whether this is bulk or surface superconductivity, see [153].

5.1.4 Other incommensurate host-guest elements and compounds

Bismuth is not alone as an incommensurate host-guest element. Many other elements form such complex structures under pressure. The first of these to be discovered was found in barium at pressures above 120 kbar, in the Ba-IV phase [148]. The structure is extremely close to that of Bi-III discussed above, with the body-centred tetragonal host lattice (I) possessing open channels where the guest atoms sit.

There are many further layers of complexity in Ba-IV. Firstly, there are two distinct guest lattices, one C-face-centred tetragonal (C) and one C-face-centred monoclinic (M). The monoclinic cell is essentially a small distortion of the tetragonal cell, and both look identical when projected down the *c*-axis. Again, the host and guest cells match in the ab plane, but are incommensurate in the c-direction. The ratio $c_I/c_{M,C} = 1.388$, and there are 10.776 atoms in one host unit cell at 121 kbar. The fraction of atoms in the C or M cell appears to vary dramatically from sample to sample.

Initial studies of the Ba-IV structure identified at least three related phases, Ba-IVa-c. The latter structure was investigated in great detail using a computational random search, as direct fits had not been successful for so complex a structure [149]. It was found that the structure is in fact commensurate, with a unit cell 72 times the volume of the basic host cell, and containing 768 atoms. There is long-range order in the host structure, but some short-range disorder and randomness in the guest.

Other Group V semimetals also exhibit the host-guest structure of Bi-III [13]. It is seen in the Sb-II structure forming above 86 kbar, (essentially identical to Bi-III), and in the equivalent As-III phase. Bi-III and Sb-II both exhibit incommensurate modulations, and in almost all respects appear to have strong similarities [138].

A picture is slowly emerging of the incommensurate host-guest structure as a generic property of high-pressure elements: such structures are also seen in Sr, Rb, K and Sc, in addition to Bi, As, Sb and Ba [138]. A review of the high-pressure host-guest structures is provided by McMahon and Nelmes [7].

Bi-III is remarkable among the host-guest elements due to the comparatively low pressures required for its formation: most other known host-guest phases require pressures in excess of 80 kbar, where high-quality measurements are difficult. The literature contains reports of the resistivity of Ba-IV under pressure, but few other elements have been measured in detail [150]. Several such incommensurate host-guest phases are known to be superconducting - see Table 7.

The prototypical incommensurate host-guest chain compound is $Hg_{3-\delta}AsF_6$, with $\delta \approx 0.2$. This

compound consists of a tetragonal lattice of AsF_6 tetrahedra, intersected by Hg chains with a period incommensurate with the tetragonal lattice [154, 155]. This intriguing material is metallic and superconducting ($T_c \approx 4$ K), though there is some debate about the nature of the superconductivity with some authors suggesting the superconductivity is a mercury surface layer (see [153] and references therein).

5.1.5 Calculations on incommensurate host-guest elements

Incommensurate host-guest lattices provide a unique challenge to conventional approaches. The materials lack a unit cell, and it is unclear how to generalise concepts such as the Fermi surface to a system where the Brillouin zone is infinitesimal. Ab initio approaches must therefore proceed using approximant unit cells [156, 157, 158, 71].

DFT calculations have been carried out on Ba-IV using the structure pseudo-Ba-IV, which contains 8 host atoms and three guest atoms in a commensurate cell, with $c_H/c_G = 1.5$ (the experimental value is 1.388) [156]. Calculations on the Group V semimetals noted that the ratio $c_H/c_G = 1.309$ for Bi-III and Sb-II is close to $4/3$, thus a supercell consisting of four guest and three host cells should be a reasonable model [71]. These calculations reproduced the experimental phase boundaries of the Bi-III and Sb-II phases, suggesting such an approximation is valid. In addition, we have performed calculations on Bi-III using an In_5Bi_3 approximant, discussed below. It was noted by McMahon that In_5Bi_3 possesses many structural similarities to Bi-III [13], being essentially a commensurate form ($c_H/c_G = 4/3$) with the guest lattice as a C-face-centred unit cell rather than a body-centred one.

DFT calculations on Ba-IV yielded an interesting result. The host atoms were found to possess a significantly different electronic structure to the guest atoms, with guest atoms being significantly more d-like than host atoms. Electrons are therefore more localised on the host atoms. Thus, Ba-IV is a curious example of "*an intermetallic compound, in which both components are actually the same element*" [156]. However, calculations on the Group V semimetals found that was not the case for Bi-III and Ba-IV, where both host and guest atoms have almost identical electronic structures [71, 149].

A detailed ab initio investigation of the Group V semimetals has been undertaken by Hausserman *et al.* [71]. They suggest that the Bi-III structure occupies an intermediate position between the nearly simple-cubic Bi-I phase (with an effective atomic coordination of six) and the bcc- Bi phase (atomic coordination of 11.3). Bi-III would have an effective coordination of nine, but no simple structure exists which such a coordination; the structure that forms must therefore be highly complex. The DFT calculations accurately reproduce the modulations of the guest chains (even in the approximant commensurate structure), and attribute these to Bi-Bi covalent bonding.

The pressure dependence of the electronic structure of Bi was also considered by Hausserman *et al.* At ambient pressure, the Bi p-bands exhibit significant bonding-antibonding splitting, and the Fermi level lies between them; ambient-pressure Bi-I is therefore almost (but not quite) semiconducting. Applied pressure broadens the p-bands: in the Bi-II and Bi-III phases the Fermi level lies in a shallow valley between the p-bands, and in bcc Bi the valley has disappeared completely. It should be remarked that this cannot be the full story - merely considering p-band broadening would im-

ply Bi-I should become more metallic under pressure, but in fact the reverse is true. These smooth changes in the DOS imply there is not a valence change in Bi, in stark contrast to the alkaline earth metals such as Ba, where electrons are shifted from s- to d-bands under applied pressure.

The overall evolution of Bi structures under pressure can be understood - as with everything else in physics - in terms of balancing competing energy terms [71]. The band energy E_{band} is reduced by open-packed structures with tightly-bonded Bi atoms, such as the Bi-I structure. However, the competing Madelung energy E_{Mad}, which essentially represents Coulomb repulsion between atoms, prefers high-symmetry densely-packed structures (such as bcc Bi). Under applied pressure, the significance of E_{Mad} increases, thereby favouring transitions to low-volume, high-symmetry states. The complex Bi-III phase is a stepping stone along this path, where the interplay between the competing energy terms, combined with a preference for ninefold coordination and a desire for Bi-Bi covalently-bonded pairs, favours the formation of complex structures.

Further insight into the electronic explanations for the formation of host-guest structures was given by Loa *et al.*, looking at the Ba-IVc structure [149]. Broadly the argument is similar - at the pressures where Ba-IV forms, E_{band} is reduced for the host-guest structures with respect to simpler close-packed structures, thus the host-guest structure actually forms out of a more densely-packed structure. However, there are a number of other complexities, in particular that for barium the s-d transfer of electron density also plays a significant role, unlike in bismuth.

5.1.6 Low-energy phonon modes arising from incommensurate chains

One of the more striking predictions of the properties of incommensurate materials concerns their phonon spectrum. Because the c-axis lattice parameters are incommensurate, in an infinite crystal every possible realisation of a guest atom position along the z-direction with respect to a given host atom must be realised[156]. Equivalently, there should be no energy cost in sliding the chain of guest atoms with respect to the host. This is confirmed by ab initio calculations, which predicted the existence of a corresponding zero frequency phonon mode, or phason[156]. At $q = 0$ (i.e. infinite wavelength), in addition to the three conventional acoustic modes (displacements of the whole crystal in the three Cartesian directions), the phason mode is an additional fourth acoustic mode, corresponding to the motion of guest chains with respect to the host lattice.

The existence of such a mode was first theorised for incommensurate $Hg_{3-\delta}AsF_6$ [159]; precisely such behaviour was later observed by neutron diffraction [160, 155]. Recently, similar results have been observed for another incommensurate chain compound $Sr_{14}Cu_{23}O_{41}$, as shown in Fig. 5.5, though this is insulating so the coupling between electrons and phonons is irrelevant at low temperatures.

Of particular interest is the case in which the phason mode lies at low energy throughout an extended region of $q-$space. In this case, the electron-phonon coupling λ will be strongly enhanced. Recall from Section 2.3.4:

$$\lambda = 2 \int \alpha^2 F(\omega)\, \omega^{-1} d\omega. \tag{5.1}$$

where $\alpha^2 F$ is the phonon spectral function at a frequency ω. In general, a phonon mode with low frequency only at the Brillouin zone centre Γ will, in three dimensions, have a small density of states

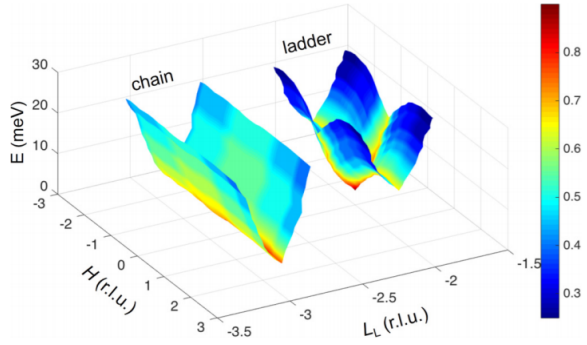

Figure 5.5: Phonon dispersion of $Sr_{14}Cu_{23}O_{41}$ obtained from inelastic neutron scattering, taken from [161]. The phonon modes corresponding to the chain are highly anisotropic, being strongly dispersive along the chain (L_L direction), but almost flat perpendicula to it (H direction) .

$F(\omega)$ near $\omega = 0$, from simple phase space arguments[9]. This is why the three normal acoustic modes do not lead to enormous electron-phonon coupling in all materials - they have a small ω only where the phase-space element is also small. However, if a phonon mode is highly anisotropic, and contrives to lie near $\omega = 0$ over a large region of the Brillouin zone, we would expect a significant weight in $F(\omega)$ at low ω, and therefore a significant increase in λ.

We suggest that precisely this situation is realised as a generic property of incommensurate host-guest elements. The phason mode has a strong dispersion among the $c-$direction (because intra-chain distances are short, so interactions are strong), but the dispersion perpendicular to the chain direction should be very flat (interchain distances are large, so chain-chain interactions are weak) - precisely the anisotropy required to enhance λ. The phason mode will therefore have low energy not only at Γ, but also at X and Y: oscillations corresponding to chains sliding throught the host with a phase difference of π between neighbouring chains will also be low-energy.

This could lead to strong-coupling superconductivity with a comparatively high T_c. It is interesting to note that many of the incommensurate host-guest materials are indeed superconductors with a rather high T_c - 5 K for Ba-IV, 7 K for Bi-III, and 4 K for Sb-II [162] - though others (Na, Rb, K) are not. That this is also the case for Bi-III is confirmed by ab initio calculations of the phonon spectrum, described in Section 5.3.7. The concept of a low-energy phonon mode giving rise to strong electron-phonon coupling will play a major role in this chapter.

In addition to enhancing λ, a shift in spectral weight to small ω in the phonon spectrum will reduce the characteristic phonon frequency. As noted by Allen, the relevant energy scale for superconductivity is the logarithmic phonon frequency [35, 17]:

$$\omega_{ln} = \exp\left(\frac{2}{\lambda}\int \alpha^2 F(\omega)\frac{\ln\omega}{\omega}d\omega\right). \tag{5.2}$$

The characteristic logarithmic phonon tempeature $\Theta_{ln} = \hbar\omega_{ln}/k_b$ will therefore be reduced by the existence of such a phason mode.

[9]Assuming phonon modes evenly-distributed in $k-$space, and a linear dispersion $\omega_k = ck$ with c the phonon velocity, the phonon density of states in three dimensions is $\sim \omega^2$, and thus contributes vanishing weight to λ in the limit $\omega \to 0$.

5.1.7 Assembling the pieces.

What might be the consequences of the low-energy phonon mode and the resulting large λ and small ω_{ln}? We suggest they are threefold. One might expect to see:

1. **Strong anharmonic phonon effects**: Significant spectral weight at low frequency will reduce ω_{ln}. This means that, at moderate temperatures $T \gtrsim \Theta_{ln}$ the atomic displacement will already be large, and the anharmonic contributions to the atomic potential will be more significant.

2. **A steep gradient to the low-temperature linear resistivity**: As explained in Sec. 2.3.4, in the linear region where $T > \Theta_{ln}$, the resistivity gradient $\rho' = d\rho/dT$ is set by the strength of the electron-phonon coupling λ (and the details of the band structure, through Ω_p). When λ is enhanced, we would expect a steep gradient and hence an unusually large ρ'. Because the characteristic phonon frequency is low, this linear region will begin at rather low temperatures.

3. **Strong coupling superconductivity**: According to the McMillan equation (Sec. 2.4.3), a high value of λ will tend to lead to superconductivity with a measurable T_c (assuming a sensible Coulomb potential μ^*, etc.). Of course, the low value of ω_{ln} will act to suppress T_c - McMillan's equation gives $T_c \sim \Theta_{ln} e^{-1}$ even for arbitarily large λ. Thus, one might expect to see superconductivity with a moderate transition temperature of order a few kelvin (since ω_{ln} is likely below 100 K), mediated by strong electron-phonon coupling.

We argue in the following sections that all these phenomena are indeed observed.

5.2 Experiment

5.2.1 Resistivity

We have measured the resistivity of Bi-III in a piston cylinder cell. Detailed low-temperature and high-field measurements have not previously been conducted on Bi-III. The resistivity drop across the superconducting transition has been observed previously [135, 57, 136, 137], and measurements in very low fields have been taken [163]. However, these measurements were typically taken in rather anhydrostatic conditions. Our piston cylinder cells provide a highly hydrostatic measurement environment (as evidenced by the sharpness of our superconducting transitions). We have greatly extended the knowledge of the resistive properties of Bi-III, with temperatures down to 220 mK and fields up to 9 T.

Two measurement runs were taken. The first was in cell run PCC1 with sample Bi #1, taking two pressure points at 26.7 and 28.4 kbar, using a 4:1 methanol:ethanol pressure medium. For the latter of these, we conducted a critical field study at temperatures down to 2 K. This sample is an offcut of the Bi twinned single crystal from Mateck, cut with the wire cutter, contacted with the spot welder using 25 um Au wire, with the contacts stabilised with DuPont 6838 epoxy cured at 160 C for 2 hours. The measurements on PCC1 were performed in collaboration with Konstantin Semeniuk.

A second (much more detailed) measurement was undertaken in PCC111, with sample Bi #10.11 and a pressure medium of Daphne 7373. Here, two pressure points were measured, the first at

31.4 ± 0.4 kbar - a record-breaking pressure for our piston cylinder cells - and the second at 26.7 ± 0.4 kbar. At 31.4 kbar, a very detailed critical field study was undertaken using both the PPMS and DMS, with measurements down to 220 mK. This sample is also from the Mateck crystal, contacted in an identical fashion.

Both rectangular samples have contacts placed on the corners. The small size (< 0.5 mm wide) and uncertainties in the contact placement mean that extraction of an absolute value for the resistivity is difficult. We therefore scale the measured voltage signal so that at ambient pressure it would agree with the literature value for Bi-I of 120 $\mu\Omega$ cm at room temperature. The pressure dependence of the ambient-temperature resistivity has been measured by a number of authors [39, 72]; the I-II transition is associated with a sharp drop in the resistivity by 80 % of its zero-pressure value; the transition to Bi-III returns the resistivity to around 50 % of its zero-pressure value.

5.2.2 Magnetisation

We have also measured the DC magnetisation of Bi-III using a moissanite anvil cell mounted in a SQUID magnetometer. Previous measurements of the magnetic properties of superconducting Bi-III have used AC susceptibility coils, and have not investigated the response to field [137]. By varying the applied field from 0.5 mT to 20 mT, we have obtained a critical field curve for the lower critical field B_{c1} of Bi-III.

Measurements were taken in two runs using different samples in a SQUID moissanite anvil cell (SMAC). The first run (SMAC16-3, on sample Bi #16-3) served as an exploratory study at comparatively low pressures. In the second run (SMAC16-7, on sample Bi #16-7) we measured a number of points from 25 kbar (where there was no superconducting signal, as expected) up to 100 kbar, well beyond the nominal 77 kbar upper limit of Bi-III stability. Both cells used glycerol as a pressure medium.

Samples for both cells were cleaved from the Mateck Bi single crystal with a scalpel. "Cleaving" implies a rather more controlled process than in fact occurs: obtaining a SMAC sample typically involves cutting into a piece of Bi on a glass slide, then investigating the slide under a microscope to find tiny pieces of a suitable size and shape. The $\sim 100\,\mu$m samples are much too small to reliably cut with a scalpel blade or wire saw. Bismuth poses a particular challenge because it is so soft: attempts to cut small pieces typically just bend the larger piece, and at this lengthscale bismuth tends to break into approximately cuboid pieces, when flat rectangles are desirable for the SMAC. However, with sufficient patience and much painstaking hunting through tiny fragments of bismuth, suitable samples can be found. The use of a focused ion beam to mill samples to a precise shape would allow accurate volume determination.

The tiny size and correspondingly tiny mass of the SMAC samples means that obtaining an absolute value for the magnetisation (in A m^{-1}) or the SI volume susceptibility is difficult. In particular, the ideal SMAC sample is a thin flat plate, because such a sample will fit neatly in the gasket hole without the risk of it touching the anvils, but such a sample has a large demagnetising factor [164], and this factor cannot accurately be corrected for - the usual assumption that the sample is an ellipsoid is obviously false. Here, we therefore present the data in units of volume magnetisation using the best estimate of the sample geometry (which has geometric errors of at least 20 %) without at-

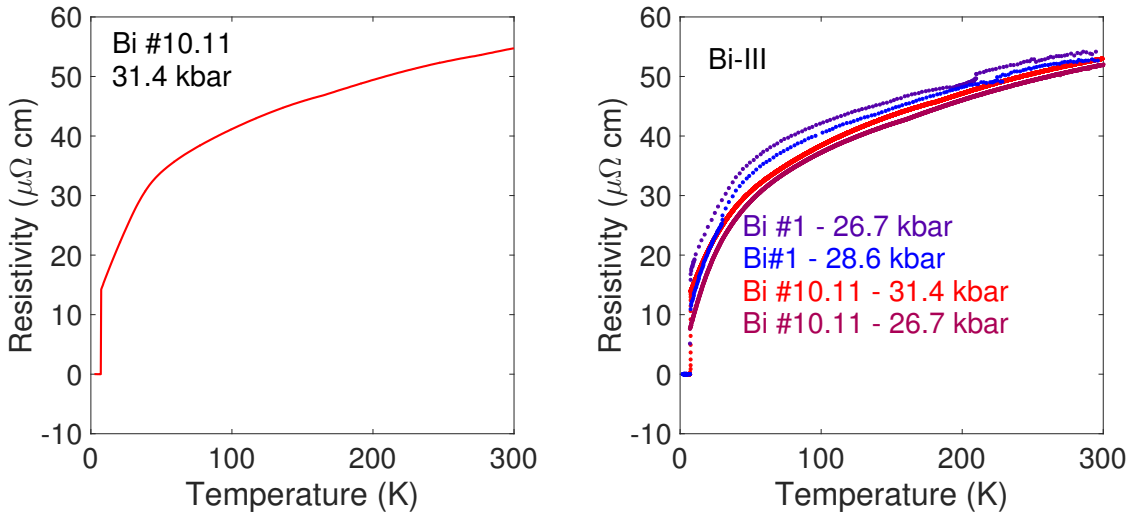

Figure 5.6: Left: resistivity $\rho(T)$ of Bi-III at 31.4 kbar as a function of temperature. Right: comparison of $\rho(T)$ for both samples at both measured pressures. The results for different measurements, even on different Bi samples, agre well.

tempting to correct for the demagnetising factor. Somewhat to our surprise, we found that this in fact gave sensible sizes for a susceptibility jump at T_c of $\chi \approx -1$, implying Bi-III is a bulk superconductor. Any slight excesses over this value likely arise from the demagnetising factor.

5.3 Results and analysis

5.3.1 Normal-state resistivity

Throughout this section, we will in general discuss in detail only data from sample Bi#10.11 in PCC111 at $p = 31.4 \pm 0.4$ kbar, where the most detailed data was taken. Similar but less extensive data was taken from Bi #10.11 at 26.7 kbar, and much less extensive data was taken on Bi #1 in PCC1. This data will typically not be shown in detail in the interests of space. Qualitatively it is identical. Quantative values will be presented in tables where relevant.

In Fig. 5.6 we plot $\rho(T)$ across the whole measured temperature range. As can be seen, the resistivity is rather different from that observed for a normal metal. There are three features of interest. The first is the obvious superconducting transition at $T_c = 7.05 \pm 0.05$ K, of which much more later. The second is the pronounced negative curvature of the resistivity; the gradient of $\rho(T)$ falls dramatically as T increases. Finally, there is the very small region of linearity, which exists at only the very lowest temperatures above T_c. Fig. 5.6 also shows a similar plot for resistivity from all four pressure points on two different samples. As can be seen, all features of $\rho(T)$ are completely reproduceable. The absolute magnitudes agree rather closely.

For most simple elements, we would expect a low-T $\rho \sim T^5$ temperature dependence (assuming phonon scattering is dominant), then a transition to linear $\rho \sim T$ behaviour when $T \geq \omega_{ln}$. Here, the resistivity is linear only at the lowest temperatures (Fig. 5.7). Even by 10 K the resistivity is

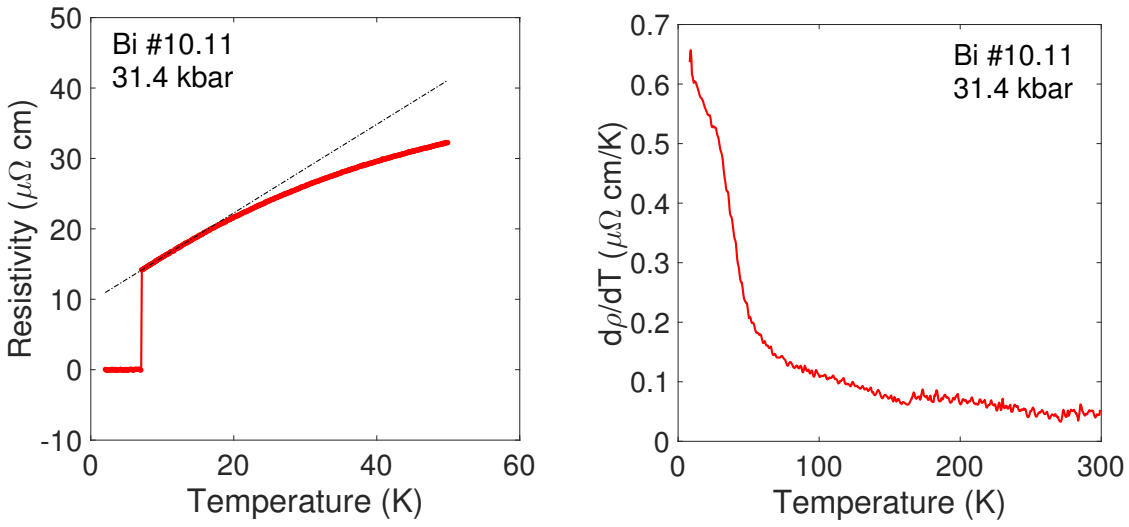

Figure 5.7: Left: $\rho(T)$ and linear fit to the low-temperature region $7.2 < T < 10$ K at 31.4 kbar. Right: resistivity gradient $d\rho(T)/dT$, found by taking the gradient of a linear fit to five-point windows. The rapidly falling gradient indicates the clear negative curvature.

starting to fall below the value predicted by a linear extrapolation of the low-temperature data.

Fig. 5.7 also shows the numerical derivative $d\rho(T)/dT$. Its sharp fall with increasing T arises from the strong negative curvature, and it possesses a maximal value of $\rho' \approx 0.6$ μΩ cm/K. This value agrees well with the low-temperature linear fit, which has gradient $\rho' = 0.614 \pm 0.002$ μΩ cm/K. This gradient is very high for an element; from the Bloch-Gruneisen relation it would imply strong electron-phonon coupling, an issue that will be returned to later.

We should note that, while we use the gradient for the resistivity as obtained from a linear fit, the region of linearity is extremely small. As can be seen from Fig. 5.7, at higher temperatures the value of the gradient falls significantly below this value. We would justify our value of ρ' as follows. Firstly, this value is broadly consistent with that obtained for the normal-state resistivity down to lower temperatures in the presence of a magnetic field which suppresses superconductivity (see Fig. 5.14). We would add the caveat that in field the situation is much more complex, as the size of the magnetoresistance is temperature-dependent, meaning that $\rho(T)$ for $B \neq 0$ is non-linear in a complicated fashion. Secondly, from the theory for Bloch-Gruneisen resistivity and resistivity saturation in Chapter 2, we would suggest that the maximal value of the gradient is the correct one to choose to estimate λ - at higher temperatures, the gradient is reduced due to anharmonic effects. An alternative analysis would be to fit straight lines from just above T_c to progressively increasing upper bounds for T; the higher the upper bound, the lower the gradient would be. However, because the resistivity is clearly not linear at higher T, this does not seem justified; by fitting over such a small window at the lowest available temperatures, we are trying to minimise the impact of anharmonicity on our value for ρ'. We would suggest that our value is reasonable, but should be considered an upper limit.

The residual resistivity ρ_0 is rather large, at ~ 10 μΩ cm, and the RRR is quite low, at ~ 4. This

does not arise from intrinsic impurities: at ambient pressure, these bismuth samples have an RRR around 100, and a $\rho_0 \approx 1.2$ μΩ cm, as expected for 99.999 % pure bismuth.

It therefore seems likely that significant disorder is introduced on the transition to the Bi-III structure: likely our samples become polycrystalline on crossing the structural transition. This supports the conlusions of McMahon's structural study, that crossing the structural phase transition boundary results in the formation of a polycrystal [13, 138]. This idea is lent further credence by the seemingly rather variable value of ρ_0 between measurements. This is seen in more detail in Fig. 5.10, showing the low-temperature resistivity for all four measurements. Linear fits were made to the data for $7.5 < T < 10$ K, to obtain the residual resistivity ρ_0 and the resistivity gradient ρ'. The resulting fit parameters are summarised in Table 8.

The value of ρ_0 varies significantly at different pressures, even within exactly the same bismuth sample. As seen in Fig. 5.6 the high-temperature resistivity by contrast varies by only a factor of ~ 10 %. We would therefore suggest that the low-temperature resistivity is set by scattering from polycrystalline grain boundaries, and these boundaries form essentially randomly as the II-III structural transition is crossed.

It would be of considerable scientific interest to conduct measurements on single crystals of Bi-III. In particular, do quantum oscillations exist? In a technical sense the first Brillouin zone and hence Fermi surface must be infinitesimal in size (because the unit cell is infinite in extent), though in reality the material clearly possesses a finite charge carrier density as it is a metal. Just as an integral gives a finite value from a sum over infinitely many infinitesimal pieces, so the sum over infinitely many infinitely small Fermi surface pockets may yield the metallic electronic properties of host-guest elements.

Obtaining single crystals would be challenging. McMahon outlines a possible mechanism, of taking the sample to well above the stability range of Bi-III then reducing pressure [138]. With this technique, single crystals were obtained for structural studies; alas, this approach lies well outside the pressure range of our piston cylinder cells. It could perhaps be done in a moissanite anvil resistivity cell; however, we would have no control over the orientation of the crystallographic axes of the resulting crystal, so observing quantum oscillations may prove to be challenging.

The temperature dependence of $\rho(T)$ cannot be described by a simple power law dependence. To demonstrate this, we subtract from the data the residual resistivity as obtained from a linear fit to the normal-state resistivity below 10 K, $\rho_0 = 9.6$ μΩ cm, then plot the result on a log-log plot (Fig. 5.8). The solid line is a fit to $\Delta\rho(T) = AT^{\alpha}$ for $100 < T < 300$ K, which gives a best fit of $\alpha = 0.36$ (with neglibible statistical error). Plainly, this fit does not adequately describe the data at lower temperatures.

Fig. 5.8 also shows the effective temperature dependence of the exponent, $\alpha(T)$, obtained by fitting the above model in 5 K windows, and moving the window up in 1 K steps. At the lowest temperatures, the exponent climbs to nearly $\alpha = 1$ (as evidenced earlier by the nearly-linear low-temperature resistivity), but as T increases it rapidly falls to $\alpha \approx 0.2$.

The reader may be intrigued by the jump in the exponent $\alpha(T)$ apparent at $T \approx 180$ K visible in Fig. 5.8. This corresponds to a change of gradient in the resistivity, most obviously seen by taking the numerical derivative $d\rho(T)/dT$ (Fig. 5.9). This feature appeared reliably in all runs at 31.4

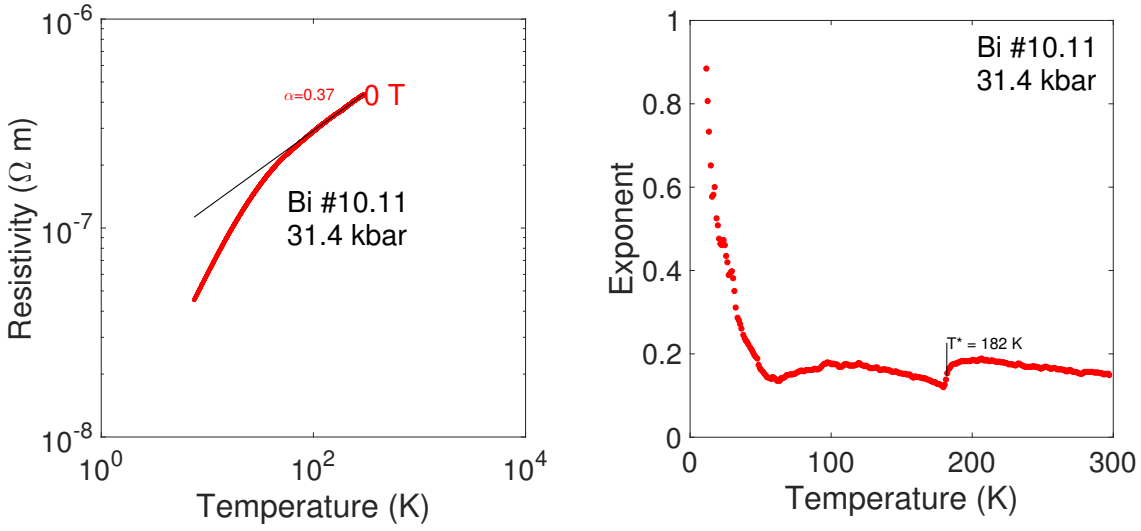

Figure 5.8: Left: ideal resistivity $\Delta\rho(T)$ and power law fit for $100 < T < 300$ K (black line), with an exponent $\alpha = 0.37$. Right: temperature-dependent exponent $\alpha(T)$, obtained by fitting a power law model in 5 K windows, offsetting the window by 1 K for each point. The arrow at $T = 182$ K corresponds to an anomaly also observed in the resistivity gradient, as discussed in the text.

kbar with PCC111, including multiple different cooldowns. It does not correspond to the pressure medium freezing: at these pressures the Daphne 7373 pressure medium is solid at slightly above room temperature, and three other samples measured simultaneously in the same cell exhibited no such change. An explanation is currently lacking. One possibility may be that it is a remanent of the I-III structural transition, which may be expected to happen at ~ 180 K at these pressures according to some authors (as described in Section 5.1.3). However, the transition to Bi-I is a first-order structural transition associated with a dramatic rearrangement of the atoms and a correspondingly large discontinuous jump in the resistivity, which was clearly seen at lower pressures.

A similar kink in $\rho(T)$ is visible in the data from Bi #10.11 at 26.7 kbar, where it appears at ~ 200 K. The data from Bi #1 in PCC1, while too noisy to numerically differentiate accurately, may in fact show an anomaly at ~ 200 K as well. Further investigation is required.

As remarked upon in Chapter 2, conventional models of the resistivity do not straightforwardly give the negative curvature ($\alpha < 1$) observed here; possible mechanisms have been considered in Section 2.3.5. We have found that a saturating-resistor model fits our data well, but there is little physical justification for it. The calculations of Gunnarsson *et al.* for Nb_3Sn produce a similar negative curvature, but their DFT methods are not straightforwadly applicable to the Bi-III structure - although they do note that such curvature is promoted by large, complex unit cells [31, 30, 165]. The most likely explanation is phonon anharmonicity: if the characteristic phonon temperature increases sharply with T, such curvature can occur as explained in Section 2.3.5. This would be promoted by a low Debye temperature, as would be expected from the phonon spectrum. The characteristic Debye temperature is indeed clearly quite low: $\rho(T)$ is linear only at the lowest temperatures $T \lesssim 10$ K (implying $\Theta_{ln} \lesssim 40$ K), suggesting the amplitude of oscillations of the atoms is

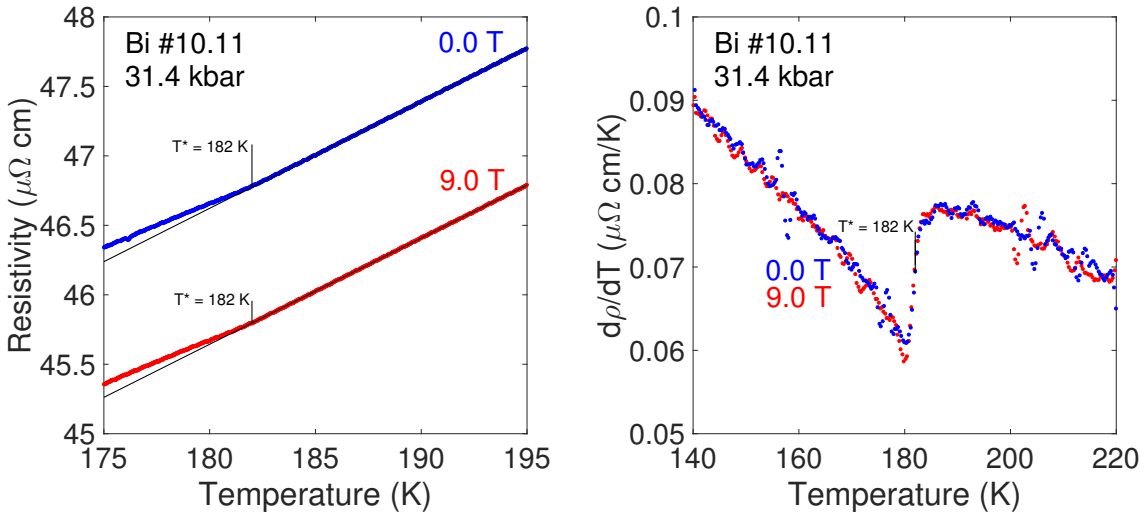

Figure 5.9: Left: $\rho(T)$ in two different fields at 31.4 kbar, showing the clearly-visible change of gradient at around 180 K. The 0 T trace is offset by 1 μΩ cm for clarity; in reality the traces lie on top of each other. Right: the numerical derivative $d\rho(T)/dT$, showing the jump more clearly.

large. Our ab initio calculations of the phonon spectrum further suggest it is highly anharmonic (see Section 5.3.7). Interestingly, exact the same shape of $\rho(T)$ would seem to exist in incommensurate host-guest Ba, as discussed in Section 5.3.10.

5.3.2 Superconducting resistivity and upper critical field

In Fig. 5.10 we show the details of the superconducting transition for all four pressure points. In zero field all measurements yielded an extremely sharp transition.

Critical field measurements of varying detail were taken for all four pressure points, as presented in Fig. 5.11. While the exact dependence of $\rho(T)$ on field varies between measurements, qualitatively all samples show identical behaviour. As expected, an applied field suppresses the superconducting transition temperature T_c. What is remarkable is the scale of field required to destroy the superconducting pairing, which is in excess of 2 T for all measurements. The top right panel of Fig. 5.11 shows measurements in PCC111 at 31.4 kbar down to 200 mK. Here even in an applied field of 2.5 T there is a clear onset to the transition. The high critical field implies type II superconductivity, as confirmed by the magnetisation measurements. The resistivity in fields therefore probes $B_{c2}(T)$.

In Fig. 5.12, we present the fitted upper critical field curves $B_{c2}(T)$ for Bi-III at all four pressure points. The fitting procedure was conducted as follows. A power-law form $\rho(T) = \rho_0 + AT^\alpha$ was fitted to the high-temperature normal-state resistivity. This fit was extrapolated to lower temperatures, and the point at which the measured $\rho(T)$ fell to 50 % of the fitted $\rho(T)$ was defined as the transition temperature $T_c(B)$. The resulting data was used to obtain a curve $B_{c2}(T)$.

To estimate the zero-temperature upper critical field, we considered two forms of $B_{c2}(T)$. The first is based on a simple phenomenological Ginzburg-Landau model [166, 167, 168], and gives:

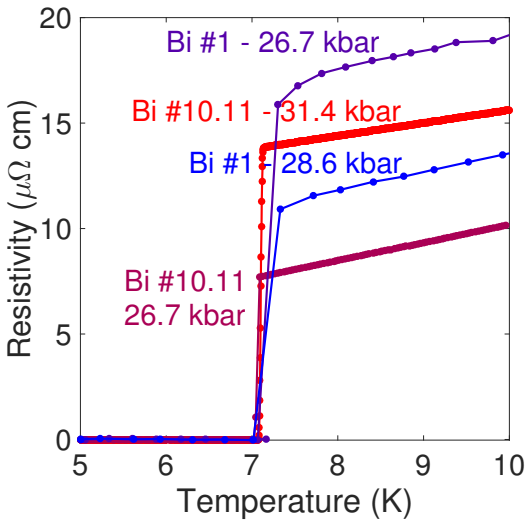

Figure 5.10: Resisitivity $\rho(T)$ across the transition, showing the sharp transition, with a width of at most 0.06 K.

Sample	Observed T_c (K)	T_c from GLT fit (K)	$B_{c2}^{GLT}(0)$ (T)	ρ_0 (μΩ cm)	ρ' (μΩ cm/K)
Bi #10.11 - 26.7 kbar	7.05 ± 0.05	7.09 ± 0.03	2.41 ± 0.01	1.673 ± 0.005	0.8509 ± 0.007
Bi #10.11 - 31.4 kbar	7.05 ± 0.03	7.10 ± 0.02	2.466 ± 0.009	9.486 ± 0.001	0.614 ± 0.002
Bi #1 - 26.7 kbar	7.06 ± 0.04	7.10 ± 0.02	2.72 ± 0.04	10.2 ± 0.7	0.91 ± 0.07
Bi #1 - 28.6 kbar	7.06 ± 0.04	7.06 ± 0.02	2.45 ± 0.02	4.81 ± 0.10	0.876 ± 0.011

Table 8: Superconducting transition temperatures, fitted upper critical field $B_{c2}(0)$, and fitted residual resistivity ρ_0 and resistivity gradient ρ' for the four samples. For observed values, as read from the zero-field T sweeps, the error bars denote the width of the transition. For the fitted parameters, the errors are the 95 % confidence limits of the non-linear fit. The values of ρ_0 and ρ' were obtained from a linear fit to the normal-state 0 T data between 7.5 and 10 K; error bars denote the standard error in this fit.

$$B_{c2}^{GLT}(T) = B_{c2}(0)\frac{1-\left(\frac{T}{T_c}\right)^2}{1+\left(\frac{T}{T_c}\right)^2}. \tag{5.3}$$

The two free parameters of the fit were $B_{c2}(0)$, the zero-temperature limit of the critical field, and the zero-field transition temperature T_c.

This model fitted the data well at all pressures; the resulting properties are summarised in Table 8. We also considered the model of Werthamer, Helfand and Hohenberg (WHH) for the upper critical field; this gives an implicit expression for $B_{c2}(T)$ via a solution of the linearised Gorkov equations [169, 170]. For a BCS one-band type II superconductor in the dirty limit, the critical field relation is:

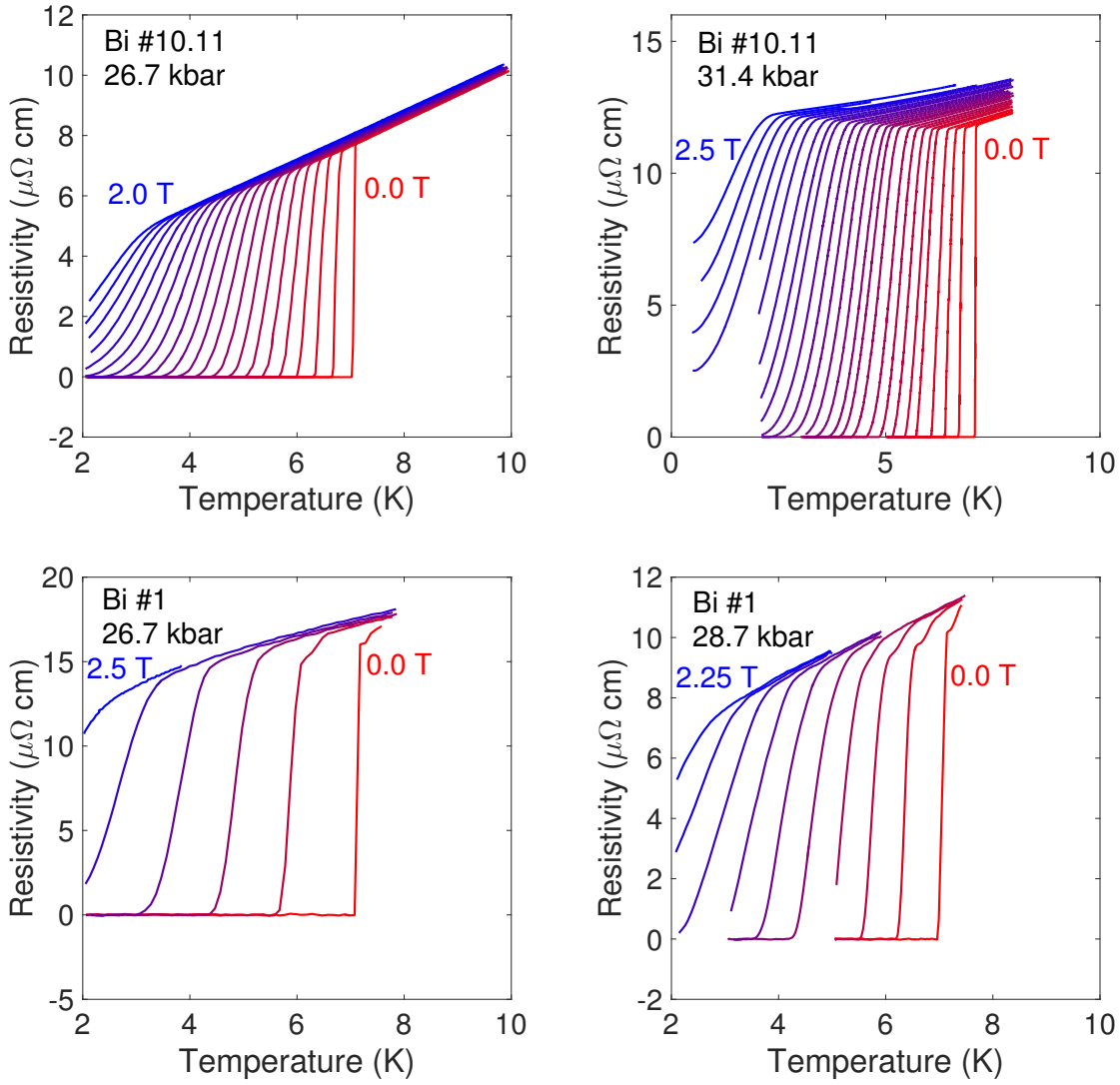

Figure 5.11: Low-temperature resistivity in field of Bi-III. Sweeps are evenly-spaced in 0.1, 0.1, 0.5 and 0.25 T increments for the top left, top right, bottom left and bottom right figures respectively.

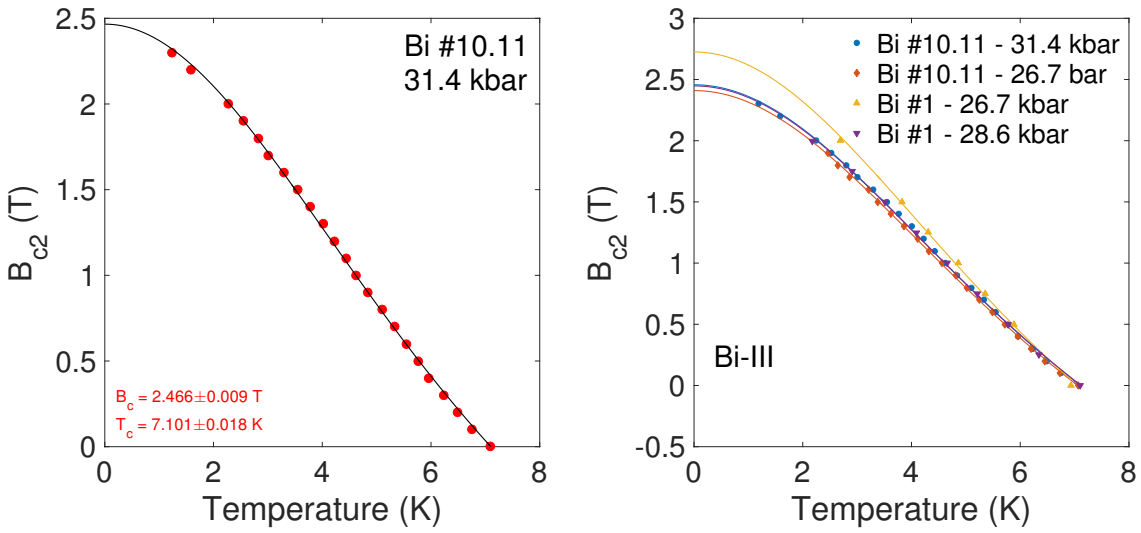

Figure 5.12: Critical field curves $B_{c2}(T)$. Solid line is a fit to the phenomenological Ginzburg-Landau model. At 31.4 kbar data on Bi #10.11 were taken down to low temperature (left). Curves for all four pressure points give comparable results (right).

$$\ln\frac{1}{t} = \sum_{n=-\infty}^{n=\infty}\left\{\frac{1}{|2n+1|} - \left[2n+1| + \frac{\bar{h}}{t} + \frac{\left(\alpha\bar{h}/t\right)^2}{|2n+1| + \frac{\left(\bar{h}+\lambda_{SO}\right)}{t}}\right]^{-1}\right\} \tag{5.4}$$

$$t = \frac{T}{T_c} \tag{5.5}$$

$$\bar{h}(T) = \frac{4}{\pi^2}\frac{B_{c2}(T)}{T_c \frac{dB_{c2}}{dT}\Big|_{T_c}}. \tag{5.6}$$

Here α is the Maki parameter, which measures the relative importance of orbital versus Pauli pair breaking mechanisms, and λ_{SO} is the spin-orbit scattering constant. A useful overview of the application of the WHH theory is given by [171].

The WHH model gives $B_{c2} \sim T$ as $t \to 1$; to obtain T_c and $\frac{dB_{c2}}{dT}\Big|_{T_c}$ we fitted a straight line to the experimental $B_{c2}(T)$ for $5 < T < 7.1$ K (in fact, the linear region of $B_{c2}(T)$ extends over a rather wider temperature region). The WHH critical field curve was then calculated by numerically solving the above equation for $\bar{h}(t)$, truncating the sum at 5000 terms (including more terms has a negligable impact on the value of $\bar{h}$). The results for Bi #10.11 are shown in Fig. 5.13. Clearly, the BCS WHH model cannot fit our data; the minimum value $\alpha = 0$ gives a low-temperature value $B_{c2}^{WHH}(0)$ that underestimates the experimental value by ~ 20 %. Table 9 shows the values obtained from the linear fits.

Sample	$\frac{dB_{c2}}{dT}\Big\vert_{T_c}$ from linear fit (T/K)	T_c from linear fit	B_{c2}^{Pauli} (T)	$B_{c2}^{orb,dirty}$ (T)	$B_{c2}^{orb,clean}$ (T)	WHH β
Bi #10.11 - 26.7 kbar	-0.410 ± 0.007	6.94 ± 0.12	12.8	1.96	2.07	0.85
Bi #10.11 - 31.4 kbar	-0.428 ± 0.009	6.95 ± 0.14	12.8	2.05	2.17	0.83
Bi #1 - 26.7 kbar	-0.475 ± 0.004	6.93 ± 0.07	12.8	2.27	2.40	0.83
Bi #1 - 28.6 kbar	-0.444 ± 0.003	6.92 ± 0.07	12.7	2.12	2.24	0.80

Table 9: Parameters obtained from WHH theory, and limiting critical fields. Linear fits to the experimental $B_{c2}(T)$ were performed above $T = 5$ K, though the linear region appears to extend to lower temperature. Pauli and orbital limiting critical fields are calculated as described in the text. The parameter $\beta = -B_{c2}^{GLT}(0)/\left(dB_{c2}/dT\Big\vert_{T_c} T_c\right)$ is 0.69 in the BCS dirty limit and 0.73 in the BCS clean limit according to the WHH theory; all our measured values are significantly higher.

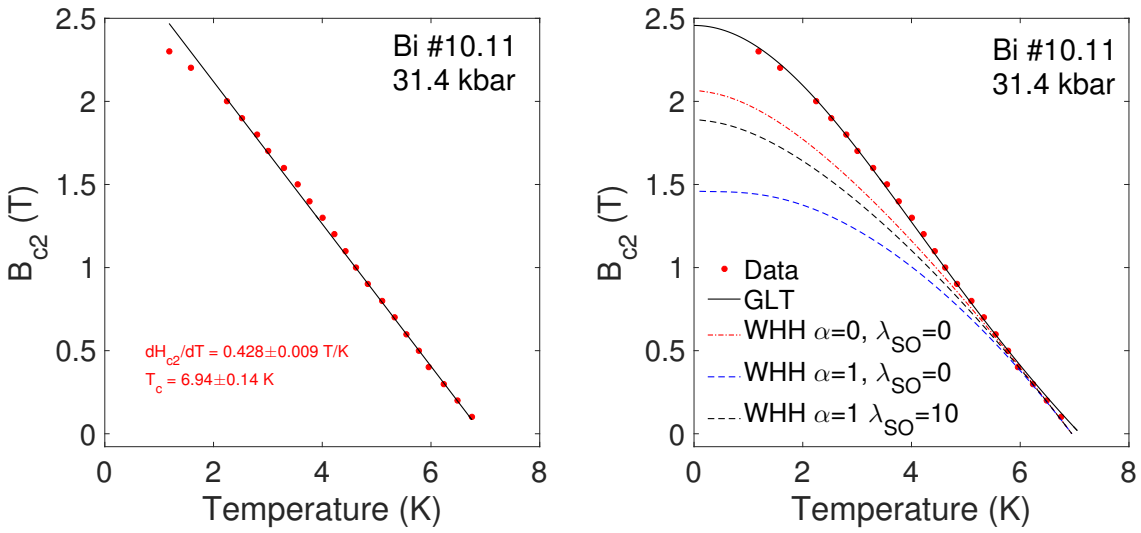

Figure 5.13: Attempts to fit the WHH model to our data. First, we fit a straight line to the experimental $B_{c2}(T)$ for $5 < T < 7.1$ K to obtain the gradient and transition temperature (left). In fact, $B_{c2}(T)$ remains linear over a significantly larger temperature range than that used in the fit. Then we use these parameters to calculate the WHH $B_{c2}(T)$ (assuming single band dirty-limit BCS superconductivity). Red circles are the data, the solid black line shows the Ginzburg-Landau phenomenological model, and dashed lines show WHH calculations with various choices of α and λ_{SO}; none provide a good fit to the data.

5.3.3 Superconducting parameters and pair breaking mechanisms

In Table 8 we summarise the superconducting parameters of Bi-III for our four measurements using the model $B_{c2}^{GLT}(T)$. For these four points the observed value of T_c (taken from the 0 T temperature sweep) is completely independent of pressure, with $T_c = 7.05 \pm 0.05$ K. The Ginzburg-Landau fit to $B_{c2}(T)$ gives a very slightly higher $T_c = 7.10 \pm 0.03$ K.

The fitted values of $B_{c2}(0)$ are rather more variable, ranging from 2.41 to 2.72 T. While the stated statistical error in the fits is small (≤ 0.02 T), this is likely a significant underestimate of the true error. The fit is sensitive to points at low temperature (in particular, below $T = 1$ K), but for all measurements except at 31.4 kbar these points are lacking. A more realistic estimate of the error would suggest $B_{c2}(0) = 2.5 \pm 0.2$ T. There appears to be no trend in the measured critical field values: the measurements at 26.7 kbar give both the lowest and highest critical field, though this may be due to the errors in the fitting process.

One possibility to consider in trying to interpret the variability of the critical field data is the role of vortex pinning due to sample disorder. This has been observed in another high-pressure element, lithium above 400 kbar [172]: lithium was initially thought to be superconducting with $B_{c2}(0) \approx 3$ T, but this was later attributed to sample disorder induced by large uniaxial shear; measurements in more hydrostatic conditions suggested lithium is in a fact a type I superconductor with a critical field of only a few mT [173].

If pinning by disorder was significant, one might expect a positive correlation between ρ_0 and

$B_{c2}(0)$. However, while ρ_0 varies by a factor of $\sim 6\times$, the values of $B_{c2}(0)$ agree to within ~ 15 %.

We can rather confidently state a superconducting transition temperature of $T_c = 7.05 \pm 0.05$ K for Bi-III in the pressure region $26.7 - 31.4$ kbar. This agrees very well with previous values of $6.9 - 7.25$ K [137, 135]. The later magnetisation measurements will show that $T_c(p)$ is constant up to significantly higher pressures of at least 50 kbar. Usually one might expect $T_c(p)$ to exhibit two possible behaviours. One possibility, for superconductivity mediated by fluctuations associated with some sort of quantum critical transition, is that $T_c(p)$ forms a dome centred on the quantum critical point. This is the case for the cuprates, ferromagnetic superconductors such as UGe_2 or materials such as $Ca_3Ir_4Sn_{13}$ near a structural quantum critical point; it seems unlikely here as the structural transition is first order [3, 26]. Alternatively, for conventional superconductors $T_c(p)$ might be expected to shift monotonically with pressure, as the Debye temperature and the electron density are modifed. For the elements this typically leads to a fall in T_c with increasing pressure; precisely this behaviour is exploited in the Sn or Pb manometers used to determine pressure in piston cylinder cells [174]. It seems rather remarkable that a significant change in the interatomic spacing could leave the transition temperature completely unchanged.

Two mechanisms set the upper critical field in type II superconductors [171]. Orbital pair breaking occurs when Abrikosov vortex cores overlap. In the WHH theory, it can be expressed in the clean and dirty limit (with $\alpha = 0$, $\lambda_{SO} = 0$) in terms of the gradient of B_{c2} as:

$$B_{c2}^{orb}(0) = -\beta T_c \frac{dB_{c2}}{dT}\Big|_{T_c} \tag{5.7}$$

where $\beta = 0.69$ in the dirty limit and $\beta = 0.73$ in the clean limit.

Pauli pair breaking arises when Cooper pairs become Zeeman-split. The Pauli pair breaking field is found by balancing the normal-state Zeeman energy with the superconducting gap energy:

$$\frac{1}{2}\chi_P B_P^2 = \frac{1}{2}N(E_F)\Delta^2 \tag{5.8}$$

where Δ is the gap energy, χ_P the normal-state Pauli susceptibility, and $N(E_F)$ the density of states at the Fermi level. [171] Assuming the standard BCS relation $\Delta(T = 0) = 1.76 k_B T_c$ and an electron g-factor of 2, gives:

$$B_P(0) = 1.84 T_c \tag{5.9}$$

where B_P is in T and T_c is in K. Table 9 summarises the pair breaking fields. The value of $B_P(0)$ is very much higher than the experimental value. Values of $B_{c2}^{orb}(0)$ are around 20 % below the experimental $B_{c2}(0)$, i.e. the factor $\beta \approx 0.83$.

The poor fit of the WHH model may arise from violation of one (or all) of the model assumptions: the calculation considers BCS weak coupling ($\lambda \ll 1$) superconductivity from one band in the dirty limit. We do not known how many bands take part in superconductivity, and our system is - despite the large $B_{c2}(0)$ - not necessarily in the dirty limit, as discussed in Section 5.3.8.

The clean-limit BCS WHH calculation corresponds to the same values for $B_{c2}(T)$ near $T = T_c$, but an increase of $B_{c2}(T)$ near $T = 0$ by ~ 6 %. This brings the WHH curve closer to the experimental results, but still gives a significant underestimate of $B_{c2}(0)$. Increasing α only reduces the value of $B_{c2}(0)$. A clean-limit single-band weak-coupling WHH calculation - with any values of α or λ_{SO} -

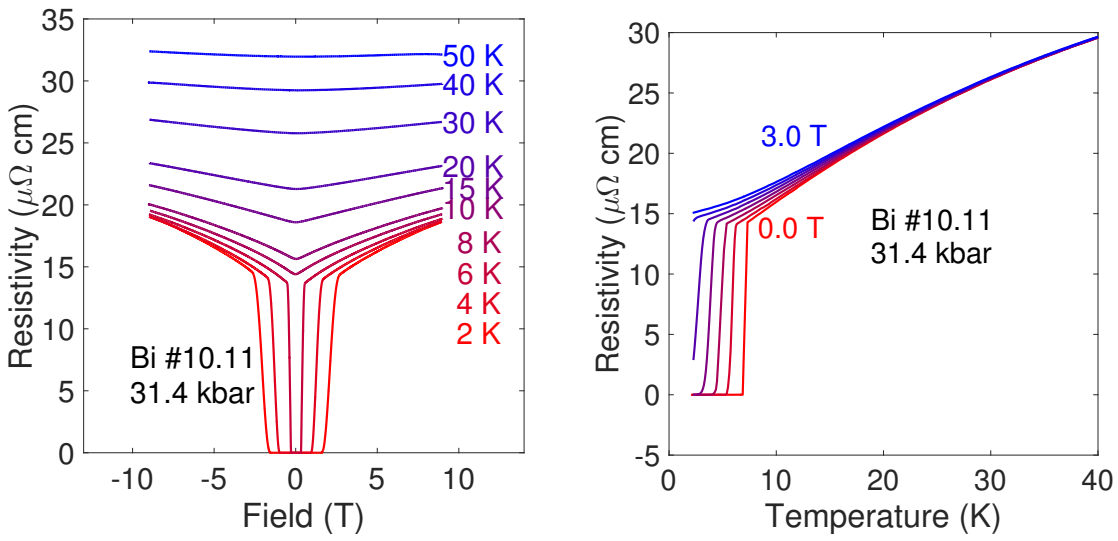

Figure 5.14: Left: magnetoresistance $\rho(B)$ for Bi-III. Right: resistivity up to 40 K from 0 to 3 T in 0.5 T increments.

would therefore also be a poor fit to the data.

Corrections to the BCS values of the WHH model when $\lambda > 1$ were worked out by Bulaevskii *et al.* assuming an Einstein phonon spectrum [175]. These showed that increasing λ above 1 increases β; a value $\lambda = 4$ gives $\beta \approx 0.9$ in the dirty limit and $\beta \approx 1.0$ in the clean limit. The Einstein phonon assumption may be a significant simplification, but would appear to suggest that values of λ in excess of 1 could explain the anomalously large values of β.

5.3.4 Magnetoresistance

In addition to temperature sweeps, at 31.4 kbar we also measured the longitudinal magnetoresistance (MR) $\rho(B)$ at a number of temperatures. A subset of the data is shown in Fig. 5.14. As expected, it is symmetric in field indicating negligable offset of the contacts. At lower temperatures $T < T_c$, a transition from the superconducting to normal state is visible when $|B|$ becomes large enough. The magnitude of the magnetoresistance falls with temperature - at higher temperatures an applied field has less effect on the resistivity. This is more clearly demonstrated in the right-hand panel of Fig. 5.14, where temperature sweeps up to 40 K in fixed fields are shown. As can be seen, just above T_c an applied field has a significant impact on the resistivity, while at 40 K it has almost no effect.

At the lowest temperatures, the MR of Bi-III exhibits a rather unexpected negative curvature. Fig. 5.15 shows the fractional magnetoresistance (FMR), defined by:

$$F(B) = \frac{\rho(B) - \rho(0)}{\rho(0)}. \tag{5.10}$$

We neglect the superconducting data $T < T_c$ for this measurement, as of course in the supercon-

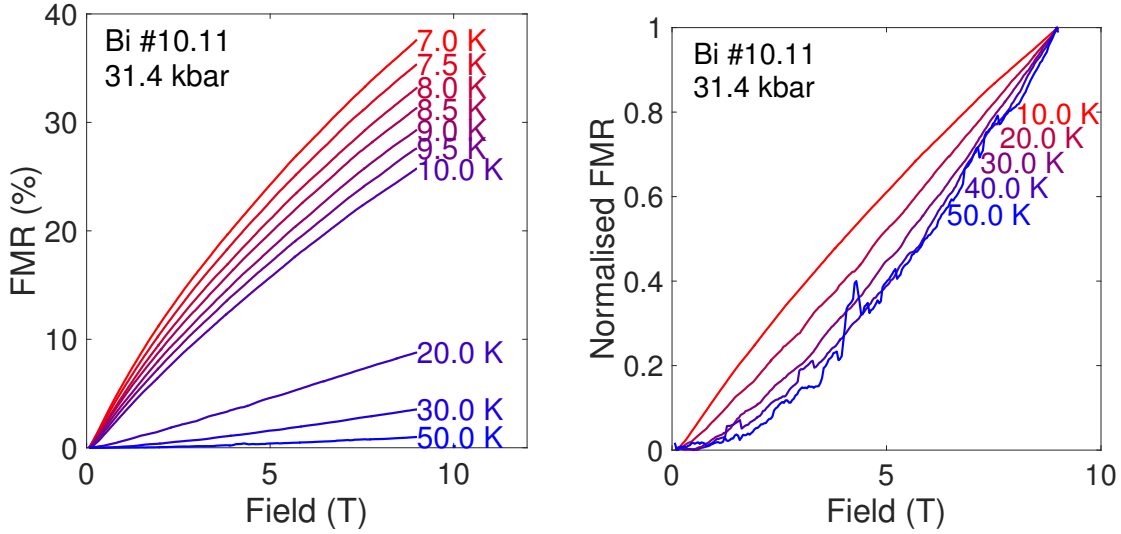

Figure 5.15: Left: fractional MR in the normal state for Bi-III at 31.4 kbar. Right: the same after normalisation to the 9 T value, showing a clear transition from negative to positive curvature.

ducting state $\rho(0)$ vanishes. To eliminate the effects of any contact offset, we take only the symmetric part of the resistivity, $\rho(B) = \frac{1}{2}(\rho_{meas}(B) + \rho_{meas}(-B))$ where $\rho_{meas}(B)$ is the resistivity measured in positive and negative fields.

This scaling removes the constant offset due to the temperature dependence of ρ. There is a clear change from negative to positive curvature as a function of temperature; this can be more clearly seen in the right-hand panel of Fig. 5.15, where $F(B)$ is normalised to its 9 T value. Note that for the higher temperatures the data is rather noisy, because the absolute changes in ρ from its zero-field value are small, so voltage noise has more impact on the normalised quantity.

In an attempt to quantify the change in curvature, we assume the high-field resistivity $\rho(B)$ can be fit by a power law, $\rho(B) = \rho(0) + AB^n$ where $\rho(0)$, A and n are free parameters. To allow us to include data for $T < T_c$, we apply an arbitrary $B = 3$ T cutoff for the low end of the fit. Modifying the cutoff to e.g. 1 T qualitatively changes nothing (the exact fitted values vary by up to 10 %).

Fig. 5.16 shows the resulting fits and the exponent n. As can be seen the power law form fits the data well above 3 T, and the exponent rises continuously from below 1 (negative curvature) at low temperatures to above 1 at higher temperatures.

What behaviour might we expect from the magnetoresistance? Firstly, up to 9 T there is no evidence of quantum oscillations (while, for these samples, in the Bi-I state quantum oscillations were clearly observed above 1 T). This may be related to the high residual resistivity ρ_0, as well as the fact that (unlike Bi-I) Bi-III appears to be a good metal, so the fields required to observe quantum oscillations may be significantly higher than those applied here.

Recall from Chapter 2 that Lorentz magnetoresistance is a multiband phenomenon. Appealing

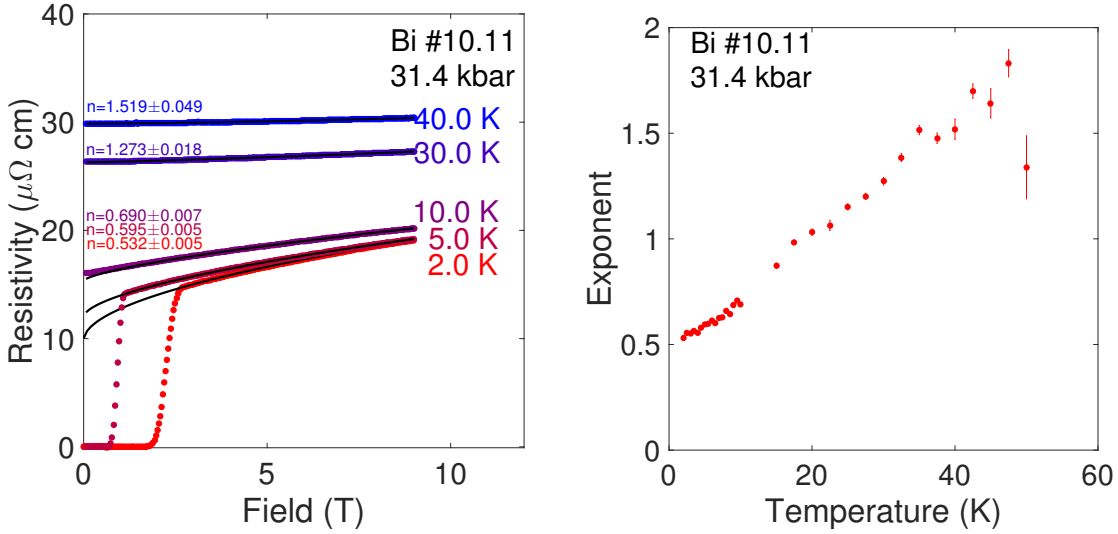

Figure 5.16: Left: resistivity $\rho(B)$ and power law fit (solid black line) for $B > 3$ T at a selection of temperatures. Coloured text indicates fitting exponent n and its 95 % confidence limits. Right: value of n as a function of temperature. The 50 K point is likely an outlier; at these temperatures the magnetoresistance is extremely small thus voltage noise can significantly impact the data.

to a two-band model, we expect an MR of the form:

$$\frac{\rho(B)-\rho(0)}{\rho(0)} \sim \frac{(\omega_c\tau)^2}{1+a\,(\omega_c\tau)^2} \tag{5.11}$$

where $a \sim n_e - n_h$ and $\omega_c = eB/m$. We would thus expect that:

1. The low-field MR is always quadratic (assuming τ is field-independent, a reasonable assumption at low fields).
2. The high-field MR will either increase without limit for a compensated conductor ($a = 0$), or saturate for an uncompensated one ($a \neq 0$).

Neither of these appears to occur here. There is no evidence the low-temperature MR is quadratic over any extended low-field range, and it also does not show any tendency to saturate, at least in fields up to 9 T, instead exhibiting weak negative curvature. This suggests the simple two-band model is inappropriate here. It is interesting to note that the clear negative curvature to the magnetoresistance is very similar in shape to that in $Hg_{3-\delta}AsF_6$, another incommensurate chain compound [154].

For many metals, if a single scattering time $\tau(T)$ adequately describes the resistivity, then Kohler's rule should be obeyed:

$$\frac{\rho(B)-\rho(0)}{\rho(0)} = f\left(\frac{B}{\rho(0)}\right) \tag{5.12}$$

where f is a universal *temperature-independent* function. A plot of the FMR against $B/\rho(0)$ should then scale FMR sweeps at different temperatures onto a single curve. Kohler's rule is typically taken

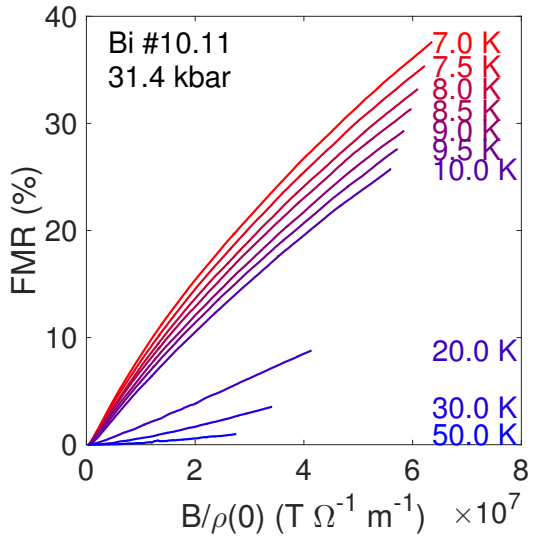

Figure 5.17: Kohler plot for Bi-III; no universal Kohler scaling is observed.

as evidence for obedience to Fermi liquid behaviour: it arises because in Boltzmann transport theory, the FMR is a function only of $\omega_c\tau = eB\tau/m$, and $\rho(0) \sim \tau^{-1}$. For a detailed overview see Chan *et al.*, , who discuss the observation of Kohler scaling in the strange-metal cuprates, where it is rather unexpected [176]. Spain *et al.* consider the case of graphite, where the presence of multiple bands and a temperature-dependent carrier concentration cause Kohler's rule to be violated [177].

Fig. 5.17 shows such a plot. Plainly, the curves do not overlap: Kohler's rule is not obeyed in Bi-III. This most likely arises because the approximations required for Kohler's rule are not obeyed. Either the carrier density varies appreciably with temperature, or multiple bands take part in charge transport. The former seems unlikely, as DFT calculations suggest the Fermi energy for Bi-III is at least 1 eV above the band edge; DFT calculations also imply that the latter is true, and Fig. 5.17 provides experimental support for this [71]. Therefore we conclude the resistivity of Bi-III cannot be described by a simple single-band Fermi-liquid model.

5.3.5 Magnetisation

Fig. 5.18 shows DC magnetisation measurements on Bi-III in SMAC16-7 at 35 kbar, showing the three-step background-subtraction process undertaken. First, the empty cell signal is subtracted from the data: the empty cell's raw $M(T)$ data (at a number of fixed B fields) was smoothed with a five-point moving average to remove random noise, then replaced with a 1000-point cubic smoothing spline to avoid problems with interpolation on a sparse dataset. Using the raw data does not provide good background-subtraction results: there is random noise in both the measured data and the background, and the discrete nature of the background, combined with the use of linear interpolation, lead to zigzag artifacts in the background-subtracted data.

Clear evidence of Meissner flux expulsion is visible in the raw data, without subtracting any background (top left panel of Fig. 5.18). This is testament to the power of the SQUID magnetome-

ter's fitting algorithm: for SMAC16-7, the sample volume was 9.6×10^{-13} m^3, so the $70 \times 8 \times 8$ mm) cell's volume is approximately *five million* times larger. However, because it possesses a non-dipolar contribution to the measured $V(z)$, the cell's background is almost entirely removed and the sharp drop in $M(T)$ associated with the tiny Bi-III sample turning superconducting can be seen clearly.

The measured background is shown in Fig. 5.19. For simplicity, we have scaled the measured magnetic moment $Z(T)$ by the volume of the Bi-III sample (9.6×10^{-13} m^3), to provide a magnetisation in A m^{-1}. This allows direct comparison with the measured magnetisation of the Bi-III sample in Fig. 5.18. From this background data a two-dimensional linear interpolation surface $M(T, B)$ was constructed to provide a background $M(T)$ at any measurement B even if a background was not taken at that field.

Subtraction of the cell background noticeably reduces the low-temperature tail in the measured $M(T)$ arising from the cell. However, as can be seen, there is still a temperature-independent offset in $M(T)$, which varies from run to run - we surmise this arises from tiny amounts of ferromagnetic impurities in the cell. To remove this, we subtract the mean of the magnetisation above $T = 7.5$ K, well within the normal state, on the basis that the component of the magnetisation signal will be unmeasurably small above T_c.

Finally, we scale the background-subtracted magnetisation to obtain the SI volume susceptibility $\chi(T) = M(T)/H$. We assume that $B = \mu_0 H$ where B is the applied field (i.e any demagetising factor is neglected), in which case $\chi = \frac{M}{795775B}$ where M is in A m^{-1} and B in T.

The resulting susceptibility tends to a low-temperature value of ~ -1.4; theory would predict a value of -1 for a bulk superconductor, and in fact such good agreement is quite remarkable considering the rather significant errors: there may be a remanent field in the SQUID magnet which can shift the true applied field by ~ 1 mT from its nominal value, the sample volume is measured rather inaccurately, the sample is approximated as a cuboid, and no account is taken of any demagnetising factor despite the fact this factor may be moderately large given the sample geometry.

In Fig. 5.20, we plot the measured magnetisation $\chi(T)$ (having rescaled the magnetic moment by the estimated sample volume) for Bi-III at a number of different pressures for SMAC16-7. Above 29 kbar, a clear superconducting transition can be observed, with an onset transition temperature $T_c \sim 7.0$ K. The finite transition width arises because B_{c1} is temperature-dependent, and (unlike for the resistivity measurements), zero-field measurements would not yield a visible magnetometry signal. Additionally, due to the smaller volume of the SMACs with respect to the PCCs, the pressure conditions are likely less hydrostatic. This latter factor is less significant: as we will establish, T_c of Bi-III is rather insensitive to pressure at lower pressures, so a pressure inhomogeneity of a few kbar will have little impact on T_c.

At 0 kbar, after depressurising the cell, no transition is observable, as expected. From 29 to 52 kbar, there is little difference in the size of the jump in χ, while at higher pressures, the size of the susceptibility jump seems to increase to unphysical values well above 1. The origin of this behaviour is unclear, but we would ascribe it to an increasing demagnetisation factor arising from an increasingly flattened sample. As the pressure is increased, the conditions become more anhydrostatic, and as the gasket thins the anvils may begin to apply unaxial pressure on the sample. This will tend to make it thinner and wider, thereby increasing the demagnetising factor and hence the measured

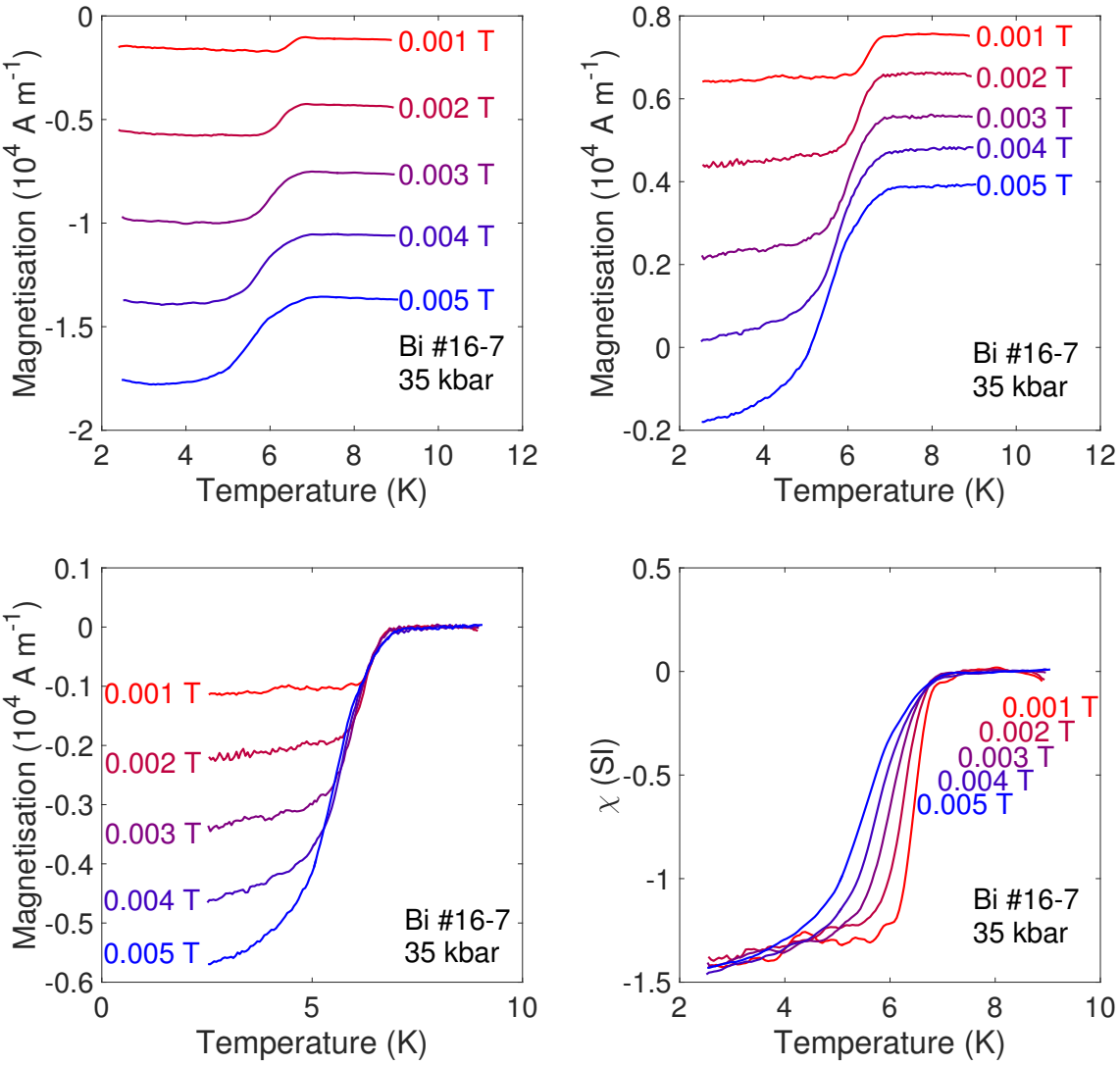

Figure 5.18: Background subtraction process for obtaining the SI volume susceptibility. Top left: raw measured magnetisation. Top right: after subtraction of the empty cell. Bottom left: after subtraction of the mean high-temperature magnetisation. Bottom right: after scaling by the applied field.

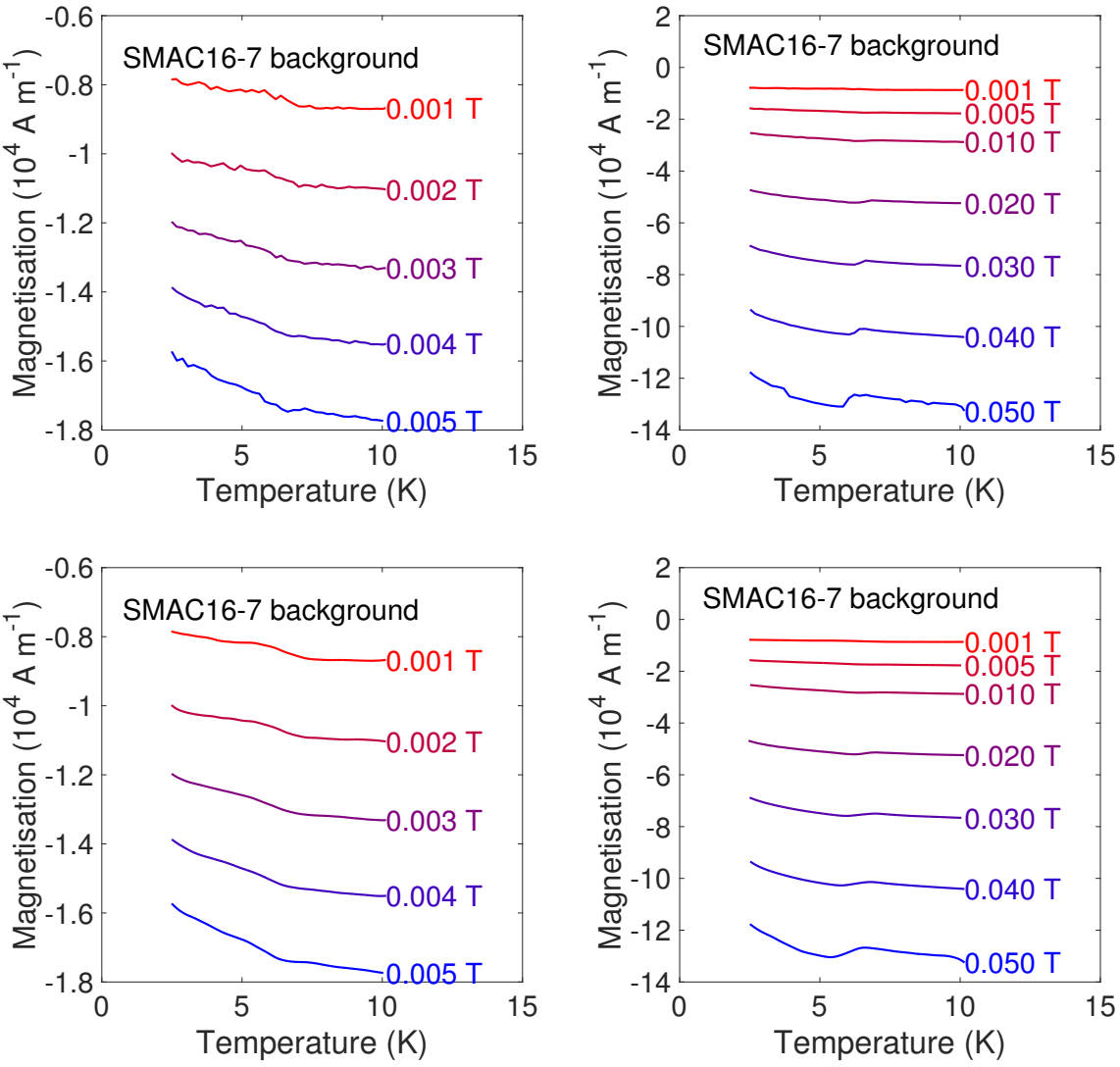

Figure 5.19: Top: raw data for the cell background of SMAC16-7, at low fields (top left) and higher fields (top right). Bottom: magnetisation used for background-subtraction after smoothing and spline fitting.

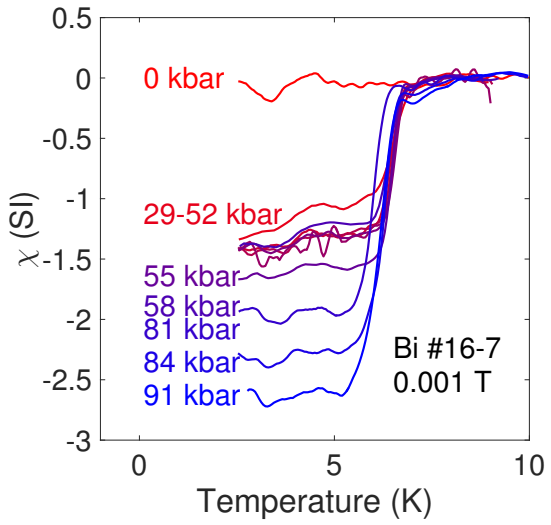

Figure 5.20: Susceptibility $\chi(T)$ at a number of pressures for Bi #16-7.

value of χ. An alternative explanation, of course, would be that the volume fraction of the superconductivity in Bi-III increases sharply above around 55 kbar, and our original scaling based on the sample volume is incorrect.

Fig. 5.21 plots the susceptibility jump $M(T)$ from SMAC16-7 at all measured pressures in a number of fields. Qualitatively all the plots are identical. At every measured pressure point, an increase in the applied field shifts the lower end of the transition down, broadening it. For lower field $B < 6$ mT, after scaling to obtain $\chi(T)$ all T sweeps tend to the same low-temperature value, but for higher fields the size of the jump is smaller. This is the behaviour expected for a type II superconductor: when $B > B_{c1}$, some flux can penetrate the sample, thus χ tends towards zero from its low-field value of -1.

Further evidence for type II superconductivity is in the discrepany between field-cooled (FC) and zero-field-cooled (ZFC) measurements. For a type II superconductor, cooling in an applied field will trap magnetic flux in the sample, resulting in a smaller observed flux expulsion compared to zero-field cooling. Such behaviour can be clearly observed in Fig. 5.22. Here, the sample was first cooled in zero field, then a field was applied and measurements were taken while warming through T_c; leaving the same field applied, $\chi(T)$ was measured while the sample was cooled again and warmed again. As can be seen, the size of the drop in $\chi(T)$ is smaller by a factor of ~ 5 for the FC measurements when compared to the ZFC results. For a type I superconductor there would be no such discrepancy.

For the sake of completeness, in Fig. 5.23 we show $\chi(T)$, arrived at in the same fashion, for cell SMAC16-3. Here the data is less comprehensive and more variable, but qualitatively the same: there is clear evidence for a superconducting transition. The transition onset appears at a slightly higher temperature, with $T_c \approx 7.4$ K; however, the broadness of the transition means it is hard to give an accurate value.

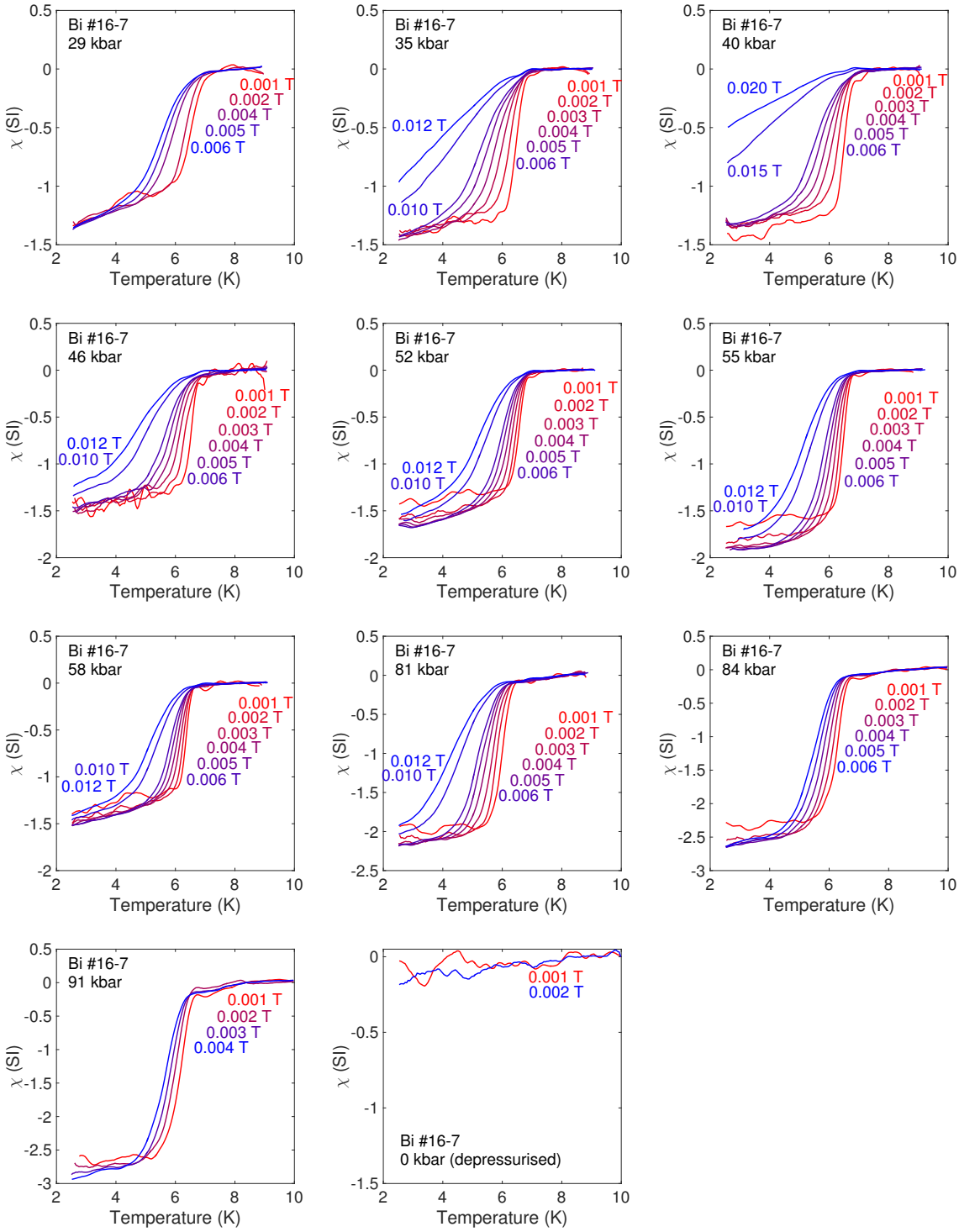

Figure 5.21: Susceptibility $\chi(T)$ at a number of pressures (see individual panels for pressures and applied fields).

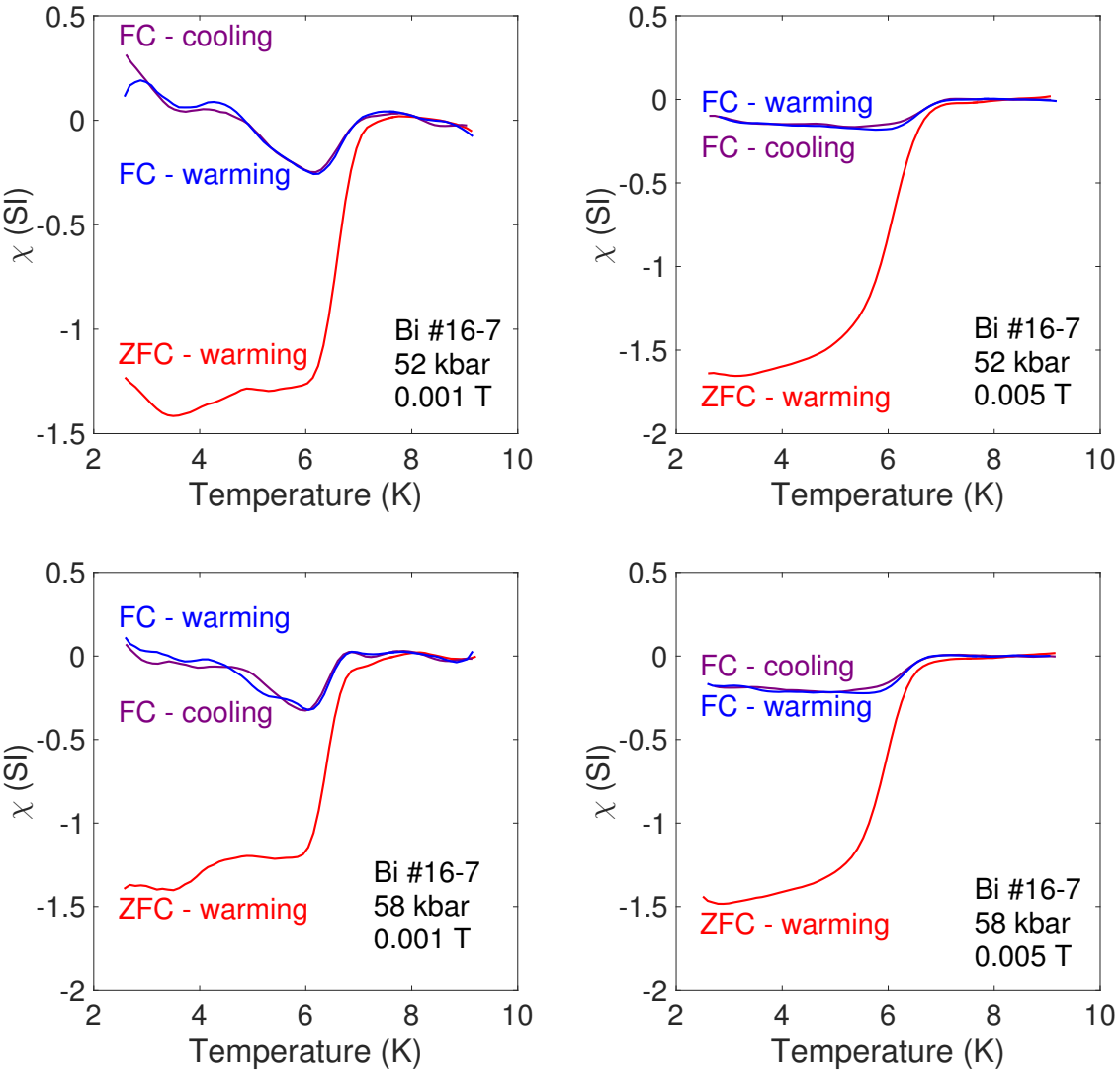

Figure 5.22: Discrepancy between measurements taken when the sample was zero-field-cooled (ZFC) through the transition, and field-cooled (FC). The size of the measured flux expulsion is significantly smaller in the FC case.

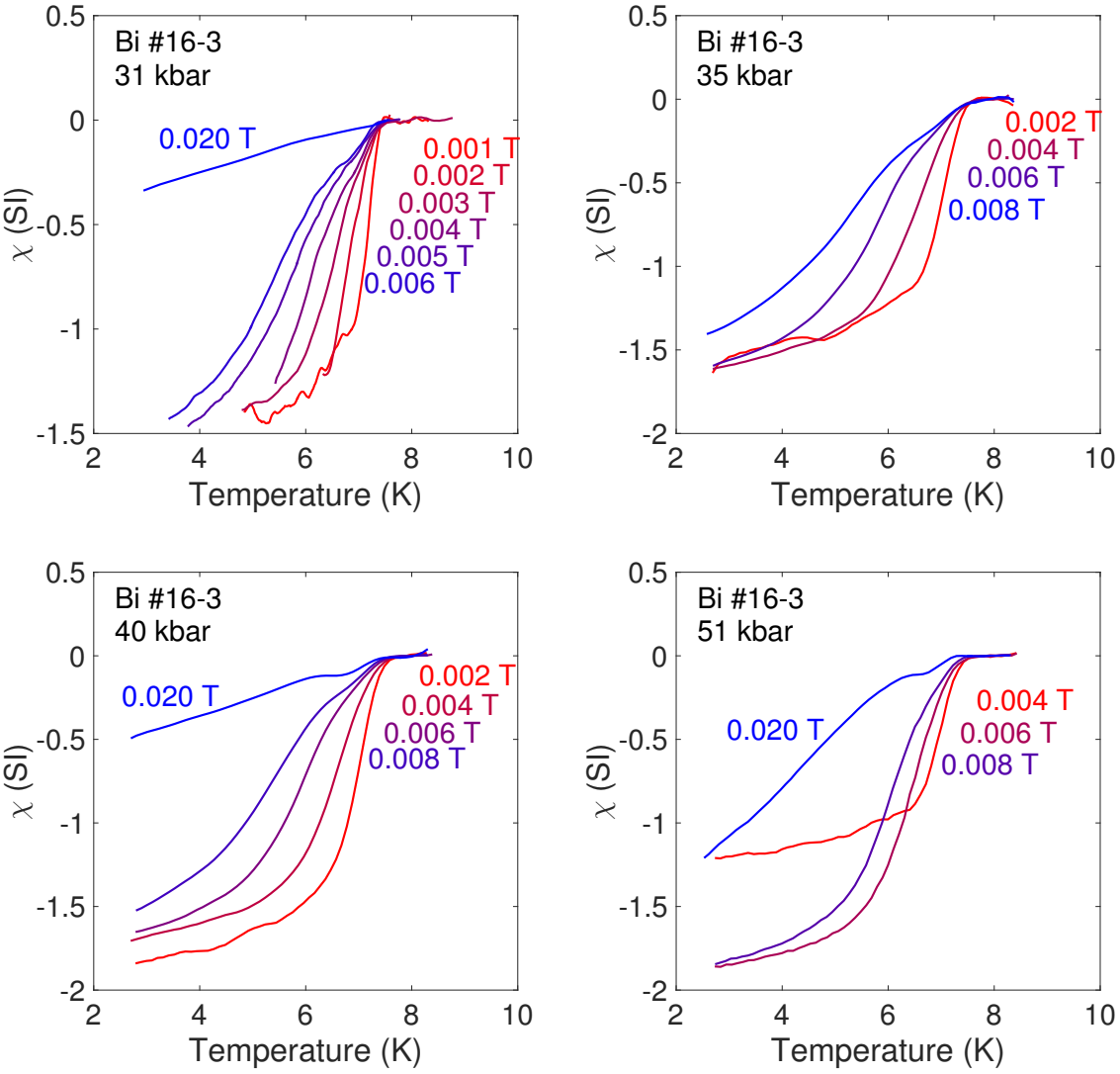

Figure 5.23: SI volume susceptibility $\chi(T)$ for SMAC16-3 at four pressures.

Measurement of $\chi(T)$ at a number of fields allow an estimate of the lower critical field B_{c1}. This is significantly more challenging than measuring B_{c2} via the resistivity. An applied field rapidly broadens the transition; in simple terms, the lower end of the transition is set by $B_{c1}(T)$, and is suppressed to zero temperature by fields of a few mT, while the upper end is set by $B_{c2}(T)$, which is > 1 T. We have a small and noisy signal, and a cell background which grows rapidly with field. Additionally, the lower critical field is comparable in magnitude to the remanent field in the cryostat's superconducting magnet, ~ 1 mT, meaning the stated value of B at these low fields may not be accurate [34]. We should therefore emphasise that the determination of B_{c1} is rather inaccurate - we would estimate errors of ~ 33 %, based on the scatter of the data - but it can give an order-of-magnitude value.

We use the following approach to distinguish between the low-temperature Meissner state and the flux lattice region. At each field, a linear fit to the low- and high-temperature data is taken. We subtract off the low-temperature fit, and define the transition as the region where $\chi(T)$ lies between 30 % and 80 % of its high-temperature extrapolation. A straight line is fitted to this region and extrapolated until it touches the lower and upper fits at temperatures T_{c1} and T_{c2}. This is used to obtain $T_{c1}(B)$, which can be reversed to give the lower critical field curve $B_{c1}(T)$. This approach gave reasonable estimates of $B_{c1}(T)$ both at low fields (when the transition is sharp) and higher fields (when it is broad). An example of this fitting procedure is shown in Fig. 5.24. Fig. 5.25 shows the critical field curves for SMAC16-7 at a number of pressures. The empirical model $B_{c1}(T) = B_{c1}(0)\left(1-(T/T_c)^2\right)$ is fit to the data, with $B_{c1}(0)$ and T_c free parameters. We should note that this fitting procedure also introduces a significant error. We typically can obtain sensible values for the transition temperature $T_{c1}(B)$ only at fairly high temperatures (i.e. low applied fields), and must then extrapolate data taken over the interval $4-6$ K down to 0 K.

The crude estimate for the lower critical field of Bi-III is then $B_{c1}(0) = 15 \pm 5$ mT, obtained by taking the mean of the value at every pressure, with the scatter as the error. Fig. 5.25 plots $B_{c1}(p)$, the lower critical field as a function of pressure. We do not believe that, given the significant inaccuracies that accumulate in the data analysis, any conclusions can be drawn about the pressure dependence of $B_{c1}(p)$. For cell SMAC16-3, the data is of lower quality and there are fewer field points available for the fit; the same procedure also obtains a lower critical field in the region $10-20$ mT.

A better estimate of B_{c1} would not be trivial to obtain. Data is needed at lower temperatures, but this requires higher fields, which increase the cell background and unavoidably broaden the transition. Conclusive proof of type II superconductivity would be provided by magnetisation isotherms $M(B)$. This would show clear hysteresis and the characteristic magnetisation curve of a type II superconductor ($M \propto -B$ for $B < B_{c1}$, then M falling towards zero for $B_{c1} < B < B_{c2}$). However, we did not find it possible to attain sensible data from such measurements.

This likely arises due to complexities from the background magnetisation of the cell. Recall that to obtain $\chi(T)$, we first subtract off the high-temperature magnetisation, on the assumption that the sample signal is negligably small for $T > T_c$ and therefore the dominant contribution is the cell background. This step is crucial for obtaining a sensible normalised $\chi(T)$; simply subtracting the cell background is not sufficient. The high-temperature background is not identical in value from run to run with the same cell, likely because the exact position of the cell varies, as does the magneti-

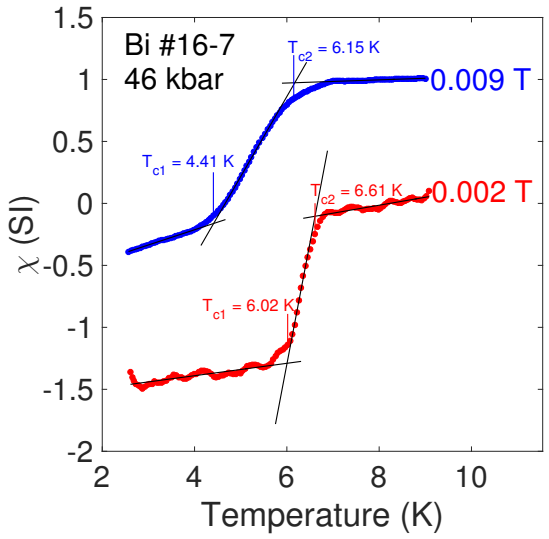

Figure 5.24: Fitting procedure used to estimate the lower critical field. The transition temperature is defined as T_{c1}, the point where the low-temperature fit crosses the transition region. This region is defined by fitting a straight line to the low-temperature data and subtracting this, then finding the points where the data falls to 30 % and 80 % of the extrapolated high-temperature linear fit. Curves are offset by $\chi = 1$ for clarity.

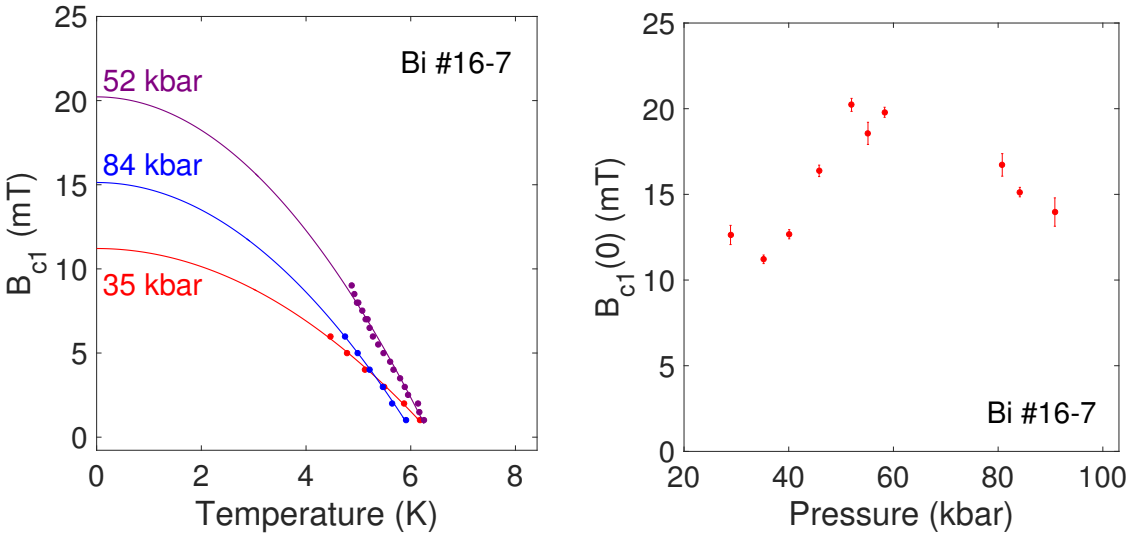

Figure 5.25: Pressure dependence of the lower critical field, $B_{c1}(p)$, as obtained from fits to the critical field curve for each pressure point.

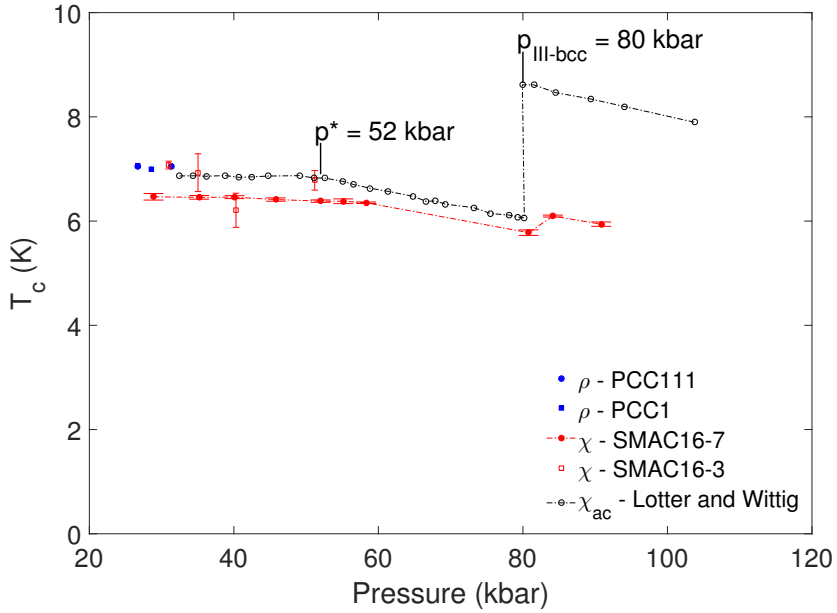

Figure 5.26: Pressure dependence of T_c for our four measurements, and comparison to the data of Lotter and Wittig [137]. Arrows show location of the Lifshitz transition hypothesised by Lotter and Wittig at $p = p^*$, and the III-bcc structural phase transition. The location of $p_{III-bcc}$ would appear to be quite variable - Lotter and Wittig observed it at 81 kbar, while the structural data of McMahon *et al.* indicate it occurs at 77 kbar at room temperature [13, 138], the DFT calculations of Hausserman *et al.* imply it should occur at > 150 kbar [71], and we do not observe it up to 91 kbar.

sation of tiny quantities of ferromagnetic impurities in the cell. With a magnetisation field sweep, this background cannot accurately be removed. In addition, at higher fields $B > B_{c1}$, while the sample magnetisation begins to drop in magnitude the cell background continues to rise, therefore the signal-to-noise ratio falls sharply. Perhaps a more elaborate data analysis routine would allow such measurements to be undertaken. However, we believe that simply taking a scan $M(B)$ at fixed T with the empty cell, then $M(B)$ at the same T with the full cell, and subtracting one from the other, would not be sufficient.

5.3.6 Pressure dependence of the transition

In Fig. 5.26, we plot $T_c(p)$, the pressure dependence of the superconducting transition temperature, along with the results of Lotter and Wittig [137]. Our results are in fairly good agreement. The slight discrepancy between the susceptibility values likely arises from how T_c is defined; Lotter and Wittig give no details of their definition. While the zero-field resistive transition is extremely sharp (with a width $\Delta T_c \approx 0.08$ K), the transition measured by the SQUID is significantly broader and quite noisy in the lowest fields. We therefore define T_c for χ as that obtained by the fit $B_{c1}(T) \sim 1 - (T/T_c)^2$. This would appear to be a slight underestimate of the true zero-field T_c, which cannot be obtained in a SQUID measurement (we typically measure in a minimum field of 1 mT which is ~ 10 % of B_{c1}). For the SQUID cell SMAC16-3, the transition width in the lowest field is rather broad and there are few datapoints available,.

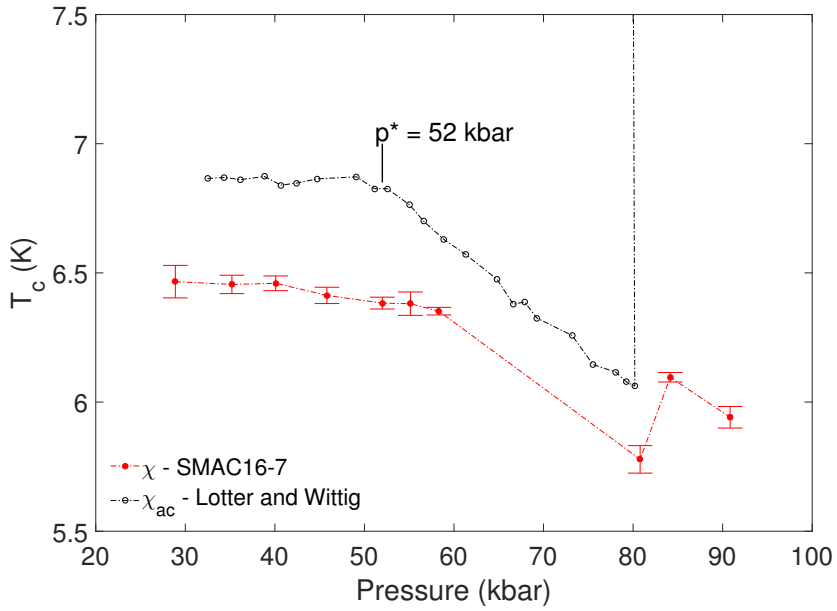

Figure 5.27: Pressure dependence of T_c for SMAC16-7 and comparison to the data of Lotter and Wittig [137], . Arrows show location of the Lifshitz transition hypothesised by Lotter and Wittig at $p = p^*$. $T_c(p)$ is approximately constant up top^*, above which it undergoes a slight downturn, clearly visible in the data of Lotter and Wittig and also observed in our data.

There are two important results. Firstly, we find that superconducting Bi-III exists from 26.7 kbar up to around 91 kbar. This is in reasonable agreement with previous authors (though the upper limit of the Bi-III phase extends to much higher pressures than expected: at room temperature the structural transition to bcc Bi occurs at 77 kbar). The DFT results of Hausserman *et al.* are in reasonable agreement; they indicate that the low-temperature I-III transition occurs at 35.4 kbar, and the high-pressure structural transition from Bi-III to bcc Bi should occur at 15.5 GPa [71].

In addition, we confirm two rather unexpected results from measurements by Lotter and Wittig, who have previously investigated $T_c(p)$ for bismuth using an AC susceptibility anvil cell [137]. They found that T_c is approximately independent of pressure up until a critical pressure $p^* \approx 52$ kbar, at which pressure the gradient dT_c/dp changes without an apparent discontinuity in $T_c(p)$. We also observe this behaviour, though our data is rather sparse at high pressures and the effect is small (Fig. 5.27).

The observation that $T_c(p)$ should be pressure-*independent* is rather remarkable - it implies there is either no change in the Bi-III band structure and phonon spectrum as a function of pressure, or that any changes cancel out to leave T_c unchanged. Certainly the volume does change significantly throughout the extended region of pressure stability of the Bi-III structure [13, 138]. It may be that, at lower pressures, T_c is so pressure-independent because it is intimately linked to the low-energy phason mode. This low-frequency phonon spectral weight will act to reduce ω_{ln} and enhance λ, behaviour which will not be significantly altered by pressure - this mode arises from the (absence of) lattice symmetry.

Lotter and Wittig have previously observed that T_c begins to fall above p^* without an apparent

jump, and we confirm this behaviour. They previously ascribed this observation to a Lifshitz transition in the Fermi surface. McMahon's more recent structural measurements indicate there is no structural transition - at least at room temperature - up to 77 kbar, although it is likely an X-ray study would not be able to see so subtle a transition. Our values and behaviour of T_c agree quite well with Lotter and Wittig's results. This is something that could be investigated in further detail with high-pressure resistivity measurements in a moissanite anvil cell: the Fermi surface deformation associated with a Lifshitz transition would likely be accompanied by a change in the Hall coefficient.

It is interesting to note that p^*would appear to correspond to approximately the same pressure where $B_{c1}(0)$ reaches a maximum (Fig. 5.25). As we have remarked previously, the errors in obtaining B_{c1} are rather large. It would require careful measurements, with many finely spaced pressure points, each consisting of a large number of finely-space temperature sweeps taken ideally down to below 2 K, to check if this effect is genuine.

5.3.7 Ab initio calculations

Throughout this chapter, we have discussed at length the presence of an additional phonon (or 'phason') mode in the phonon spectrum of an incommensurate crystal. Good evidence for the theoretical and experimental existence of such phason modes has been found in other incommensurate lattices such as $HgAsF_6$ and $Sr_{14}Cu_{23}O_{41}$, but what about for incommensurate host-guest elements?

The phonon spectrum of Bi-III was calculated from first principles using a displacement-force method, based on DFT calculations done in QuantumEspresso. This work was done by Bartomeu Monserrat and Chris Pickard from the Earth Sciences Department of Cambridge University. As outlined previously, DFT calculations on incommensurate materials are, in principle, impossible, so approximants must be used. The procedure is as follows: first, a number of candidate approximants have their structures relaxed using DFT. A balance must be found between structures with the lowest energy (i.e. better approximations to the true, stable structure) and structures with higher symmetry (otherwise the phonon calculations are prohibitively slow). Once a suitable structure has been found, its phonon spectrum is calculated using a displacement-force method: the effective spring constant is calculated from the force on each atom, and the resulting network of springs used to calculate the phonon spectrum.

With this technique, we demonstrate unambiguously the existence of the additional low-energy mode arising from the incommensurate structure. There are numerous complexities to such a calculation. In particular, the use of a smaller 21-atom approximant unit cell, which corresponded to a lower-energy structure (and much faster phonon spectrum calculations), was found to lead to inaccurate results because the chain-host interaction remained strong, as evidenced by a textured energy surface for motion of the chains with respect to the host lattice. The use of a 42-atom approximant structure containing two chains was necessary to obtain a flat energy landscape, suggesting as expected that the lack of chain-host interactions is truly a consequence of the incommensurate nature of the structure. This two-chain structure should possess not one but two phason modes, both strongly dispersive in the ΓZ direction but nearly flat in the ΓX direction (where X and Z are

respectively at $(1\,0\,0)$ and $(0\,0\,1)$ in the Brillouin zone).

Precisely the expected behaviour is observed. As can be seen in Fig. 5.28, at the Γ point of the first Brillouin zone, in addition to the usual three acoustic phonon modes (arising from dimensionality of the crystal), there are two additional phason modes. They are slightly gapped at the $\Gamma-$point, as predicted by theory and observed in $Sr_{14}Cu_{23}O_{41}$ [161]. While it was not possible to obtain a quantitative value for the electron-phonon coupling of each mode to compare with experiment, the value of λ calculated for the phason mode was estimated to be around $10\times$ larger than for any other single mode, supporting the suggestion that the flat phason mode gives rise to strong electron-phonon coupling.

Fig. 5.28 demonstrates that there are a few additional complexities to the phonon spectrum. In particular, it appears that there is hybridisation between one phason mode and one acoustic mode. A phason mode with a low-energy gap at Γ (dashed red line) rises to quite high energy at X, while a single acoustic mode with zero energy at Γ has its energy dramatically reduced at X with respect to the other two acoustic modes. At X, the energy of this "acoustic" mode is identical to the other, unhybridised phason mode. A projection of the atomic oscillation of the modes along the chain direction, conducted by Bartomeu Monserrat, demonstrates that precisely this hybridisation is occuring (Fig. 5.29): at X, both modes with low energy correspond to oscillations along the c-direction.

The electron-phonon coupling contribution from the phason modes can also be estimated from the ab initio phonon spectrum; obtaining an accurate value is impossible, as the (very large) supercell can only be sampled at a small number of $q-$points, but it was found that the contribution to λ from the phason modes was around an order of magnitude larger than from the other modes.

Calculations of the optical plasma frequency Ω_p for Bi-III, required to estimate λ, were conducted by Diandian Wang in the Quantum Matter group, using DFT as implemented by Wien2K. The OPTIC package was used to calculate Ω_p including spin-orbit coupling. A 32-atom approximant based on the In_5Bi_3 unit cell was used for detailed calculations, possessing $c_H/c_G = 1.333$ (the real structure has $c_H/c_G = 1.309$); the calculated Ω_p is not strongly dependent on the approximant (Fig 5.30). Due to the complexity of the structure, a very large number of k-points (in excess of 5,000) was required to obtain convergence in the value of Ω_p. The converged value (at 10,000 k-points) was $\Omega_{p,eV} = 3.5 \pm 0.4$ eV, where the error reflects the span of $\Omega_{p,x}$ and $\Omega_{p,z}$. We use $\Omega_p = \frac{1}{3}(2\Omega_{p,x} + \Omega_{p,z})$, as $\Omega_{p,x} = \Omega_{p,y}$. Assuming our samples are polycrystalline, we would expect the experimentally-observed value to similarly be an average over Ω_p. Arguably, an average over the square of the plasma frequency would be more appropriate (as this reflects the carrier density which is the underlying physical quantity); this gives the same result to within error. Fig. 5.30 shows the convergence as a function of k-point number.

5.3.8 Superconducting properties and electron-phonon coupling

As discussed in Section 2.3.4, the gradient of the linear part of the resistivity provides an estimate of the electron-phonon coupling strength. This can be compared with results from band structure calculations and the measured parameters of the superconductivity. Table 10 summarises the salient physical properties obtained from SQUID measurements and ab initio calculations. Because the

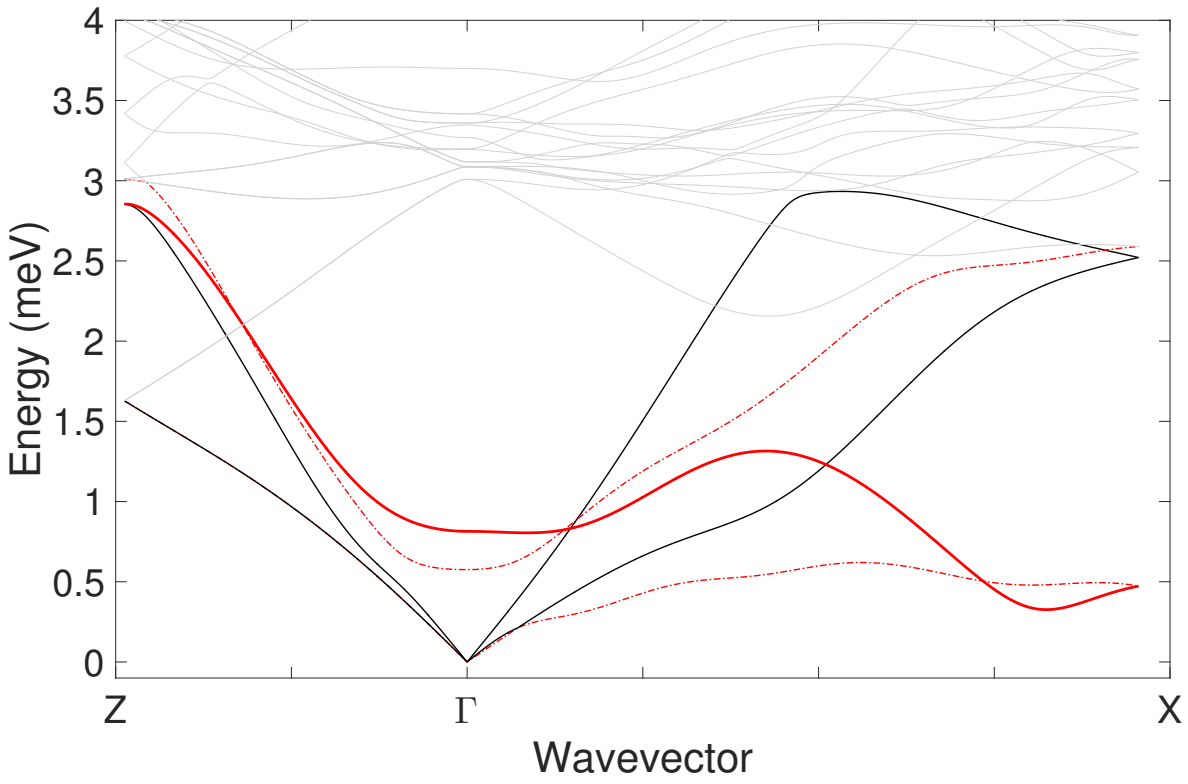

Figure 5.28: Calculated phonon spectrum for Bi-III using a 42-atom approximant unit cell containing two chains and an $8 \times 1 \times 1$ supercell. Light grey lines show optical phonon modes; there are a large number as the unit cell is large, and they extend to an energy of 12 meV, not shown here. Black lines are the two conventional acoustic phonon modes. Solid red line is a phason mode corresponding to chains moving through the host latice: this is strongly dispersive in the ΓZ direction (along the chains), but almost flat in the ΓX-direction (the $a-b$ plane), exactly as predicted. The dashed red lines correspond to the hybridised acoustic and phason mode: at Γ the lower dashed line is acoustic in character and the upper line corresponds to the sliding mode, while at X the two modes have swapped character.

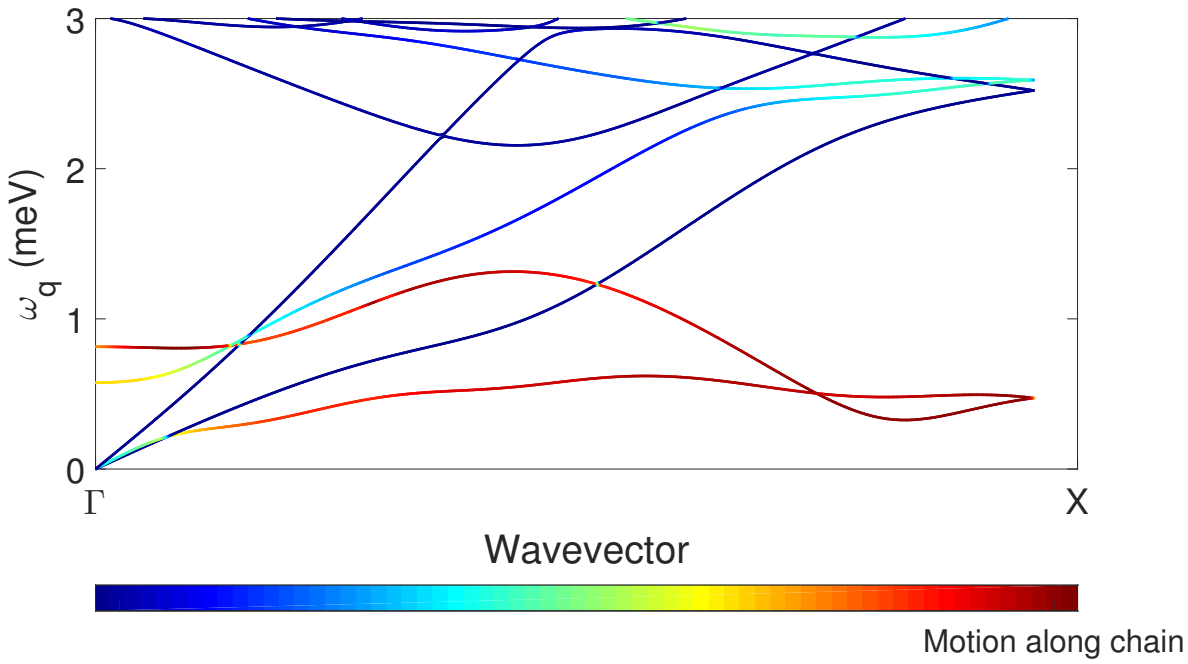

Figure 5.29: Phonon dispersion projected along the chain direction, demonstrating the clear hybridisation of the low-energy acoustic mode and the second phason mode. Near $q = X$, the character of both low-energy modes is clearly that of motion along the chain. Only the 10 lowest-energy modes are shown for clarity.

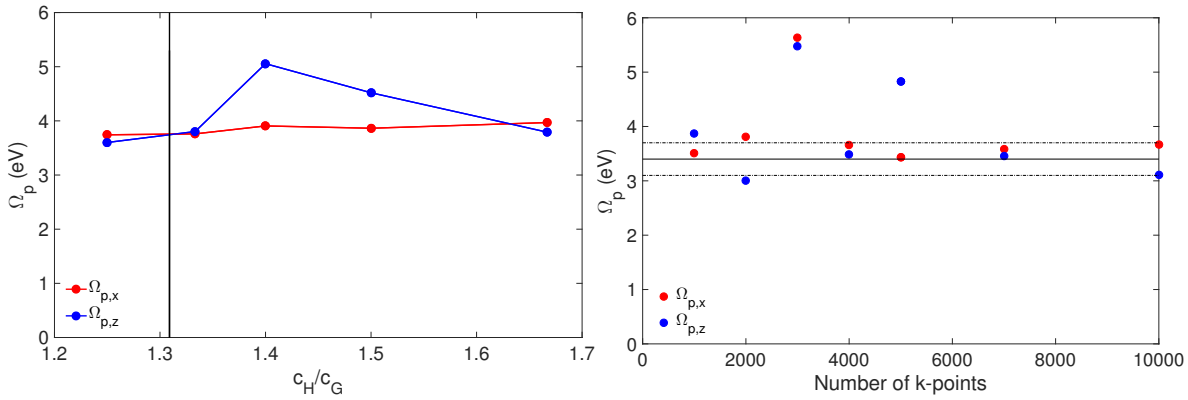

Figure 5.30: Calculated value of the plasma frequency obtained from DFT. The result is not strongly dependent on the approximant: different structures, with different numbers of atoms in the unit cell and different c_H/c_G ratios, give similar results (left) when calculated with 1000 $k-$points. Solid vertical line shows the experimental value of c_H/c_G for Bi-III. Very large numbers of k-points are required to achieve convergence using the $c_H/c_G = 1.333$ modified In_5Bi_3 approximant (right): solid (dashed) horizontal lines show the value (error), based on the mean value at 10,000 $k-$points..

Property	Symbol	Value
Lower critical field	B_{c1}	15 ± 5 mT
Plasma frequency	Ω_p	$\Omega_p = 3.5 \pm 0.4$ eV

Table 10: Physical properties of Bi-III, measured from SQUID anvil cells or obtained from ab initio calculation.

results from the resistivity differ quite considerably at different pressures, we consider them on a point-by-point basis, as will be discussed later. The relevant properties are $B_{c2}(0)$, for which we use the value obtained from the Ginzburg-Landau fit, the transition temperature T_c, which we take as the observed zero-field value, and the zero-temperature resistivity ρ_0 and gradient $\rho' = d\rho/dT$, obtained from linear fits from 7.5 to 10 K; these properties are summarised in Table 8. As remarked previously, given the small region of temperature over which the resistivity is linear, these values should probably be considered an upper limit to ρ'.

From the measured superconducting critical fields, we obtain the superconducting coherence length ξ_{sc}, Ginzburg-Landau parameter κ_{sc}, and superconducting London penetration depth λ_{sc}, using the following standard relations [178, 179]:

$$B_{c2} = \frac{\Phi_0}{2\pi\xi_{sc}^2} \tag{5.13}$$

$$\kappa_{sc} = \frac{\lambda_{sc}}{\xi_{sc}} = \sqrt{\frac{B_{c2}}{2B_{c1}}} \tag{5.14}$$

Additionally, using the DFT plasma frequency, we can obtain information about the Fermi surface and the electron-phonon coupling. Using Allen's method, we calculate the electron-phonon coupling [16, 17]:

$$\lambda = \frac{\hbar\epsilon_0\Omega_p^2\rho'}{2\pi k_b}. \tag{5.15}$$

This simplifies to:

$$\lambda = 0.248\Omega_p^2\rho' \tag{5.16}$$

where Ω_p is in eV and ρ' in $\mu\Omega$ cm K^{-1}.

Using the definition of the plasma frequency $\Omega_p^2 = ne^2/\epsilon_0 m$, and assuming a spherical Fermi surface $\left(n = k_F^3/3\pi^2\right)$, we can estimate the Fermi wavevector:

$$k_F = \left(\frac{3\pi^2\epsilon_0 m_e\Omega_p^2}{e^2}\right)^{1/3}. \tag{5.17}$$

The spherical Fermi surface assumption is not perfect, as $\Omega_{p,x} \neq \Omega_{p,z}$, but the errors are only ~ 10 %. Using this spherical Fermi surface approximation we can also estimate the low-temperature scattering length l_0 from the residual resistivity ρ_0. Using that $l = \tau v_F = \tau\hbar k_F/m$, and $\rho = m/ne^2\tau$, we obtain:

$$l_0 = \frac{3\pi^2\hbar}{k_F^2 e^2\rho_0}. \tag{5.18}$$

Finally, using the McMillan equation, with the correction of Allen and Dynes, we can obtain an estimate for the characteristic phonon temperature:

$$\Theta_{ln} = 1.2T_c e^{\frac{1.04(1+\lambda)}{\lambda-\mu^*(1+0.62\lambda)}} \tag{5.19}$$

In Table 11, we give the values of these properties for Bi-III at the four measured pressure points. Errors were estimated by analytically propagating the errors of Tables 10 and 8, except in the case of Θ_{ln} (which is a rather complicated function of λ), where we assumed the fractional error in Θ_{ln} is the same as that in λ. The significant errors in Ω_p and B_{c1} overwhelmingly dominate the error propagation.

5.3.9 Discussion of superconducting properties

From Table 11 we would conclude that Bi-III is unambiguously a type II superconductor ($\kappa_{sc} \approx 9$) between the dirty and clean limit, with l_0 being at least $2.7 \times \xi_{sc}$. This implies that the surprisingly high B_{c2} is an intrinsic property of Bi-III, and is not promoted by disorder. Such an assumption requires that the Fermi surface can be approximated as a single spherical sheet, with a carrier density given accurately by the ab initio plasma frequency. An experimental determination of the carrier density could be performed with Hall effect measurements. The clean-limit hypothesis is lent support by the observation that B_{c2} is almost independent of ρ_0 despite the latter varying by nearly an order of magnitude: in the dirty limit we have $\xi_{sc} \sim l_0^{1/2}$ and therefore $B_{c2} \sim \rho_0$, so would expect a very significant enhancement in B_{c2} for the most disordered samples.

Most surprising is the very large value of λ - in excess of 2.5 for 3 out of 4 pressure points. From this we would conclude Bi-III is a strong-coupling superconductor. As discussed above, this should not be a surprise given the unusual phonon spectrum. The phonon temperature $\Theta_{ln} \approx 40 - 50$ K is rather low, which is again to be expected based on the phonon spectrum. The value of Θ_{ln} obtained from the superconducting parameters is broadly consistent with the temperature regime of linear resistivity, which should extend above $\sim \Theta_D/4$; we observe linear resistivity up to around 10 K implying a phonon temperature of at most 40 K (this assumes $\Theta_{ln} \approx \Theta_D$; whether this holds will depend on the details of the phonon spectrum). Above this temperature the steep curvature of the resistivity likely arises from phonon anharmonicity, which will be promoted in systems with a low Θ_{ln}.

The dominant uncertainties in the numerical values arise from the values of Ω_p and B_{c1}. We use $B_{c1} = 15 \pm 5$ mT, but an examination of Fig. 5.25 suggests that if the pressure dependence of B_{c1} is a real phenomenon, at these pressures a value $B_{c1} = 12 \pm 2$ mT is more appropriate. In addition, our value for Ω_p - on which λ depends sensitively - is only approximate. Reference to Fig. 5.30 suggests it is may be an underestimate - if we neglect the two points which are clearly outliers, a better estimate of Ω_p may be ~ 3.6 eV. This small change increases λ by ~ 4 %. Using the lower value of B_{c1} increases ξ_{sc} and κ_{sc} by ~ 11 %; the other parameters do not change significantly.

The point at 31.4 kbar would appear to be a clear outlier in terms of the resistivity gradient, and therefore λ. It is tempting to ascribe this to some experimental complication or a simple mistake in scaling factors, but this is not the case. The much lower value of ρ' for this point (~ 30 % lower than

Property	Symbol	Bi #10.11 - 26.7 kbar	Bi #10.11 - 31.4 kbar	Bi #1 - 26.7 kbar	Bi #1 - 28.6 kbar
Ginzburg-Landau parameter	κ_{sc}	9.0 ± 1.5	9.0 ± 1.5	9.5 ± 1.6	9.0 ± 1.5
Superconducting coherence length (nm)	ξ_{sc}	11.69 ± 0.02	11.5 ± 0.02	11.000 ± 0.008	11.59 ± 0.05
Superconducting London penetration depth (nm)	λ_{sc}	105 ± 17	104 ± 17	105 ± 17	104 ± 17
Electron-phonon coupling strength	λ	2.6 ± 0.6	1.9 ± 0.4	2.8 ± 0.7	2.7 ± 0.6
Logarithmic phonon temperature (K)	Θ_{ln}	42 ± 10	52 ± 12	41 ± 10	42 ± 10
Fermi wavevector Å^{-1}	k_F	0.65 ± 0.05	0.65 ± 0.05	0.65 ± 0.05	0.65 ± 0.05
Scattering length (nm)	l_0	178 ± 27	31 ± 5	29 ± 5	62 ± 9

Table 11: Properties of Bi-III calculated from our measured and ab initio values. The values for k_F depend only on the optical plasma frequency Ω_p so are unchanged from point to point.

	T_c (K)	B_{c2} (T)	Reference
Niobium	9.25	0.404	[181]
Vanadium	5.43	0.27	[182]
Technetium	7.77	0.262	[183]
Bi-III	7.05 ± 0.05	~ 2.5	This work

Table 12: Transition temperatures and upper critical fields for the three ambient-pressure superconductors niobium, vanadium and technetium, and our measured values for Bi-III.

Property	Symbol	Pb	Bi-III
Transition temperature	T_c	7.195 K	7.05 ± 0.05 K
Critical field	B_c	0.080 T (B_c)	2.5 T (B_{c2})
Electron phonon coupling strength	λ	1.55	$1.9 - 2.8$
Resistivity gradient	ρ'	0.071 μΩ cm K^{-1}	$0.6 - 0.9$ μΩ cm K^{-1}
Plasma frequency	Ω_p	9.12 eV	3.5 eV
Phonon temperature	Θ_{ln}	56 K	$\sim 40 - 50$ K

Table 13: Comparison of the properties of Bi-III and Pb at ambient pressure; data for Pb is taken from [16, 35, 184]. Pb is a type I superconductor characterised by a single critical field B_c.

for the other points) was observed in multiple cooldowns on the same cell, including measurements on two different cryostats. All yielded the same gradient to within 4 %. In addition, note that the 300 K value of this pressure point's resistivity agrees well with the three other pressure points (Fig. 5.6). We would speculate that it may be related to distance from the structural phase transition: this point is at the highest pressure by a considerable factor. Further careful measurements should investigate $\rho'(p)$, although this may be challenging in a piston cylinder cell where the upper limit of the accesible pressures is < 35 kbar.

5.3.10 Comparison to other materials

The large fields required to suppress superconductivity imply that superconductivity in Bi is of type II. Type II superconductivity is the norm among superconducting alloys, but is exceptionally rare among the elements [180]. Table 8 compares the properties of the three ambient-pressure type II superconductors to those of Bi-III; of particular note is the high critical field for Bi-III, $6\times$ larger than that of niobium.

Bismuth's nearest neighbour in the periodic table bears an interesting set of similarities to Bi-III. Elemental lead at ambient pressure is also a strong-coupling superconductor with $T_c = 7.20$. Its parameters, compared to those of Bi-III, are summarised in Table 13. In Fig. 5.31, we plot the data for Bi-III compared to that measured by us for lead. Despite the very similar values of T_c, the differences are striking. The crossover from $\rho \sim T^5$ to $\rho \sim T^1$ for Pb as T increases is clear, in contrast to the negative curvature in Bi-III.

One might question why - given that T_c and λ are so similar - Pb is a type I superconductor while Bi-III is type II, with such a large critical field. We would suggest that this arises primarily from discrepancies in the plasma frequency (or, equivalently, carrier density). From Ginzburg-Landau

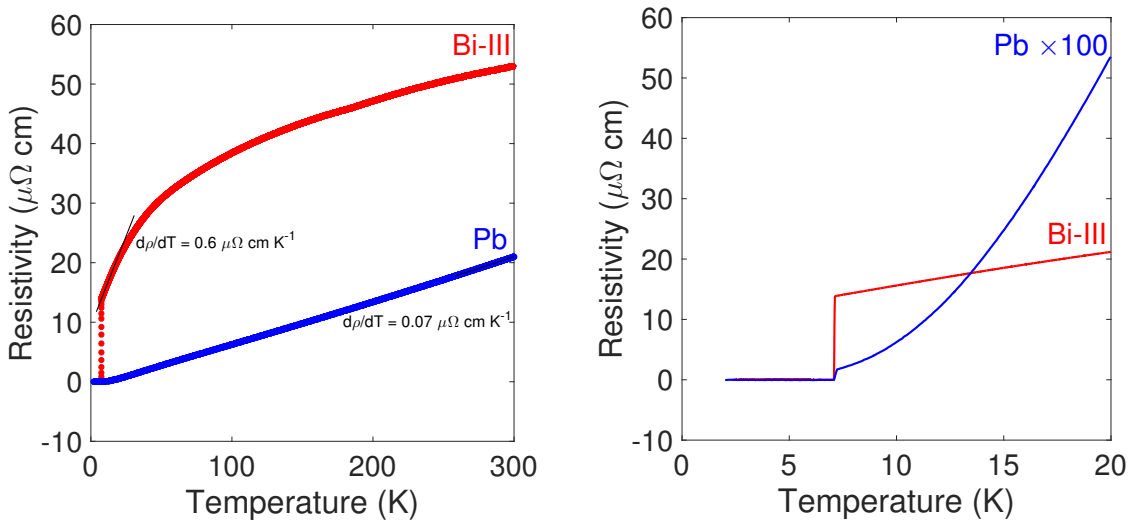

Figure 5.31: Resistivity of Bi-III at 31.4 kbar compared to Pb, from 2 to 300 K (left) and below 20 K (right). Despite the nearly identical values of T_c, the similarly high values of λ, and the nearness in the periodic table, $\rho(T)$ is qualitatively very different.

theory, we have (assuming equivalence between the superfluid density and carrier density, $n_s = n/2$):

$$\lambda_{sc} = \frac{(1+\lambda)^{1/2} c}{\Omega_p}. \tag{5.20}$$

where c is the speed of light. A large plasma frequency will then tend to reduce λ_{sc} and κ_{sc}, thereby promoting type I superconductivity.

The alloy In_5Bi_3 is structurally very similar to a commensurate version of Bi-III, as noted by McMahon [13]; in In_5Bi_3 the host and guest lattices do match up ($c_H/c_G = 4/3$, compared to $c_H/c_G = 1.309$ in Bi-III), but the guest atoms are in a C-face-centred primitive unit cell rather than a body-centred one. In_5Bi_3 is also a type II superconductor: $T_c = 4.18$ K and $B_{c2} = 0.2$ T [185]. Mori *et al.* estimate λ from the McMillan equation, giving $\lambda \approx 0.9$. [185]

Existing literature on In_5Bi_3 is rather sparse, and we could not accurately obtain a value of ρ' from published graphs, therefore we resolved to obtain our own data. Jiasheng Chen of the Quantum Matter group was successful in producing polycrystalline samples in an RF furnace. In all respects they agree very well with literature data: with an RRR of 33 they are comparable in quality to previous published results [185].

The absolute value of the resistivity we observe to be 104 μΩ cm at room temperature. This agrees fairly well with the value of $\sim$ 110 μΩ cm given by Mori *et al.* [185] and $\sim$ 112 μΩ cm of Crucenau *et al.* [187]. The 5 % discrepancy can easily be explained by uncertainties in the geometric factor arising from the finite-sized contacts. An early report of superconductivity in In_5Bi_3 instead gives a value of 60.2 ± 0.6 μΩ cm at 300 K, and a similar T_c of 4.16 K [188]; this rather precise value would appear to be an outlier.

If we scale our data to that of Mori *et al.* at 280 K (their highest measured temperature) the

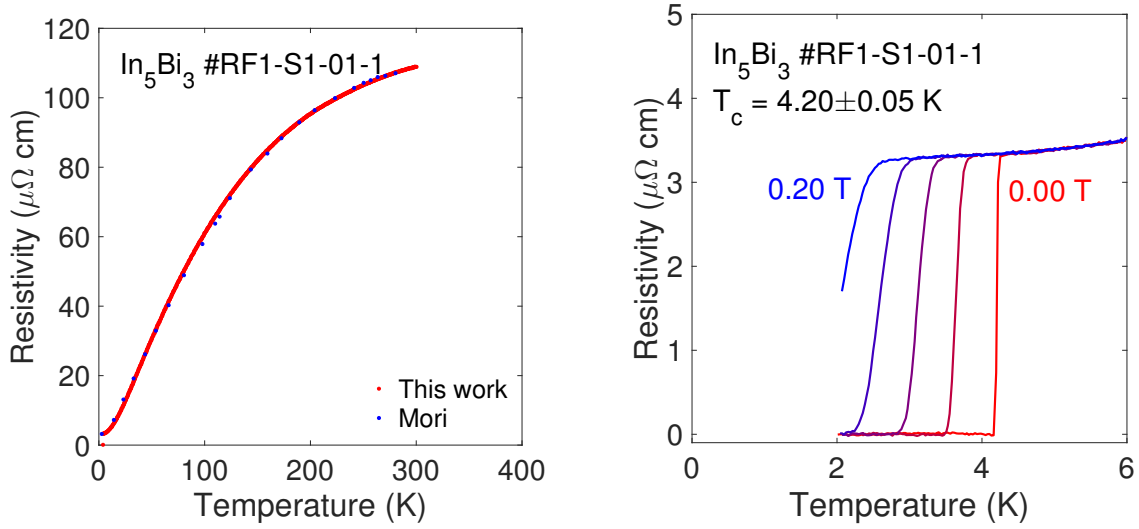

Figure 5.32: Left: Measured resistivity of In_5Bi_3 (red points), after rescaling our data by $\times 1.052$ to match it to Mori's at 280 K. Blue points indicate data digitised from Fig. 5 of [186]; as can be seen, agreement is excellent. Right: low-temperature superconducting transition in our samples of In_5Bi_3 in applied fields from 0.00 to 0.20 T in 0.05 T increments.

qualitative and quantitative agreement in $\rho(T)$ is essentially exact, as demonstrated in Fig. 5.32. Our samples' superconducting properties also agree well with the literature.

We have taken specific heat measurements of In_5Bi_3. They indicate a bulk superconducting transition at $T_c = 4.17 \pm 0.03$ K (the resistive $T_c = 4.20 \pm 0.05$ K), and a low-temperature (normal-state) electronic heat capacity coefficient $\gamma = 16.7 \pm 0.9$ mJ mol^{-1} K^{-2} (Fig. 5.33). As expected, in zero field the electronic heat capacity tends to zero at the lowest temperatures as the sample is superconducting.

The marked saturation in $\rho(T)$ clearly observable in Fig. 5.32 has been remarked on before [185], but never adequately explained. Mori *et al.* invoked the saturating-resistor model based on the Ioeffe-Regel criteria (see Section 2.3.5); an alternative explanation would be phonon anharmonicity. The similarities to Bi-III are striking, and investigations of this little-studied material at ambient pressure could provide further insight into the incommensurate host-guest elements.

We applied the method of Allen to estimate the electron-phonon coupling in In_5Bi_3 and lead. For these materials, heat capacity measurements are available at zero pressure, and this can be used as a check on λ [16, 17]. The heat capacity calculated from DFT is proportional to the density of states at the Fermi level including all electron mass enhancement effects *except* electron-phonon coupling, thus the ratio of the experimental to DFT heat capacities is equal to $\lambda + 1$. We use [16, 17]:

$$\lambda_{tr} = 0.248 \Omega_p^2 \rho' \tag{5.21}$$

$$\lambda_\gamma = \frac{\gamma_{exp}}{\gamma_{DFT}} - 1 \tag{5.22}$$

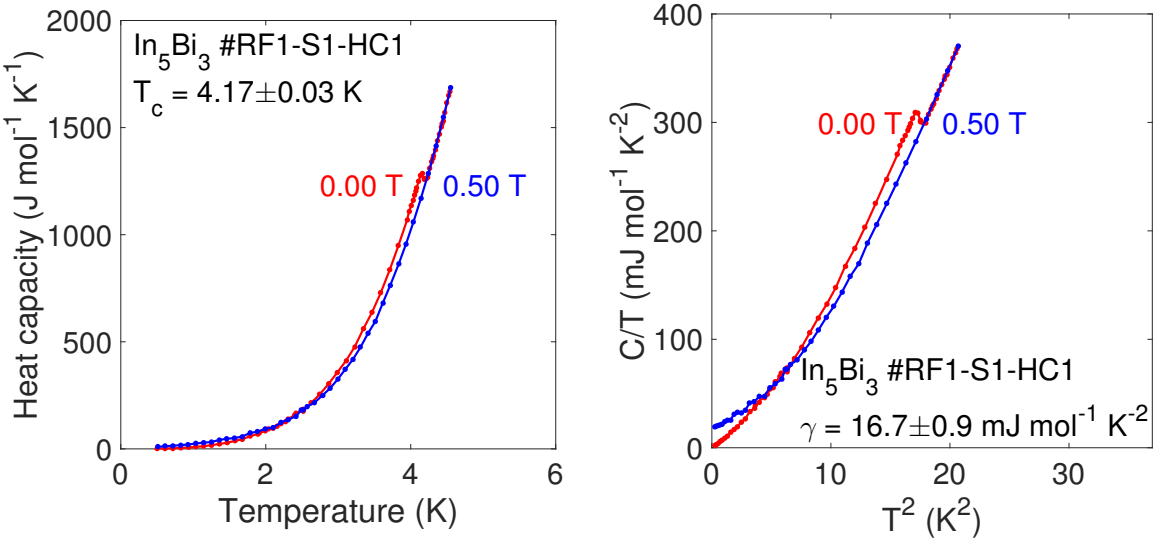

Figure 5.33: Left: Measured heat capacity of In_5Bi_3 in zero field and $B > B_{c2}$, down to 0.4 K. The superconducting transition at $T_c = 4.17 \pm 0.03$ K is clearly visible. Right: plot of C/T against T^2. A straight-line fit to the low-temperature data yields the electronic specifi heat coefficient $\gamma = 16.7$ mJ mol^{-1} K^{-2}.

where Ω_p is the optical plasma frequency in eV, ρ' is the resistivity gradient in $\mu\Omega$ cm K^{-1}, γ_{exp} is the experimental heat capacity, and γ_{DFT} is the heat capacity calculated from DFT. DFT calculations were performed by Malte Grosche and Diandian Wang. Results are shown in Table 14. As can be seen, the agreement between λ_{tr} and λ_γ is fairly good, with the discrepancy being in general < 15 %. This should not be a surprise; Allen provides a table of such values for many elements and remarks on the generally fairly good agreement [16].

For In_5Bi_3, there is no secure literature value available for any of the parameters, so we rely on our own measurements. The quoted Ω_p is an average of $\Omega_{p,x}$ and $\Omega_{p,z}$ as described for the Bi-III, with a grid of 20,000 $k-$points including spin-orbit coupling; it may be that the values change for finer $k-$grids, and λ_{tr} is sensitively dependent on Ω_p. The value of γ_{DFT} is set by $N(E_F)$, and the DFT calculations show this is rather jagged near E_F, so the value for γ_{DFT} may be incorrect by about 15 %. The inaccuracies in the measured heat capacity appear small, but this is based on only a single measurement and should be checked with other samples . Finally, the value of ρ' is rather uncertain. As Fig. 5.32 shows, $\rho(T)$ exhibits strong negative curvature; we therefore take ρ' as the maximum in $d\rho/dT$, but this may not correctly account for the curvature. Our value of the 300 K resistivity lies within ~ 5 % of most literature values but is significantly larger than that of Ullmaier *et al.* [188]. We would note that considering only a 15 % overestimate of γ_{DFT} would bring λ_γ into agreement with λ_{tr}. Mori *et al.* give the value of λ estimated from the McMillan equation and T_c as 0.9, which agrees quite well with our λ_γ. However, this relies on an estimate of the Debye temperature which does not match well with that required for a Bloch-Gruneisen fit to the resistivity in the presence of saturation, which is ~ 300 K [185]. This would imply that we never obtain the high-temperature limit $T \gtrsim \Theta_D/4$ before the effects of saturation become significant; in the absence of a detailed

model for the saturation, we cannot make further progress.

Bi-III shows marked similarities with superconducting amorphous bismuth (a-Bi). Amorphous films formed by evaporation onto low-temperature substrates are superconducting with $T_c = 6.1$ K and extremely strong electron-phonon coupling, $\lambda = 2.46$ [192, 193]. The Eliashberg function $\alpha^2F(\omega)$ of a-Bi has been previously measured with tunnelling experiments, and found to be dominated by very low-energy phonon modes giving rise to strong electron-phonon coupling [193]. The average phonon frequency $\langle\omega\rangle$ was 2.86 meV, corresponding to a phonon temperature of 31.5 K. The upper critical field B_{c2} of a-Bi is 2.6 T, startlingly near to our value for Bi-III [194].

Such strong similarities are unsurprising: a-Bi and Bi-III are both composed of the same element, both lack a unit cell, and both likely possess low-energy phonon modes. However, we do not believe our Bi-III is amorphous bismuth stabilised by pressure: our T_c is significantly higher than reported for a-Bi, our measured low-temperature resistivity is lower by a factor of 10, and the Bi-III phase appears stable from 200 mK to 300 K (as indicated by the continuous $\rho(T)$ trace), while a-Bi converts to crystalline Bi-I above 20 K [192, 195].

Our results for Bi-III can perhaps be interpreted as a more extreme case of the situation occurring in the quasi-scutterudite $(Ca_xSr_{1-x})_3Rh_4Sn_{13}$ [26]. This material is close to a structural transition caused by a soft phonon mode; the low-energy phonon mode gives rise to $T-$linear resistivity at low temperatures, pronounced negative curvature to the resistivity and superconductivity with $T_c \approx 8$ K. In $(Ca_xSr_{1-x})_3Rh_4Sn_{13}$ the soft phonon mode falls to low energy only at the M-point of the Brillouin zone $\left(q = \left(\frac{1}{2}\ \frac{1}{2}\ 0\right)\right)$, while for Bi-III we expect it to remain at low energies throughout an extended region of reciprocal space. A similar argument applies for $(Ca_xSr_{1-x})_3Rh_4Sn_{13}$, also a strong-coupling superconductor [196, 197]. In Table 14 we also show the values of λ_{tr} and λ_γ for $Ca_3Rh_4Sn_{13}$, which agree well.

Another related family of materials are the strong-coupling A15 superconductors such as Nb_3Sn and V_3Si. These, again, possess similar properties to Bi-III, likely for similar reasons. They are known to have high values of λ, and as a result all possess high values of $T_c \approx 20$ K and high upper critical fields, as well as pronounced saturation in the resistivity. Some attempts have been made to quantitatively calculate the details of the resistivity saturation by Gunnarsson *et al.* [32].

Of final and most particular interest is a comparison to other incommensurate host-guest materials. The first of these is the prototypical compound $Hg_{3-\delta}AsF_6$. As mentioned previously, this material is also superconducting (T_c =4 K). There has been a prolonged debate in the literature as to whether this is bulk superconductivity or surface superconductivity of extruded Hg, but magnetisation measurements imply superconductivity does arise from the bulk.

Secondly, there are the other incommensurate host-guest elemental structures formed under pressure. Isoelectronic Sb-II forms a host-guest phase above 88 kbar, with $T_c = 3.6$ K; the resistivity has not been measured in detail [162]. The prototypical incommensurate host-guest element Ba-IV is also superconducting. Bridgman cell measurements of the resistivity indicate it is markedly similar to our results for Bi-III: there is a very steep gradient ρ' at low temperatures, and extremely pronounced negative curvature (Fig. 5.34) [150]. If our hypothesis regarding strong-coupling superconductivity caused by the low-energy phason mode is correct, we would expect both materials to be strong-coupling type II superconductors.

Material	Ω_p(eV)	γ_{DFT} (mJ mol^{-1} K^{-2})	ρ' ($\mu\Omega$ cm K^{-1})	γ_{exp} (mJ mol^{-1} K^{-2})	References	λ_{tr}	λ_{γ}
Pb	8.91	1.26	0.071	3.0	[16, 189, 190]	1.40	1.38
$Ca_3Rh_4Sn_{13}$	2.53	27.84	$0.8-0.9$	60	[26, 191]	$1.27-1.43$	1.16
In_5Bi_3	2.68	8.95	$0.66-0.76$	$15.8-17.6$	This work	$1.18-1.35$	$0.76-0.97$
Bi-III	3.5	49.26	$0.62-0.91$	-	This work	$1.9-2.8$	-

Table 14: Comparison of electron-phonon coupling strength obtained from gradient of the resistivity and heat capacity. The values of Ω_p and γ_{DFT} were calculated using Wien2K and the OPTIC package. The values of ρ' and γ_{exp} were taken from literature data or measured by us.

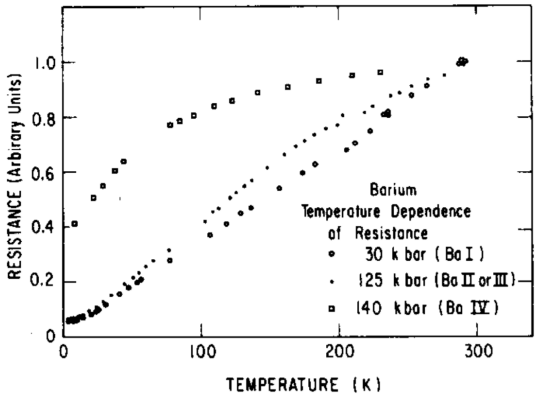

Figure 5.34: Resistivity of barium at high pressures, taken from [150]. At 140 kbar barium is in the Ba-IV phase; the resistivity exhibits marked negative curvature of a simple shape to that we observe for Bi-III. Ba-IV is known to be superconducting, and was recently found to be a host-guest lattice. [13, 150, 149].

5.4 Conclusions

We have presented an investigation of the superconducting and normal-state properties of the incommensurate host-guest phase Bi-III, with resistivity measurements in a piston cylinder allowing highly hydrostatic conditions. The key results are:

1. Bi-III is a type II superconductor with an upper critical field $B_{c2} = 2.5 \pm 0.2$ T and a lower critical field $B_{c1} \approx 0.01$ T, giving it a Ginzburg-Landau parameter of around 9. Both T_c and B_{c2} appear by pressures within the range $26.7 - 31.4$ kbar.

2. Measurements on the DC magnetisation have been taken to around 100 kbar. Our pressure dependence $T_c(p)$ is in good agreement with the surprising result obtained by Lotter and Wittig using AC susceptibility, being (unexpectedly) constant up to ~ 50 kbar, then exhibiting a discontinuity in the gradient but not the value of T_c [137]. Mechanisms for such behaviour remain unclear and would be interesting to explore.

3. The physical properties of Bi-III can be well explained using an unusually large value of the electron-phonon coupling strength $\lambda \approx 1.9 - 2.8$, and a Debye temperature of a few tens of kelvin. Such strong electron-phonon coupling consistently explains the low-temperature gradient of the resistivity, the small linear region, the significant negative curvature at higher temperatures, the enhancement of $B_{c2}(0)$ with respect to the BCS value from the WHH model, and the type II nature of the superconductivity,

4. This strong electron-phonon coupling may be a consequence of the phason mode that arises directly from the incommensurate nature of the crystal structure. We have presented a heuristic argument for why such a phason mode should remain at low energies over a significant region of the Brillouin zone, and explained why this enhances electron-phonon coupling. We have then demonstrated that precisely such a mode does occur using an ab initio calculation

of the phonon spectrum, and argued that our experimental data provides some evidence for this.

5. Such a phason mode is a generic property of incommensurate host-guest elemental structures. We would expect other examples to also be strong coupling superconductors.

5.5 Outlook

We have only found indirect evidence of the impact of the phason mode on the properties of Bi-III. The most obvious experimental tool for direct measurement would be inelastic neutron scattering. Neutron scattering measurements have long been used to determine phonon spectra for incommensurate lattices, and the one-dimensional phason mode in $Sr_{14}Cu_{23}O_{41}$ has recently been observed directly (see Fig. 5.5) [161]. We would expect the phonon spectrum for Bi-III to be similar; this could be ascertained with high-pressure neutron scattering measurements. While high-pressure inelastic neutron scattering is challenging, such measurements can be done. An alternative tool is inelastic x-ray scattering, which has previously been used to probe the high-pressure phonon spectrum of Rb [198]. Measurements of the phonon spectrum were made along the q_c direction, where it was found that the dispersion agreed well with the simple linear chain model used to introduce the theoretical topic of phonons, as expected for non-interacting one-dimensional chains. Measurements in the q_a direction should be made for Bi, if a single crystal could be obtained. An alternative technique could be Raman scattering, which allows observation of phonon modes and is more straightforward to do under pressure. Such experiments have already been conducted on the incommensurate host-guest phase of Sb, though the results were inconclusive [162].

Bismuth is the most easily accessible incommensurate host-guest element due to the low pressures required. The physical properties (and particularly the resistivity) of very few other such materials have been measured, though it would appear that many elemental host-guest structures are superconducting, a fact which may not be coincidental [199, 150, 152, 151]. The resistivity of Ba-IV ($T_c = 4$ K) has been measured, and appears very similar to our own data, exhibiting a steep gradient at low temperatures and a pronounced curvature [150]. This suggests that our interpretation of the resistivity of Bi-III - a steep gradient due to large λ and small Θ_{ln}, strong curvature due to significant anharmonicity - may be applicable to Ba-IV, and perhaps other incommensurate host guest elements. Two obvious candidate elemental phases are Ba-IV (the prototypical incommensurate host-guest element), and Sb-II (isoelectronic to Bi, with similar structural and electronic properties). We would expect both materials to exhibit a similar $\rho(T)$, and similar type II strong coupling superconductivity. The pressures required for such measurements are within the range of a diamond anvil cell.

Finally, it would be interesting to investigate the physical properties of host-guest lattices when the material in question is a compound rather than an element. Alloying of Bi with isoelectronic antimony has long been used to study the semimetal-to-semiconductor transition which occurs in the Bi-I phase under pressure, and these $Bi_{1-x}Sb_x$ alloys have recently attracted renewed interest as topological insulators [88]. It has been shown that, with sufficiently high pressures, such alloys also undergo a transition to an incommensurate host-guest phase [200]. In itself this is unsurprising, as

bismuth and antimony both form such phases under pressure; one might expect that the transition pressure would simply increase from 27 to 86 kbar with increasing x. However, the Bi-III and Sb-II phases are also both superconducting; it therefore seems very likely that $Bi_{1-x}Sb_x$ compounds, when driven into the host-guest phase by applied pressure, would also be superconducting (and, again, presumably a type II strong coupling superconductor). This has never been tested experimentally, and in fact may provide rather low-hanging fruit: the equilibrium between Bi and Sb solid solutions is complex, and pressure may drive a phase separation which means that for $x \leq 0.2$, the critical pressure required to produce is only ~ 28 kbar, accessible by high-quality piston cylinder cell measurements [200]. We would expect the presence of Sb to slightly suppress the superconducting transition temperature with respect to pure Bi; the resulting host-guest alloy may be significantly more disordered, which could provide more pinning centres and result in a much higher B_{c2}.

To summarise, the study of the incommensurate host-guest systems has only just begun. There are many further measurements necessary to understand the impact of such an unusual phonon spectrum on the measurable properties. The emergence of superconductivity seems a common theme; the details of that superconductivity, and the implications for the normal state, have yet to be worked out.

References

[1] J. Bardeen, L. N. Cooper, and J. R. Schrieffer. Theory of Superconductivity. *Physical Review*, 108(5):1175–1204, December 1957.

[2] Jiasheng Chen, Konstantin Semeniuk, Zhuo Feng, Pascal Reiss, Philip Brown, Yang Zou, Peter W. Logg, Giulio I. Lampronti, and F. Malte Grosche. Unconventional Superconductivity in the Layered Iron Germanide YFe_2Ge_2. *Physical Review Letters*, 116(12):127001, March 2016.

[3] S. S. Saxena, P. Agarwal, K. Ahilan, F. M. Grosche, R. K. W. Haselwimmer, M. J. Steiner, E. Pugh, I. R. Walker, S. R. Julian, P. Monthoux, G. G. Lonzarich, A. Huxley, I. Sheikin, D. Braithwaite, and J. Flouquet. Superconductivity on the border of itinerant-electron ferromagnetism in UGe_2. *Nature*, 406(6796):587–592, August 2000.

[4] K. Shimizu, K. Suhara, M. Ikumo, M. I. Eremets, and K. Amaya. Superconductivity in oxygen. *Nature*, 393(6687):767, June 1998.

[5] A. P. Drozdov, M. I. Eremets, I. A. Troyan, V. Ksenofontov, and S. I. Shylin. Conventional superconductivity at 203 kelvin at high pressures in the sulfur hydride system. *Nature*, 525(7567):73–76, September 2015.

[6] N. W. Ashcroft. Metallic Hydrogen: A High-Temperature Superconductor? *Physical Review Letters*, 21(26):1748–1749, December 1968.

[7] Malcolm I. McMahon and Richard J. Nelmes. High-pressure structures and phase transformations in elemental metals. *Chemical Society Reviews*, 35(10):943–963, September 2006.

[8] J-P Issi. Low Temperature Transport Properties of the Group V Semimetals. *Australian Journal of Physics*, 32(6):585, 1979.

[9] K. Behnia, L. Balicas, and Y. Kopelevich. Signatures of Electron Fractionalization in Ultraquantum Bismuth. *Science*, 317(5845):1729–1731, September 2007.

[10] Huan Yang, Benoit Fauque, Liam Malone, Arlei B. Antunes, Zengwei Zhu, Ctirad Uher, and Kamran Behnia. Phase diagram of bismuth in the extreme quantum limit. *Nature Communications*, 1(4):1–5, July 2010.

[11] P. Chudzinski and T. Giamarchi. Collective excitations and low-temperature transport properties of bismuth. *Phys. Rev. B*, 84(12):125105, September 2011.

[12] N. P. Armitage, Riccardo Tediosi, F. Levy, E. Giannini, L. Forro, and D. van der Marel. Infrared Conductivity of Elemental Bismuth under Pressure: Evidence for an Avoided Lifshitz-Type Semimetal-Semiconductor Transition. *Physical Review Letters*, 104(23):237401, June 2010.

[13] M. McMahon, O. Degtyareva, and R. Nelmes. Ba-IV-Type Incommensurate Crystal Structure in Group-V Metals. *Physical Review Letters*, 85(23):4896–4899, December 2000.

[14] N.W. Ashcroft and N.D. Mermin. *Solid State Physics*. 1976.

[15] W. L. McMillan. Transition Temperature of Strong-Coupled Superconductors. *Physical Review*, 167(2):331–344, March 1968.

[16] Philip B. Allen. Empirical electron-phonon λ values from resistivity of cubic metallic elements. *Physical Review B*, 36(5):2920–2923, August 1987.

[17] Philip B. Allen. The electron phonon coupling constant λ. In *Handbook of superconductivity*. New York, 1999.

[18] B. N. Harmon and S. K. Sinha. Electron-phonon spectral function and mass enhancement of niobium. *Physical Review B*, 16(9):3919–3924, November 1977.

[19] James R. Chelikowsky and Steven G. Louie. *Quantum Theory of Real Materials*. Springer Science & Business Media, February 1996.

[20] C. M. Hurd. *The Hall Effect in Metals and Alloys*. Plenum Press, 1972.

[21] S. Watts, S. Wirth, S. von Molnar, A. Barry, and J. Coey. Evidence for two-band magnetotransport in half-metallic chromium dioxide. *Phys. Rev. B*, 61(14):9621–9628, April 2000.

[22] A.B. Pippard. *Magnetoresistance in Metals*. Cambridge Studies in Low Temperature Physics. Cambridge University Press, 1989.

[23] Y. Zou, M. Sutherland, . Friedemann, S. M. Hayden, D. Rothfuss, A. Fleischmann, C Enss, and F. M. Grosche. Low temperature thermal and electrical transport properties of $ZrZn_2$ in high magnetic field. *Journal of Physics: Conference Series*, 391:012116, December 2012.

[24] M. Sutherland, R. P. Smith, N. Marcano, Y. Zou, S. E. Rowley, F. M. Grosche, N. Kimura, S. M. Hayden, S. Takashima, M. Nohara, and et al. Transport and thermodynamic evidence for a marginal Fermi-liquid state in $ZrZn_2$. *Phys. Rev. B*, 85(3):035118, January 2012.

[25] R. Lortz, Y. Wang, U. Tutsch, S. Abe, C. Meingast, P. Popovich, W. Knafo, N. Shitsevalova, Yu. B. Paderno, and A. Junod. Superconductivity mediated by a soft phonon mode: Specific heat, resistivity, thermal expansion, and magnetization of YB_6. *Physical Review B*, 73(2):024512, January 2006.

[26] S. K. Goh, D. A. Tompsett, P. J. Saines, H. C. Chang, T. Matsumoto, M. Imai, K. Yoshimura, and F. M. Grosche. Ambient Pressure Structural Quantum Critical Point in the Phase Diagram of $Ca_3(Sr_xRh_{1-x})_4Sn_13$. *Physical Review Letters*, 114(9):097002, March 2015.

[27] G. Grimvall. The Electron-Phonon Interaction in Normal Metals. *Physica Scripta*, 14(1-2):63, 1976.

[28] H. Wiesmann, M. Gurvitch, H. Lutz, A. Ghosh, B. Schwarz, Myron Strongin, P. B. Allen, and J. W. Halley. Simple Model for Characterizing the Electrical Resistivity in A15 Superconductors. *Physical Review Letters*, 38(14):782–785, April 1977.

[29] M. Gurvitch. Ioffe-Regel criterion and resistivity of metals. *Physical Review B*, 24(12):7404–7407, December 1981.

[30] M. Calandra and O. Gunnarsson. Saturation of Electrical Resistivity in Metals at Large Temperatures. *Physical Review Letters*, 87(26):266601, December 2001.

[31] M. Calandra and O. Gunnarsson. Electrical resistivity at large temperatures: Saturation and lack thereof. *Physical Review B*, 66(20):205105, November 2002.

[32] O. Gunnarsson, M. Calandra, and J. E. Han. Saturation of electrical resistivity. *Reviews of Modern Physics*, 75(4):1085–1099, October 2003.

[33] P. B. Allen, J. C. K. Hui, W. E. Pickett, C. M. Varma, and Z. Fisk. Anharmonicity as an explanation for anomalous resistance of high-Tc superconductors. *Solid State Communications*, 18(9):1157–1159, January 1976.

[34] P. Logg. *Superconductivity in the proximity of a quantum critical point*. PhD thesis, University of Cambridge, 2014.

[35] P. B. Allen and R. C. Dynes. Transition temperature of strong-coupled superconductors reanalyzed. *Physical Review B*, 12(3):905–922, August 1975.

[36] Y. Zou. *Quantum Critical Phenomena in Intermetallic Compounds*. PhD thesis, Cambridge University, 2014.

[37] *S700X SQUID Magnetometer User Manual v0.96*. Cryogenic Ltd., 2012.

[38] I. R. Walker. Nonmagnetic piston cylinder pressure cell for use at 35 kbar and above. *Review of Scientific Instruments*, 70(8):3402, 1999.

[39] A. Eiling and J. S. Schilling. Pressure and temperature dependence of electrical resistivity of Pb and Sn from 1-300k and 0-10 GPa - use as continuous resistive pressure monitor accurate over wide temperature range; superconductivity under pressure in Pb, Sn and In. *Journal of Physics F: Metal Physics*, 11(3):623, 1981.

[40] M. I. Eremets. *High Pressure Experimental Methods*. Oxford University Press, Oxford, New York, February 1996.

[41] D. J. Dunstan and I. L. Spain. Technology of diamond anvil high-pressure cells: I. Principles, design and construction. *Journal of Physics E: Scientific Instruments*, 22(11):913, 1989.

[42] Patricia Lebre Alireza and Gilbert George Lonzarich. Miniature anvil cell for high-pressure measurements in a commercial superconducting quantum interference device magnetometer. *Review of Scientific Instruments*, 80(2):023906, February 2009.

[43] H. K. Mao, J. Xu, and P. M. Bell. Calibration of the ruby pressure gauge to 800 kbar under quasi-hydrostatic conditions. *Journal of Geophysical Research: Solid Earth*, 91(B5):4673–4676, April 1986.

[44] L Shubnikov and W. J. de Haas. A New Phenomenon in the Change of Resistance in a Magnetic Field of Single Crystals of Bismuth. *Nature*, 126:500, 1930.

[45] W. J. de Haas and P. M. van Alphen. *Proc. Netherlands Roy. Acad. Sci.*, 33:1106, 1930.

[46] F. Y. Yang, Kai Liu, Kimin Hong, D. H. Reich, P. C. Searson, and C. L. Chien. Large Magnetoresistance of Electrodeposited Single-Crystal Bismuth Thin Films. *Science*, 284(5418):1335–1337, May 1999.

[47] F. Yang, Kai Liu, Kimin Hong, D. Reich, P. Searson, C. Chien, Y. Leprince-Wang, Kui Yu-Zhang, and Ke Han. Shubnikov-de Haas oscillations in electrodeposited single-crystal bismuth films. *Phys. Rev. B*, 61(10):6631–6636, March 2000.

[48] N. C. Norman. *Chemistry of Arsenic, Antimony and Bismuth*. Springer Science & Business Media, December 1997. Google-Books-ID: vVhpurkfeN4C.

[49] Yuki Fuseya, Masao Ogata, and Hidetoshi Fukuyama. Transport Properties and Diamagnetism of Dirac Electrons in Bismuth. *Journal of the Physical Society of Japan*, 84(1):012001, December 2014.

[50] A. B. Shick, J. B. Ketterson, D. L. Novikov, and A. J. Freeman. Electronic structure, phase stability, and semimetal-semiconductor transitions in Bi. *Phys. Rev. B*, 60(23):15484–15487, December 1999.

[51] Ph. Hofmann. The surfaces of bismuth: Structural and electronic properties. *Progress in Surface Science*, 81(5):191–245, 2006.

[52] Yi Liu and Roland E. Allen. Electronic structure of the semimetals Bi and Sb. *Physical Review B*, 52(3):1566–1577, July 1995.

[53] V.S. Edel'man. Electrons in bismuth. *Advances in Physics*, 25(6):555–613, November 1976.

[54] J.-P. Michenaud and J.-P. Issi. Electron and hole transport in bismuth. *Journal of Physics C: Solid State Physics*, 5(21):3061, 1972.

[55] M. P. Vecchi and M. S. Dresselhaus. Temperature dependence of the band parameters of bismuth. *Phys. Rev. B*, 10(2):771–774, July 1974.

[56] Brage Norin. Temperature and Pressure Dependence of the Band Structure in Bismuth. *Phys. Scr.*, 15(5-6):341–348, May 1977.

[57] D. Balla and N. B. Brandt. Investigation of the effect of uniform compression on the temperature dependence of the electrical Conductivity of bismuth. *Soviet Physics JETP*, 20(5):1111, 1965.

[58] Aurelie Collaudin, Benoit Fauque, Yuki Fuseya, Woun Kang, and Kamran Behnia. Angle Dependence of the Orbital Magnetoresistance in Bismuth. *Physical Review X*, 5(2):021022, June 2015.

[59] Kamran Behnia, Marie-Aude Measson, and Yakov Kopelevich. Oscillating Nernst-Ettingshausen Effect in Bismuth across the Quantum Limit. *Physical Review Letters*, 98(16):166602, April 2007.

[60] Zengwei Zhu, Benoit Fauque, Liam Malone, Arlei Borba Antunes, Yuki Fuseya, and Kamran Behnia. Landau spectrum and twin boundaries of bismuth in the extreme quantum limit. *Proceedings of the National Academy of Sciences of the United States of America*, 109(37):14813–14818, September 2012.

[61] L. Li, J. G. Checkelsky, Y. S. Hor, C. Uher, A. F. Hebard, R. J. Cava, and N. P. Ong. Phase Transitions of Dirac Electrons in Bismuth. *Science*, 321(5888):547–550, July 2008.

[62] Zengwei Zhu, Aurelie Collaudin, Benoit Fauque, Woun Kang, and Kamran Behnia. Field-induced polarization of Dirac valleys in bismuth. *Nature Physics*, 8(1):89–94, January 2012.

[63] R. Kuchler, L. Steinke, R. Daou, M. Brando, K. Behnia, and F. Steglich. Thermodynamic evidence for valley-dependent density of states in bulk bismuth. *Nature Materials*, 13(5):461–465, March 2014.

[64] Om Prakash, Anil Kumar, A. Thamizhavel, and S. Ramakrishnan. Discovery of superconductivity in pure Bi single crystal. *arXiv:1603.04310 [cond-mat]*, March 2016. arXiv: 1603.04310.

[65] B. Weitzel and H. Micklitz. Superconductivity in granular systems built from well-defined rhombohedral Bi-clusters: Evidence for Bi-surface superconductivity. *Physical Review Letters*, 66(3):385–388, January 1991.

[66] Zaahel Mata-Pinzon, Ariel A. Valladares, Renela M. Valladares, and Alexander Valladares. Superconductivity in Bismuth. A New Look at an Old Problem. *PLOS ONE*, 11(1):e0147645, January 2016.

[67] P. Kapitza. The Study of the Specific Resistance of Bismuth Crystals and Its Change in Strong Magnetic Fields and Some Allied Problems. *Proceedings of the Royal Society of London A: Mathematical, Physical and Engineering Sciences*, 119(782):358–443, June 1928.

[68] W. F. Berg. Mechanical Twinning in Bismuth Crystals. *Nature*, 134:143–143, 1934.

[69] E. O. Hall. *Twinning and Diffusionless Transformations in Metals*. Butterworth Scientific, London, 1954.

[70] Rodney Brown. Shubnikov-de Haas Measurements in Bismuth. *Phys. Rev. B*, 2(4):928–938, August 1970.

[71] Ulrich Haussermann, Karin Soderberg, and Rolf Norrestam. Comparative Study of the High-Pressure Behavior of As, Sb, and Bi. *Journal of the American Chemical Society*, 124(51):15359–15367, December 2002.

[72] G. Andersson, B. Sundqvist, and G. Backstrom. A high-pressure cell for electrical resistance measurements at hydrostatic pressures up to 8 GPa: Results for Bi, Ba, Ni, and Si. *Journal of Applied Physics*, 65(10):3943–3950, May 1989.

[73] R. Jaggi, A.L. Jain, and H. Weibel. Pressure dependence of the galvanomagnetic effects in bismuth. *Physics Letters*, 7(3):181–182, November 1963.

[74] N. B. Brandt, Y. P Gaidukov, E. S. Itskevich, and N. Y. Minina. Influence of pressure on oscillation effects in bismuth. *Soviet Physics JETP*, 20(2):301, 1965.

[75] E. S. Itskevich, I. P. Krechetova, and L. M. Fisher. Deformation of the bismuth Fermi surface by pressures up to 8 kbar. *Soviet Physics JETP*, 25(1):41, 1967.

[76] E. S. Itskevich and L. M. Fisher. Change of the parameters of the electron energy spectrum in bismuth under pressure. *Soviet Physics JETP*, 26(6):1072, 1968.

[77] E. S. Itskevich and L. M. Fisher. Shubnikov-de Haas effect in bismuth under a pressure of 15 kbar. *Soviet Physics JETP*, 26(1):66, 1968.

[78] P. C. Souers and G. Jura. Negative Temperature Coefficient of Resistance in Bismuth I. *Science*, 143(3605):467–469, January 1964.

[79] V. A. Venttsel and A. V. Rahkmanina. Semimetal-semiconductor transition in bismuth under the Influence of pressure. *Soviet Physics - Solid State*, 14(9):2325, 1973.

[80] N. B. Brandt, K. Dittman, and Y. G. Ponomarev. Metal-semiconductor transitions in BiSb alloys under pressure. *Soviet Physics - Solid State*, 13(10):2408, 1972.

[81] W. Kraak, R. Herrmann, and H. Haupt. Investigation of the Charge Carrier Scattering in Bi under High Hydrostatic Pressure. *phys. stat. sol. (b)*, 109(2):785–792, February 1982.

[82] C. Uher and W. P. Pratt. High-Precision, Ultralow-Temperature Resistivity Measurements on Bismuth. *Physical Review Letters*, 39(8):491–494, August 1977.

[83] N. B. Brandt and Y. G. Ponomarev. Concerning the effect of pressure on the energy spectrum of the electrons in bismuth-antimony alloys. *Soviet Physics JETP*, 23(2):244, 1966.

[84] N. B. Brandt, R Muller, and Ya. G. Ponomarev. An investigation of the dispersion law for carriers in bismuth doped with acceptor-type impurities. *Sov. Phys. JETP*, 44(6):1196, 1976.

[85] H. Kruger, R. Herrmann, B. Fellmuth, and W. Kraak. Measurement of the Cyclotron Masses in n-Conducting BiSb under High Hydrostatic Pressure. *physica status solidi (b)*, 93(2):661–667, June 1979.

[86] L. S. Lerner, K. F. Cuff., and L. R. Williams. Energy-Band Parameters and Relative Band-Edge Motions in the Bi-Sb Alloy System near the Semimetal—Semiconductor Transition. *Reviews of Modern Physics*, 40(4):770–775, October 1968.

[87] Stuart Golin. Band Structure of Bismuth: Pseudopotential Approach. *Physical Review*, 166(3):643–651, February 1968.

[88] Jeffrey C. Y. Teo, Liang Fu, and C. L. Kane. Surface states and topological invariants in three-dimensional topological insulators: Application to $Bi_{1-x}Sb_x$. *Physical Review B*, 78(4):045426, July 2008.

[89] D. Hsieh, D. Qian, L. Wray, Y. Xia, Y. S. Hor, R. J. Cava, and M. Z. Hasan. A topological Dirac insulator in a quantum spin Hall phase. *Nature*, 452(7190):970–974, April 2008.

[90] C. A. Hoffman, J. R. Meyer, F. J. Bartoli, A. Di Venere, X. J. Yi, C. L. Hou, H. C. Wang, J. B. Ketterson, and G. K. Wong. Semimetal-to-semiconductor transition in bismuth thin films. *Physical Review B*, 48(15):11431–11434, October 1993.

[91] Mei Lu, R. Zieve, A. van Hulst, H. Jaeger, T. Rosenbaum, and S. Radelaar. Low-temperature electrical-transport properties of single-crystal bismuth films under pressure. *Phys. Rev. B*, 53(3):1609–1615, January 1996.

[92] Xu Du, Shan-Wen Tsai, Dmitrii Maslov, and Arthur Hebard. Metal-Insulator-Like Behavior in Semimetallic Bismuth and Graphite. *Physical Review Letters*, 94(16), April 2005.

[93] A. A. Abrikosov. Transition of a bismuth-type semimetal to an excitonic insulator in a strong magnetic field. *J Low Temp Phys*, 10(1-2):3–34, January 1973.

[94] Joel Moore. Topological insulators: The next generation. *Nature Physics*, 5(6):378–380, June 2009.

[95] Hongjian Du, Xia Sun, Xiaogang Liu, Xiaojun Wu, Jufeng Wang, Mingyang Tian, Aidi Zhao, Yi Luo, Jinlong Yang, Bing Wang, and J. G. Hou. Surface Landau levels and spin states in bismuth (111) ultrathin films. *Nature Communications*, 7:10814, March 2016.

[96] Christian R. Ast and Hartmut Hochst. Fermi Surface of Bi(111) Measured by Photoemission Spectroscopy. *Physical Review Letters*, 87(17):177602, October 2001.

[97] Akinori Tanaka, Masayuki Hatano, Kazutoshi Takahashi, Hiroyuki Sasaki, Shoji Suzuki, and Shigeru Sato. Bulk and surface electronic structures of the semimetal Bi studied by angle-resolved photoemission spectroscopy. *Physical Review B*, 59(3):1786–1791, January 1999.

[98] Christian R. Ast and Hartmut Hochst. Electronic structure of a bismuth bilayer. *Physical Review B*, 67(11):113102, March 2003.

[99] S. Agergaard, Ch Sondergaard, H. Li, M. B. Nielsen, S. V. Hoffmann, Z. Li, and Ph Hofmann. The effect of reduced dimensionality on a semimetal: the electronic structure of the Bi(110) surface. *New Journal of Physics*, 3(1):15, 2001.

[100] Y. Ohtsubo, J. Mauchain, J. Faure, E. Papalazarou, M. Marsi, P. Le Fevre, F. Bertran, A. Taleb-Ibrahimi, and L. Perfetti. Giant Anisotropy of Spin-Orbit Splitting at the Bismuth Surface. *Physical Review Letters*, 109(22):226404, November 2012.

[101] Yu. M. Koroteev, G. Bihlmayer, J. E. Gayone, E. V. Chulkov, S. Blugel, P. M. Echenique, and Ph. Hofmann. Strong Spin-Orbit Splitting on Bi Surfaces. *Physical Review Letters*, 93(4):046403, July 2004.

[102] T. Hirahara, T. Nagao, I. Matsuda, G. Bihlmayer, E. V. Chulkov, Yu. M. Koroteev, P. M. Echenique, M. Saito, and S. Hasegawa. Role of Spin-Orbit Coupling and Hybridization Effects in the Electronic Structure of Ultrathin Bi Films. *Physical Review Letters*, 97(14):146803, October 2006.

[103] T. Hirahara, K. Miyamoto, I. Matsuda, T. Kadono, A. Kimura, T. Nagao, G. Bihlmayer, E. V. Chulkov, S. Qiao, K. Shimada, H. Namatame, M. Taniguchi, and S. Hasegawa. Direct observation of spin splitting in bismuth surface states. *Physical Review B*, 76(15):153305, October 2007.

[104] Wei Ning, Fengyu Kong, Chuanying Xi, David Graf, Haifeng Du, Yuyan Han, Jiyong Yang, Kun Yang, Mingliang Tian, and Yuheng Zhang. Evidence of Topological Two-Dimensional Metallic Surface States in Thin Bismuth Nanoribbons. *ACS Nano*, 8(7):7506–7512, July 2014.

[105] Wei Ning, Fengyu Kong, Yuyan Han, Haifeng Du, Jiyong Yang, Mingliang Tian, and Yuheng Zhang. Robust surface state transport in thin bismuth nanoribbons. *Scientific Reports*, 4:7086, November 2014.

[106] Shunhao Xiao, Dahai Wei, and Xiaofeng Jin. Bi(111) Thin Film with Insulating Interior but Metallic Surfaces. *Physical Review Letters*, 109(16):166805, October 2012.

[107] T. Hirahara, I. Matsuda, S. Yamazaki, N. Miyata, S. Hasegawa, and T. Nagao. Large surface-state conductivity in ultrathin Bi films. *Applied Physics Letters*, 91(20):202106, November 2007.

[108] Yin Shu-Li, Liang Xue-Jin, and Zhao Hong-Wu. Effect of a Highly Metallic Surface State on the Magneto-Transport Properties of Single Crystal Bi Films. *Chinese Physics Letters*, 30(8):087305, 2013.

[109] Babak Seradjeh, Jiansheng Wu, and Philip Phillips. Signatures of Surface States in Bismuth at High Magnetic Fields. *Physical Review Letters*, 103(13):136803, September 2009.

[110] Yoshiyuki Ohtsubo, Luca Perfetti, Mark Oliver Goerbig, Patrick Le Fevre, Francois Bertran, and Amina Taleb-Ibrahimi. Non-trivial surface-band dispersion on Bi(111). *New Journal of Physics*, 15(3):033041, 2013.

[111] L. Perfetti, J. Faure, E. Papalazarou, J. Mauchain, M. Marsi, M. O. Goerbig, A. Taleb-Ibrahimi, and Y. Ohtsubo. New aspects of electronic excitations at the bismuth surface: Topology, thermalization and coupling to coherent phonons. *Journal of Electron Spectroscopy and Related Phenomena*, 201:60–65, May 2015.

[112] S. Ito, B. Feng, M. Arita, A. Takayama, R.-Y. Liu, T. Someya, W.-C. Chen, T. Iimori, H. Namatame, M. Taniguchi, C.-M. Cheng, S.-J. Tang, F. Komori, K. Kobayashi, T.-C. Chiang, and I. Matsuda. Proving Nontrivial Topology of Pure Bismuth by Quantum Confinement. *Physical Review Letters*, 117(23):236402, December 2016.

[113] Zheng Liu, Chao-Xing Liu, Yong-Shi Wu, Wen-Hui Duan, Feng Liu, and Jian Wu. Stable Nontrivial Z_2 Topology in Ultrathin Bi (111) Films: A First-Principles Study. *Physical Review Letters*, 107(13):136805, September 2011.

[114] Stuart Golin. Band Model for Bismuth-Antimony Alloys. *Physical Review*, 176(3):830–832, December 1968.

[115] X Gonze, J-P Michenaud, and J-P Vigneron. Ab initio calculations of bismuth properties, including spin-orbit coupling. *Phys. Scr.*, 37(5):785–789, May 1988.

[116] X. Gonze, J.-P. Michenaud, and J.-P. Vigneron. First-principles study of As, Sb, and Bi electronic properties. *Physical Review B*, 41(17):11827–11836, June 1990.

[117] J. H. Xu, E. G. Wang, C. S. Ting, and W. P. Su. Tight-binding theory of the electronic structures for rhombohedral semimetals. *Physical Review B*, 48(23):17271–17279, December 1993.

[118] J. Heremans and O. P. Hansen. Influence of non-parabolicity on intravalley electron-phonon scattering; the case of bismuth. *Journal of Physics C: Solid State Physics*, 12(17):3483, 1979.

[119] J. Heremans and O. P. Hansen. Temperature dependence of excess carrier density and thermopower in tin-doped bismuth. Pseudo-parabolic model. *Journal of Physics C: Solid State Physics*, 16(23):4623, 1983.

[120] Robert Hartman. Temperature Dependence of the Low-Field Galvanomagnetic Coefficients of Bismuth. *Physical Review*, 181(3):1070–1086, May 1969.

[121] Paul Syers, Dohun Kim, Michael S. Fuhrer, and Johnpierre Paglione. Tuning Bulk and Surface Conduction in the Proposed Topological Kondo Insulator SmB_6. *Physical Review Letters*, 114(9):096601, March 2015.

[122] Katsukuni Yoshida. Anomalous Electric Fields in Semimetals under High Magnetic Fields. *Journal of the Physical Society of Japan*, 39(6):1473–1481, December 1975.

[123] Katsukuni Yoshida. An Anomalous Behavior of the Longitudinal Magnetoresistance in Semimetals. *Journal of the Physical Society of Japan*, 41(2):574–581, August 1976.

[124] Xiaochun Huang, Lingxiao Zhao, Yujia Long, Peipei Wang, Dong Chen, Zhanhai Yang, Hui Liang, Mianqi Xue, Hongming Weng, Zhong Fang, Xi Dai, and Genfu Chen. Observation of the chiral anomaly induced negative magneto-resistance in 3d Weyl semi-metal TaAs. *Physical Review X*, 5(3), August 2015. arXiv: 1503.01304.

[125] Hui Li, Hongtao He, Hai-Zhou Lu, Huachen Zhang, Hongchao Liu, Rong Ma, Zhiyong Fan, Shun-Qing Shen, and Jiannong Wang. Negative magnetoresistance in Dirac semimetal Cd3as2. *Nature Communications*, 7:10301, January 2016.

[126] R. D. dos Reis, M. O. Ajeesh, N. Kumar, F. Arnold, C. Shekhar, M. Naumann, M. Schmidt, M. Nicklas, and E. Hassinger. On the search for the chiral anomaly in Weyl semimetals: the negative longitudinal magnetoresistance. *New Journal of Physics*, 18(8):085006, 2016.

[127] Frank Arnold, Chandra Shekhar, Shu-Chun Wu, Yan Sun, Ricardo Donizeth dos Reis, Nitesh Kumar, Marcel Naumann, Mukkattu O. Ajeesh, Marcus Schmidt, Adolfo G. Grushin, Jens H. Bardarson, Michael Baenitz, Dmitry Sokolov, Horst Borrmann, Michael Nicklas, Claudia Felser, Elena Hassinger, and Binghai Yan. Negative magnetoresistance without well-defined chirality in the Weyl semimetal TaP. *Nature Communications*, 7:11615, May 2016.

[128] A. A. Nikolaeva, L. A. Konopko, T. E. Huber, E. P. Sineavsky, R. A. Khamidullin, and A. C. Tsurkan. Negative magnetoresistance in transverse and longitudinal magnetic fields in Bi nanowires. *Journal of Physics: Conference Series*, 150(2):022065, 2009.

[129] Mingliang Tian, Jian Wang, Qi Zhang, Nitesh Kumar, Thomas E. Mallouk, and Moses H. W. Chan. Superconductivity and Quantum Oscillations in Crystalline Bi Nanowire. *Nano Letters*, 9(9):3196–3202, September 2009.

[130] Kevin A. Parendo, L. M. Hernandez, A. Bhattacharya, and A. M. Goldman. Anomalous parallel-field negative magnetoresistance in ultrathin films near the superconductor-insulator transition. *Physical Review B*, 70(21):212510, December 2004.

[131] J. A. Chervenak and J. M. Valles. Absence of a zero-temperature vortex solid phase in strongly disordered superconducting Bi films. *Physical Review B*, 61(14):R9245–R9248, April 2000.

[132] D. B. Haviland, Y. Liu, and A. M. Goldman. Onset of superconductivity in the two-dimensional limit. *Physical Review Letters*, 62(18):2180–2183, May 1989.

[133] P. Bridgman. Polymorphism, Principally of the Elements, up to 50,000 kg/cm^2. *Phys. Rev.*, 48(11):893–906, December 1935.

[134] P. W. Bridgman. The Resistance of 72 Elements, Alloys and Compounds to 100,000 Kg/cm2. *Proc. Am. Acad. Arts Sci.*, 81(4):228, 1952.

[135] N. B. Brandt and N. I. Ginzburg. Investigation of crystalline modifications of bismuth and certain questions in the method of obtaining high pressures at low temperatures. *Soviet Physics - Solid State*, 3(11):2510, 1962.

[136] N. B. Brandt and N. I Ginzburg. Critical fields of the crystalline modifications Bi II and Bi III. *Soviet Physics JETP*, 17(2):326, 1963.

[137] N Lotter and J Wittig. Evidence for an Electronic Phase Transition in Bismuth under Pressure. *Europhysics Letters (EPL)*, 6(7):659–662, August 1988.

[138] M. McMahon, O. Degtyareva, R. Nelmes, S. van Smaalen, and L. Palatinus. Incommensurate modulations of Bi-III and Sb-II. *Phys. Rev. B*, 75(18), May 2007.

[139] F. Bundy. Phase Diagram of Bismuth to 130 000 kg/cm^2, 500 C. *Phys. Rev.*, 110(2):314–318, April 1958.

[140] W. Klement, A. Jayaraman, and G. C. Kennedy. Phase diagram of astatine, antimony, and bismuth at pressures up to 70 kbars. *Phys. Rev.*, 131(2):632, 1963.

[141] M. A. Il'ina and E. S. Itskevich. Phase diagram of bismuth at low temperatures. *Soviet Physics - Solid State*, 8(8):1873, 1967.

[142] Elvin M. Compy. Phase Diagram of Bismuth at Low Temperatures. *Journal of Applied Physics*, 41(5):2014, 1970.

[143] Shasuke Yomo, Nobuo Mari, and Tadayasu Mitsui. Pressure-Temperature Phase Diagram of Bismuth at Low Temperatures. *J. Phys. Soc. Jpn.*, 32(3):667–676, March 1972.

[144] Clarke G Homan. Phase diagram of Bi up to 140 kbars. *Journal of Physics and Chemistry of Solids*, 36(11):1249–1254, November 1975.

[145] M. A. Il'ina and E. S. Itskevich. New superconducting modifications of bismuth. *JETP Lett.*, 11:15, 1970.

[146] John Francis Cannon. Behaviour of the elements at high pressure. *J. Phys. Chem. Ref. Data*, 3(3):781, 1974.

[147] Yufeng Li, Enyu Wang, Xiyu Zhu, and Hai-Hu Wen. Pressure-induced superconductivity in Bi single crystals. *Physical Review B*, 95(2):024510, January 2017.

[148] R. J. Nelmes, D. R. Allan, M. I. McMahon, and S. A. Belmonte. Self-Hosting Incommensurate Structure of Barium IV. *Physical Review Letters*, 83(20):4081–4084, November 1999.

[149] I. Loa, R. J. Nelmes, L. F. Lundegaard, and M. I. McMahon. Extraordinarily complex crystal structure with mesoscopic patterning in barium at high pressure. *Nature Materials*, 11(7):627–632, July 2012.

[150] A. R. Moodenbaugh and Z. Fisk. The electrical resistivity of barium and yttrium at high pressure. *Physics Letters A*, 43(6):479–480, April 1973.

[151] J. Wittig and B. T. Matthias. Superconductivity of Barium Under Pressure. *Physical Review Letters*, 22(13):634–636, March 1969.

[152] J. Wittig. A study of the superconductivity of antimony under pressure and a search for superconductivity in arsenic. *Journal of Physics and Chemistry of Solids*, 30(6):1407–1410, June 1969.

[153] F. Gross, H. Veith, K. Andres, M. Weger, and A. G. McDiarmid. Bulk superconductivity of $Hg_{3-\delta}AsF_6$. *Physical Review B*, 34(5):3503–3505, September 1986.

[154] C. K. Chiang, R. Spal, A. Denenstein, A. J. Heeger, N. D. Miro, and A. G. MacDiarmid. Anomalous electrical properties of linear chain mercury compounds. *Solid State Communications*, 22(5):293–298, May 1977.

[155] I. U. Heilmann, J. D. Axe, J. M. Hastings, G. Shirane, A. J. Heeger, and A. G. MacDiarmid. Neutron investigation of the dynamical properties of the mercury-chain compound $Hg_{3-\delta}AsF_6$. *Physical Review B*, 20(2):751–762, July 1979.

[156] Stewart K. Reed and Graeme J. Ackland. Theoretical and Computational Study of High-Pressure Structures in Barium. *Physical Review Letters*, 84(24):5580–5583, June 2000.

[157] J. J. M. Buiting, M. Weger, and F. M. Mueller. Electronic structure of the incommensurate metal $Hg_{3-\delta}AsF_6$. *Journal of Physics F: Metal Physics*, 14(10):2343, 1984.

[158] R. A. de Groot, J. J. M. Buiting, M. Weger, and F. M. Mueller. Self-consistent electronic-band-structure calculation for $Hg_{3-\delta}AsF_6$. *Physical Review B*, 31(5):2881–2885, March 1985.

[159] J. D. Axe and Per Bak. Long-wavelength excitations in incommensurate intergrowth compounds with application to $Hg_{3-\delta}AsF_6$. *Physical Review B*, 26(9):4963–4973, November 1982.

[160] J. M. Hastings, J. P. Pouget, G. Shirane, A. J. Heeger, N. D. Miro, and A. G. MacDiarmid. One-Dimensional Phonons and "Phase-Ordering" Phase Transition in $Hg_{3-\delta}AsF_6$. *Physical Review Letters*, 39(23):1484–1487, December 1977.

[161] Xi Chen, Dipanshu Bansal, Sean Sullivan, Douglas L. Abernathy, Jianshi Zhou, Olivier Delaire, and Li Shi. Weak coupling of acoustic-like phonons and magnon dynamics in incommensurate spin ladder compound $Sr_{14}Cu_{24}O_{41}$. *arXiv:1605.02133 [cond-mat]*, May 2016. arXiv: 1605.02133.

[162] Olga Degtyareva, Viktor V. Struzhkin, and Russell J. Hemley. High-pressure Raman spectroscopy of antimony: As-type, incommensurate host-guest, and bcc phases. *Solid State Communications*, 141(3):164–167, January 2007.

[163] E.M. Compy. Critical fields of superconducting bismuth at high pressure. *Physics Letters*, 18(3):228–229, September 1965.

[164] Charles Kittel. *Introduction to Solid State Physics, 8th Edition - Charles Kittel*. 2004.

[165] O. Gunnarsson, M. Calandra, and J. E. Han. Colloquium. *Reviews of Modern Physics*, 75(4):1085–1099, October 2003.

[166] John A. Woollam, Robert B. Somoano, and Paul O'Connor. Positive Curvature of the H_{c2}-versus-T_c Boundaries in Layered Superconductors. *Physical Review Letters*, 32(13):712–714, April 1974.

[167] C. K. Jones, J. K. Hulm, and B. S. Chandrasekhar. Upper Critical Field of Solid Solution Alloys of the Transition Elements. *Reviews of Modern Physics*, 36(1):74–76, January 1964.

[168] M. Tinkham. Effect of Fluxoid Quantization on Transitions of Superconducting Films. *Physical Review*, 129(6):2413–2422, March 1963.

[169] E. Helfand and N. R. Werthamer. Temperature and Purity Dependence of the Superconducting Critical Field, H_{c2}. II. *Physical Review*, 147(1):288–294, July 1966.

[170] N. R. Werthamer, E. Helfand, and P. C. Hohenberg. Temperature and Purity Dependence of the Superconducting Critical Field, H_{c2}. III. Electron Spin and Spin-Orbit Effects. *Physical Review*, 147(1):295–302, July 1966.

[171] Seunghyun Khim, Bumsung Lee, Jae Wook Kim, Eun Sang Choi, G. R. Stewart, and Kee Hoon Kim. Pauli-limiting effects in the upper critical fields of a clean LiFeAs single crystal. *Physical Review B*, 84(10):104502, September 2011.

[172] Katsuya Shimizu, Hiroto Ishikawa, Daigoroh Takao, Takehiko Yagi, and Kiichi Amaya. Superconductivity in compressed lithium at 20 K. *Nature*, 419(6907):597–599, October 2002.

[173] Shanti Deemyad and James S. Schilling. Superconducting Phase Diagram of Li Metal in Nearly Hydrostatic Pressures up to 67 GPa. *Physical Review Letters*, 91(16):167001, October 2003.

[174] B. Lorenz and C. W. Chu. High Pressure Effects on Superconductivity. In Prof Dr Anant V. Narlikar, editor, *Frontiers in Superconducting Materials*, pages 459–497. Springer Berlin Heidelberg, 2005.

[175] L. N. Bulaevskii, O. V. Dolgov, and M. O. Ptitsyn. Properties of strong-coupled superconductors. *Physical Review B*, 38(16):11290–11295, December 1988.

[176] M. K. Chan, M. J. Veit, C. J. Dorow, Y. Ge, Y. Li, W. Tabis, Y. Tang, X. Zhao, N. Barisic, and M. Greven. In-Plane Magnetoresistance Obeys Kohler's Rule in the Pseudogap Phase of Cuprate Superconductors. *Physical Review Letters*, 113(17):177005, October 2014.

[177] I. L. Spain and R. O. Dillon. Kohler's rule and other scaling relationships for the magnetoresistance of graphite. *Carbon*, 14(1):23–26, January 1976.

[178] J. R. Waldram. *Superconductivity of Metals and Cuprates*. January 1996.

[179] C. P. Poole. *Handbook of superconductivity*. 1999.

[180] G. W. Webb, F. Marsiglio, and J. E. Hirsch. Superconductivity in the elements, alloys and simple compounds. *Physica C: Superconductivity and its Applications*, 514:17–27, July 2015.

[181] Thorsten Stromberg. *The superconducting properties of high purity niobium*. PhD thesis, Iowa State University, 1965.

[182] S. T. Sekula and R. H. Kernohan. Magnetic Properties of Superconducting Vanadium. *Physical Review B*, 5(3):904–911, February 1972.

[183] G. Kostorz, L. L. Isaacs, R. L. Panosh, and C. C. Koch. Anisotropy of the Upper Critical Field of Superconducting Technetium. *Physical Review Letters*, 27(6):304–307, August 1971.

[184] G. Chanin and J. P. Torre. Critical-Field Curve of Superconducting Lead. *Physical Review B*, 5(11):4357–4364, June 1972.

[185] Katsunori Mori, Norihito Tamura, and Yoshitami Saito. Superconductivity and Electrical Resistivity Saturation in Intermetallic Compound In_5Bi_3. *Journal of the Physical Society of Japan*, 50(4):1275–1280, April 1981.

[186] N. Mori, S. Yomo, and T. Mitsui. The bismuth II-III phase transition at low temperatures. *Physics Letters A*, 34(3):190–191, February 1971.

[187] E. Cruceanu, E. Hering, and H. Schwarz. Electrical conductivity and superconductivity in In5bi3. *Physics Letters A*, 32(5):295–296, August 1970.

[188] H. Ullmaier, R. H. Kernohan, E. Cruceanu, and E. Hering. Superconductivity of In_5Bi_3. *Journal of Low Temperature Physics*, 5(1):71–79, July 1971.

[189] B. J. C. van der Hoeven and P. H. Keesom. Specific Heat of Lead and Lead Alloys Between 0.4 and 4.2 K. *Physical Review*, 137(1A):A103–A107, January 1965.

[190] N. Phillips, M. Lambert, and W. Gardner. Lattice Heat Capacity of Superconducting Mercury and Lead. *Reviews of Modern Physics*, 36(1):131–134, January 1964.

[191] Wing Chi Yu, Yiu Wing Cheung, Paul J. Saines, Masaki Imai, Takuya Matsumoto, Chishiro Michioka, Kazuyoshi Yoshimura, and Swee K. Goh. Strong Coupling Superconductivity in the Vicinity of the Structural Quantum Critical Point in $(\mathrm{ca}_x\mathrm{sr}_{1-x})_3\mathrm{rh}_4\mathrm{sn}_{13}$. *Physical Review Letters*, 115(20):207003, November 2015.

[192] J. S. Shier and D. M. Ginsberg. Superconducting Transitions of Amorphous Bismuth Alloys. *Physical Review*, 147(1):384–391, July 1966.

[193] T. T. Chen, J. T. Chen, J. D. Leslie, and H. J. T. Smith. Phonon Spectrum of Superconducting Amorphous Bismuth and Gallium by Electron Tunneling. *Physical Review Letters*, 22(11):526–530, March 1969.

[194] Kazuo Watanabe, Koshichi Noto, Naoki Toyota, and Yoshio Muto. Upper Critical Fields of Amorphous Bi and Bi-Pb Alloys. *Journal of the Physical Society of Japan*, 53(4):1444–1447, April 1984.

[195] T. Hamada, K. Yamakawa, and F. E. Fujita. Superconductivity of vacuum-deposited bismuth films. *Journal of Physics F: Metal Physics*, 11(3):657, 1981.

[196] Lina E. Klintberg, Swee K. Goh, Patricia L. Alireza, Paul J. Saines, David A. Tompsett, Peter W. Logg, Jinhu Yang, Bin Chen, Kazuyoshi Yoshimura, and F. Malte Grosche. Pressure- and Composition-Induced Structural Quantum Phase Transition in the Cubic Superconductor $(SrCa)_3Ir4Sn_{13}$. *Physical Review Letters*, 109(23):237008, December 2012.

[197] D. A. Tompsett. Electronic structure and phonon instabilities in the vicinity of the quantum phase transition and superconductivity of $(SrCa)_3Ir4Sn_{13}$. *Physical Review B*, 89(7):075117, February 2014.

[198] I. Loa, L. F. Lundegaard, M. I. McMahon, S. R. Evans, A. Bossak, and M. Krisch. Lattice Dynamics of Incommensurate Composite Rb-IV and a Realization of the Monatomic Linear Chain Model. *Physical Review Letters*, 99(3):035501, July 2007.

[199] K. J. Dunn and F. P. Bundy. Pressure-induced superconductivity in strontium and barium. *Physical Review B*, 25(1):194–197, January 1982.

[200] U. Haussermann, O. Degtyareva, A. S. Mikhaylushkin, K. Soderberg, S. I. Simak, M. I. McMahon, R. J. Nelmes, and R. Norrestam. BiSb under high pressure: Effect of alloying on the incommensurate Bi-III type composite structure. *Physical Review B*, 69(13):134203, April 2004.

A Other measurements of the semimetal-semiconductor transition in bismuth

In this section we present additional results on measurements of the Bi-I phase, in a number of other pressure cells, as well as some more results on PCC10. These are qualitatively identical to the measurements of Bi #6.1 and #7.1 presented in Chapter 4.

A.1 Introduction

We have conducted pressure studies of a total of five samples of Bi-I, with varying levels of detail. In this section, we present largely identical plots to those shown in Chapter 4 for the additional samples Bi #1 in PCC1, Bi #2 in PCC2, and Bi #10.11 in PCC111. Where relevant, we also plot some additonal data for PCC10, which may prove useful to future experimentalists.

A.2 Results

Figs. A.1-A.3 show the resistivity for the three additional samples as a function of pressure

Fig. A.4 shows the resistivity at $T = 295$ K. This has been measured by a number of authors [57, 39, 72], as the various high-pressure structural transitions are often used as fixed points for high-pressure calibrations. Qualitatively, our results agree well with previous authors: $\rho(T = 295\,\mathrm{K})$ rises with pressure, by a factor of around $1.5 - 2\times$. As noted by Balla and Brandt, the exact ratio appears to differ (in precisely this range) depending on whether current is applied perpendicular or parallel to the trigonal axis [57]. For all our samples, current is nominally perpendicular to the trigonal axis; however, our samples are twinned. We note that there is significant scatter to the data; in particular, for Bi #1, at $\sim 15 - 20$ kbar there is a marked fall in $\rho(T = 295\,\mathrm{K})$. The reasons for this are unclear. Even for PCC10, where a large number of closely-spaced pressure points were taken, there is not a perfectly monotonic increase with pressure.

The conductivity and resistivity at 4.2 K are shown in Figs. A.5-A.7. As shown in Fig. A.7, the seemingly discontinuous jump in $\sigma_{4.2}$ across $p \approx 20$ kbar is also clearly observed in the detailed data of Bi #1.

Fig. A.8 plots the RRR, on both linear and log scales, for all samples. This could prove to be a useful guide for future experimentalists. The RRR falls quite rapidly as soon as the cell is pressurised. The upturn in the low-temperature resistivity occurs quite reliably at $p = 20 \pm 1$ kbar.

In Fig. A.9, we show the carrier density obtained by comparing our $\rho(T)$ to the scattering data of Armitage *et al.*; as found for the samples in PCC10, the results appear rather unphysical.

Fig. A.10 attempts Arrhenius plots for the three other samples. The marked saturation in $\rho(T)$ below $T \approx 10$ K at higher pressures is very clearly visible in the data of Bi #1.

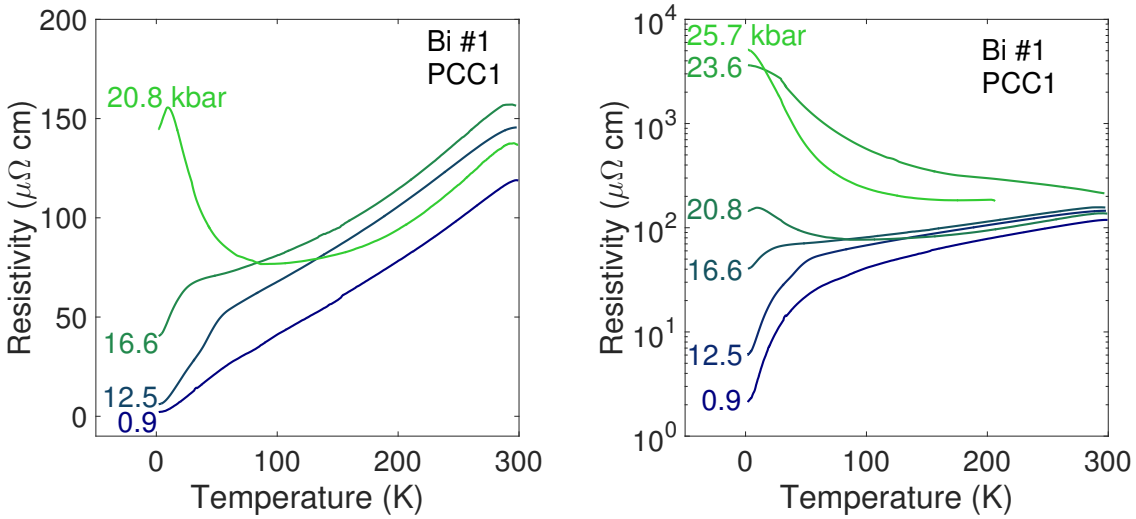

Figure A.1: Temperature dependence of the resistivity for sample Bi #1 in PCC1, on normal (left) and semilog (right) axes (note that the normal axes do not include traces at the highest pressure as these obscure the data).

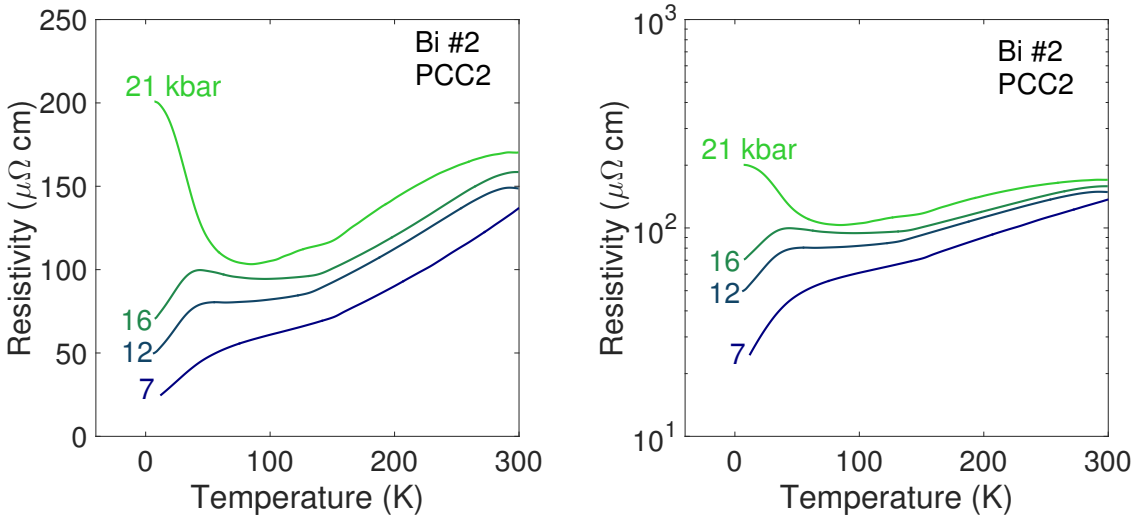

Figure A.2: Temperature dependence of the resistivity for sample Bi #2 in PCC2, on normal (left) and semilog (right) axes.

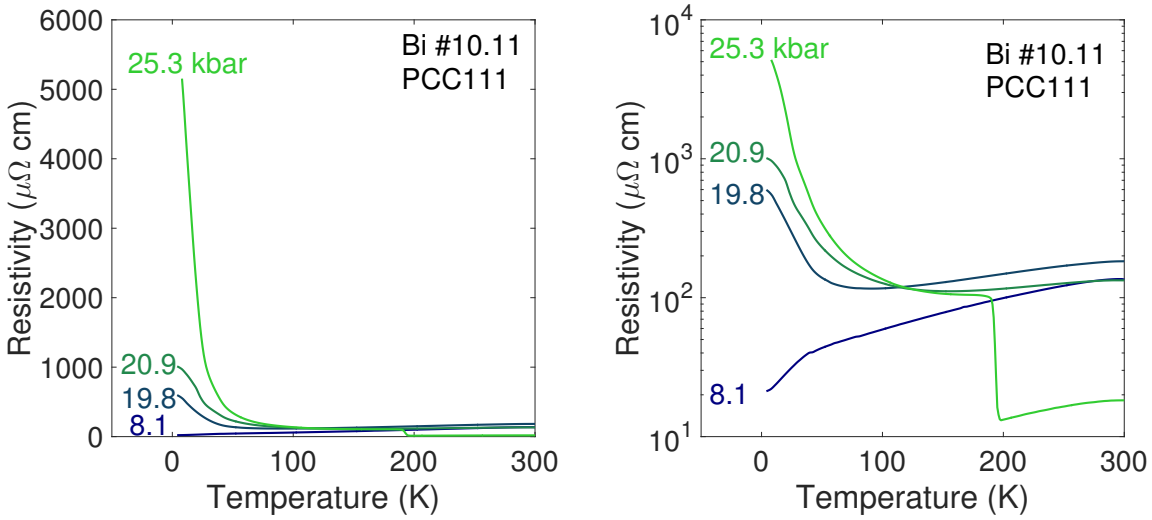

Figure A.3: Temperature dependence of the resistivity for sample Bi #10.11 in PCC111, on normal (left) and semilog (right) axes. In the 25.3 kbar trace, the sharp jump at $T \approx 200$ K corresponds to the II-I structural phase transition.

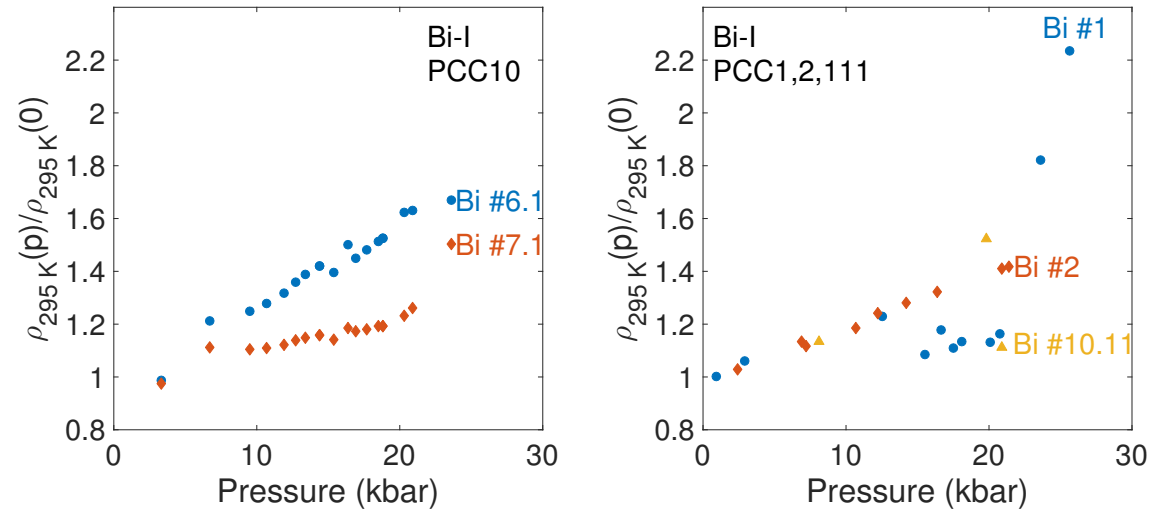

Figure A.4: Pressure dependence of the ratio of the resistivity at 295 K under pressure to the literature value at zero pressure, for (left) samples in PCC10 (blue circles: Bi #6.1; red triangles: Bi #7.1) and (right) samples in other cells (blue circles: Bi #1; red triangles: Bi #2; yellow triangles: Bi #10.11).

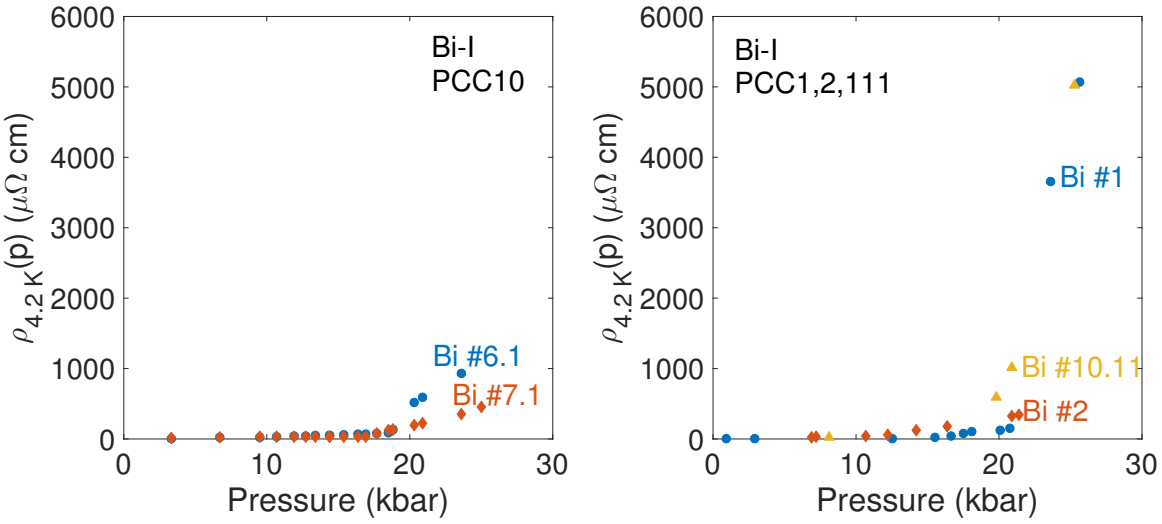

Figure A.5: Pressure dependence of the resistivity at 4.2 K under pressure, for (left) samples in PCC10 (blue circles: Bi #6.1; red triangles: Bi #7.1) and (right) samples in other cells (blue circles: Bi #1; red triangles: Bi #2; yellow triangles: Bi #10.11).

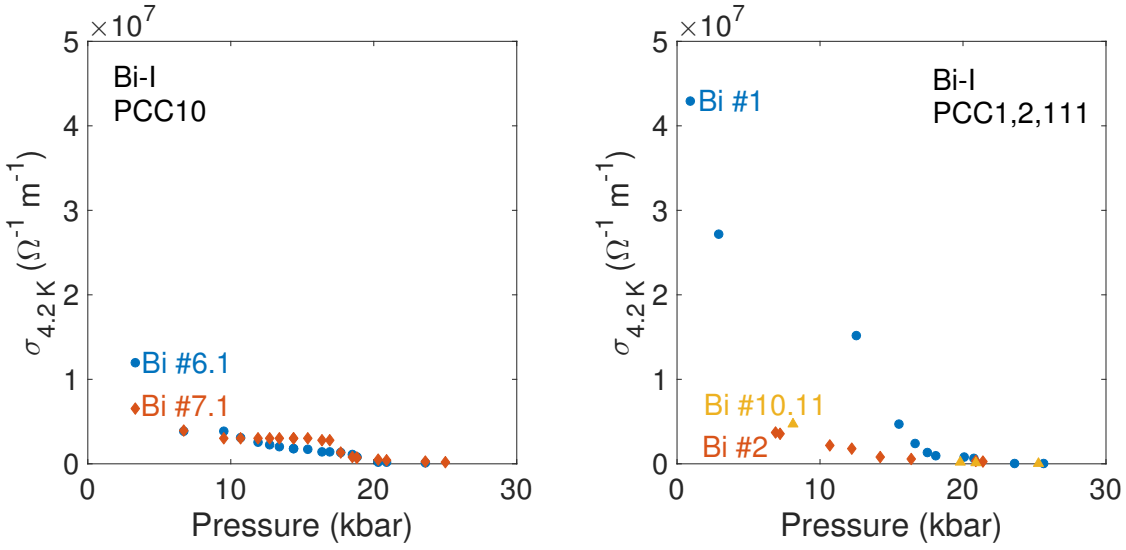

Figure A.6: Pressure dependence of the conductivity $\sigma_{4.2\,K} = 1/\rho_{4.2\,K}$ at 4.2 K under pressure, for (left) samples in PCC10 (blue circles: Bi #6.1; red triangles: Bi #7.1) and (right) samples in other cells (blue circles: Bi #1; red triangles: Bi #2; yellow triangles: Bi #10.11).

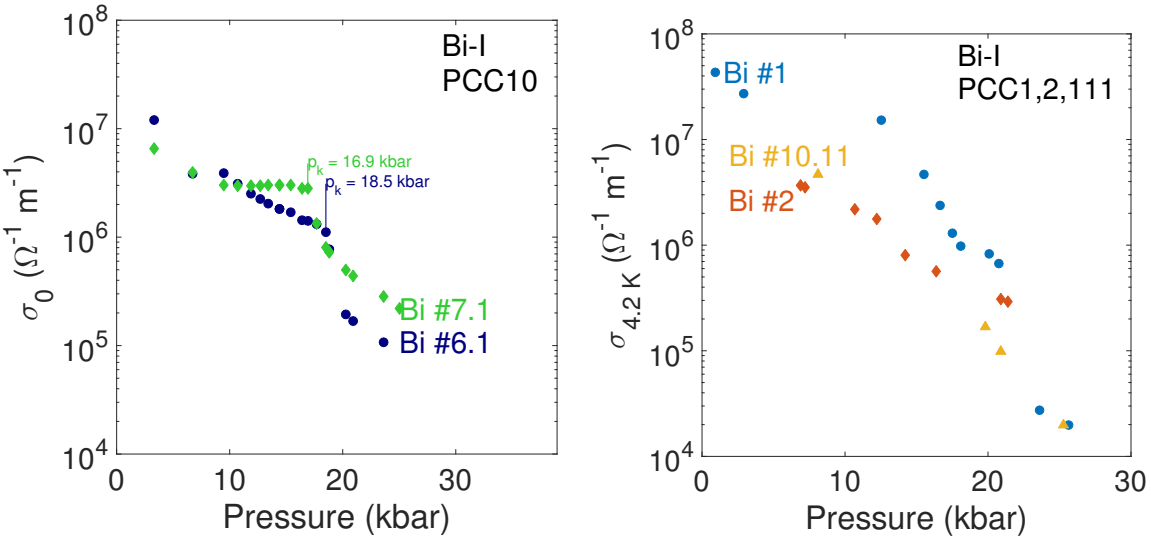

Figure A.7: Pressure dependence of the conductivity $\sigma_{4.2\,\mathrm{K}} = 1/\rho_{4.2\,\mathrm{K}}$ at 4.2 K under pressure with logarithmic y-axis, for (left) samples in PCC10 (blue circles: Bi #6.1; red triangles: Bi #7.1) and (right) samples in other cells (blue circles: Bi #1; red triangles: Bi #2; yellow triangles: Bi #10.11).

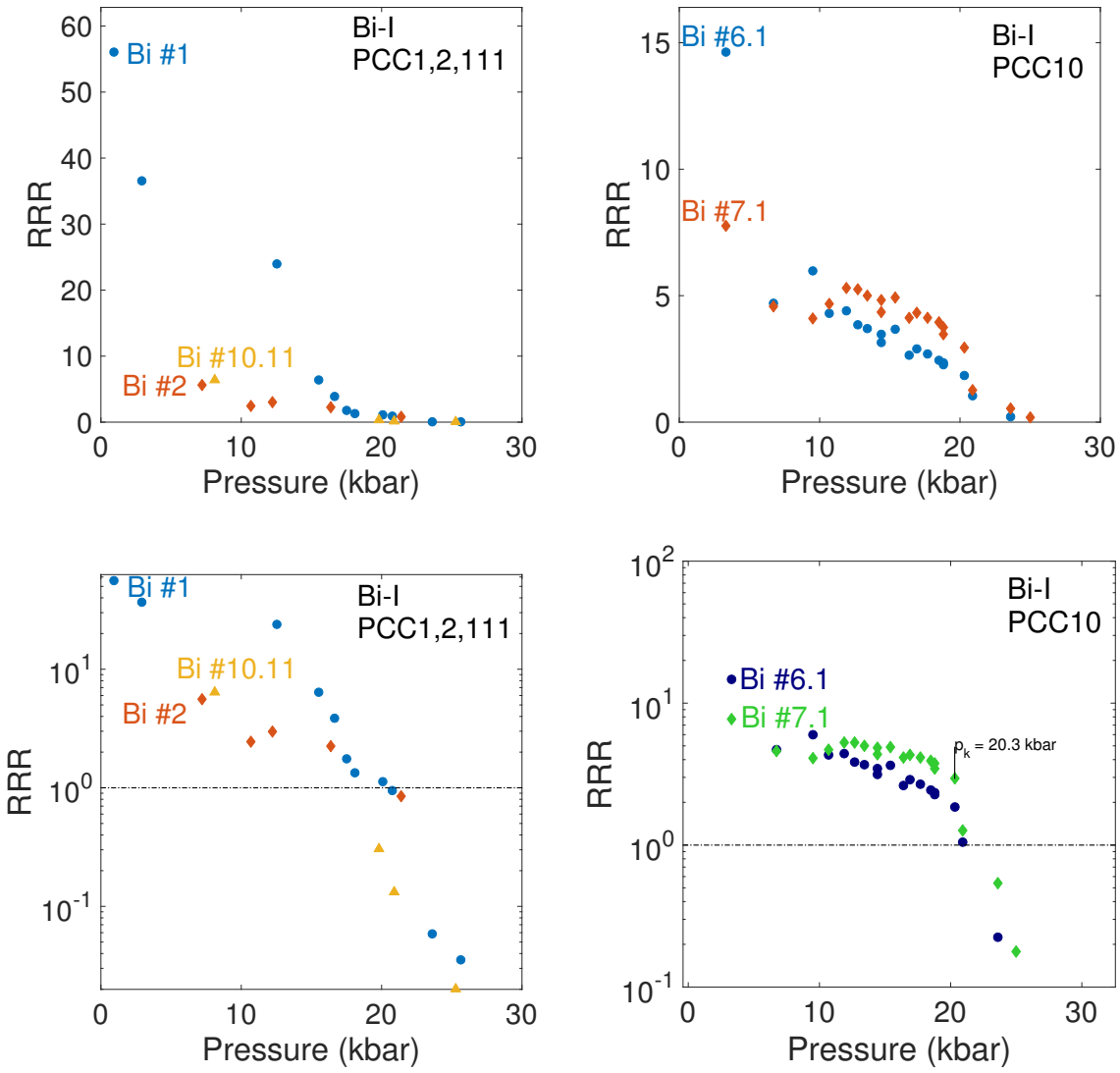

Figure A.8: Pressure dependence of the residual resistance ratio RRR $= \rho_{300}/\rho_0$ for samples in PCC1,2 and 111 (left) and PCC10 (right), on linear (top) and logarithmic (bottom) scales. The dashed line at RRR$= 1$ on the log-scale plots indicates approximately the transition between "metallic" behaviour ($\rho(T)$ increasing with T) to "semiconducting" behaviour ($\rho(T)$ falling with T).

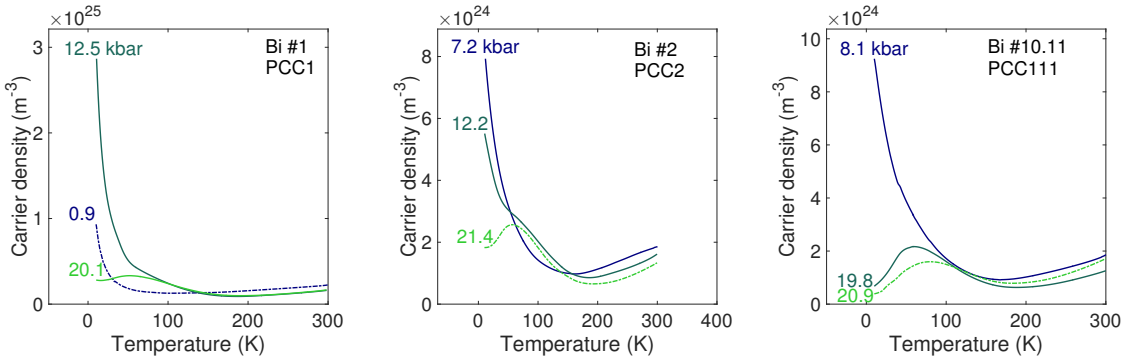

Figure A.9: Carrier density obtained from the combination of our resistivity data and Armitage's optical scattering data. Dashed lines indicate pressures that are either quite distant from a measurement by Armitage, or extrapolations to higher pressure.

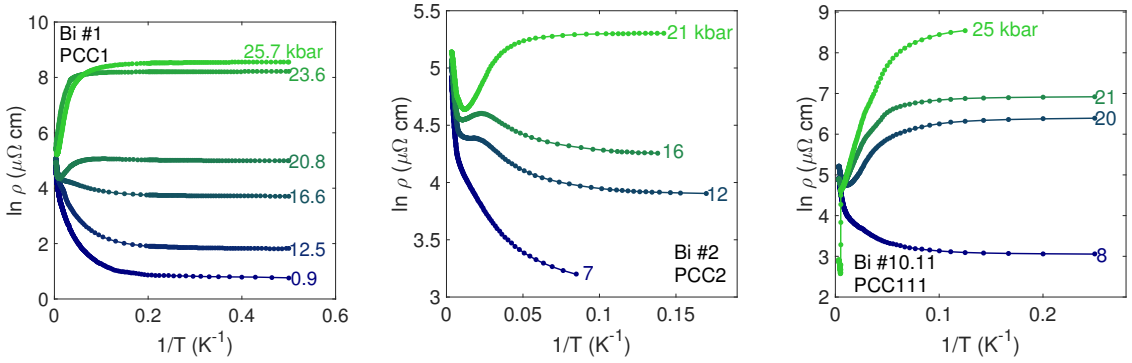

Figure A.10: Arrhenius plots for $\rho(T)$ for several bismuth samples at a number of pressures: Bi #1 (left), Bi #2 (center) and Bi #10.11 (right).